Measuring and Modeling Viscoelastic Relaxation of the Lithosphere with Application to the Northern Volcanic Zone, Iceland

Thesis by

Christopher J. DiCaprio

In Partial Fulfillment of the Requirements

for the Degree of

Doctor of Philosophy

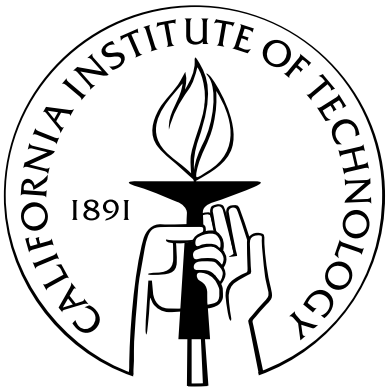

California Institute of Technology

Pasadena, California

2010

(Defended June 29, 2009)

© 2010

Christopher J. DiCaprio

All Rights Reserved

Acknowledgements

In thinking about who has played a role in my arrival at this point, I have come to realize just how many people it took to get here. Mark Simons has been my research adviser during my time at Caltech and has had a hand in all of the work presented in this thesis. He has allowed and encouraged me to pursue my scientific interests and guided my growth as a scientist. I have found his insight and disciplined approach to science to be invaluable. In addition, I have enjoyed working with members of our research group. Current members are Ravi Kanda, Nina Lin, Belle Philibosian, Sarah Minson, and Francisco Ortega. Matt Pritchard, Rowena Lohman, and Brian Savage where there to guide me in in the early stages of my graduate school career. Special thanks must go to Eric Hetland for his help with a large portion of this work. I have also benefited from working with Shelley Kenner, Charles Williams, and Paul Rosen. I would also like to thank the members of my thesis committee, Mike Gurnis, Jean-Philippe Avouac, and Tom Heaton who has also served as my academic adviser. Hans Fleischmann, Professor Emeritus of Applied and Engineering Physics at Cornell University, was my adviser during my undergraduate study and I owe him a large debt of gratitude for his encouragement during my time at Cornell. The Gordon and Betty Moore Foundation funded the first four years of my graduate study through the Moore/Richter fellowship.

This work would not have been possible without the assistance of Viola Carter and

Rosemary Miller – nothing gets done without them. Also, Mike Black and Scott Dungan have proven to be excellent system administrators. Both of them have spent many hours restoring computers to a working state after I brought them crashing to a halt.

I have to mention some very good friends. Mike and Jim, who decided, along with me, that California was a good idea after spending four years in upstate New York – thanks for the bike rides. I have made many friends while at Caltech. Specifically Paula, Igor, Nathan, Nicole, Vala, and Angel. Vala and Angel have been a second family to Lydia and me – thanks for the delicious meals, the bike rides, and all the rest.

My parents, Ralph and Laura DiCaprio, have provided the inspiration, encouragement, and support my entire life to pursue science (not to mention the fact that they paid for my undergraduate education). And of course, I must mention my wife, Lydia. Lydia is an intellectual partner, companion, and friend. I would, quite literally, not be where I am today if it were not for her. Thank you.

Abstract

Viscoelastic relaxation of the stress perturbation caused by an earthquake or diking event can produce measurable ground deformation over 100 km away from the source. We consider the role of viscoelastic relaxation in two different contexts. First, we explore the role that post-seismic relaxation may play in loading a fault over the entire seismic cycle. Viscous relaxation recycles the stress that is shed by the co-seismic fault, acting to reload the fault with stresses in a non-linear fashion. Under conditions of rapid post-seismic relaxation and slow tectonic loading, stress recycling via viscoelastic relaxation can lead to clustering of earthquakes in time. The second context in which we consider viscoelastic relaxation involves the lithospheric response to a mid-ocean ridge rifting episode in Northern Iceland. The diking and subsequent relaxation act as a natural rock mechanics experiment, and in measuring and modeling the post-rifting response we aim to constrain the rheological properties of the Icelandic lithosphere. In order to use post-seismic or post-rifting relaxation to probe properties of the lithosphere, we must be able to precisely measure surface deformation. To that end, we have developed a couple of new interferometric synthetic aperture radar (InSAR) processing approaches: (1) Automatically producing multiple interferograms in a common coordinate system and (2) removing displacements caused by ocean tidal loading from InSAR observations. Both of these developments are essential as we begin to consider the systematic use of tens to hundreds of interferograms.

Contents

Acknowledgements **iii**

Abstract **v**

1 Introduction **1**

1.1 Geodynamics and Geodesy 1

1.2 Thesis Overview 4

2 Post-seismic Reloading and Temporal Clustering on a Single Fault **6**

2.1 Note 6

2.2 Summary 6

2.3 Introduction 7

2.4 Methods 10

2.4.1 Lithospheric Model 10

2.4.2 Clustering Metric 13

2.5 Results 15

2.5.1 Two-Layer Model 15

2.5.2 Three-Layer Model 16

2.6 Discussion 17

2.7 Conclusions 24

3 InSAR Methods **41**

3.1 Introduction 41

3.2 Stack Processing 42

3.3 MInTS 45

4 Importance of Ocean Tidal Load Corrections for Differential InSAR **54**

4.1 Note 54

4.2 Abstract 54

4.3 Introduction 55

4.4 Examples 57

4.5 Conclusions 61

5 The Krafla Volcanic System **66**

5.1 Iceland: Divergent Boundary Laboratory 66

5.2 Geologic Setting 68

5.3 The 1975 – 1984 Krafla Fires 70

5.4 Post-Rifting Deformation in the NVZ 71

5.5 Other Measurements of Iceland Rheology 73

6 InSAR Observations of Post-Rifting Deformation in the Northern Volcanic Zone, Iceland **78**

6.1 Introduction 78

6.2 Characteristic Interferograms: Qualitative Analysis 79

6.3 Rift Perpendicular Profile 81

6.3.1 Introduction 81

6.3.2 Methods 82

6.3.3 Results 85

6.4 GPS 86

6.5 Time Series Analysis of Full Interferograms: MInTS 86

6.6 Discussion and Conclusions 89

7 Modeling Post-Rifting Relaxation in the Northern Volcanic Zone, Iceland 127

7.1 Introduction 127

7.2 The Structure of the Icelandic Lithosphere 130

7.3 Methods 133

7.3.1 Model Spin-up 134

7.4 Two-Dimensional Models 135

7.4.1 Two-Layer Models 135

7.4.1.1 Laterally Homogeneous Models 136

7.4.1.2 Heterogeneous Structure Below Fissure Swarm 137

7.4.2 Models with Dipping Moho 139

7.5 Three-Dimensional Models 140

7.6 Elastic Models 143

7.7 Discussion and Conclusions 144

List of Figures

2.1 Lithospheric model cross-section 27

2.2 Cumulative stress released on the fault 28

2.3 Distribution of normalized interseismic intervals 29

2.4 Amount of clustering versus W_{KS05} for two-layer models 30

2.5 Distribution of normalized interseismic intervals and Cumulative stress released on the fault 31

2.6 Amount of clustering in an earthquake sequence 32

2.7 Amount of clustering in an earthquake sequence 33

2.8 Distribution of normalized, logarithmic interseismic times for several values of W 34

2.9 The ratio of the number of intra-cluster earthquakes to the inter-cluster earthquakes as a function of the fraction of noise 35

2.10 Distribution of normalized interseismic times for three-layer models 36

2.11 Average shear stress over the coseismic fault for two earthquake sequences . . 37

2.12 Strain energy and yield stress perturbation 38

2.13 Average shear stress over coseismic fault as a function of time 39

3.1 Two-pass InSAR processing workflow 48

3.2 Stack InSAR processing workflow 50

3.3 Residual interferogram for stack processing in radar coordinates 52

3.4 Residual interferogram for stack processing after geocoding 53

4.1 OTL displacement time series across northern Iceland 62

4.2 Synthetic interferogram of expected OTL displacements in northern Iceland . 63

4.3 Synthetic wide swath interferogram of expected OTL displacements in Peru . 64

4.4 OTL displacement gradient in the western United States 65

5.1 Map of Iceland with plate boundary 74

5.2 1987 – 1992 GPS displacements in the NVZ 75

5.3 Map of the NVZ volcanic systems 76

5.4 Estimates of the widening of the Krafla fissure swarm during 1975 – 1985 rifting episode 77

6.1 SAR coverage of the NVZ 91

6.2 Interferometric baseline plots 92

6.3 Interferogram track 9 1996/06/04 – 1993/07/31 102

6.4 Interferogram track 1 1995/06/19 – 1992/09/18 103

6.5 Interferogram with atmospheric noise 104

6.6 Singular values of two-dimensional velocity inversion 105

6.7 Model-space vectors of two-dimensional velocity inversion 106

6.8 Average two-dimensional velocity for two separate time periods. 107

6.9 Residuals from two-dimensional velocity inversion 108

6.10 GPS velocities 109

6.11 Locations of GPS sites 110

6.12 InSAR pairs and spline basis for MInTS 111

6.13 L-curve for MInTS regularization 112

6.14 Snapshots of MInTS velocity time series 113

6.15 Residual interferograms of MInTS time series 114

6.16 Detailed DEM of the NVZ 117

6.17 Snapshots of MInTS velocity time series separated into linear and spline components 118

6.18 MInTS cumulative displacement solution 119

6.19 Linear portion of MInTS displacement 120

6.20 Spline portion of MInTS displacement 121

6.21 MInTS displacement time series at four locations 122

6.22 Amount of opening and measured InSAR displacement along a rift parallel profile 124

6.23 Interferogram with profile locations 125

7.1 Viscoelastic spin-up 149

7.2 Schematic of Lithospheric FEM Model 150

7.3 Laterally homogeneous models 152

7.4 Laterally homogeneous models compared to GPS 154

7.5 Early post-rifting velocities for homogeneous models 155

7.6 Early post-rifting velocities for homogeneous models 156

7.7 Shallow viscosity anomaly models 157

7.8 Shallow viscosity anomaly models 158

7.9 Testing anomaly depth 159

7.10 Elastic weak zone models 160

7.11 Elastic weak zone models compared to GPS 162

7.12 FEM model with dipping Moho 163

7.13 Thick/thin, strong/weak crust models 165

7.14 Thick/thin, strong/weak crust models compared to GPS 167

7.15 Three-dimensional FEM model with dipping Moho 168

7.16 Displacements from three-dimensional FEM model with dipping Moho and InSAR time series 169

7.17 Three-dimensional FEM model with dipping Moho and axially located rheological gradients. 172

7.18 Displacements from three-dimensional FEM model with dipping Moho and axially located rheological gradients compared to InSAR time series 173

7.19 Elastic diking model surface displacements 176

List of Tables

2.1 Definitions of notations used in text. 40

6.1 InSAR data set 126

7.1 Elastic model parameters 177

7.2 Summary of model results 178

Chapter 1

Introduction

1.1 Geodynamics and Geodesy

The past two decades have seen large advances in both geodetic techniques and sophistication in modeling geodynamical processes. The rise of space based geodetic techniques has allowed for high resolution, high precision measurements of ground motion on a global scale. Modeling of geodynamic processes such as viscoelastic relaxation has gone from analytical and semi-analytical techniques for simple, linear stratified rheological models (e.g., Heki et al., 1993; Pollitz, 1992) to sophisticated three-dimensional finite element models with arbitrary variations in material properties in all spatial dimensions (e.g., Parker et al., 2004; Aagaard et al., 2007). The availability of computing power has, in part, facilitated these advances, allowing rapid computation of radar interferograms and large finite element models (often in parallel). These tools have allowed geoscientists to explore mechanisms for lithospheric deformation beyond simple elastic models, including poroelasticity, fault creep, and viscoelastic flow. High precision geodetic measurements that span several years allow us to identify these time-dependent deformation mechanisms.

This thesis focuses on the measurement of ground deformation using interferometric synthetic aperture radar (InSAR) and modeling of post-seismic and post-diking deformation

as a viscoelastic relaxation processes via finite element models. The goal has been to increase our understanding of the role of viscoelastic processes in the seismic cycle in general, and to probe possible rheological parameter models of the Icelandic lithosphere with likely lateral heterogeneities.

Post-seismic deformation via viscoelastic relaxation has been proposed by many authors (e.g., Nur & Mavko, 1974; Savage & Prescott, 1978; Spence & Turcotte, 1979). Pollitz et al. (2001) concluded that a non-linear viscosity (i.e., stress dependent effective viscosity) may be necessary to explain temporal changes in the apparent effective viscosity for post-seismic deformation for the 1992 Landers and 1999 Hector Mine earthquakes. Freed & Bürgmann (2004) used finite element methods to model the post-seismic deformation with nonlinear rheologies.

Li & Rice (1987) proposed the need for laterally heterogeneous material properties at the San Andreas fault system, but were not able to model them. Using FEM techniques, Fay & Humphreys (2005) and Schmalzle et al. (2006) were able to model laterally heterogeneous structures in strike slip systems. Pollitz (2003) proposed an alternative, non FEM, method for computing post-seismic viscoelastic relaxation in a laterally heterogeneous medium.

Other mechanisms exist to explain post-seismic and post-diking deformation. Savage & Prescott (1978) observed that for a strike slip system, aseismic slip on the down-dip extension of the fault could produce the same surface deformation as viscoelastic relaxation. Afterslip mechanisms have been proposed for a number of regions including the Sumatra mega-thrust (e.g., Chlieh et al., 2007; Hsu et al., 2006), the North Anatolian fault (Burgmann et al., 2002), and elsewhere. In addition, both poroelasticity (Peltzer et al., 1996; Fialko, 2004) and viscoelastic rebound (Pollitz et al., 2000) have been proposed as post-seismic deformation mechanisms in the Eastern California Shear Zone.

Questions about the strength of the continental lithosphere are still debated. The classical model with a strong, brittle upper crust, a weak lower crust, and a strong, viscous upper mantle is often referred to as the jelly sandwich model. Jackson (2002) proposed an alternative with a strong upper and lower crust and weak mantle later referred to as the crème brûlée model. Similarly, in Iceland there is a question as to whether the crust is thin and hot, containing large amounts (5 – 10 %) of partial melt (Björnsson, 2008), and therefore quite weak, or thick and cold with very little partial melt (Menke & Levin, 1994) and high strength.

In this thesis we endeavor to improve the geodetic rigor of InSAR measurements. GPS has long been a high precision geodetic technique used for measuring small strains associated with secular plate motion, tectonic loading, and post-seismic response (e.g Thatcher et al., 1999; Sella et al., 2002; Hsu et al., 2008). InSAR has often been used to measure co-seismic displacements (e.g., Massonnet et al., 1993; Zebker et al., 1994; Simons et al., 2002), but, more recently, has been applied to smaller displacement, interseismic studies (e.g., Fialko, 2006).

Iceland is an ideal region for geodynamic study given its location at the confluence of a oceanic spreading ridge and a hot spot (Einarsson, 1991). In the Northern Volcanic Zone (NVZ), which forms the plate boundary in northern Iceland, episodic diking events accommodate the divergent tectonics. The most recent event occurred along the Krafla fissure swarm, beginning in 1975 and ending in 1984. The sudden change in the stress state of the lithosphere caused by the rifting acts as a probe into the time dependent rheology of the lithosphere. In this thesis, we measure the deformation following the rifting event using InSAR and use those measurements to gain an understanding of the rheological structure of the Icelandic lithosphere in the region via finite element modeling of viscoelastic relaxation.

1.2 Thesis Overview

Chapter 2 (DiCaprio et al., 2008) deals with the consequences of a simple viscoelastic lithosphere for earthquake repeat times. We investigate the time variable loading of the fault due to recycling of stress via viscoelastic relaxation. When the fault has small changes in yield stress from one earthquake to the next, the stress recycling can result in clustered earthquake sequences. The presence of clustering depends only on the presence of a relatively small amount of noise in the yield stress. We find a non-dimensional number that describes the system's propensity for clustered behavior and a new way to quantify clustered time series.

New InSAR processing methods are covered in chapters 4 and 3. In chapter 4 (DiCaprio & Simons, 2008) we highlight the importance of accounting for ocean tidal loading in differential InSAR data. This is commonly done in GPS analysis and should be considered for InSAR as it strives to become a more formal geodetic technique. A new method for processing multiple interferograms into a common coordinate system for the purpose of stacking or time series analysis is discussed in chapter 3 along with a time series technique used to analyse some of the available InSAR data presented in this thesis.

Chapters 5 – 7 focus on observation and models of post-rifting deformation in the Krafla segment of the NVZ of Iceland. Chapter 5 is an introduction to Icelandic geology and the rifting along the Krafla fissure swarm. In chapter 6 we use a large amount of InSAR data in an attempt to recover the time dependence of the surface deformation field. The spatial variations in the deformation field contain information about the spatial distribution of rheologies while the time dependence helps us to constrain the values of the rheological constants.

In chapter 6, we begin with a two-dimensional velocity inversion of a subset of the interferograms. We extract deformation data in a profile across the rift axis. The data set is divided into three time periods, and we solve for the rift-perpendicular and vertical velocities assuming that there is no rift-parallel motion. We investigate the time dependent deformation field of the full interferograms from a particular look geometry (i.e., all data from a single radar track) using an inversion method called MInTS (Multiscale Interferometric Time Series). This approach allows for the decoupling of the data covariances making it computationally feasible to simultaneously use all pixels in an interferogram.

In chapter 7, we discuss the use of finite element models to explore possible rheological models of the Icelandic lithosphere and compare the predicted deformation to InSAR data. We explore the role of local lateral gradients in crustal viscosity near the rift axis. The effects on surface deformation of crust to mantle viscosity ratios and Moho depth are also tested in an attempt to illuminate the thin-hot crust verses thick-cold crust question.

Understanding the basic mechanics of the post-rifting process and building an intuition for the role of different rheologies, vertical structure, and lateral heterogeneity is important in guiding our modeling efforts. Several two-dimensional finite element models of post-rifting deformation guide our intuition for how both vertical and lateral heterogeneities in rheology influence surface deformation.

Chapter 2

Post-seismic Reloading and Temporal Clustering on a Single Fault

2.1 Note

This chapter has been published as DiCaprio, C. J., Simons, M., Kenner, S. J., & Williams, C. A., 2008, Post-seismic Reloading and Temporal Clustering on a Single Fault, *Geophysical Journal International*, **172**(2), 581–592.

2.2 Summary

Geologic studies show evidence for temporal clustering of large earthquakes on individual fault systems. Since post-seismic deformation due to the inelastic rheology of the lithosphere may result in a variable loading rate on a fault throughout the interseismic period, it is reasonable to expect that the rheology of the non-seismogenic lower crust and mantle lithosphere may play a role in controlling earthquake recurrence times. We study this phenomenon using a two-dimensional, finite element method continuum model of the lithosphere containing a single strike-slip fault. This model builds on a previous study using a one-dimensional spring-dashpot-slider analogue of a single fault system to study the

role of Maxwell viscoelastic relaxation in producing non-periodic earthquakes. In our two-dimensional model, the seismogenic portion of the fault slips when a predetermined yield stress is exceeded; stress accumulated on the seismogenic fault is shed to the viscoelastic layers below and recycled back to the seismogenic fault through viscoelastic relaxation. We find that random variation of the fault yield stress from one earthquake to the next can cause the earthquake sequence to be clustered; the amount of clustering depends on a non-dimensional number, W, called the Wallace number defined as the standard deviation of the randomly varied fault yield stress divided by the effective viscosity of the system times the tectonic loading rate. A new clustering metric, based on the bimodal distribution of interseismic intervals, allows us to investigate clustering behavior of systems over a wide range of model parameters and those with multiple viscoelastic layers. For models with $W \gtrsim 1$ clustering increases with increasing W, while those with $W \lesssim 1$ are unclustered, or quasi-periodic.

2.3 Introduction

Several geologic studies show evidence of temporal clustering of large earthquakes on individual faults. Wallace (1987) finds changes in slip rates along range front faults in the Great Basin over the past 10 million years; in addition, subprovinces of the Great Basin tend to have clusters of earthquakes while other areas are inactive. Similarly, Friedrich et al. (2003) find that the faults bounding the Wasatch range exhibit temporal clustering. A paleoseismic study of the Dead Sea transform shows strong temporal clustering of events over the past 50,000 years (Marco et al., 1996; Begin et al., 2005). Trenching studies on the Carrizo Plain segment of the San Andreas Fault (Grant & Sieh, 1994) and near Wrightwood, California (Weldon et al., 2004) show that earthquakes on a single fault segment can cluster in time.

Many modeling studies have previously addressed clustering of large earthquakes. Ben-Zion et al. (1999) used a model of an upper crust with damage rheology overlying a viscoelastic substrate to model multiple evolving fault systems that exhibit clustering behavior. Lyakhovsky et al. (2001) found similar results from a model of a single strike-slip fault system. In a study of changing fault slip rates due to changing fault friction, Chery & Vernant (2006) showed that an elastically weak lithosphere contributes to large fluctuations in fault slip rate; large fault rate variations were present in models with a strain weakening fault with a short weakening time relative to the tectonic loading rate. Chery et al. (2001) showed that the viscoelastic post-seismic deformation from one fault could bring a neighboring fault closer to failure. The two parallel strike-slip fault system exhibited temporal clustering behavior under certain values of low crustal viscosity and tectonic strain rate. Similar results have been found for a model of the San Andreas fault that has two seismogenic segments on a single strike-slip fault separated by an aseismically slipping segment (Lynch et al., 2003). Generally, it appears that any rheology with memory (e.g., viscoelastic and damage rheologies) is susceptible to clustering behavior. Here we focus on viscoelastic rheologies since they are the most commonly adopted constitutive laws in the lithospheric modeling community.

After an earthquake, post-seismic viscoelastic deformation rates can be on the same scale as the tectonic loading rates (e.g., Savage & Prescott, 1978; Kenner & Segall, 2000; Meade & Hager, 2004). We therefore expect that recycling of stress via post-seismic relaxation may play a role in the timing of the next earthquake on a single fault. Kenner & Simons (2005) (henceforth referred to as KS05) developed a one-dimensional spring-dashpot-slider model as an analogue to a layered viscoelastic lithosphere with a single strike-slip fault to study temporal earthquake clustering due to reloading of the seismogenic fault by post-seismic

relaxation. Here, we investigate earthquake clustering due to viscoelastic relaxation using a two-dimensional, finite element method (FEM) continuum model of the lithosphere containing a single infinitely long strike-slip fault. Generally, we wish to use a more physically grounded model, since the one-dimensional model has no inherent length scale. Multiple viscoelastic layers are represented by KS05 as viscoelastic spring-and-dashpot elements connected in parallel; in this case, the clustering behavior of a system with multiple viscoelastic elements is identical to that of a system with a single viscoelastic element with an effective viscosity that is the arithmetic mean of all viscosities. However, in a two-dimensional model, the viscoelastic mantle can only communicate with the elastic upper crust through the lower crust; we would therefore expect more complex behavior. The temporal clustering behavior of the system is expected to be a function of the geometry (thickness) of the layers as well as their viscosities.

KS05 show that a viscoelastic feedback system in the lithosphere can produce clustered earthquake sequences on a single fault in their one-dimensional model. Stress transferred coseismically from the elastic element to Maxwell viscoelastic elements is recycled through viscoelastic relaxation back to the elastic element. The system is loaded by a constant velocity boundary condition representing a steady-state tectonic load. The fault is modeled by a slider block, allowed to slip with zero kinetic friction when a specified yield force is exceeded. Elasticity in the seismogenic layer is provided by a spring element and Maxwell viscoelastic behavior is provided by spring and dashpot (damper) elements connected in series. The seismogenic element and all viscoelastic elements are connected in parallel to represent various rheological layers in the lithosphere.

KS05 demonstrate that a viscoelastic feedback system can have clustered earthquake sequences when the yield stress of the block slider changes by a small random amount from

one earthquake to the next due to normally distributed noise added to the yield stress. They find that the degree of clustering is controlled by a non-dimensional number W_{KS05}, called the Wallace number after Robert Wallace who demonstrated the existence of clustered earthquakes in the Basin and Range province (Wallace, 1987).

$$W_{\mathrm{KS05}} = \frac{\overline{\Delta\tau}}{\dot{\epsilon_o}\,\eta_{eff}}, \tag{2.1}$$

where $\overline{\Delta\tau}$ is the average yield stress for all earthquakes, $\dot{\epsilon_o}$ is the applied strain rate, and η_{eff} is the effective viscosity of the system (see table 2.1 for a list of nomenclature used in the text). W_{KS05}, as originally defined, has many problems that we address in what follows. We develop a revised definition of the Wallace number that has sensitivity to the amount of noise in the system. The KS05 subscript is meant to distinguish their incorrect formulation of the Wallace number, from the reformulated one presented here.

We also propose a new clustering metric, which is insensitive to the level of noise in the yield stress and does not saturate for highly clustered systems, in contrast to the one used by KS05. The metric relies on the bimodality of earthquake recurrence times in clustered systems. As an aside, success of this new clustering metric suggests a need to reconsider the currently adopted earthquake recurrence models that assume unimodal distributions.

2.4 Methods

2.4.1 Lithospheric Model

We study an anti-plane, two-dimensional, continuum model of the lithosphere containing an infinite strike-slip fault. Two different model types are tested: one with an elastic layer over a viscoelastic layer (referred to as the two-layer model) and one with an elastic layer

over two viscoelastic layers (referred to as the three-layer model). The elastic parameters are the same for all rheological layers. A single vertical, strike-slip fault extends through the entire elastic layer and penetrates 2 km into the viscoelastic layer. Taking advantage of symmetry, we model only one side of the fault system. The model is driven at a constant velocity, v_p, along the entire right edge (making the average slip rate for the entire fault system $2v_p$). The mesh is 1004 km in horizontal extent and 204 km in vertical extent. The top and bottom boundaries of the model are free surfaces (Figure 2.1).

The coseismic fault is locked until it reaches a specified yield stress. At that point the fault is allowed to slide freely for one, nearly instantaneous, coseismic time step, resulting in complete stress drop. We have used log-normal noise to vary the yield stress from one earthquake to the next, with standard deviation $\sigma_{\Delta\tau}$. The ratio of the standard deviation to the average of the fault yield stress varies from 1% to 10%. We make no claim that log-normal noise is the most appropriate distribution to model a natural system; the appropriate distribution of noise is unknown. A log-normal noise distribution is chosen because it doesn't allow the fault yield stress to become negative which is physically unreasonable. In this study, we are concerned only with characteristic earthquakes on a particular fault (e.g., Schwartz & Coppersmith, 1984) and not with modeling a magnitude frequency distribution. Therefore, in the absence of added noise, every earthquake in our model is the same size; when noise is introduced to the fault yield stress the size of the earthquakes will vary with the yield stress as there is complete stress drop for every earthquake.

We use the quasi-static, finite element code Tecton (Melosh & Raefsky, 1980; Williams & Wadge, 2000) to model the response of a viscoelastic lithosphere to an earthquake. We take advantage of the linear nature of the system by using a spatio-temporal Green's function approach to calculate a sequence of earthquakes. The finite element code is used to calcu-

late the system response to a single earthquake which is then taken to be a spatio-temporal Green's function used to create a series of earthquakes by summing them with the appropriate amplitude scaling and time shift for the size and timing of each earthquake. This approach allows the rapid calculation of long earthquake sequences suitable for statistical analysis of temporal clustering behavior.

The model is run for several hundreds to thousands of earthquake cycles in order to gather reliable clustering statistics. Before a statistically meaningful earthquake sequence can be generated, the model must first be spun up to a steady state which requires running the model through several earthquake cycles to load the viscoelastic layers (the number of cycles needed for spin-up increases with decreasing W_{KS05}). In the case where no noise is added to the fault yield stress, spin up is achieved when the average interseismic stresses are approximately constant from one earthquake to the next (KS05, Hetland & Hager, 2006a). An earthquake sequence with random variation in the fault yield stress is considered to be spun up when the average interseismic stress over several earthquake cycles is constant. We use the integrated elastic potential, U, as a metric for the amount of elastic stress stored in each rheological layer (upper crust, lower crust, and upper mantle). The integrated elastic potential of the n^{th} layer occupying volume V_n is

$$\begin{aligned} U_n &= \int_{V_n} \frac{1}{2} \left[\lambda \epsilon^e_{kk} \delta_{ij} + 2\mu \epsilon^e_{ij} \right] \epsilon^e_{ij} \, dV \\ &= \int_{V_n} \frac{1}{2} \left[\frac{1+\nu}{E} \tau_{ij} \tau_{ij} - \frac{\nu}{E} \tau^2_{kk} \right] dV, \end{aligned} \tag{2.2}$$

where λ is the Lamé modulus, μ is the shear modulus, ν is Poisson's ratio, and E is Young's modulus. ϵ^e_{ij} is the elastic component of strain, and τ_{ij} is the stress (Chandrasekharaiah & Debnath, 1994). The integrals are performed over each material layer in the model so that

U is a measure of the total elastic stress stored in that layer.

2.4.2 Clustering Metric

Figure 2.2 compares total stress released by the fault as a function of time for clustered and unclustered (quasi-periodic) earthquake sequences. For a quasi-periodic earthquake sequence, the distribution of interseismic intervals has the same character as the distribution of yield stresses (Figure 2.3a). A clustered sequence, however, has a bimodal distribution of interseismic intervals when plotted on a logarithmic scale (Figure 2.3b). The average interseismic interval is the same for both quasi-periodic and clustered sequences, as is kinematically required because they both have the same average stress drop and long-term average displacement, but the distribution of interseismic intervals is radically different.

KS05 quantify the amount of clustering using the coefficient of variation, C_v, of the interseismic times for the earthquake sequence. C_v is the ratio of the sample standard deviation to the sample mean (Kagan & Jackson, 1991). Empirically, C_v as a metric of clustering is problematic since it is sensitive to the amount of noise applied to the yield stress and saturates for $W_{\mathrm{KS05}} \gtrsim 1000$ (Figure 2.4). The sensitivity of C_v to the noise in the yield stress manifests both when the earthquake sequence is unclustered (the C_v of the interseismic times is equal to the C_v of the input noise) and when the earthquake sequence is clustered. The distribution of the log of the interseismic intervals, $\log(T^{eq})$, reveals the bimodality of the distribution of interseismic times (Figure 2.3b); C_v is not an appropriate statistic for describing a bimodal distribution. This bimodality is not apparent on a linear scale. We propose a new metric for measuring the amount of temporal clustering of an earthquake sequence based on the distance, B_c, between the two modes of the distribution of $\log(T^{eq})$ (Figure 2.3b). The mode of small interseismic intervals is referred to as the

"intra-cluster" mode and the mode of long intereseismic intervals is the "inter-cluster" mode. The logarithmic distance between modes is a natural choice for quantifying the degree of clustering due to the interseismic interval being a Jeffreys quantity (Tarantola, 2006).

Studies of statistical distributions of earthquake recurrence intervals and seismic hazard analyses traditionally assume that the interseismic distributions are unimodal; the success of the bimodal clustering metric, B_c, in quantifying a clustered earthquake sequence suggests that this assumption may be in error. Matthews et al. (2002) uses a Brownian passage-time distribution to construct an earthquake probability model. A seismic hazard analysis of southern California (Jackson et al., 1995) assumes a log-normal distribution of earthquake recurrence times. Abaimov et al. (2007) compares empirical earthquake distributions to only unimodal distributions. These and other analyses may have to be reconsidered in light of the possibility of a bimodal distribution of interseismic times for clustered earthquake sequences.

B_c does have a shortcoming in that it does not take into consideration the relative sizes of the modes. One could imagine an earthquake sequence with a small number of short interseismic intervals and a large number of long ones. This would be considered clustered by our example (Figure 2.5a), but examination of a small portion of the earthquake sequence itself would indicate a quasi-periodic sequence (Figure 2.5b). Only the entire sequence is likely to reveal any earthquake clusters, as they are rare in this example. While this example may seem pathological (but not impossible), it does demonstrate an insensitivity of B_c to number of earthquake clusters. B_c instead measures the difference in characteristic intra-cluster and inter-cluster seismic time intervals.

2.5 Results

2.5.1 Two-Layer Model

Our reformulated definition of W is

$$W = \frac{\sigma_{\Delta\tau}}{\dot{\epsilon}_o \, \eta} = N \, W_{\mathrm{KS05}}, \tag{2.3}$$

where $\sigma_{\Delta\tau}$ is the standard deviation of the fault yield stress over the earthquake sequence, and $N = \sigma_{\Delta\tau}/\overline{\Delta\tau}$ is the fraction of noise added to the fault yield stress. We ran models with different rheological parameters, average and standard deviation, of fault yield stress, and tectonic loading rates to determine the Wallace number – i.e., the single non-dimensional number that controls the degree of clustering for the system – for a two-dimensional lithospheric model with a faulted elastic layer overlying a single viscoelastic layer (Figure 2.6). For values of $W \gtrsim 1$, B_c varies linearly with $\log(W)$. Below $W \approx 1$ there is no temporal clustering: the distribution of the logarithm of interseismic intervals is normal (reflecting the distribution of the fault yield stress) and $B_c = 0$.

As stated earlier, we chose the log-normal distribution for the fault yield stress to avoid yield stresses less than zero, but this specific distribution is not necessary to obtain the bimodal distribution of interseismic times. A yield stress distribution that is derived from the log-normal distribution, with all values below the mean discarded, produces a similar distribution of interseismic times for low Wallace number systems and a bimodal distribution of interseismic times for those with a large Wallace number (Figure 2.7).

While the amount of temporal clustering as measured by B_c is completely determined by the value of the Wallace number, the particular distribution of interseismic intervals, T^{eq}, is not. For models where $W \gtrsim 1$, changing W by varying the viscosity of the system results

in intra-cluster modes with nearly identical size and shape moving up the distribution of $\log(T^{eq})$ while the position, size, and shape of the inter-cluster is independent of η (Figure 2.8a). Of course, for the average interseismic interval, $\overline{T^{eq}}$, to be constant from one model to the next (as it must be due to kinematic considerations) the modes cannot be absolutely identical, i.e., a small, nearly undetectable change to the inter-cluster mode is all that is necessary to keep $\overline{T^{eq}}$ constant. Similar behavior is exhibited by groups of models with changing values of $\sigma_{\Delta\tau}$ and $\dot{\epsilon_o}$. However, in these cases, the intra-cluster mode remains stationary while the inter-cluster mode changes as $\sigma_{\Delta\tau}$ and $\dot{\epsilon_o}$ change (Figure 2.8b and c).

The total number of earthquakes in each mode depends on the ratio $\sigma_{\Delta\tau}/\overline{\Delta\tau}$ (Figure 2.9) in a linear fashion. The relative sizes of the modes do not change the amount of clustering as measured by B_c which quantifies the difference in interseismic interval during a clustered earthquake period and an inter-cluster period.

2.5.2 Three-Layer Model

The one-dimensional spring-dashpot-slider model used by KS05 has no inherent length scale; a system with multiple viscoelastic layers exhibits a single effective viscosity that is the arithmetic mean of all viscosities. In a horizontally layered, two-dimensional lithosphere, consisting of an elastic, seismogenic upper crust and viscoelastic layers below, viscoelastic layers not in direct contact with the elastic upper crust must communicate with it through the top-most viscoelastic layer. Therefore, we expect a more complicated scaling relationship between the model geometry and the viscosities of the individual layers determining the clustering behavior of the system than that found by KS05.

We varied the relative thickness of layers two and three, while the total thickness of the model was held constant (Figure 2.1). The viscosities of layers two and three are

4.5×10^{15} Pa s and 4.5×10^{17} Pa s, respectively. The three-layer models exhibited similar bimodal clustering behavior as the two-layer models (Figure 2.10). The intra-cluster modes are broader and shorter than those of the two-layer models. The value of B_c becomes smaller as the third layer (higher viscosity) is thickened. The upper viscoelastic layer, being in direct contact with the elastic upper crust, has a stronger influence on the degree of clustering than does the lower viscoelastic layer. When $H_2/H_3 = 1.16$, the value of B_c is nearly the same as the end-member model $\eta_2 = \eta_3 = 4.5 \times 10^{15}$ Pa s. When $H_2/H_3 = 0.06$, the value of B_c is close to halfway between the two-layer end member cases $\eta_2 = \eta_3 = 4.5 \times 10^{15}$ Pa s and $\eta_2 = \eta_3 = 4.5 \times 10^{17}$ Pa s.

2.6 Discussion

Our study using a two-dimensional, continuum FEM model finds that post-seismic recycling of stress can cause earthquakes to cluster on a single fault when the yield stress on the fault is varied randomly from one earthquake to the next, confirming the conclusions of KS05 who used a one-dimensional analogue model for the viscoelastic lithosphere. Whether or not clustering occurs depends on the value of a non-dimensional number W; earthquake sequences are quasi-periodic for $W \lesssim 1$, and clustered for larger values of W by an amount depending linearly on $\log(W)$.

In order to compare the results from the one-dimensional model KS05 with that of a continuum model, we calculated C_v and W_{KS05} for models with $\sigma_{\Delta\tau}/\overline{\Delta\tau} = 0.03 - 0.06$ and $W_{\mathrm{KS05}} = 2.5 \times 10^{-3} - 2.5 \times 10^{5}$. A system is considered quasi-periodic when $C_v \approx \sigma_{\Delta\tau}/\overline{\Delta\tau}$, i.e., the output earthquake sequence resembles the input yield stress (Figure 2.3a). Values of $C_v > \sigma_{\Delta\tau}/\overline{\Delta\tau}$ are clustered, though the degree of clustering is difficult to ascertain because C_v saturates for $W_{\mathrm{KS05}} \gtrsim 1000$. The system transitions from quasi-periodic to clustered for

values of W_{KS05} between 1 and 100 (Figure 2.4). These results are the same as those found by KS05. The general relationship between W_{KS05} and C_v is the same as in KS05, though the final values of C_v are larger for our continuum models.

The one-dimensional spring-dashpot-slider model created by KS05 uses a coupling spring to transfer stress between rheological "layers." In addition to dependence on W, the clustered behavior of the model depends on the ratio of the stiffness of the coupling spring to the stiffness of the top elastic "layer" spring. Our two-dimensional continuum model of a strike-slip fault eliminates the need for the coupling spring due to the fact that the layers are inherently coupled.

We do not expect the averaging law for multiple viscoelastic layers to be a simple arithmetic mean as it is in the one-dimensional spring-dashpot-slider analogue of KS05. Viscoelastic layers not in direct contact with the elastic upper crust must recycle their stress through the top-most viscoelastic layer, resulting in a complex relationship between the clustering behavior of the system and the viscosities and thickness of the various layers. In addition, if a particular layer has a very large viscosity compared to the others, it would no longer play a role in the recycling of stress. We would expect that adding an extra elastic layer to the model would not change the rate of stress recycling except to the extent that it effects the geometry of the viscoelastic layers (Hetland & Hager, 2006b).

For a system with multiple viscoelastic layers, there is more than one relaxation time scale, however there is only one phase of stress relaxation; there is one intra-cluster mode for models with two viscoelastic layers (Figure 2.10). When the shear modulus is the same for all materials, as in the models discussed in this paper, the first time scale is simply the Maxwell relaxation time of the second layer. The second relaxation time scale, however, is dependent on both the viscosities of the second layer and the third layer and is therefore

not easily separated (Hetland & Hager, 2006b).

While the three-layer model is not much more geologically realistic than the two-layer model, which is the primary focus of this paper, it does illuminate expected behavior of more complex models such as those with multiple viscoelastic layers or a continuous grading of viscoelastic parameters with depth. Fault systems with multiple viscoelastic layers will have a single clustered mode that is broader and lower in amplitude than the clustering mode for a system with only a single viscoelastic layer. The viscoelastic layer that is the closest to the elastic upper crust and the fault has the largest influence on the degree of clustering.

The average interseismic interval, $\overline{T^{eq}}$, can be written in terms of components of W

$$\overline{T^{eq}} = \frac{\overline{\Delta\epsilon}}{\dot{\epsilon_o}} = \frac{\overline{\Delta\tau}/G}{\dot{\epsilon_o}}, \tag{2.4}$$

where $\overline{\Delta\epsilon}$ is the average coseismic strain drop, and G is the shear modulus of the elastic layer. The characteristic relaxation time scale for an elastic layer over a Maxwell viscoelastic half-space, when the elastic parameters of the elastic layer and viscoelastic half-space are identical is (Hetland & Hager, 2005),

$$T^{hs} = 2\,\frac{\eta}{G}. \tag{2.5}$$

Combining Equations 2.3 , 2.4, and 2.5 we get

$$W = 2N\,\frac{\overline{T^{eq}}}{T^{hs}}, \tag{2.6}$$

In terms of reloading rates,

$$W = 2N \frac{r^{hs}}{r^o} \tag{2.7}$$

where $r^{hs} = 1/T^{hs}$ is the post-seismic viscoelastic reloading rate of our two-layer model (assuming it approximates an elastic layer over a viscoelastic half-space) and $r^o = 1/\overline{T^{eq}}$ is the tectonic loading rate. Thus the Wallace number is a function of the amount of noise applied to the yield stress and the ratio of the tectonic loading rate to the viscoelastic relaxation loading rate. A system with a large r^{hs}/r^o is sensitive to perturbations in the fault yield stress. The system moves close to failure soon after an earthquake due to rapid post-seismic relaxation; the fault loading then slows down to a rate much lower than the average loading rate (Figure 2.11a). If the yield stress increases from the previous earthquake, the interseismic time becomes much longer due to the slow reloading at the end of the earthquake cycle. Conversely, if the yield stress decreases, then another earthquake occurs very quickly because the yield stress is reached during the rapid reloading phase. On the other hand, a system with a low r^{hs}/r^o will not be as sensitive to changes in the fault yield stress. Because the fault is reloaded at a nearly constant rate (Figure 2.11b), small changes in the fault yield stress result in small changes in the interseismic time – the distribution of interseismic intervals reflects the distribution of yield stresses (Figure 2.3a).

Chery et al. (2001) also showed that post-seismic relaxation can influence the timing of earthquakes. A spring-dashpot-slider fault model is perturbed by the post-seismic viscoelastic deformation due to a neighboring, parallel strike-slip fault, 150 km away. The coseismic stress drop on the fault is varied randomly from one earthquake to the next. Earthquake sequences on the two faults are clustered when the ratio of the average interseismic interval to the relaxation time scale is large. This ratio is the same as W (Equation 2.7). Lynch

et al. (2003) performed a similar study of fault interaction and clustering using a continuum model. They constructed a three-dimensional finite element model of the San Andreas fault with two seismogenic fault segments separated by a freely slipping, aseismic section. A seismogenic fault segment slipped when it exceeded a given yield stress. It was found that when the viscosity of the lower crust was small, the two faults became coupled leading to clustered earthquake sequences.

Meade & Hager (2004) noted that W_{KS05} is the same as the Savage parameter: the ratio of average interseimic interval to the Maxwell viscoelastic relaxation time-scale (Savage & Prescott, 1978); Hetland & Hager (2006a) found W_{KS05} and the Savage parameter to differ by a factor of 4. Meade & Hager (2004) superposed the analytical solutions for surface displacements of an earthquake cycle for a strike-slip fault in an elastic layer over a Maxwell viscoelastic half space to analyze surface deformation for a clustered earthquake cycle. Systems with large values of the Savage parameter have a large range of surface velocities throughout the seismic cycle just as there is a large variability in the shear stress on the fault throughout the seismic cycle for our models with large $W/N = W_{\mathrm{KS05}}$ (Figure 2.11).

One could view the viscoelastic system as a stress reservoir. We expect a cluster of earthquakes to occur when there is a large decrease in the fault yield stress. There is then a large reservoir of stress in the viscoelastic layers that causes rapid post-seismic relaxation for more than one earthquake. That reservoir of stress is fed back to the seismogenic fault at a rate faster for larger values of W; while for small values of W, the stress reservoir relaxes too slowly to cause clustering. As long as the yield stress remains low after the initial decrease, a large cluster will likely occur. Notice the cluster at $t/\overline{T^{eq}} = 63$ in Figure 2.12: the cluster continues while the yield stress remains lower than that for the initial

earthquake that started the cluster; the cluster ends when the reservoir of stress from the first earthquake cannot continue to drive the cluster in the face of an increase in yield stress. The increase in yield stress after the cluster is the same magnitude as a change early in the cluster: the viscoelastic reloading is no longer rapid enough to continue the cluster.

Given a particular model geometry and viscosity, the system will evolve to a constant state of background stress, τ_f, when the fault yield stress, $\Delta\tau$, is constant (KS05). If the fault yield stress changes to $\Delta\tau'$, the system begins to move to a new state of background stress, τ_f'. Hetland & Hager (2006a) show that $\partial\tau/\partial\Delta\tau \sim W^{-1}$, where $\partial\tau = \tau_f - \tau_f'$ and $\partial\Delta\tau = \Delta\tau - \Delta\tau'$. For small values of W, changes in the fault yield stress will result in large changes in the overall state of stress of the system, meaning that deviations from a periodic rupture sequence are not likely. However, when W is large, the deviations in yield stress produce negligible changes in the overall state of stress of the system making clustered sequences possible.

Ignoring past earthquakes (which we can do when W is large, or equivalently the relaxation time is short), the stress on the fault during the interseismic period can be expressed as

$$\tau(t) = \left(1 - e^{t/T^{hs}}\right) \tau^{VE} + t\, r^o, \tag{2.8}$$

where τ^{VE} is the maximum amount of stress recycled from the viscoelastic layer(s) and r^o is the tectonic loading rate. For large W, the viscoelastic reloading occurs quickly relative to the tectonic loading; we can therefore consider the interseismic cycle to occur in two parts: a reloading phase and a tectonic phase. This two-phase interseismic period results in a significant asymmetry in the reloading curve. If, for a particular earthquake, the yield stress decreases significantly enough from the mean, then the earthquake will occur during

the reloading phase of the interseismic cycle, and the tectonic term becomes negligible. We can express the earthquake stress drop – which is the same as the yield stress in our models – at the interseismic interval time $t = T^{eq}$ as

$$\Delta\tau(T^{eq}) = \left(1 - e^{T^{eq}/T^{hs}}\right)\tau^{VE}, \tag{2.9}$$

We rearrange terms to get

$$T^{eq} = -T^{hs}\,\ln\left(1 - \frac{\Delta\tau}{\tau^{VE}}\right) = -2\,\frac{\eta}{G}\,\ln\left(1 - \frac{\Delta\tau}{\tau^{VE}}\right). \tag{2.10}$$

There is a linear relationship between $T^{hs} = 2\eta/G$ and the interseismic interval. This explains the slope of one for $W \gtrsim 1$ for the set of models with changing η in Figure 2.6. As η increases, the intra-cluster mode moves to shorter T^{eq} while the inter-cluster mode is relatively stationary (Figure 2.8). When $\Delta\tau$ increases from the average, the corresponding increase in T^{eq} is nearly independent of η. Figure 2.13 shows the asymmetry of the reloading curve and the viscosity dependence of the intra-cluster earthquake times. For $W \lesssim 1$, the tectonic term becomes more important in the analysis and the reloading curve becomes more symmetric, resulting in non-clustered, quasi-periodic behavior. We can use a similar logic to explain the inverse relationship between the degree of clustering and the applied tectonic strain rate and the standard deviation of the earthquake yield stress.

Of course, if $\Delta\tau$ is smaller than $\overline{\Delta\tau}$ for several earthquakes in a row, then the assumption is that we can ignore the effect of viscoelastic relaxation from past earthquakes no longer holds. The loading of the fault due to viscoelastic relaxation happens even faster and a long cluster of earthquakes takes place as the reservoir of stress stored in the viscoelastic layers is recycled back to the seismogenic crust.

A model studied by Ben-Zion et al. (1993) found that the viscoelastic post-seismic relaxation from a kinematically imposed large earthquake on the southern portion of the San Andreas fault could cause the nearby regions to have clustered earthquakes soon after the large event and fewer earthquakes later in the large earthquake cycle. This change in seismic rate is due to the large changes in post-seismic loading rates from a low viscosity lower crust. Specifically, small values of the ratio of viscous relaxation time to lower crustal thickness cause clustering.

2.7 Conclusions

Using a continuum, finite element approach we studied the temporal clustering of characteristic earthquakes on a single fault. We modeled an infinitely long strike-slip fault using an anti-plane two-dimensional geometry. To best identify clustering behavior, we considered histograms of interseismic times in logarithmic space. In this space, two modes clearly appear, an intra-cluster interval mode and an inter-cluster interval mode; we define a clustering metric, B_c, as the distance between these modes. Clustering is triggered by random perturbations in the fault yield stress from one earthquake to the next and occurs when the Wallace number – which is a function of the amount of noise applied to the system and the ratio of the tectonic loading rate to the viscoelastic relaxation loading rate (Equation 2.7) – is larger then 1. The degree of clustering as measured by B_c is linearly related to the log of the Wallace number.

In real geological settings, we expect the viscosity structure to be more complex than those studied in this model. The temperature gradient in the mantle and the expected temperature dependence of viscosity (e.g., Ranalli, 1990) suggests that the viscosity gradient over the lithosphere is significant. In this case, we would expect to see a broad distribution

of interseismic intervals for a temporally clustered earthquake mode. However, the rheology near the elastic upper crust has the strongest influence on the degree of clustering.

Comparison to real fault systems is difficult because of the many complexities found in real geologic settings. Aside from the problem of rheological structure mentioned above, there is the complication of fault geometry and, more importantly, interactions from other faults. Fault interactions can come in the form of strain partitioning (requiring strain rates to be estimated for a specific fault rather than a geological region) and in fault communication through post-seismic processes as previously addressed by Chery et al. (2001) and Lynch et al. (2003). The models presented here are used to study the interaction between post-seismic processes, fault loading, and temporal earthquake clustering with as few complexities as possible in order to build an intuitive understanding of the processes at hand. Having said that, it is possible to estimate values of W/N for various tectonic settings to qualitatively find the likelihood of earthquake clustering due to post-seismic viscoelastic deformation.

Typical values of earthquake stress drop are $1 - 10\,\mathrm{MPa}$ (Kanamori & Anderson, 1975). The velocity across the San Andreas fault has been measured geodetically as about 35 mm yr^{-1} (e.g., Prescott et al., 2001). The Maxwell viscosity is in the range $\eta = 10^{19} - 10^{20}\,\mathrm{Pa\ s}$ (e.g., Thatcher, 1983; Li & Rice, 1987; Kenner & Segall, 2000). If we assume $\dot{\epsilon_o} = v/d$, where $d \approx 15\,\mathrm{km}$ is the thickness of the seismogenic crust, then we get $W/N \approx 0.1 - 14$. In contrast, the Dead Sea transform has a much lower slip rate and is thought to have a low viscosity lower crust. The velocity across the fault has been measured geologically as 2 – 6 mm yr^{-1} (Klinger et al., 2000); viscosities are in the range $5 \times 10^{17} - 5 \times 10^{19}\,\mathrm{Pa\ s}$ (Al-Zoubi & ten Brink, 2002), which gives $W/N = 1 - 5000$. At a value of N of 3% we would expect that post-seismic, viscoelastic relaxation could play a role in creating temporally

clustered earthquake sequences on the Dead Sea transform but not the San Andreas fault. The effects of nonlinear viscosities complicate the problem; we would expect the recycling of stress leading to clustered behavior to be even stronger in this case as the viscosity decreases when the viscoelastic layers are coseismically stressed thus increasing the effective Wallace number.

Our results from a two-layer, single fault, finite element model agree with those found by KS05 using a one-dimensional, spring-dashpot-slider analogue. These results are also consistent with the findings of Lynch et al. (2003) and Chery et al. (2001) who studied viscoelastic relaxation and fault interaction. The clustering behavior exhibited in this study is expected to occur in any lithosphere model with time dependent rheology; that is, a rheology that is sensitive to the earthquake history (e.g., Ben-Zion et al., 1999; Chery et al., 2001; Lyakhovsky et al., 2001; Lynch et al., 2003; Chery & Vernant, 2006).

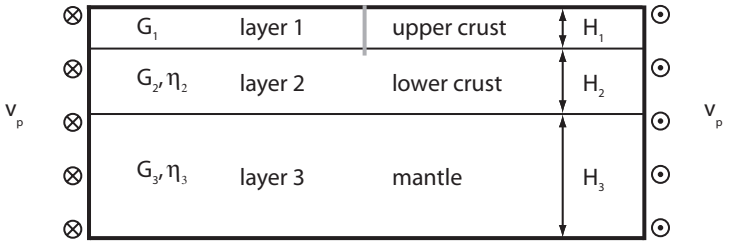

Figure 2.1: Model of infinite, anti-plane, vertical, strike-slip fault. The upper crust is purely elastic, while the lower crust and mantle layers are viscoelastic. The fault (in gray) passes through the entire elastic layer and penetrates the top two km of the viscoelastic lower crust. Tectonic loading is introduced by a constant velocity boundary condition applied to the entire far edge of the model. The fault fails when the average shear stress on the seismogenic fault reaches a predetermined yield stress. We study models with both one and two viscoelastic layers below the elastic seismogenic crust.

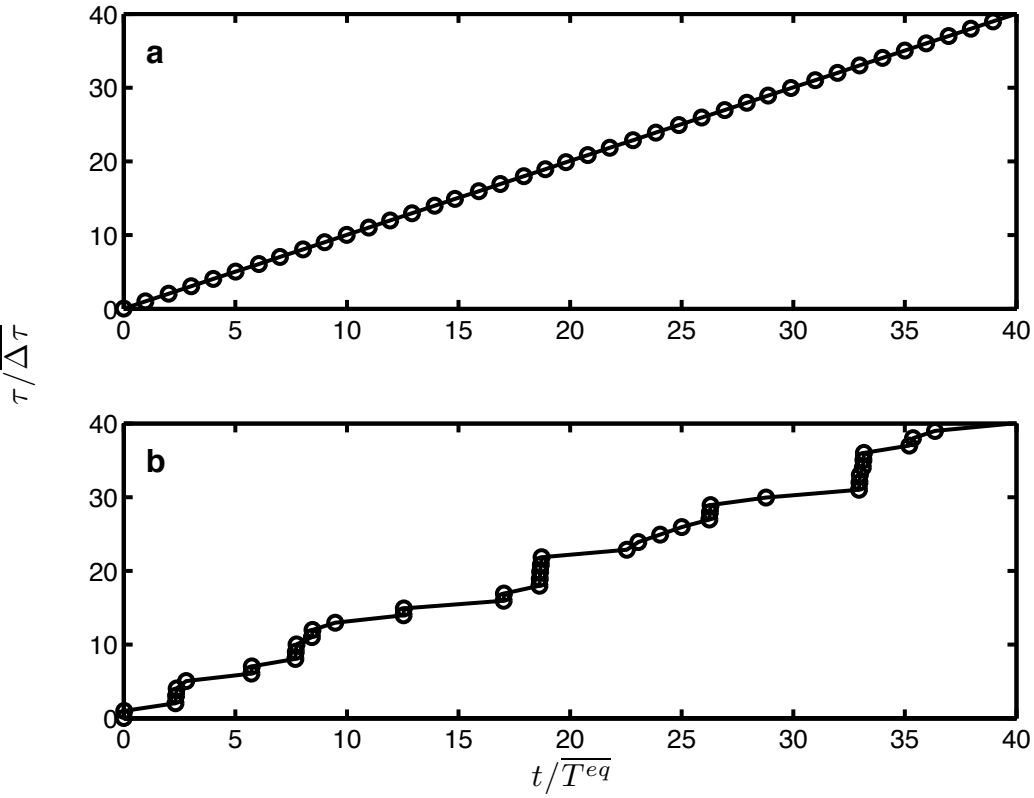

Figure 2.2: Cumulative stress released on the fault normalized by the mean yield stress versus normalized time. $\overline{T^{eq}}$ is the mean interseismic interval. The difference between the panels is the viscosity of the lower crust a) $W = 0.14$, b) $W = 1400$. In panel a there is a small amount of variance in the interseismic time that is not obvious by visual inspection of the time series.

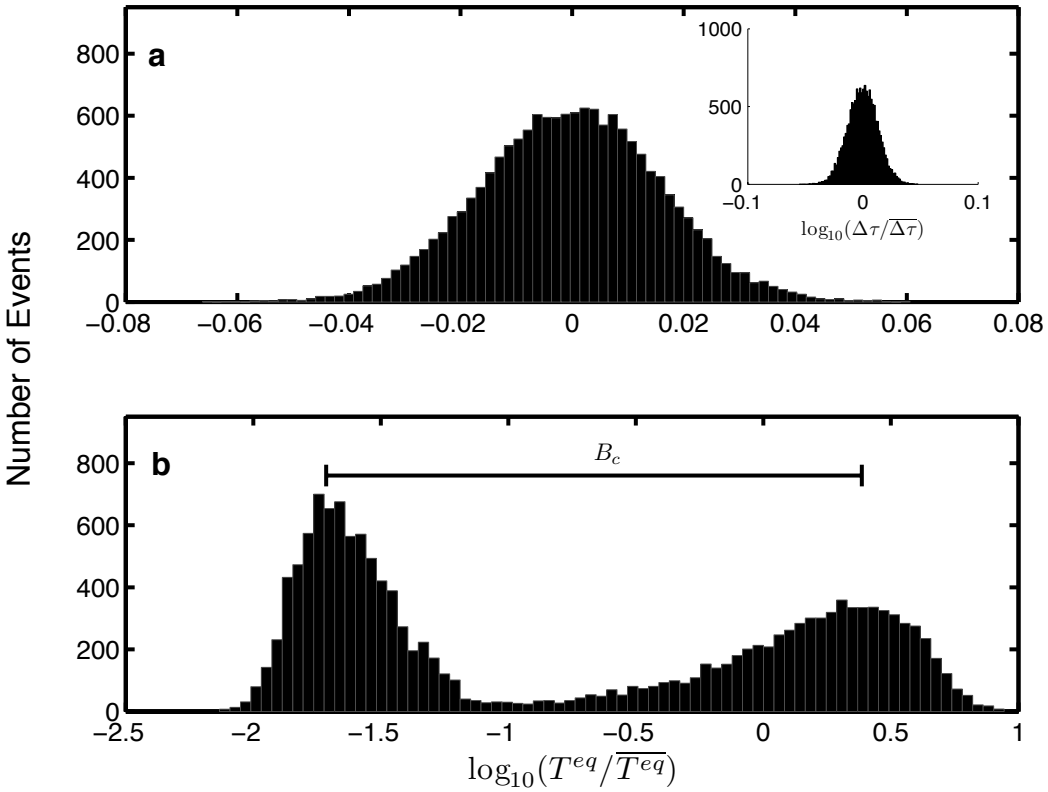

Figure 2.3: Distribution of normalized interseismic intervals on logarithmic scale for models with a) $W = 0.14$ and b) $W = 1400$. The distribution of fault yield stress for $\sigma_{\Delta\tau}/\overline{\Delta\tau} = 0.03$ is shown in the inset.

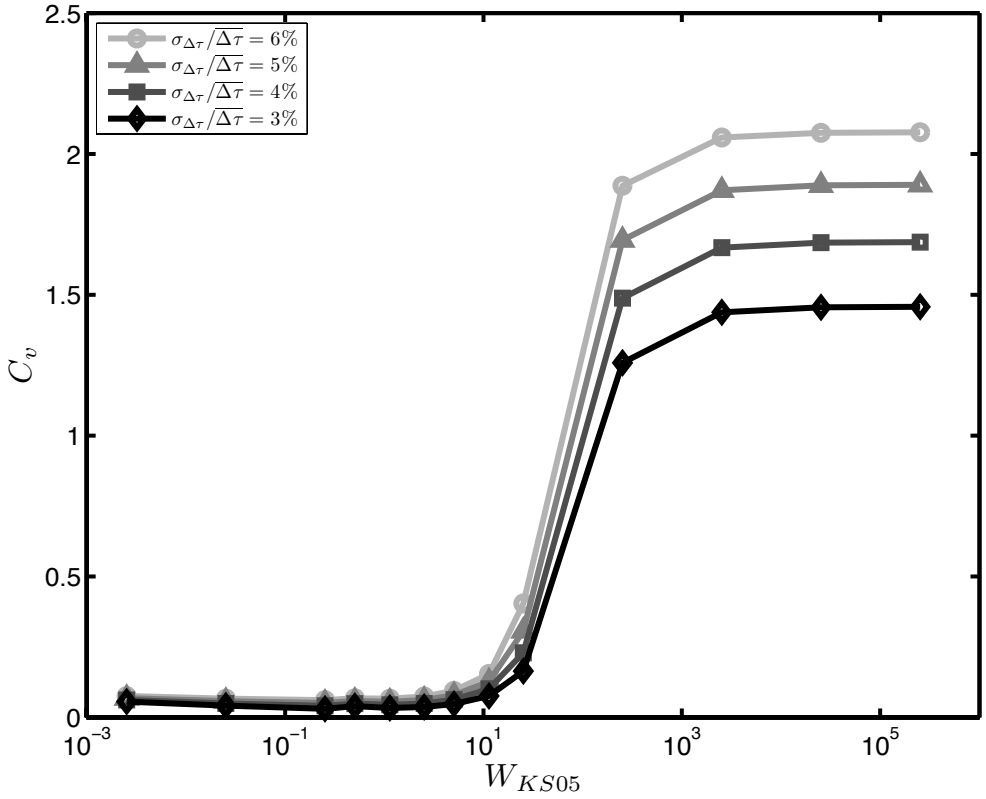

Figure 2.4: Amount of clustering as measured by the coefficient of variation, C_v, versus W_{KS05} for two-layer models. Quasi-periodic sequences have $C_v \approx \sigma_{\Delta\tau}/\overline{\Delta\tau}$, while larger values of C_v indicate a clustered sequence. Note that C_v saturates for values of $W_{\mathrm{KS05}} > 1000$.

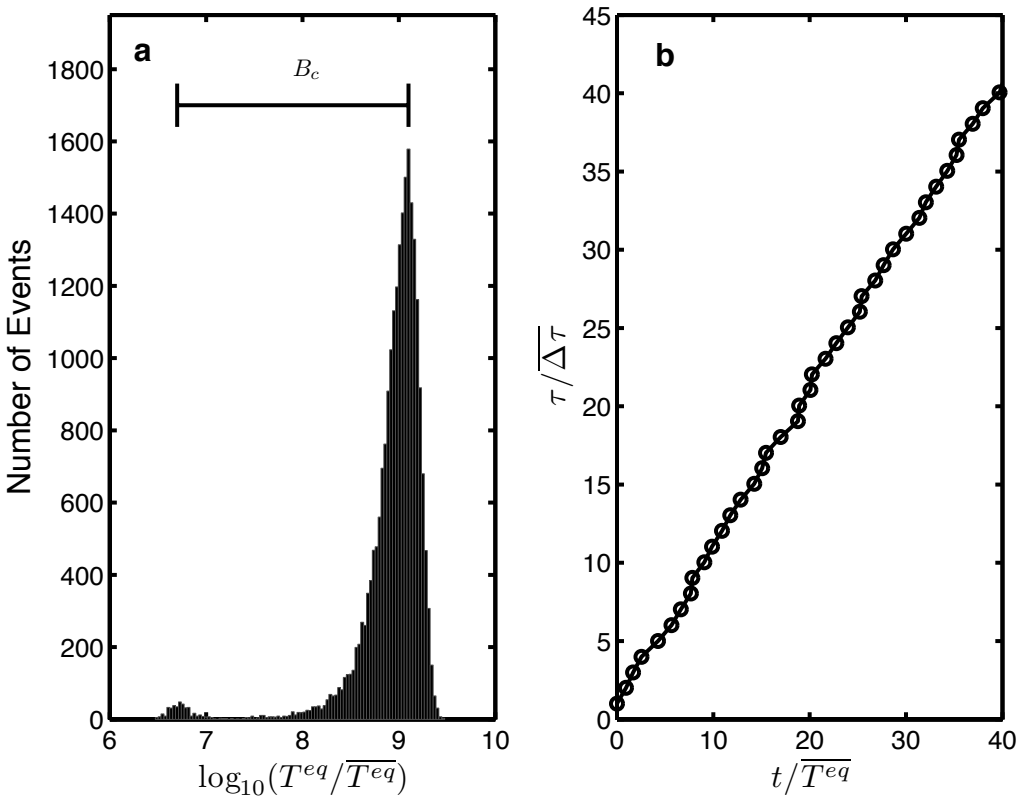

Figure 2.5: a) Distribution of normalized interseismic intervals on a logarithmic scale for a model with $W = 1.4 \times 10^4$ and $\sigma_{\Delta\tau}/\overline{\Delta\tau} = 0.005$. b) Cumulative stress released on the fault, τ, normalized by the mean yield stress $\overline{\Delta\tau}$ versus nomalized time. $\overline{T^{eq}}$ is the mean interseismic interval. The earthquake time sequence appears quasi-periodic, but it is actually clustered by our measure.

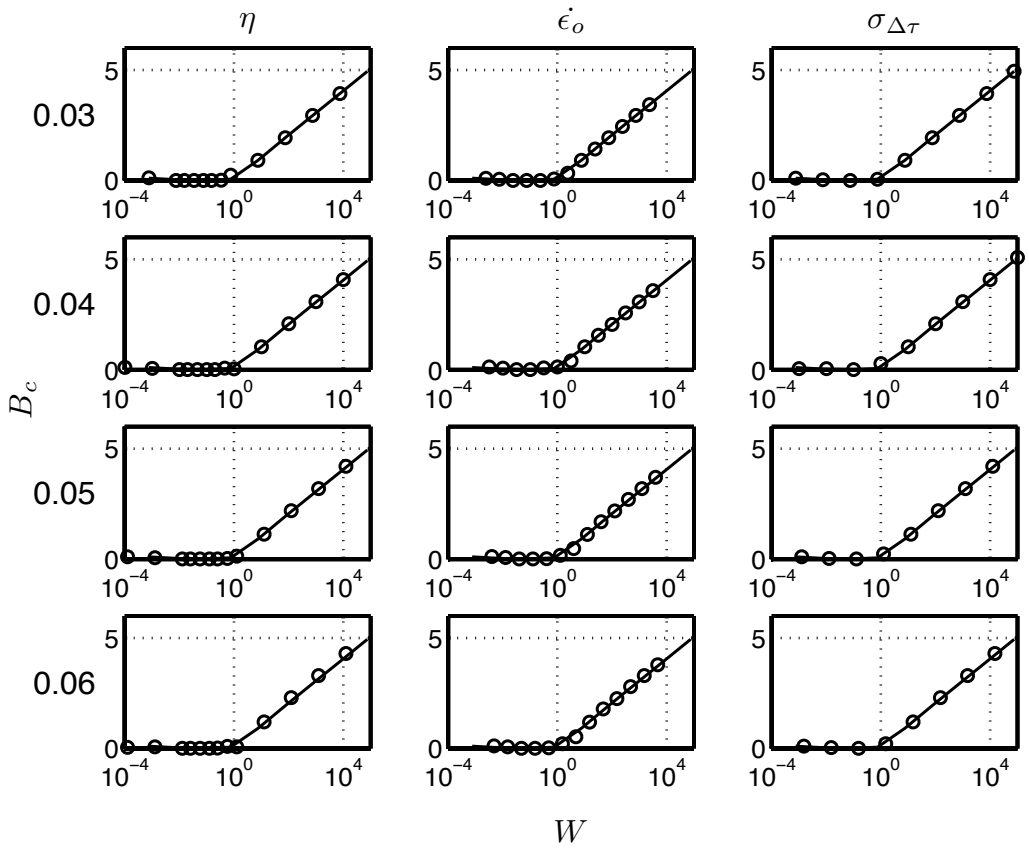

Figure 2.6: Amount of clustering in an earthquake sequence as measured by B_c increases as the Wallace number, W, increases. Each row has a different value of N (the ratio of standard deviation to mean of the fault yield stress), and each column is a set of models changing a particular parameter of W. η is the viscosity; $\dot{\epsilon_o}$ is the applied strain rate; and $\sigma_{\Delta\tau}$ is the standard deviation of the fault yield stress. The solid line is taken from the N = 0.03, $\sigma_{\Delta\tau}$ plot and is the same in every panel.

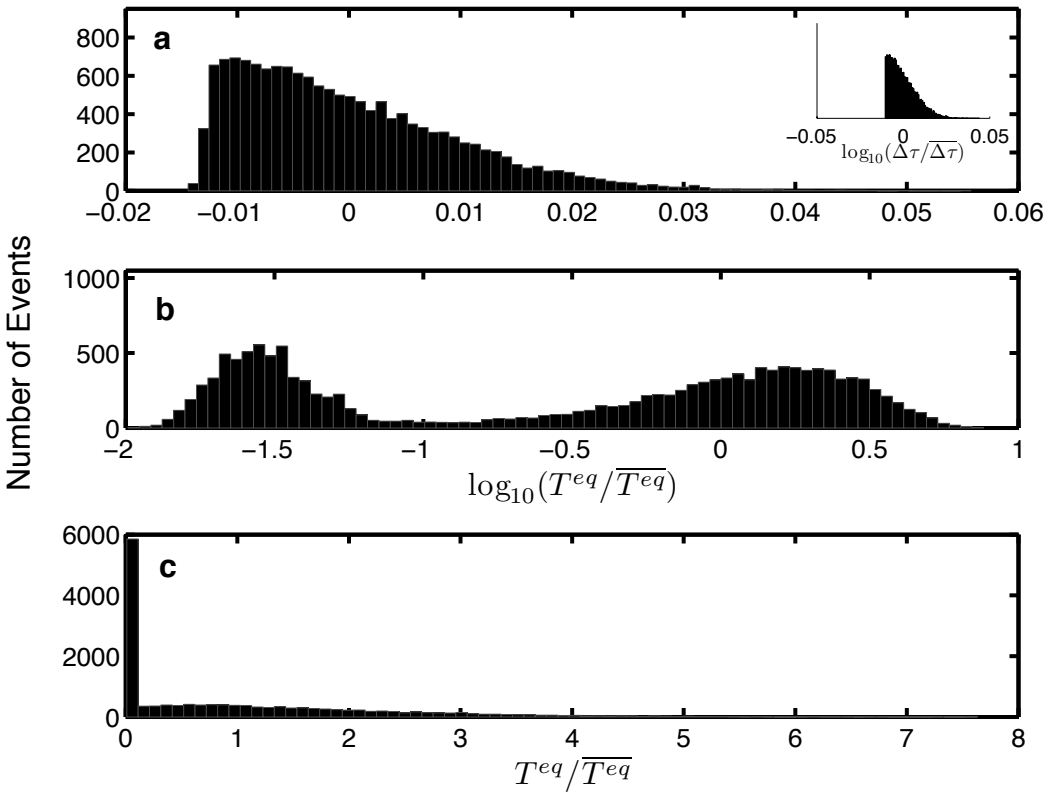

Figure 2.7: Same as Figure 2.3 with different distribution of fault yield stress.

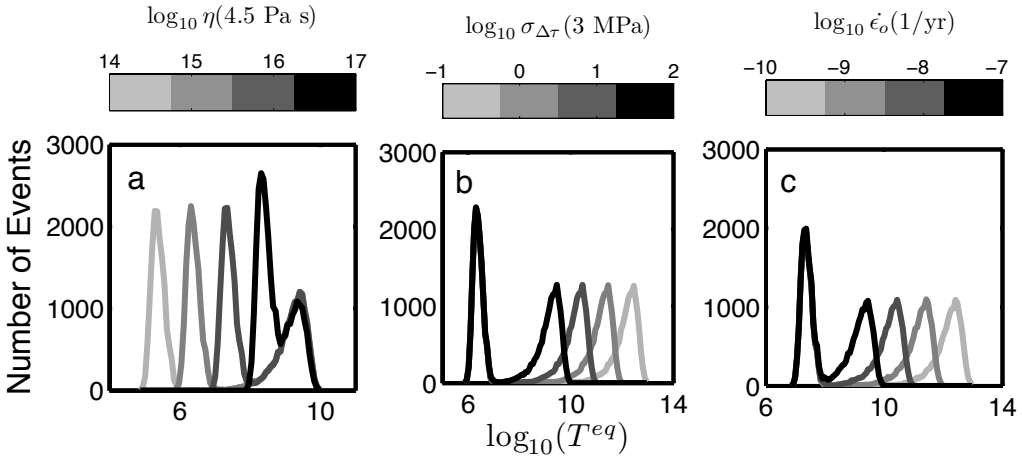

Figure 2.8: Distribution of normalized, logarithmic interseismic times for several values of W. In (a) the models have different values of viscosity, in (b) the models have different values of standard deviation of fault yield stress, and in (c) the models have different values of the applied tectonic strain rate.

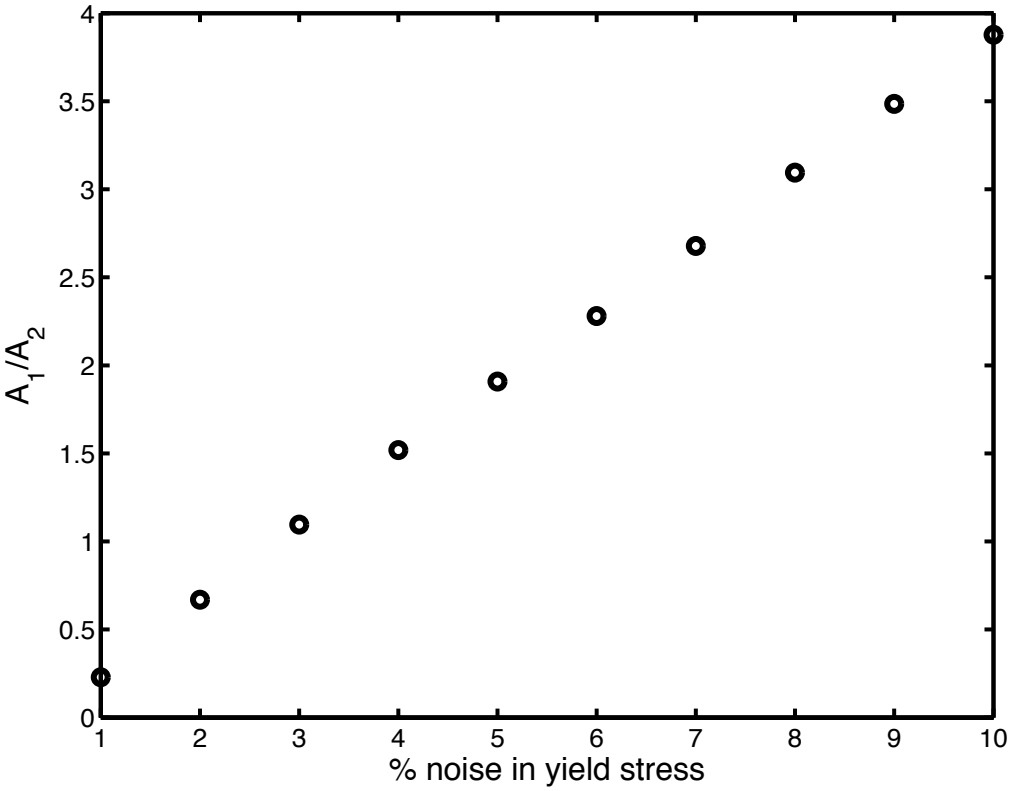

Figure 2.9: The ratio of earthquakes in the intra-cluster mode to the number of earthquakes in the inter-cluster mode as a function of the fraction of noise added to the fault yield stress.

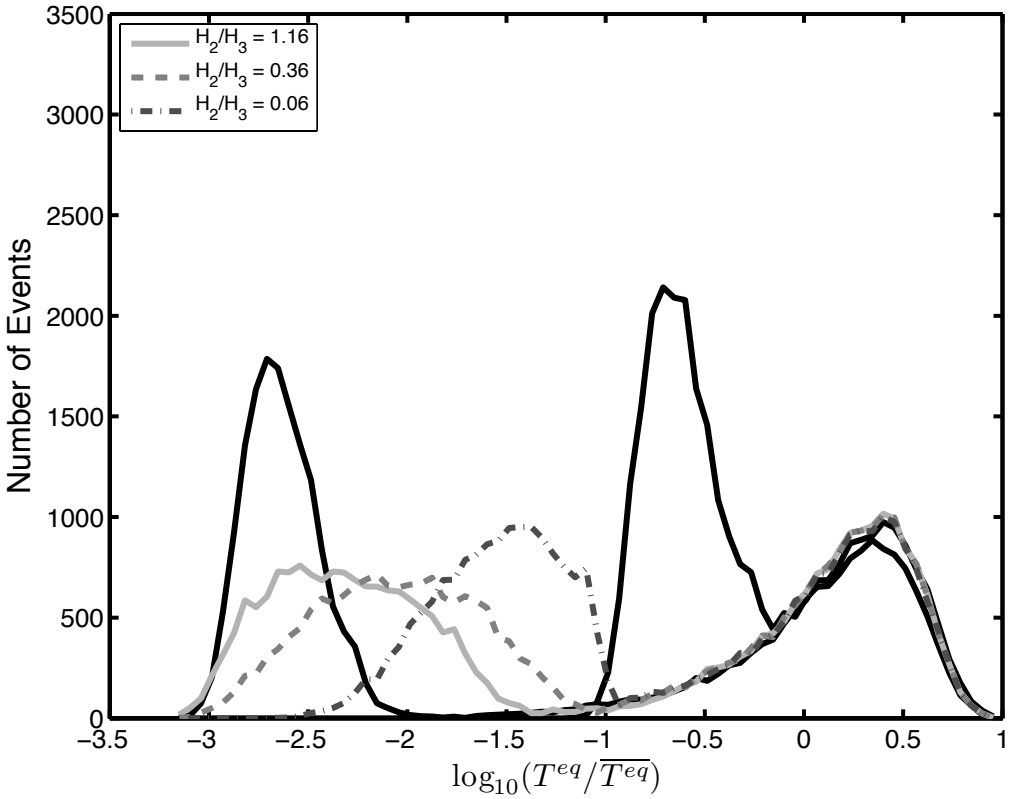

Figure 2.10: Distribution of normalized interseismic times in logarithmic space for models with an elastic layer over two viscoelastic layers (three-layer model). $\eta_2 = 4.5 \times 10^{15}$ Pa s and $\eta_3 = 4.5 \times 10^{17}$ Pa s (see Figure 2.1 for model description). The total thickness of the viscoelastic layers is kept constant as the ratio of the layer thicknesses is changed. The black solid lines are the end-member cases of $\eta_2 = \eta_3 = 4.5 \times 10^{15}$ Pa s (intra-cluster mode on the left) and $\eta_2 = \eta_3 = 4.5 \times 10^{17}$ Pa s (inter-cluster mode on the right).

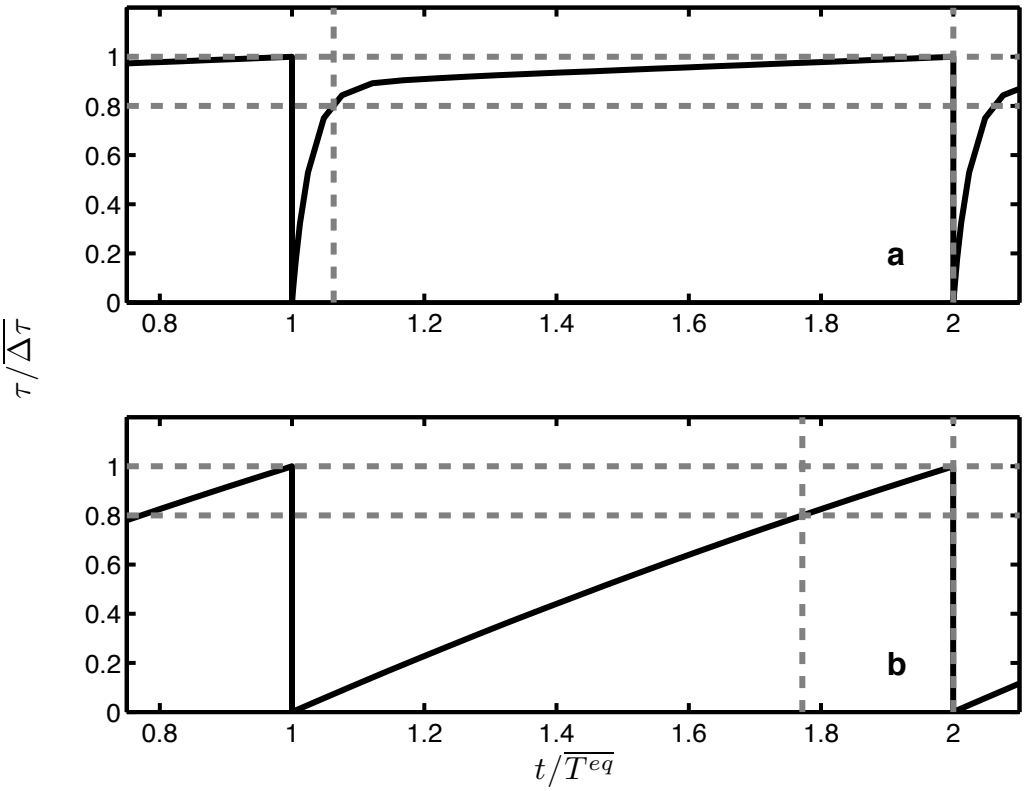

Figure 2.11: Average shear stress over the coseismic fault for two earthquake sequences. No noise has been added to the yield stress, so no clustering occurs. The dashed lines indicate the change in interseismic interval for a given change in yield stress. a) When $W/N = 85$, the shear stress rises rapidly early in the interseismic period due to rapid viscoelastic relaxation (relative to the tectonic loading rate). The loading rate then slows as the viscoelastic relaxation in the lower crust and the mantle slows. This nonlinear loading results in sensitivity to changes in the yield stress from one earthquake to the next. b) When $W/N = 0.85$ the shear stress approaches the yield stress almost linearly throughout the entire earthquake sequences. Changes in the yield stress lead to approximately proportional changes in the interseismic time.

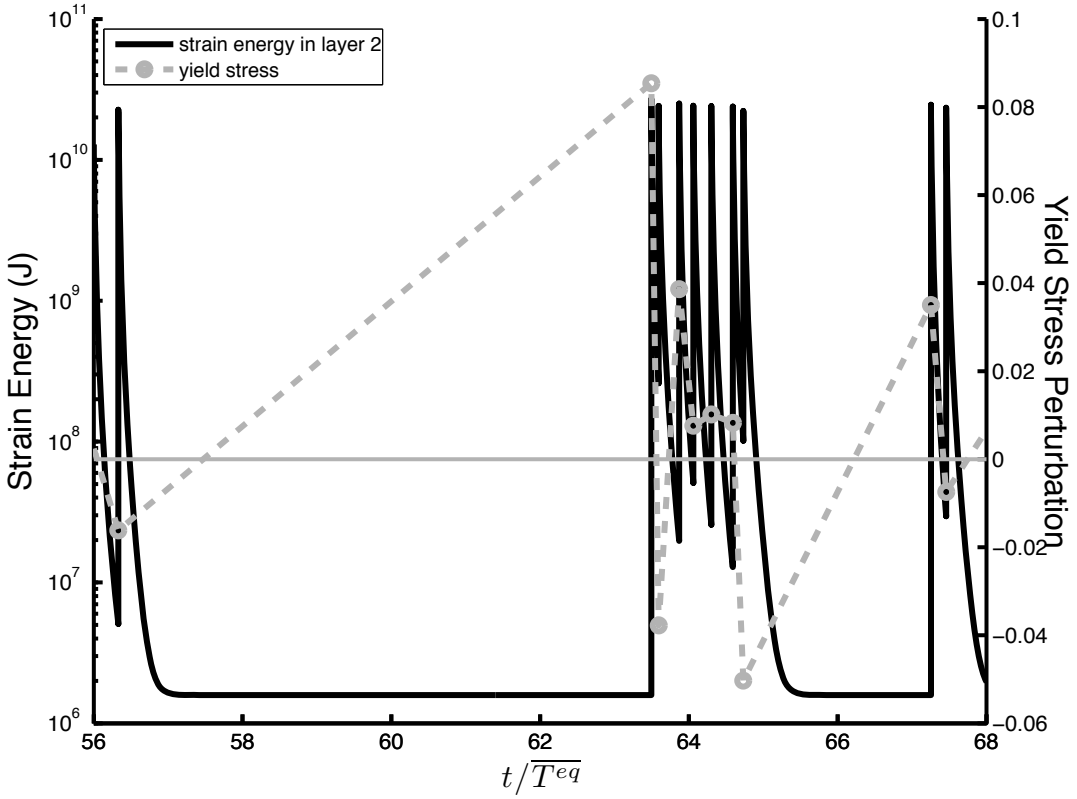

Figure 2.12: Strain energy (solid line) in the viscoelastic layer and the yield stress perturbation for a representative time period in a two-layer model with $\sigma_{\Delta\tau}/\overline{\Delta\tau} = 0.03$ and $W = 7.6$. An earthquake cluster occurs when a reservoir of stress in the viscoelastic layer due to a large stress drop continues to drive the reloading of the fault. Long inter-cluster periods occur when the reservoir of stress is exhausted and the yield stress increases.

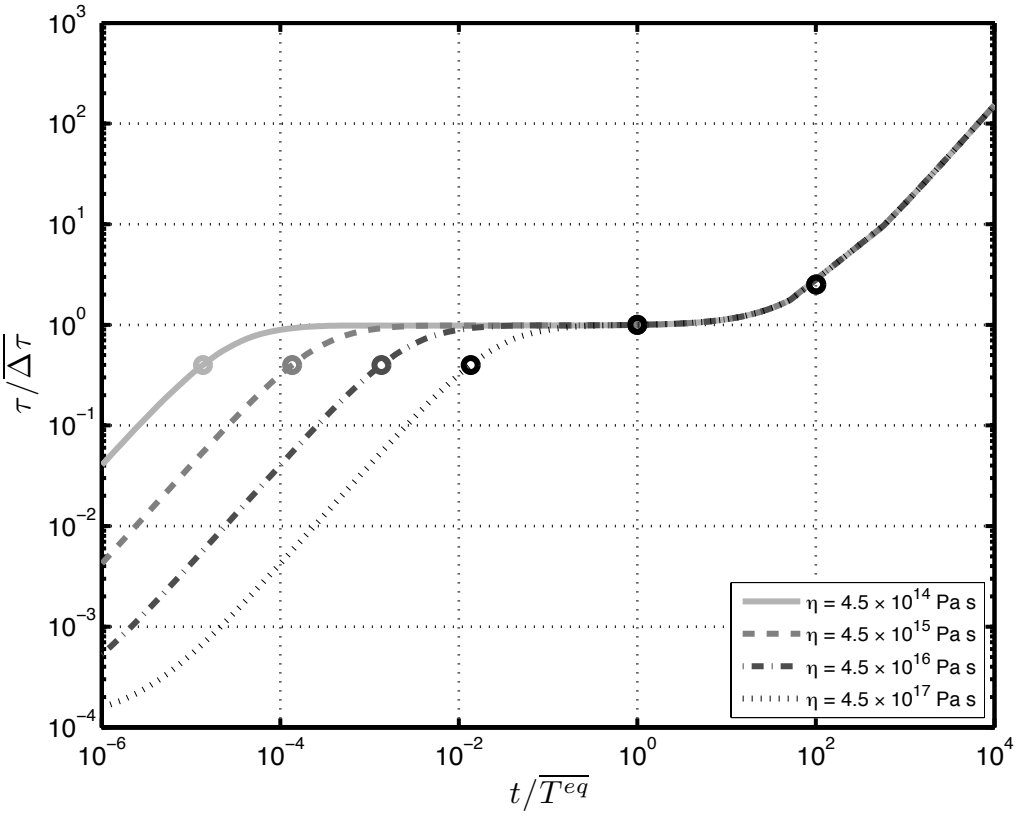

Figure 2.13: Average shear stress over coseismic fault as a function of time. The circles are at $\overline{\Delta\tau}$ and $\overline{\Delta\tau} \pm \sigma_{\Delta\tau}$. For systems with a large Wallace number, reloading comes in two phases: a viscoelastic rebound phase and a tectonic loading phase. The average fault yield stress falls on the flat portion of the reloading curve, while clustered periods occur during the viscoelastic rebound phase and inter-cluster periods are in the tectonic loading phase.

W_{KS05}	Wallace number defined by KS05,
W	New Wallace number
C_v	Coefficient of variation, old clustering metric
B_c	New clustering metric based on distribution of $\log_{10}(T^{eq})$
$\overline{\Delta\tau}$	Average earthquake yield stress
$\sigma_{\Delta\tau}$	Standard deviation of earthquake yield stress
N	$\sigma_{\Delta\tau}/\overline{\Delta\tau}$
$\dot{\epsilon_o}$	Applied strain rate
η_{eff}	Effective viscosity of the 1D system used by KS05
η_i	Viscosity of i^{th} layer
G_i	Shear modulus of i^{th} layer
$\overline{T^{eq}}$	Average interseismic time
$\overline{\Delta\epsilon}$	Average seismic strain drop
T^{hs}	Characteristic relaxation time of an elastic layer over a viscoelastic half space

Table 2.1: Definitions of notations used in text.

Chapter 3

InSAR Methods

3.1 Introduction

Differential interferometric synthetic aperture radar (InSAR) gives us the ability to measure ground displacements with sub-centimeter precision with a ground resolution (pixel size) on the order of 10 m. An additional benefit is the ability to observe remote areas without the need to install equipment. For details on InSAR see Massonnet et al. (1993); Rosen et al. (2000); Burgmann et al. (2000); Hanssen (2002); Simons & Rosen (2007). Briefly, a moving radar (typically on a satellite or airplane platform) images a swath of the ground surface recording both amplitude and phase information of the backscattered radar signal. If the radar images the same swath of ground twice, a displacement map can be formed by differencing the returned radar phase. The change in phase is proportional to the change in distance between the radar antenna and the ground that occurred during the time period between acquisitions. A single interferogram only measures the ground displacement in one vector component referred to as the radar line-of-sight (LOS). Given data availability, it is possible to combine images from various look geometries to reconstruct the three-dimensional displacement vector (e.g., Fialko et al., 2001; Wright et al., 2004).

We may wish to combine several interferograms into a single image in some "average"

sense in order to improve the signal-to-noise ratio. In addition, if we are interested in the time dependent deformation field we can use multiple interferograms to gain time resolution in our displacement data. Either of these applications requires all interferograms to be located in a common coordinate system. An approach to easily co-register several interferograms into such a common coordinate system is based on the two-pass approach used by the ROI_PAC InSAR processing software (Rosen et al., 2004) and described in section 3.2. Our method, which we call stack processing, also has the benefit of increasing the success rate of creating interferograms. A method for creating deformation time series from InSAR data, called MInTS, is described in section 3.3. Scientific results using MInTS on InSAR data from Iceland can be found in section 6.5.

3.2 Stack Processing

The ability to create interferogram stacks or perform time series analysis in InSAR data requires that all the interferograms of interest be in a common coordinate system or reference frame. A geographic coordinate system is one possibility; however, this choice of reference frame results in interferograms at the resolution of the digital elevation model used for georeferencing rather than the natural resolution of the original radar images or the interferometric processing.

Our stack processing method uses the range-azimuth coordinate system of a single SAR image as a common coordinate system. We choose a single "master" SAR image to define the stack coordinate system and morph all interferograms into this coordinate system after creation of the unwrapped interferogram. The master coordinate system is actually the estimated coordinate system of the master SAR image calculated using *a priori* orbit information of the radar satellite. In addition, stack processing reduces the number of times

a synthetic radar amplitude image (based on the slope of the surface topography) is cross-correlated with an actual radar amplitude image, thereby reducing the failure rate of the interferometry process.

In standard two-pass processing, an interferogram is formed in the radar coordinates of one of the SAR images. The interferometric phase is due to both ground displacement in the radar line-of-sight and the topography of the ground surface (ignoring sources of error). If we wish to construct a differential interferogram that contains only information about ground displacement, we must remove the effect of topography. Removal of the topographic phase is typically done by transforming a DEM into the radar coordinate system of the interferogram, calculating its effect on the interferometric phase, and subtracting that phase from the interferogram. The DEM is first converted to an estimated radar coordinate system; this is the coordinate system based on *a priori* orbit parameters for the radar platform. The estimated coordinate system is expected to be close, but not identical, to the actual radar coordinate system for a given scene. An empirical affine transformation between the orbit derived reference frame and the actual reference frame is found through a process of automatic ground control point (GCP) estimation. These GCPs are derived by cross-correlating the amplitude of two images. For a given DEM, an artificial amplitude image in the simulated reference frame is calculated based on the estimated amplitude of the backscattered radar derived from the radar viewing geometry and the surface slope of the topography. This artificial amplitude is then cross-correlated with the actual amplitude to find the transformation that will morph the DEM into the actual radar coordinates. In truth, the actual radar amplitude depends not only on the viewing geometry and surface slope but on the roughness and dielectric constant of the reflecting surface. We are therefore comparing two fundamentally different images, and it

is not uncommon for the co-registration to fail. Figure 3.1 is a flow diagram for traditional two-pass processing described above. One benefit of the approach described below will be to reduce the rate at which this problem occurs.

The Perl scripts that perform the stack processing procedure described here are based on existing modules in ROI_PAC (Rosen et al., 2004). Our stack processing procedure consists of two parts. The first sets up the master coordinate frame for the stack and creates a DEM and real radar amplitude image in that same reference frame. A single radar image (referred to as an SLC) is chosen to define the master coordinate system. This part is performed with the Perl script `make_stack_master.pl`. A key difference between the traditional processing method and stack processing is that instead of creating an artificial radar amplitude from the DEM, an actual radar amplitude image is created using the master SLC. Following the creation of the master DEM and radar amplitude image, interferograms can be easily created (with the `process_stack.pl` script). In order to remove the effect of topography from the interferogram, the DEM must be transformed into the real radar coordinate frame of each particular interferogram. But because we have an actual radar amplitude image, the cross-correlation to find the affine transformation needed is more likely to succeed. A cross-correlation between a simulated, DEM-based, amplitude and a true amplitude is only performed once for all the stacked interferograms. We then use the affine transformation between the coordinate frame of the interferogram and the master coordinate system to transform the interferogram into the common master coordinate system used to stack all interferograms. The DEM and radar amplitude image in the master coordinate frame is re-used for every interferogram created for the stack. Figure 3.2 is a flow diagram for `make_stack_master.pl` and `process_stack.pl`.

Figure 3.3 shows the difference between a radar image processed using the traditional

method and one processed using the new stacking method. The error between the final geocoded images using the two methods is shown in Figure 3.4. The errors are small and due to the slight difference in DEM removal which results from slightly differing affine transformations to the interferogram's coordinate frame. The patch with large errors, seen in both Figures, is due to an unwrapping error that occurred in the traditionally processed image and merely reflects the small statistical difference in the amount of decorrelation between the images.

We have written additional scripts that work with the ROI_PAC InSAR processing software (Rosen et al., 2004) to processes interferograms into a stack coordinate frame. Our method allows for the use of an ERS1/2 image master for both Envisat and ERS interferograms. It should be possible to create an ERS1/2 interferogram using an Envisat master, though this has not been tested. Stack processing has also been successfully tested with data from ALOS, the Japanese L-Band SAR satellite.

3.3 MInTS

This section describes techniques that are the result of work by E. Hetland, P. Muse, and M. Simons. Early testing and debugging of these methods have been carried out by the author with scientific application presented in section 6.5.

A displacement time series can be constructed from several interferograms that do not necessarily share common radar scenes using the small baseline subset (SBAS) approach (Berardino et al., 2002). SBAS has been used for InSAR data from the Asal rift in the Afar region by Doubre & Peltzer (2007). They were able to identify subsidence of the rift floor and fault slip both as steady creep and short slip events. The shortcomings of the SBAS technique include the lack of a formal method for regularizing the solution in regions where

one or more interferograms are decorrelated; the need to *a priori* set a pixel or region of pixels to zero displacement; temporal parametrization that depends on the radar acquisition times; and neglect of known intra-image correlation among the pixels. In order to address these concerns, a system for performing time series analysis on InSAR data called MInTS (Multiscale Interferometric Time Series) is under development (Hetland et al., 2009).

The formation of a deformation time series from a set of interferograms in MInTS combines logical approaches to both the temporal and spatial variations in the signal. A time series is constructed as a superposition of several individual components e.g., a linear rate, sinusoidal signals at multiple periods, logarithmic or exponential decays, Heaviside functions, etc. The inclusion of these time functions are chosen *a priori* based on what physical processes one believes should be present in the interferograms. Other deformation that cannot be described by a simple analytic form – whether it is expected to exist and cannot be easily described analytically or unknown deformation that one hopes to detect using MInTS – is captured with a damped sum of spline basis functions. The choice of these particular functions is not unique and can change based on the situation; any linear combination of time dependent functions can be conceivably used in the analysis.

Rather than letting the (often irregular) sampling rate of the interferograms dictate the parametrization of the time series, MInTS parametrizes time in a way that is appropriate for each constituent time function included in the inversion. The separate parametrization for each time constituent also allows for more precise specification for how the regularization is achieved – i.e., allowing explicit *a priori* assumptions to go into the regularization.

In addition to using the arbitrary time parametrization described above, MInTS distinguishes itself from other InSAR time series analysis methods by avoiding a pixel-by-pixel approach (e.g., Berardino et al., 2002). A pixel-by-pixel estimation of the time series ig-

nores the spatial covariances between pixels in an interferogram that are known to exist (e.g., Emardson et al., 2003; Lohman & Simons, 2005). However, including the complete covariance matrix in a single inversion is computationally intractable due to the shear number of pixels involved; it is estimated that inverting the full covariance matrix could take a single CPU about two years. The solution is to decompose the interferograms into multiple band-passed components using a wavelet decomposition. The covariance structure of an interferogram is such that the pixel-to-pixel covariance decreases as the distance between the pixels increases (Lohman & Simons, 2005); as we eliminate the longer wavelengths by filtering, we reduce the needed size of the covariance matrix for each subsequent wavelet scale. The current implementation of MInTS assumes that at each wavelet scale, the individual wavelet coefficients are independent of all others and therefore have no covariance (i.e., the covariance structure is diagonalized). This is a reasonable assumption as the wavelet decomposition averages over approximately the correlation wavelength, eliminating much of the covariance between wavelet coefficients. Future developments of MInTS can include a more formal statement of covariance between wavelet coefficients and/or smoothing over the wavelet and spatial domains.

Figure 3.1: Standard ROI_PAC 2-pass interferometric processing workflow. Data are blue ellipses, processing steps are tan boxes, and affine transformations between coordinate systems are green boxes. The coordinate systems which the affine transformation maps are shown in the box. A SLC is a single look complex radar image containing both amplitude and phase information; DEM is digital elevation model; AMP is the simulated radar amplitude based on the surface slope of the topography. Coordinate transformations are represented by an arrow, $\Rightarrow$. The coordinate systems shown are X_1^R, the radar coordinates of first image; X_2^R, the radar coordinates of second image; X_1^S, the simulated radar coordinates of first image estimated from orbital parameters; and X^G, the geographic coordinates. Flow chart adapted from Simons & Rosen (2007).

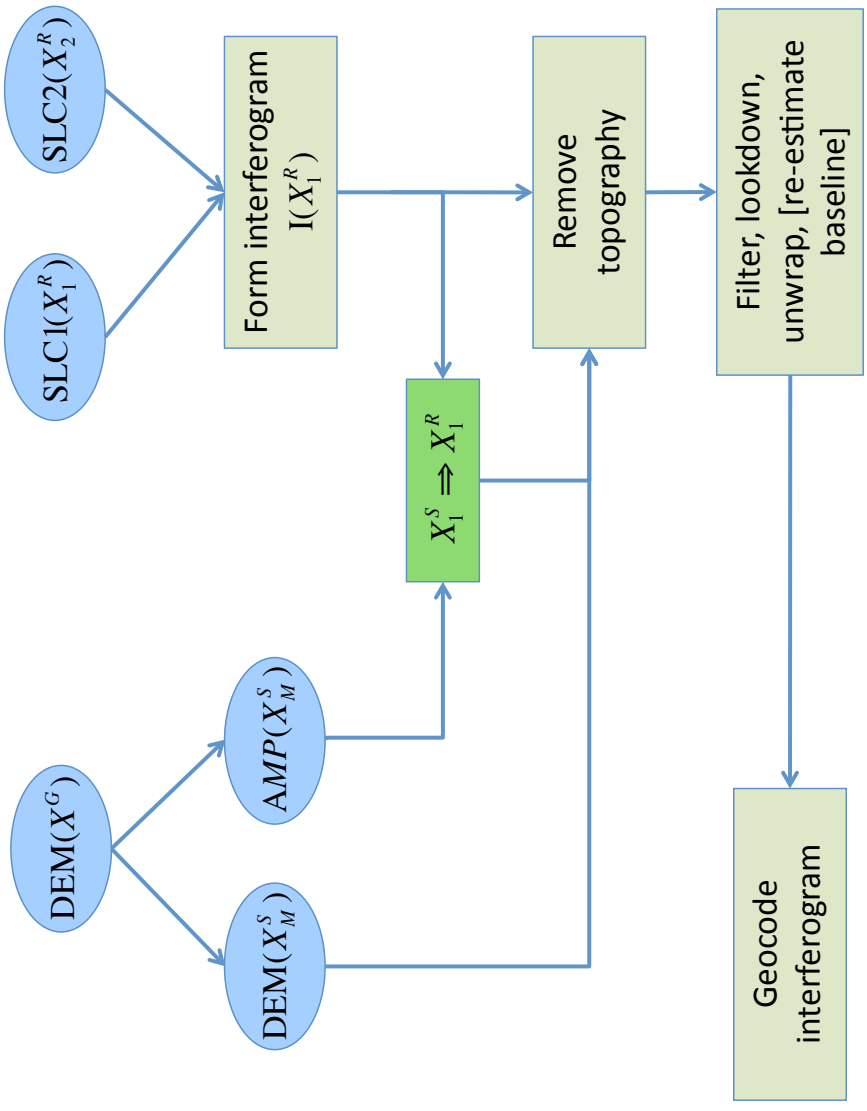

`process_2pass.pl`

Figure 3.2: Stack interferometric processing workflow. See Figure 3.1 for description of most terms. SLCM is the SLC of the master radar image used to define the master coordinate system. X_M^R is the radar coordinate system of the master image, and X_M^S is the simulated radar coordinate system used as the master reference frame. In the penultimate step, interferograms that have been processed into the same master coordinate system are combined to create the final product of interest (e.g., average velocity calculation, time series inversion, etc).

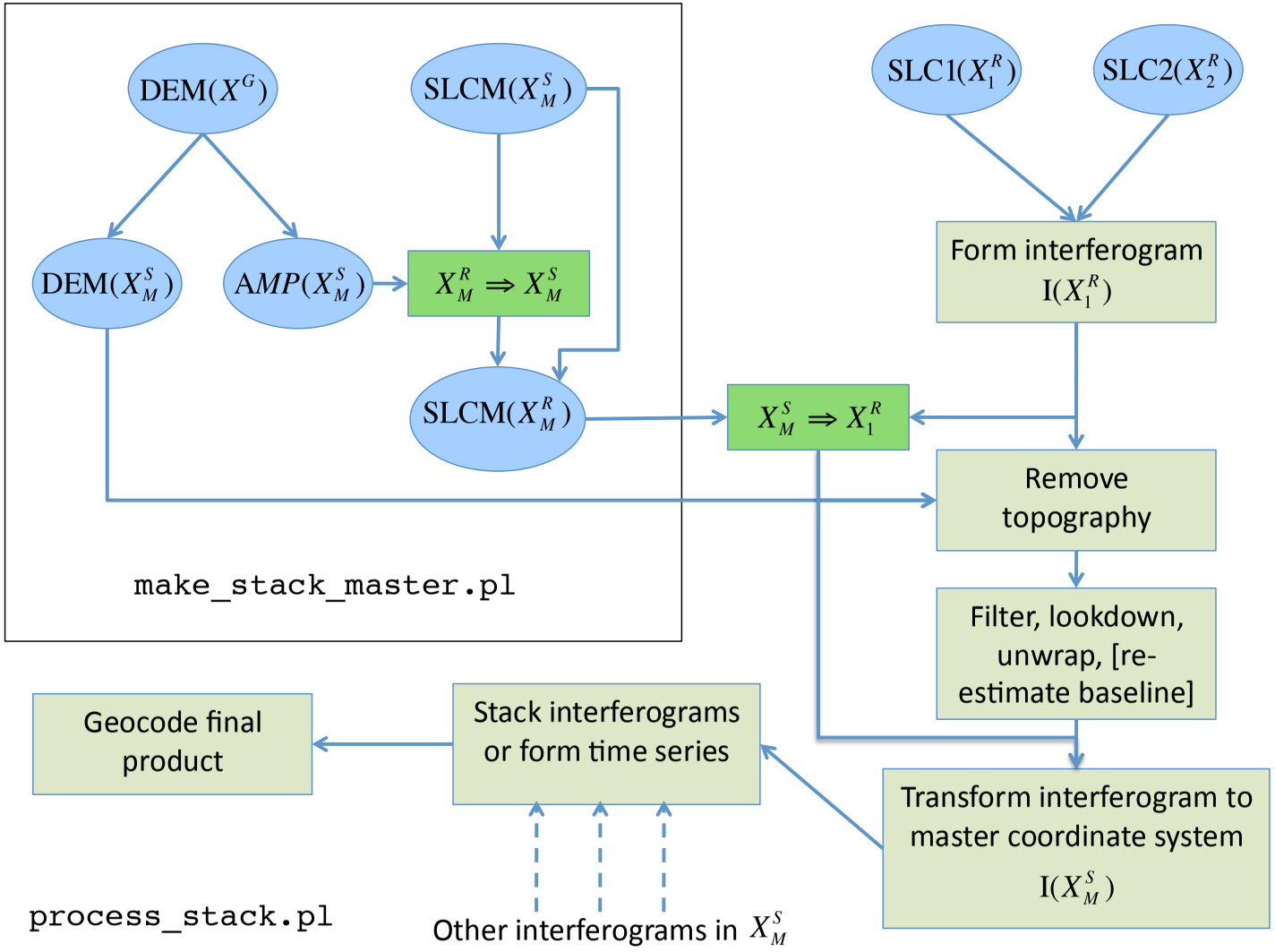
DEM(X^G)
SLCM(X_M^S)
DEM(X_M^S)
AMP(X_M^S)
$X_M^R \Rightarrow X_M^S$
SLCM(X_M^R)
make_stack_master.pl
SLC1(X_1^R)
SLC2(X_2^R)
Form interferogram I(X_1^R)
$X_M^S \Rightarrow X_1^R$
Remove topography
Filter, lookdown, unwrap, [re-estimate baseline]
Transform interferogram to master coordinate system I(X_M^S)
Stack interferograms or form time series
Geocode final product
process_stack.pl
Other interferograms in X_M^S

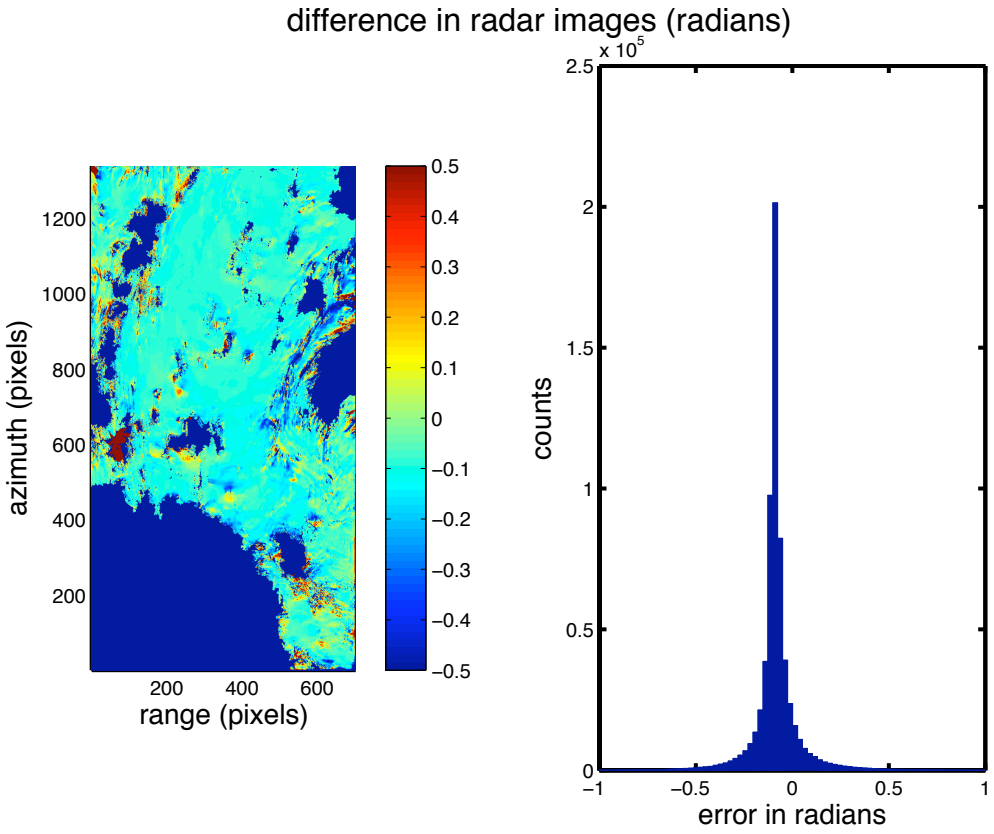

Figure 3.3: Difference between interferograms from ERS/Envisat track 9 frames 2277–2295 (northern Iceland) in radar coordinates using traditional two-pass processing and stack-processing. Left: image of differences in geographic coordinates. Right: histogram of differences. The image used to create the stack coordinate system is ERS2 orbit 6877 (1996/08/13). The interferogram is composed of images from ERS2 orbit 6376 (1996/07/09) and ERS1 orbit 11677 (1993/10/09).

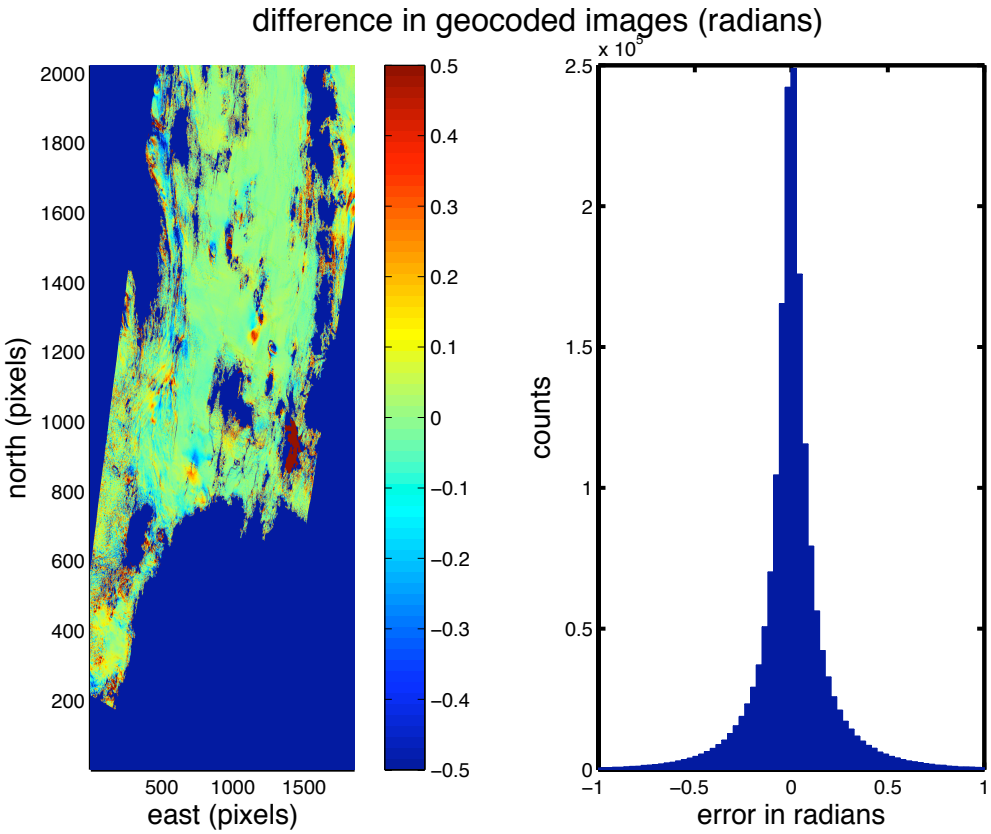

Figure 3.4: Same as Figure 3.3 for the corresponding geocoded image.

Chapter 4

Importance of Ocean Tidal Load Corrections for Differential InSAR

4.1 Note

This chapter has been published as DiCaprio, C. & Simons, M., 2008, Importance of Ocean Tidal Load Corrections for Differential InSAR, *Geophysical Research Letters*, **35**(22), L22309.

4.2 Abstract

Large time series of interferometric synthetic aperture radar (InSAR) measurements make it possible to detect slow tectonic motions of the Earth's surface on the order of millimeters per year. Here, we illustrate the importance of correcting InSAR data for the effects of ground displacements due to ocean tidal loads (OTL). These loads can cause displacement gradients greater than 3 cm per 100 km, which is larger than the accuracy of InSAR techniques, and can be a significant percentage of the measured displacement due to slow tectonic processes. We demonstrate the importance of OTL with predicted displacements from selected regions of tectonic interest.

4.3 Introduction

As the amount of available radar satellite data increases, the ability to use interferometric synthetic aperture radar (InSAR) to study small amplitude deformation (on the order of millimeters per year) and to create long time series of surface motion becomes more of a reality (e.g., Simons & Rosen, 2007). When using InSAR to measure small displacements, unwanted sources of deformation can be significant. One may wish to remove or otherwise account for surface deformation such as changes in ground water and both seasonal and non-seasonal mass loading. Here, we focus on displacements from mass loading due to ocean tides, generally referred to as ocean tidal loading (OTL). OTL deformation is of particular concern when using InSAR to study processes occurring over length scales of order 100 km. Many sources of long-term deformation that we may be interested in studying can have wavelengths this scale or larger, including inter-seismic loading of seismogenic faults and post-seismic inelastic deformation.

InSAR measurements are sensitive to other non-tectonic effects that we do not address in this paper including solid body tides, pole-tides, non-tidal mass loading both seasonal and non-seasonal, and ionospheric and tropospheric phase delay (e.g., Simons & Rosen, 2007). The wavelength of solid body tides and pole tides are expected to be one to two orders of magnitude greater than the OTL (e.g., Blewitt, 2007). They are, therefore, negligible in InSAR processing because at the scale of an interferogram they primarily introduce an additive constant to the phase; such constituents are not normally resolved in standard differential InSAR as interferometry only has the ability to measure relative displacement within an image. Generally, non-tidal, non-seasonal, mass loading is expected to be much smaller than the OTL signal near the coast and can be safely ignored in most InSAR analyses

(Dong et al., 2002). Seasonal signals that are non-tidal may be significant for particular regions (e.g., those close to aquifers or glaciers), but they are not easily estimated generically and must be dealt with on a case-by-case basis.

OTL displacements are the elastic response of the Earth to the redistribution of water mass from the ocean tides (e.g., Agnew, 2007). OTL can introduce deformation gradients of several millimeters to centimeters across an interferogram near coastal regions, and therefore needs to be considered carefully. For example, in South-West England, vertical ground displacements due to tidal loading can range over 10 cm (Penna et al., 2008) and displacement gradients can be larger than 3 cm per 100 km. Corrections for OTL displacements are commonly performed during analysis of GPS and VLBI time series (e.g., Urschl et al., 2005), but are not currently considered for InSAR processing. The effect of the OTL is readily calculated using existing tools; thus, model predictions should be subtracted from an interferogram before tectonic analysis. The dominant component of OTL displacement is vertical and the line-of-sight look angle of most SAR satellites makes them sensitive to vertical ground deformation (e.g., a representative look angle for ERS and Envisat is about 23° degrees from vertical).

Even if we are not interested in long-wavelength deformation, the OTL signal may be of concern during the InSAR processing stage since it is common in InSAR processing to re-estimate the satellite baseline. By re-estimating the baseline we aim to eliminate errors due to uncertainties in the satellite orbits. The re-estimation process removes long-wavelength signals from the interferogram, meaning that any real long-wavelength deformation, as well as any long-wavelength variation in propagation delay, would be mapped into the satellite baseline. If not removed, long-wavelength OTL deformation can cause errors in the baseline re-estimation process.

Accounting for the OTL displacements in InSAR data analysis becomes more important as more radar satellite data becomes available, and we are able to measure slow processes. For example, a formal time series analysis of InSAR data would include, in addition to estimates of error, all known sources of deformation. Accounting for non-tectonic sources of deformation such as OTL can also help with more rigorous integration of InSAR with GPS observations.

4.4 Examples

In order to calculate the displacement due to the ocean tidal loads we use the SPOTL software (Agnew, 1997). Alternate means of computing the OTL include the "Ocean Tide Loading Provider" web site (http://www.oso.chalmers.se/ loading/), which uses OLFG/OLMPP (Scherneck, 1991); GOTIC2 (Matsumoto et al., 2005); and CARGA (Bos & Baker, 2005).

The SPOTL program *nloadf* calculates the OTL amplitude and phase for a specific tidal constituent at a particular location using any number of global and/or local tidal models and convolving the resultant water height with the Green's functions for the Earth's elastic response to mass loading. The program *hartid* uses the derived harmonic tide constituents and predicts the OTL displacement at a particular time. Several studies have compared OTL models to GPS data (Thomas et al., 2007; Melachroinos et al., 2007; Vergnolle et al., 2008; Penna et al., 2008). Penna et al. (2008) showed that for particular GPS sites, removing the M2 OTL displacements predicted by the CARGA software can reduce the amplitude of displacements at the period associated with the M2 tide to the level of the noise in the GPS time series; although the ability of OTL models to correct geodetic data depends on many factors including location and required precision for the geological application. The SPOTL package has also been shown to accurately predict the OTL displacement.

Penna et al. (2008) compared several OTL softwares and found that those that did not use water mass redistribution (including SPOTL) showed no greater than 1-2 mm difference in predicted vertical displacements near the coast and discrepancies less than 0.2-0.5 mm inland.

In all of the following examples, the amplitude and phase from tidal constituents M2, S2, N2, K2, K1, O1, P1, and Q1 for version 00.2 of the Goddard Ocean Tide Model (GOT00.2) (Ray, 1999) were input into *hartid* to calculate the displacement at a given time and location. GOT00.2 was chosen among several available modern ocean tide models. Penna et al. (2007) show that GOT00.2 and four other ocean tide models are in close agreement for the purpose of calculating OTL displacements in all regions considered in this paper. We used the elastic Green's functions from the Gutenberg-Bullen Earth Model (Farrell, 1972). The examples shown are for regions of tectonic interest that have sizable OTL displacements.

One should consider which tidal model is best for the region of interest (e.g., Baker & Bos, 2003; Melachroinos et al., 2007; Penna et al., 2007). Commonly used modern ocean tidal models include CSR4.0 (Eanes & Bettadpur, 1995), FES2004 (Lefevre et al., 2002), GOT00.2 (Ray, 1999), NAO99b (Matsumoto et al., 2000), and TPXO6.2 (Egbert & Erofeeva, 2002). Thomas et al. (2007) found that these models are indistinguishable within measurement noise for a small number of GPS stations. However, Baker & Bos (2003) state that no single ocean tide model is applicable to all parts of the world. Penna et al. (2007) map the scatter in OTL displacement predictions from several different tidal models and found that model discrepancies are particularly large near shallow seas. In addition, Penna et al. (2008) found that at several coastal sites the calculated OTL displacement is sensitive to the specific tide model used at the several millimeter level.

In most differential InSAR applications, we are only concerned with the relative displacements within a particular interferogram and not the absolute displacements. Figure 4.1 shows the relative displacements due to the OTL between two extremal points in a typical radar footprint as a function of time for northern Iceland. A given satellite typically images the same location at approximately the same time of day; such a sampling is shown in the bottom plot of Figure 4.1. Because the period of the tidal maximum is not twenty four hours, a different amplitude of the OTL displacement is sampled each day. A particular SAR pair is usually chosen based on the geophysical target and available data without regard to the magnitude of the OTL displacement across the interferogram; therefore, users of InSAR are likely to encounter the maximum OTL displacement in some of their interferograms. In addition, using a regularly sampled SAR data set (i.e., using every available acquisition of a regularly sampled target) will result in aliasing of the OTL signal. For example, ERS and Envisat have a repeat time of 35 days giving an aliased period of 95.3 days for the M2 (principal lunar semi-diurnal) tidal constituent.

Figures 4.2 and 4.3 show predicted displacements in the radar line-of-sight (LOS) direction as they would be measured by InSAR due purely to the OTL for northern Iceland and Peru respectively. These displacements were produced by calculating the OTL displacement projected into the LOS and differencing the displacement for the two acquisition times. InSAR measurements have a constant shift ambiguity and only relative displacements within the image are actually measured; therefore to facilitate inter-comparisons we remove the median displacement from both figures. The use of wide swath radar images has become more common with the current generation of SAR satellites. Wide swath images have a lower resolution but provide a swath width about a factor of three larger than the normal strip-map swath width, and are thus useful for capturing an entire plate boundary in a

single image (e.g., Simons & Rosen, 2007). For satellite tracks parallel to the coastline, a wide swath image is expected to have a larger relative OTL displacement compared to a normal swath image. In Figure 4.3 the across track OTL displacement for the wide swath image is over 26 mm while the deformation across the strip-map image is about 12 mm.

We expect the OTL to map into the baseline re-estimation if it is not removed prior to the re-estimation process. To first order, baseline re-estimation will reduce the long wavelength ramp across an interferogram by recalculating the reference phase – the interferometric phase due to the reference surface (often a sphere or ellipsoid approximating the surface of the Earth without topography). The reference phase for a spherical reference surface is given by Hanssen (2002)

$$\phi_{ref} = -\frac{4\pi}{\lambda}\left(R_1 - \sqrt{(\rho_1 + B_v)^2 + R_e^2 - \frac{\rho_1 + B_v}{\rho_1}(D\cos\frac{B_h}{\rho_1} + \sqrt{E}\sin\frac{B_h}{\rho_1})}\right), \qquad (4.1)$$

where

$$D = (\rho_1^2 + R_e^2 - R_1^2)$$

$$E = 4\rho_1^2 R_e^2 - D^2.$$

R_1 is the range coordinate of the reference radar image, B_v is the vertical baseline, and B_h is the horizontal baseline. λ, R_e, and ρ_1 are the radar wavelength, Earth radius, and position of the reference satellite, respectively. Using Equation 4.1, the predicted baseline given a phase ramp across the image depends on the assumed geometry of the satellites, but in general, an OTL displacement of five cm across the image results in baseline re-estimation errors of tens of cm, larger than the relative precision of reported orbits. If the baseline is not re-estimated during processing, then it is common to estimate a bi-linear ramp from

the interferogram during modelling. Figures 4.2 and 4.3 also show residual displacements after removing a best fitting bi-linear ramp.

The influence of the OTL on displacement gradients will decrease away from the coast. For any particular geographic region, the horizontal gradient in OTL displacements across the interferogram is a measure of the sensitivity of the interferogram to the OTL. Figure 4.4 shows the magnitude of the horizontal gradient in the vertical displacement amplitude of the OTL due to the M2 tidal constituent for the western United States which is tectonically active both near the coast and several hundreds of km inland (the M2 being the largest constituent and the vertical displacement having the largest effect on an interferogram). More than about 200 km away from the coast the OTL gradient is relatively small.

4.5 Conclusions

As InSAR is more commonly used as a high precision geodesy technique for small amplitude, long-wavelength processes, the correct handling of the OTL becomes important. We have shown that the size of the OTL displacement is comparable to both InSAR accuracy and rate of deformation for scientifically interesting targets near coastlines. The OTL correction is relatively insignificant if the target is a large, rapid deformation (e.g., co-seismic studies); however, when investigating smaller amplitude displacement processes the OTL should be considered. The orbits of the SAR satellites may be known well enough that re-estimation of the orbits is not necessary and we can therefore recover long-wavelength features previously ignored in InSAR analysis. Even when baseline re-estimation removes the long-wavelength ramp from an interferogram, the OTL can map into baseline errors and should therefore be removed prior to such processing.

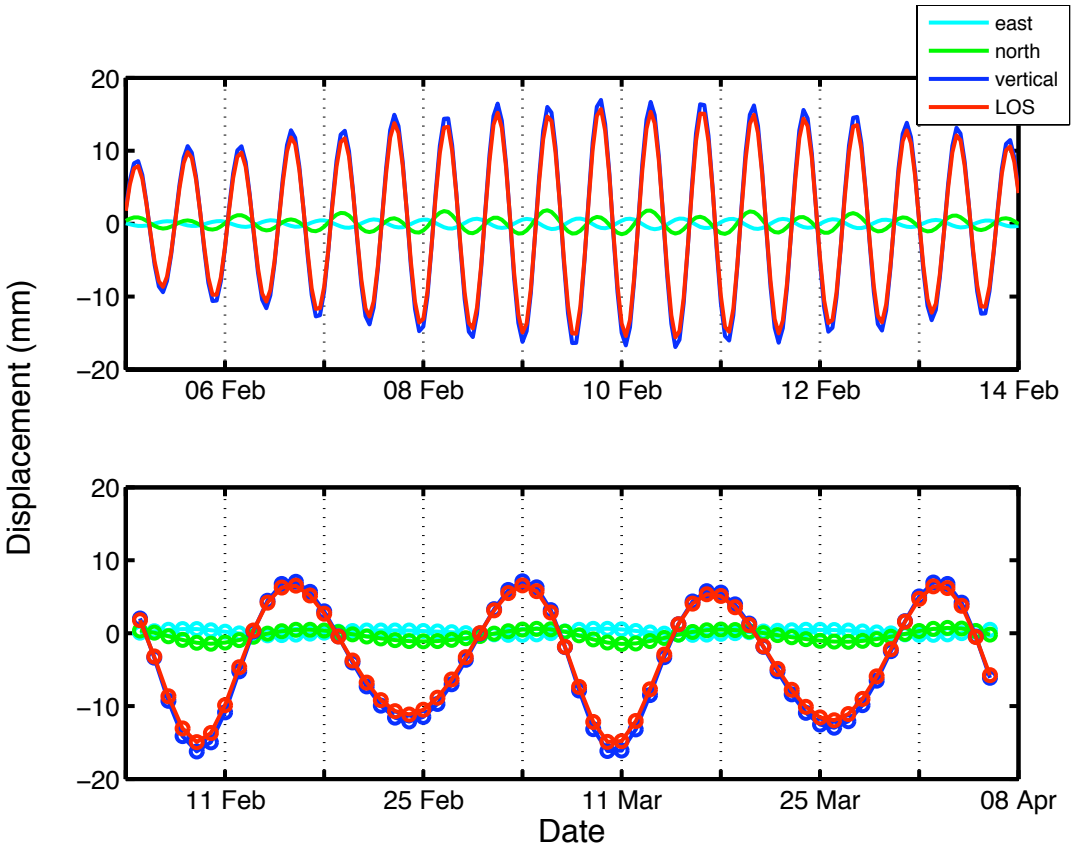

Figure 4.1: Top: time series of relative displacements in northern Iceland due to OTL for a period in 2001. The displacements are taken at the point (16.30W, 66.27N) relative to (17.15W, 64.45N) giving the relative displacement north to south for a typical interferogram (see Figure 4.2). LOS (line-of-sight) is taken from the radar geometry of ERS track 1. Bottom: time series sampled at the same time every day to demonstrate the shift in tidal maximum relative to the time of day. Note the different time scales and tick intervals for the two plots. Tick marks are at zero hours UTC.

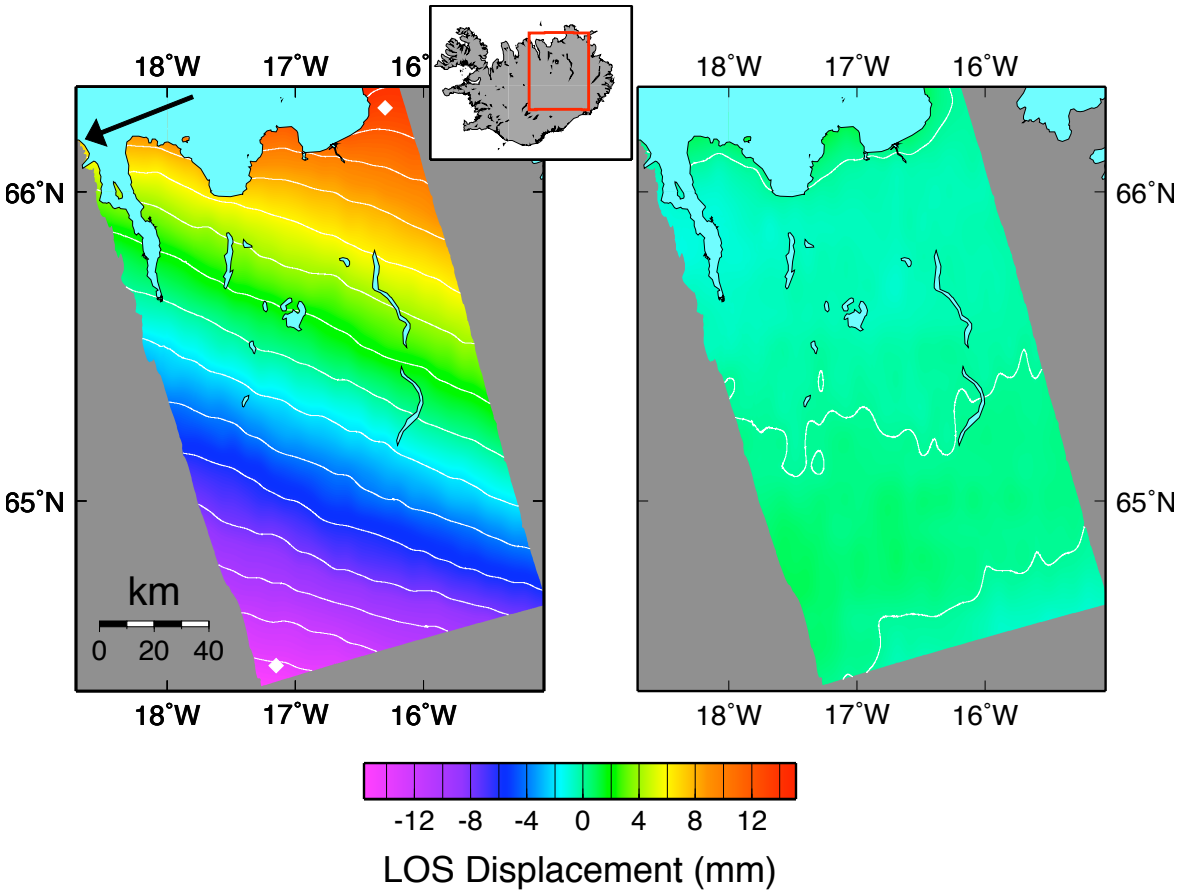

Figure 4.2: Left: synthetic interferogram of peak expected relative displacements due only to ocean tidal load displacements in northern Iceland. The displacement would be expected for a fictitious interferogram constructed from radar acquisitions at 2003-01-26 12:00:00 and 2002-03-29 12:00:00. The radar geometry is from track 1 of the ERS and Envisat satellites. The arrow indicates the surface projection of the approximate radar line-of-sight (LOS) direction from ground to satellite. LOS displacement is the projection of the displacement vector along the LOS direction. The two white diamonds indicate the points used to calculate relative displacements in Figure 4.1. Right: residual after removing best fitting bi-linear ramp from predicted OTL displacement. Contour intervals are 2 mm.

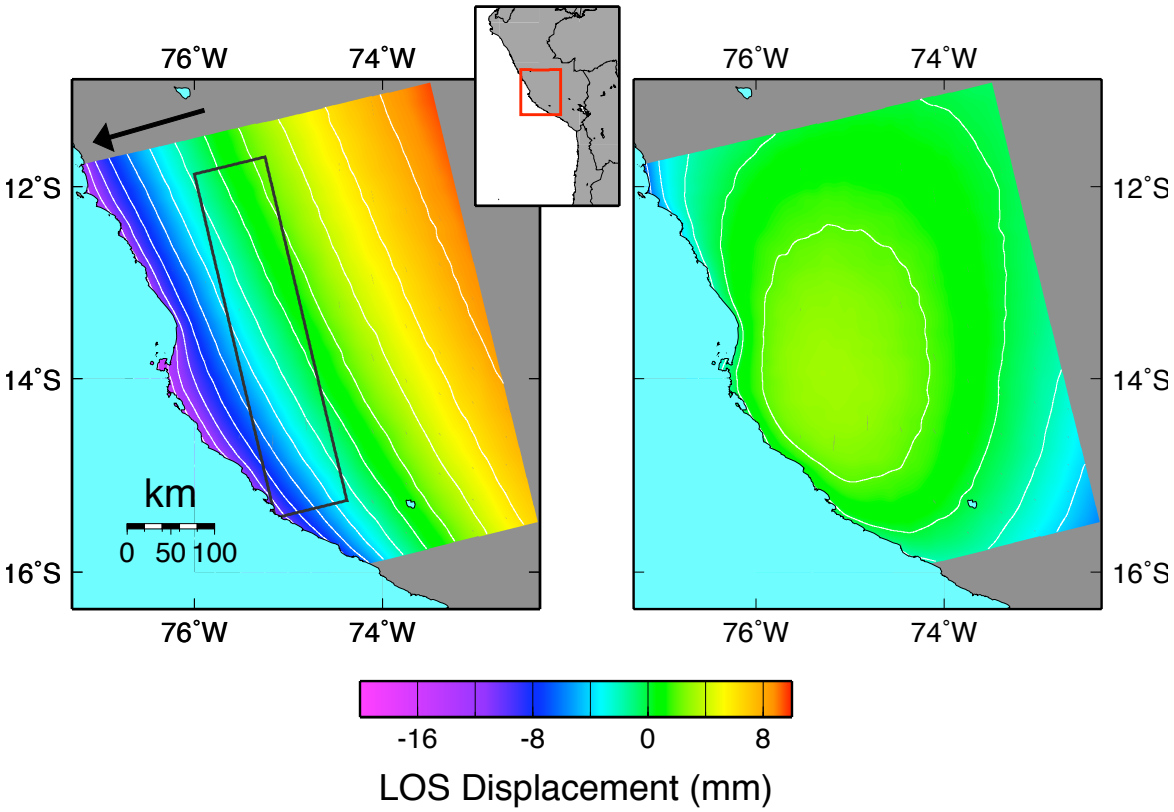

Figure 4.3: Same as Figure 4.2 for a wide swath scene of the Peruvian subduction zone. The gray box is the footprint of a normal strip-map swath. Acquisition times are 2004-07-03 12:00:00 and 2002-01-07 12:00:00. The radar geometry is from the wide swath track 447 of the Envisat satellite. Contour intervals are 2 mm.

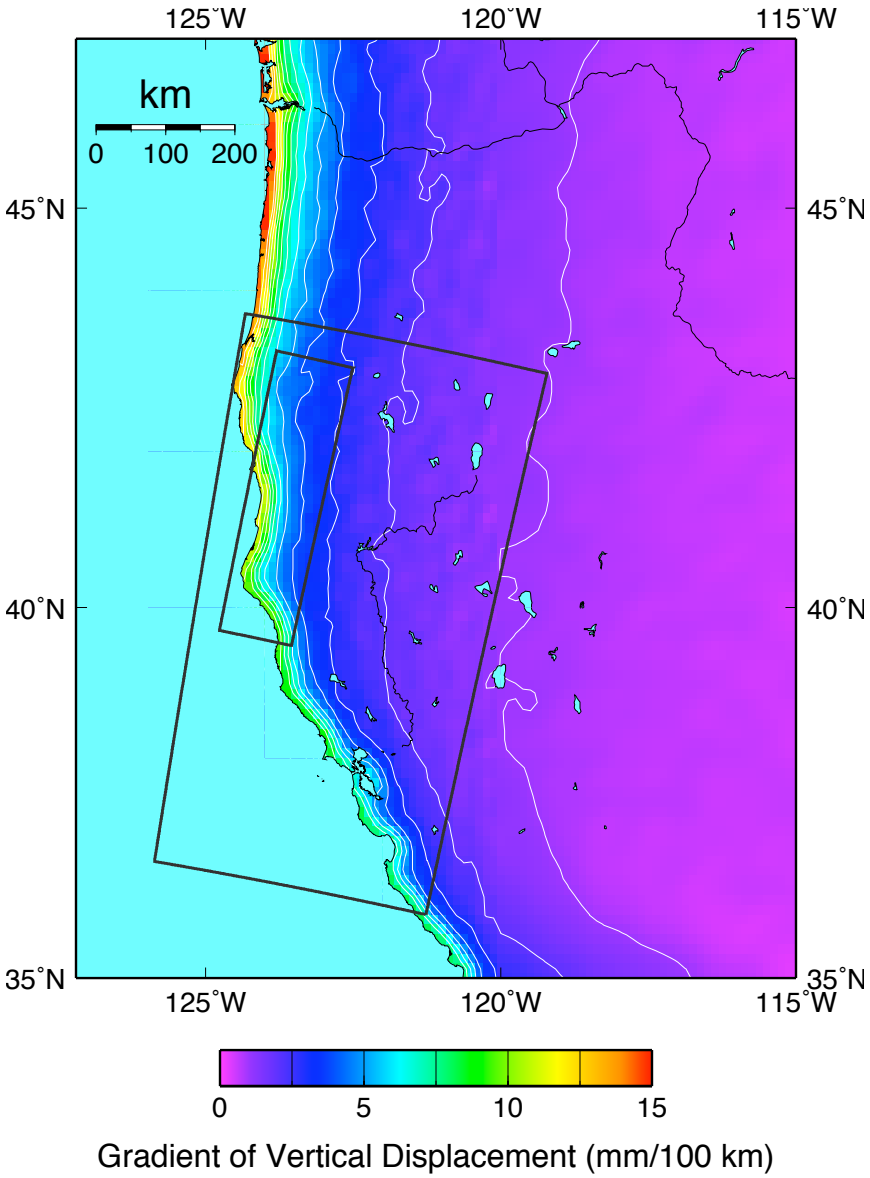

Figure 4.4: Magnitude of the horizontal gradient of the vertical OTL displacement of the M2 constituent for the western United States. Boxes show characteristic footprints of wide swath and strip-map images. Contour intervals are 1 mm/100 km.

Chapter 5

The Krafla Volcanic System

5.1 Iceland: Divergent Boundary Laboratory

The island of Iceland is located on the divergent plate boundary of the Mid-Atlantic Ridge. Its subaerial nature allows geoscientists a rare opportunity to study the dynamics of spreading plate boundaries; although, at the same time, it is a unique geological setting precisely for the same reason. The anomalously thick Icelandic crust is hypothesized to be due to the increased melt production stemming from the interaction of the Mid-Atlantic Ridge with a mantle upwelling (Morgan, 1971; Bjornsson, 1985; Ito et al., 2003; Allen et al., 2002a), although an alternative explanation in which excess Icelandic volcanism is caused by a subducted and trapped fragment of crust has also been proposed (e.g., Foulger & Anderson, 2005).

The divergent plate boundary in Iceland consists of several volcanic systems that intermittently experience large volcanic and diking events that accommodate the divergent tectonics and build the island (Gudmundsson, 1995, 2000). The most recent rifting event began in December of 1975 along the Krafla fissure swarm in the Northern Volcanic Zone (NVZ) of Iceland (Bjornsson et al., 1979) (Figure 5.1). The rifting and accompanying volcanism lasted approximately a decade. A strong post-rifting signal is detected in the NVZ

following the rifting episode; Heki et al. (1993) report campaign GPS measurements from 1987 and 1990 of 63 sites surrounding the Krafla fissure swarm showing horizontal velocities up to 3 times the average spreading rate as measured by Demets et al. (1994). Most of the GPS sites were remeasured in 1992 (Figure 5.2): the maximum spreading rate had slowed, but was still much larger than the average plate spreading rate (Hofton & Foulger, 1996).

The 1975 – 1984 Krafla rifting episode provides a deformational impulse to the Icelandic lithosphere, and thus the measured response to the rifting may help us to constrain the rheological structure of the lithosphere in this region. The post-rifting response can potentially help answer questions about the broad structure of the Icelandic crust – whether it is hot and thin as suggested by Beblo et al. (1983) and Björnsson (2008) or cold and thick as suggested by Menke & Levin (1994) and Staples et al. (1997) – and local rheological structure beneath the Krafla fissure system (Pedersen et al., 2009).

Previous studies (Foulger et al., 1992; Heki et al., 1993; Hofton & Foulger, 1996; Pollitz & Sacks, 1996) have modeled the GPS data as due to viscous or viscoelastic flow in Iceland's lower crust and upper mantle in response to the rifting episode. These previous studies have used a one-dimensional (i.e., vertically layered) rheological structure and linear Maxwell or standard-linear-solid viscoelasticity. Information about the structure of the Icelandic lithosphere (e.g., Brandsdottir et al., 1997; Allen et al., 2002b) and the availability of modern solid modeling software allow us to explore the role of lateral heterogeneity in Iceland's rheological structure. InSAR data compliment previously gathered GPS data and add temporal resolution to our knowledge of post-rifting displacements.

5.2 Geologic Setting

The sub-aerial mid-ocean rift that forms Iceland is a natural laboratory for geophysical study. Geophysical and geological evidence points to an origin resulting from a mantle upwelling impinging on the mid-Atlantic spreading center between the North American and Eurasian plates (e.g., Saemundsson, 1974, 1979; Bjornsson, 1985; Einarsson, 1991). Plate tectonic spreading is concentrated along three volcanic zones connecting the Kolbeinsey ridge to the north of Iceland with the Reykjanes ridge to the south. The volcanic spreading centers in Iceland are the Northern Volcanic Zone (NVZ), the Western Volcanic Zone (WVZ), and the Eastern Volcanic Zone (EVZ). They are offset to the east from the southward and northward continuing off-shore ridges; the South Iceland Seismic Zone (SISZ) connects the WVZ and the EVZ to the Reykjanes ridge, and the Tjörnes Fracture Zone (TFZ) connects the NVZ to the Kolbeinsey Ridge (Figure 5.1). The NVZ has undergone eastward jumps, and the locus of spreading in southern Iceland is migrating from the WVZ to the EVZ today, possibly due to the Atlantic plate boundary drifting west of the mantle hot spot (Saemundsson, 1979; Einarsson, 1991).

The NVZ consists of five en echelon volcanic systems and their associated fissure swarms (Figure 5.3) (Einarsson, 1991). Each fissure swarm is up to 20 km wide and 100 km long (Saemundsson, 1979). The Krafla, Askja, and Kverkfjoll systems have well-developed central calderas with associated magma chambers (Einarsson, 1991). They form the North-South striking plate boundary, though the individual fissures and their swarms are aligned approximately perpendicular to the Demets et al. (1994) plate spreading direction of N106°E (Tryggvason, 1984).

Several rifting episodes in the NVZ have been recorded in historic time (Sigmundsson,

2006). These events are a response to the extensional tectonic stress at the divergent plate boundary and are possibly triggered by magma flowing into and pressurizing the magma chamber of a fissure swarm's central volcano (Einarsson, 1991). In 1618, the northern portion of the Theistareykir fissure swarm opened. In 1724 – 1725, the Krafla fissure swarm underwent a rifting episode similar to the one in 1975 – 1985; this episode rifted further south than the most recent one but not as far north (Tryggvason, 1984). In 1874 – 1875, the Askja fissure swarm rifted up to 80 km north of the central volcano; the southern extent of the rifting is not known.

There are few opportunities to study divergent plate boundaries in such detail as most of them are located under water. The Afar depression in eastern Africa offers another such opportunity. Unlike Iceland, which is a mature spreading zone, the Afar is a nascent spreading ridge (Hirn et al., 1993). The Asal rift, part of the Afar depression, is also thought to be a spreading region influenced by a mantle upwelling (Hirn et al., 1993).

Two rift segments in the Afar have experienced rifting in recent time. The Asal-Ghoubbet rift underwent an episode in 1978. Cattin et al. (2005) document a sudden change in the post-rifting surface velocities and infer the deformation to be primarily due to dike injection at depth rather then viscoelastic relaxation; though Vigny et al. (2007) suggest that the change in velocities is merely due to the decay in velocities from viscous relaxation. Using an Elsasser model (a thin elastic plate over a viscous channel), Vigny et al. (2007) estimate a diffusivity nearly two orders of magnitude smaller than the diffusivity estimate for Krafla (Foulger et al., 1992). The diffusivity controls the rate of viscous relaxation in the system and is proportional to the elastic plate thickness divided by the viscosity. This implies that the elastic upper crust may be thinner or the lower crust/mantle is more viscous than at Krafla.

The other active segment in the Afar is the Dabbahu. In September 2005 a 60 km long dike intrusion occurred. InSAR measurements give approximately 6 m of extension (Ayele et al., 2007; Barisin et al., 2009). Wright et al. (2006) report up to 8 m of diking with a maximum depth of 9 to 12 km. The volume of magma is comparable to the Krafla Fires, but the diking occurred over approximately one week rather than ten years. Keir et al. (2009) report more diking in June and July of 2006 that was not accompanied by subsidence of a local magma chamber. A broad uplift pattern detected in InSAR measurements hint at deep magma accumulation. Observations of post-rifting deformation have been reported (Bennati et al., 2008); however, no results of the measured post-rifting deformation and possible causes have been published in peer reviewed journals.

5.3 The 1975 – 1984 Krafla Fires

The rifting and volcanism of the latest Krafla episode is described in detail by Tryggvason (1984). The widening occurred over a 90 km long segment of the Krafla fissure swarm, most of which was confined to a 1 – 2 km wide zone and was perpendicular to the strike of the fissure swarm. Rifting took place episodically in approximately 20 discrete rifting events, each of which was accompanied by subsidence of the center of the Krafla volcano caldera. Total widening is estimated based on geodetic measurements in northern Iceland, compensated for the estimated contraction in the flanks of the fissure zone due to the release of tensile strain (Figure 5.4). The maximum opening is approximately 9 m and the average is 5 – 6 m, thought to be a conservative estimate of the amount of opening. Tryggvason (1984) observed that the southern termination of the 1975 – 1985 Krafla rifting coincides with the overlap of the Krafla fissure swarm with the region of the Askja fissure swarm that opened in 1874 – 1875. In the north, the amount of opening decreases as the Krafla

fissure swarm approaches the Tjörnes Fracture Zone (TFZ), which has experienced several strike-slip earthquakes.

5.4 Post-Rifting Deformation in the NVZ

Several authors have suggested viscous or viscoelastic relaxation as the source of surface velocities following the 1975 – 1984 Krafla rifting episode. Foulger et al. (1992) and Heki et al. (1993) modeled the 1987 and 1990 post-rifting GPS data using an elastic layer over a Newtonian viscous channel for an infinitely long dike (Foulger et al., 1992) and a finite length dike (Heki et al., 1993). The studies of Pollitz & Sacks (1996) and Hofton & Foulger (1996) considered a vertically stratified, laterally homogeneous viscoelastic lithosphere.

The preferred rheological model of Pollitz & Sacks (1996) roughly agrees with the cold, thick crust model of Iceland with a crustal viscosity of 3.3×10^{19} Pa s and a mantle viscosity of 3.3×10^{18} Pa s. The authors found that there is some trade off between the chosen rheological model and the amount of opening; increasing the crustal viscosity increases the required amount of opening on the central portion of the Krafla rift. Conversely, Hofton & Foulger (1996) find that their best fitting model has a crustal viscosity of 1.1×10^{18} Pa s, agreeing with the thin, hot crustal model.

Pollitz & Sacks (1996) and Hofton & Foulger (1996) do not include any lateral heterogeneity, but Pedersen et al. (2009) have looked at the effect of such heterogeneity for a model of stretching Icelandic lithosphere. No rifting or magmatic sources were included, the only load being a constant velocity tectonic boundary condition. They found that an elastic upper crust that thins towards the rift axis has a significant effect on the vertical motion for their viscoelastic models. Lithospheric stretching models with a diffuse zone of weak crust and low viscosity below the rift axis were found to agree with the deformation at

Askja as measured by InSAR (Pedersen et al., 2009). Jouanne et al. (2006) model campaign GPS data over the northern Krafla fissure swarm, covering 1997 – 2002 using a laterally heterogeneous model got 6×10^{19} Pa s for the lower crust and 6×10^{20} Pa s for the mantle; though their GPS coverage did not capture most of the deformation observed in the InSAR data due to the density of sites.

Several localized studies of the deformation of the Krafla volcano have focused on possible magmatic sources of deformation. Radar interferograms of the Krafla region covering 1992 to 1999 reveal three major features: a narrow zone of negative displacement along the rift axis, a small (approximately 5 km) circular deformation near the center of the Krafla caldera, and a broad (several tens of km) double-lobed pattern centered 15 km north of Krafla (de Zeeuw-van Dalfsen et al., 2004). The linear deformation feature has been alternately attributed to continued spreading and post-rifting relaxation (de Zeeuw-van Dalfsen et al., 2004) and cooling magma (Sigmundsson et al., 1997; Henriot et al., 2001); although, Pedersen et al. (2009) showed that this type of axial depression may be a result of tectonic stretching of an axially located weak zone. The small circular pattern is thought to be the cooling (Sigmundsson et al., 1997) or draining (de Zeeuw-van Dalfsen et al., 2004, 2005) of the shallow magma chamber known to exist beneath the Krafla volcano (Brandsdottir et al., 1997). The broad inflation signal seen by de Zeeuw-van Dalfsen et al. (2004) is modeled as a deep accumulating magma chamber at the Moho. de Zeeuw-van Dalfsen et al. (2004) claim that the expected post-rifting deformation from Pollitz & Sacks (1996) is only 15% of the total broad deformation seen in interferograms covering 1993 to 1999 and that a deep magma source accounts for the rest of the deformation.

The modeling results of de Zeeuw-van Dalfsen et al. (2004) raise the possibility that the continued deformation at the Krafla fissure swarm may be the result of continued

magmatic activity rather than viscoelastic relaxation. They successfully matched the broad deformation pattern seen in four interferograms covering 1993 – 1999 with an inflating Mogi source at 21 km depth. Hofton & Foulger (1996) noted the possibility that the 1987 – 1992 GPS velocities could be explained with continuous, aseismic diking at depth. In fact, any displacement field can be successfully modeled with an arbitrary distribution of elastic deformation sources. We must rely on other information such as the time dependence of the deformation field (chapter 6), seismicity, and likely rheologies from rock mechanics experiments to identify likely deformation mechanisms.

5.5 Other Measurements of Iceland Rheology

Glacial rebound observations and modeling indicate an average viscosity for the Icelandic mantle of $10^{18} - 10^{19}$ Pa s (Sigmundsson, 1991; Sigmundsson & Einarsson, 1992). LaFemina et al. (2005) used viscoelastic coupling models compared to GPS measurements in the Western and Eastern Volcanic Zones to estimate mean viscosities of $10^{19} - 10^{20}$ Pa s in that region of Iceland. Post-seismic study in the SISZ detected a month-long transient in InSAR data and a year timescale transient in GPS data. The year timescale transient was modeled as viscoelastic deformation resulting in estimates of lower crust and mantle viscosities of $0.5 - 1 \times 10^{19}$ Pa s and 3×10^{18} Pa s, respectively (Árnadóttir et al., 2005).

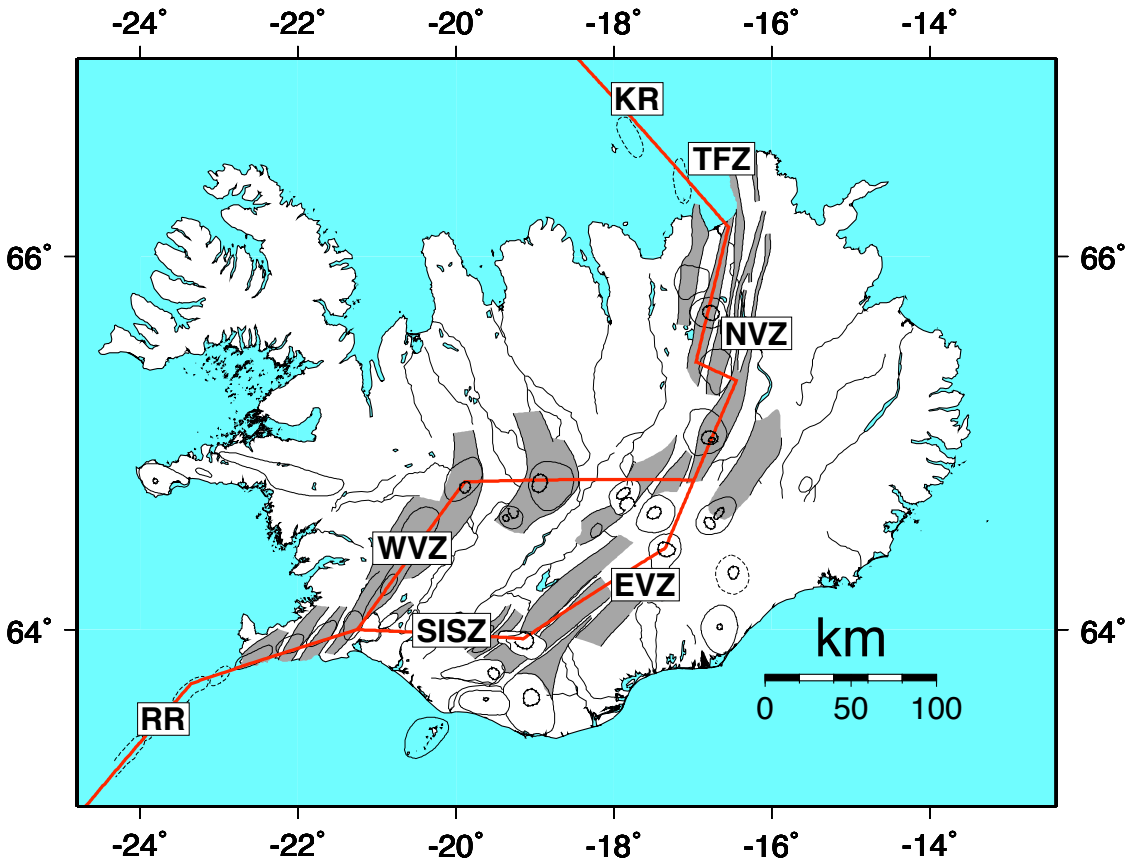

Figure 5.1: Plate boundary in Iceland. Nominal boundary is in red, volcanoes and central calderas are drawn in black, and the fissure swarms are in grey. The zones are: KR, Kolbeinsey Ridge; TFZ, Tjörnes Fracture Zone; NVZ, Northern Volcanic Zone; EVZ, East Volcanic Zone; WVZ; West Volcanic Zone; SISZ, South Iceland Seismic Zone; RR, Reykjanes Ridge. Adapted from Gudmundsson (2000).

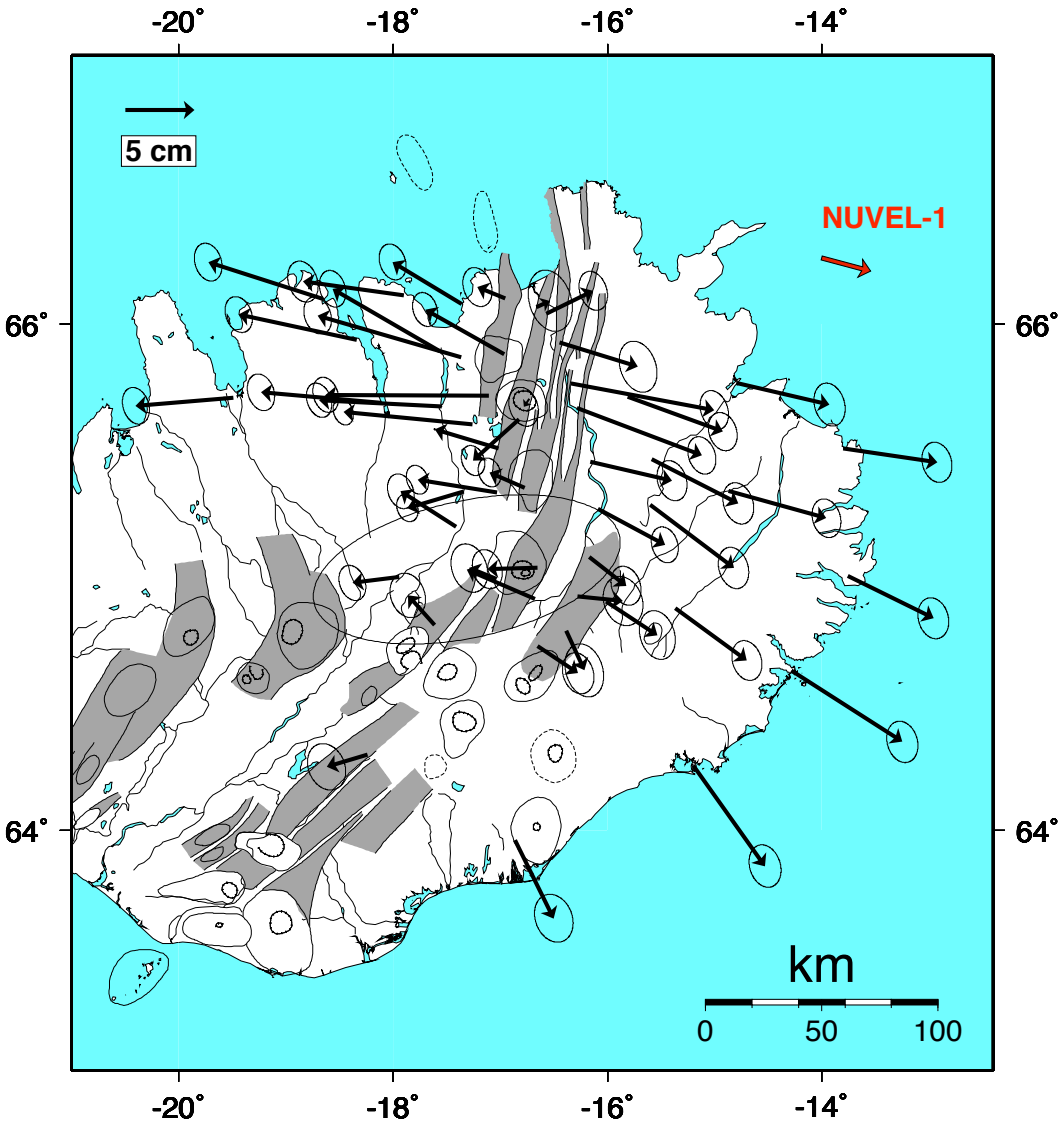

Figure 5.2: Displacement in the Northern Volcanic Zone from 1987 to 1992 as measured by campaign GPS relative to the rift axis (Hofton & Foulger, 1996). Ellipses are one standard deviation errors. The red arrow indicates the secular velocity of the Eurasian plate acording to the NUVEL-1 model (Demets et al., 1994).

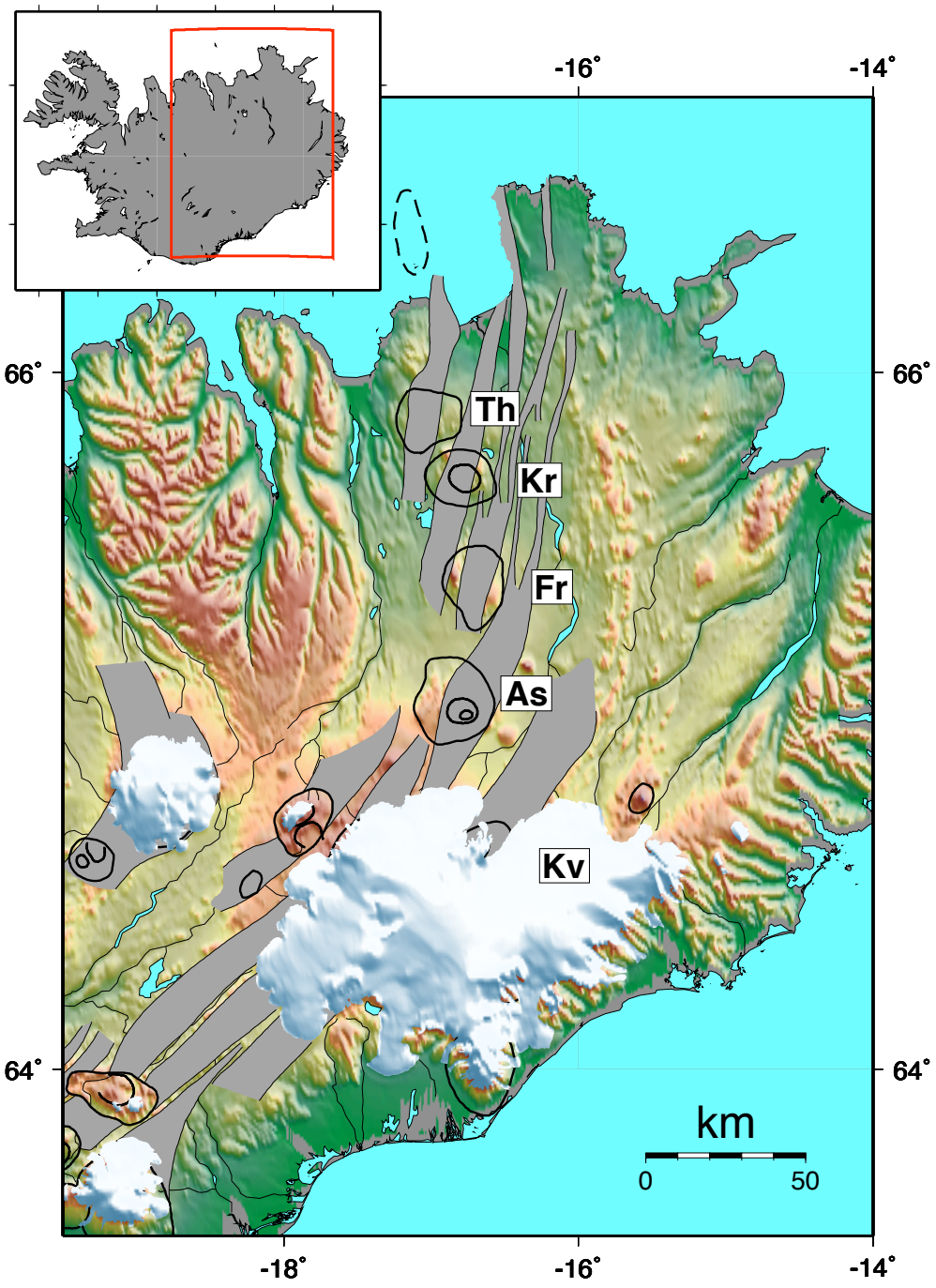

Figure 5.3: Map of Northern Volcanic Zone of Iceland. Inset shows mapped region. Central volcanoes and associated fissure swarms are shown. Volcanoes are labeled Th: Theistareykir, K: Krafla, Fr: Fremri-Námar, A: Askja, Kv: Kverkfjoll. Adapted from Sigmundsson (2006)

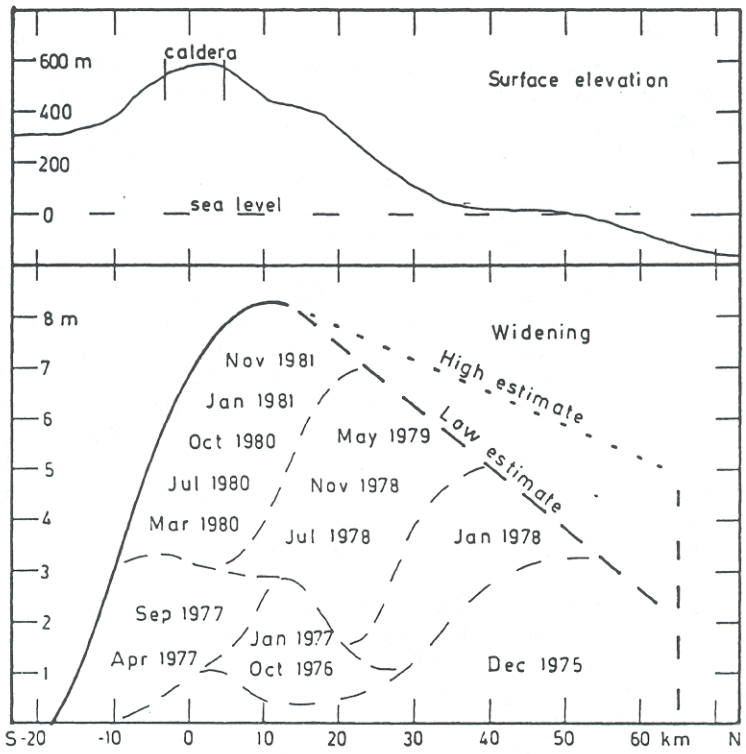

Figure 5.4: Estimates of the widening of the Krafla fissure swarm during the 1975 – 1985 rifting episode from Tryggvason (1984). The abscissa is the distance along the rift axis. Top: surface topography. Bottom: amount of widening as measured by several geodetic techniques

Chapter 6

InSAR Observations of Post-Rifting Deformation in the Northern Volcanic Zone, Iceland

6.1 Introduction

As described in Chapter 3, interferometric synthetic aperture radar (InSAR) provides high spatial resolution (on the order of 10^1 m) geodetic data over large areas (on the order of 10^2 km^2) with precision of one centimeter or less. Here, we use InSAR as our primary geodetic data source in measuring the post-rifting response at the Krafla volcanic system.

A limitation of satellite-based InSAR from the previous decade is the relative dearth of data from ascending orbits. Because InSAR only measures ground displacement in the radar line-of-sight (LOS), availability of images from both ascending and descending orbits is invaluable in constraining the displacement field. As we will show later in Section 6.3, *a priori* assumptions about the expected direction of displacement combined with both ascending and descending interferograms can give us a multi-dimensional picture of the displacement field. In addition, we have limited ourselves to SAR data from the months of May through October due to snow cover causing decorrelation of the radar phase, Decorrelation also occurs over lakes and riverbeds.

The coverage of the SAR data used in this study is shown in Figure 6.1. Ascending tracks 273, 1, and 203 and descending tracks 281, 9, and 238 cover the NVZ. Interferograms were formed using the ROI_PAC InSAR software (Rosen et al., 2004). All interferograms are composed of two frames (either 2277 and 2295 or 1305 and 1323). We have a total of 165 radar images forming 304 interferograms with low amounts of decorrelation. One hundred thirty-five of those have low amounts of atmospheric noise (determined by inspection). See table 6.1 for details on the number of interferograms in each orbital track. Data from the ERS1/2 and Envisat SAR satellites covers the NVZ from 1992 to 2007 (Figure 6.2). There is a lack of coverage between 2000 and 2002 due to difficulty in forming interferograms with ERS2 data after February 2000 because of problems with the radar Doppler frequency. For all SAR data available, we have attempted to form every interferometric pair with a perpendicular baseline less than 300 m – for ERS1/2 and Envisat, pairs with larger baselines tend to suffer from baseline decorrelation (Zebker & Villasenor, 1992).

6.2 Characteristic Interferograms: Qualitative Analysis

We first describe a characteristic interferogram from the descending orbital track 9 measuring the displacement between 1996/06/04 and 1993/07/31 (Figure 6.3). The major deformation features that we observe are (1) the approximately 50 km wide, double-lobed, positive displacement located north of the Krafla caldera; (2) the localized negative displacement at the Krafla caldera presumably due to contraction and/or draining of the shallow magma chamber (Sigmundsson et al., 1997; Henriot et al., 2001; de Zeeuw-van Dalfsen et al., 2004); (3) localized negative displacement at Askja volcano attributed to the draining of the magma chamber by Sturkell et al. (2006); (4) narrow zones of negative displacement along the Askja and Krafla fissure swarm axes, possibly the product of stretching and thinning

due to plate spreading (de Zeeuw-van Dalfsen et al., 2004; Pedersen et al., 2009).

Figure 6.4 shows an interferogram from ascending track 1. The peak deformation of the broad displacement north of the Krafla caldera is on the west side of the fissure swarm compared to the peak on the east side for descending images (Figure 6.3). Descending and ascending LOS vectors have approximately the same projection into the vertical component, but the horizontal projection of the ascending LOS is, to first order, opposite to that of the descending orbit (see arrows indicating the horizontal projection of the LOS vector in Figures 6.3 and 6.4). The change in the peak displacement from the east side of the rift for the descending image to the west side for the ascending image indicates that the displacement is primarily up and away from the rift which is what we would expect from a viscoelastic response to the 1975 – 1984 diking or continued diking at depth. We explore the displacement direction more quantitatively in Section 6.3.

Interferograms are often affected by artifacts from propagation delays as the ionosphere and troposphere can have space and time varying refractive indexes. Tropospheric path delays can often mimic topography and displacement; these errors can be reduced by combining several interferograms in a "stack", taking advantage of the fact that the errors are uncorrelated over time periods longer than a day (e.g., Emardson et al., 2003; Pritchard et al., 2006). Small scale ionospheric disturbances can introduce large amounts of noise that overwhelm the deformation signal in the interferogram (Figure 6.5).

6.3 Rift Perpendicular Profile

6.3.1 Introduction

In order to focus on the dynamics of the post-rifting motion, we take profiles of the interferograms perpendicular to the Krafla fissure swarm, near the peak of the broad displacement feature. Because the recent rifting episode caused opening over about 80 km of the Krafla system we assume that, to first order, most of the variation in the deformation field will be along this rift perpendicular profile, i.e., for the purposes of this section, we treat the rift system as two-dimensional.

The location of the profile, shown in Figure 6.3, was chosen to cover the peak deformation observed in the interferograms and to avoid localized deformation at the Krafla caldera assumed to be associated with the shallow magma chamber (Sigmundsson et al., 1997; Brandsdottir et al., 1997; Henriot et al., 2001). In order to reduce the effects of noise in individual pixels, all pixels within 3 km of the profile line were projected onto the profile.

We assume that along the rift-perpendicular profile that all velocities are confined to the two-dimensional subspace defined by the vertical and rift perpendicular directions with rift parallel velocities set to zero. Wright et al. (2004) showed that when using InSAR data to invert for the full three-dimensional displacement field, the north component has the largest error when the radar satellites have a near polar orbit (as is the case for ERS1/2 and Envisat). Fortunately, the rift perpendicular direction is primarily aligned in an east-west direction (the azimuth of the profile is 105 degrees clockwise from north).

6.3.2 Methods

Our approach is to divide the InSAR data up into separate time intervals and solve for an average velocity for each time period using a least squares inversion. For a single pixel the constant rate equation is

$$\rho^a = T^a \, \vec{v_i} \cdot \hat{l}_i^a + \gamma^a \tag{6.1a}$$

$$\vec{v_i} = \begin{bmatrix} v_{\perp i} \\ \\ v_{zi} \end{bmatrix} \tag{6.1b}$$

$$\hat{l_i} = \begin{bmatrix} l_{\perp i} \\ \\ l_{zi} \end{bmatrix}, \tag{6.1c}$$

where T^a is the time span and γ^a is the constant phase ambiguity (or offset) of the a^{th} interferogram. ρ_i^a is the range change for the i^{th} pixel in the a^{th} interferogram; $\hat{l}_i^a$ is a unit vector in the radar line-of-sight; and $v_{\perp i}$ and v_{zi} are the rift-perpendicular and vertical velocities for the i^{th} pixel, respectively, that are to be solved. We set the rift perpendicular velocity to zero. Note that $\hat{l_i}$ is not constant for a single interferogram but rather a function of radar range.

It is possible to solve for a two-dimensional velocity field because we take advantage of the fact that the ascending and descending observations have LOS vectors that span a two-dimensional space (see Figures 6.4 and 6.3). The inverse problem requires that for each pixel we have at least one ascending and one descending observation; additional observations for some of the pixels are required to constrain the offsets, γ^a.

Interferometric measurements only have the ability to resolve relative displacements within an image and not the absolute displacement. Therefore, every interferogram has

an unknown integer number of 2π added to all the pixels; we eliminate this ambiguity by solving for γ^a in our inversion.

We write the complete linear system for all pixels and all interferograms as

$$d = Gm \tag{6.2a}$$

$$m = \begin{bmatrix} V \\ \\ \Gamma \end{bmatrix}, \tag{6.2b}$$

where d, is a vector of interferometric displacements; m is the model vector of pixel velocities and offsets; and G is the design matrix describing the linear relationship between d and m. This linear system approach to solving for velocities allows us to use interferograms with missing data due to regions of decorrelation and still acquire a solution for all pixels. Note that the use of the L2 norm may not be appropriate as the phase noise may not have a Gaussian distribution (Simons & Rosen, 2007). In this case, we may prefer to use an L1 norm.

We can solve the linear system (Equation 6.2) via least squares

$$m = (G^t C_d^{-1} G)^{-1} G^t C_d^{-1} d. \tag{6.3}$$

C_d is the data covariance matrix. InSAR measurements have a covariance between nearby pixels that is important to take into account. Lohman & Simons (2005) found that ignoring the off-diagonal terms of the data covariance matrix resulted in under estimating the errors in the location of a small earthquake by a factor of two. We use the sample variogram method described by Lohman & Simons (2005) to find a power law description of the

covariance structure for each interferogram:

$$\sigma_{ij}^2 = \sigma_o^2 \, 10^{-d_{ij}/r}, \tag{6.4}$$

where σ_o^2 is the variance of the interferogram, d is the distance between the i^{th} and j^{th} pixel, and the decay distance, r, is determined empirically from the sample variogram. This empirical calculation is an overestimation of the covariance as there is a portion of the interferogram that contains signal we are interested in. We ignore the inter-image covariance that is due to interferograms sharing common scenes (Emardson et al., 2003) as the resulting covariance matrix is non-invertible. A means to calculate the weighting matrix in this case is currently under investigation.

We diagonalize the covariance matrix by transforming the inverse problem by a premultiplier, T, (Menke, 1989). The pre multiplier is constructed from the eigenvalue decomposition of the inverse covariance matrix

$$C_d^{-1} = U \Lambda U^T \tag{6.5a}$$

$$T = \Lambda^{1/2} U^T. \tag{6.5b}$$

Λ and U are matrices of eigenvalues and eigenvectors of the inverse covariance matrix. The new data and design matrices are then

$$d^{'} = Td \tag{6.6a}$$

$$G^{'} = TG \tag{6.6b}$$

and Equation 6.3 can be applied with $C_d = I$.

6.3.3 Results

The interferograms are broken into two time periods: 1992 – 1996 and 1996 – 2007. We apply Equation 6.3 to find the least squares average velocities over each time period. For 1992-1996, there are three ascending and thirteen descending interferograms. For 1996-2007, there are two ascending and thirty descending interferograms. The choice of timer intervals is largely dictated by the available data. We attempted to use three time periods: 1992-1996, 1996-1999, and 1999-2007, however the lack of more than one ascending interferogram for the latter two periods resulted in large model errors (standard deviations were approximately twice the values for the inversion presented here).

A singular value decomposition of the linear system shows that the values of the offsets, γ^a, are in the null space of the solution (Figures 6.6 and 6.7). The small singular values correspond to solution modes with approximately linear ramps in the velocities and large oscillations in the offsets. We regularize the solution by minimizing the solution length for the γ^a portion. We remove any linear ramp from the velocity solutions as these components are not well constrained and highly sensitive to noise. As a result, we must also remove linear ramps from any model of the velocities before comparing to the inverted velocity field presented here. Removing ramps from interferograms is commonly done whether or not the inversion requires it, as linear ramps are features of an interferogram that are often not trusted (Simons & Rosen, 2007).

The solution with one standard deviation errors is shown in Figure 6.8. There appears to be a decay in velocities accompanied by a broadening of the deformation field, though velocities are largely constant over the observation period. The rift perpendicular velocities do not change significantly over time and most likely reflect the stretching of the lithosphere by plate tectonic spreading. The necessary detrending of the velocities results in eliminating

information about the absolute values of the horizontal velocities. We would expect a large portion of the horizontal velocities to be taken up by a linear ramp in the 80 km rift-perpendicular profile. The anomalously positive velocities near $x = -10$ km is due to transient activity at Theistareykir volcano (Section 6.5). In the time evolution of the vertical velocities, we see that the narrow peak at approximately 7 km from the rift has largely decayed while the broader slope remains. The narrow 4 km depression at the rift axis is persistent through both time periods.

An inversion using three time periods show more decay in the velocities and widening of the deformation signal, but errors are too large to make such statements with confidence.

6.4 GPS

We compare the 1987-1992 campaign GPS data (Hofton & Foulger, 1996) to the results from the previous section in Figure 6.10. The GPS stations used for comparison to the InSAR data are shown in Figure 6.11. For the purpose of comparison, the GPS data is detrended just as the InSAR data is. The horizontal velocities are similar to the InSAR results, although due to the removal of a linear ramp, they no longer reflect the absolute velocity across the rift. The vertical GPS velocities differ from the InSAR measurement, but their errors are quite large.

6.5 Time Series Analysis of Full Interferograms: MInTS

A total of 23 interferograms were used for a time series inversion using the MInTS method (Section 3.3). These interferograms are all from ERS1/2 Envisat track 9 frame 2277-2295. All interferograms are processed into a common stacking coordinate system (Section 3.2)

using ERS2 orbit 5875 as the master image.

The spatial filter bank is formed using two-dimensional Farras wavelets. We use wavelet scales 4 – 8 where each wavelet scale, s, has a total width of 2^s. Each interferogram is looked down (subsampled) by a factor of 16 resulting in approximately 320 m pixels. The Farras wavelet has a double-lobed shape; therefore, the smallest features in the filtered interferogram is on the order of 2.5 km.

The displacement time series is constructed as the sum of a linear rate and uniformly spaced B-splines. The splines are third order and have a knot spacing of 1.75 years; see Figure 6.12 for a time-line representation of data and the spline basis functions used. Regularization of the B-spline function is achieved by minimizing solution length of the spline coefficients. We minimize the least squares problem:

$$||Gm - d||^2 + \lambda\,||\mathrm{I}\; m_{spline}||^2, \tag{6.7}$$

where m is the full model coefficient vector that includes both the linear rate and the spline coefficients, and m_{spline} is the subset of m representing the splines only. The optimal value of the damping parameter, λ, is subjectively chosen via a L-curve method as a compromise between misfit and solution roughness (as measured by the second time derivative of the displacement time function) (Figure 6.13). A damping parameter value of $\lambda = 10^{0.22}$ was used for the results presented here.

The resultant MInTS velocity time series is presented in Figure 6.14. Residuals can be found in Figure 6.15. A map of Iceland surface topography is helpful for interpreting these results and is shown in Figure 6.16. The negative velocities due to cooling and draining of the shallow Krafla magma chamber are obvious and appear to decay through time. There

is a period of time in 1993 – 1997 when the Theistareykir volcano appears to have positive LOS velocities; this transient deformation is localized to the topographic expression of the volcanic edifice. There is no previously documented activity at the Theistareykir volcano for this time period. A burst of positive velocities between Krafla and Askja seen near June 2001 correlates quite well with a topographic low on the east side of the Askja fissure swarm. This deformation may be part of an unknown process that accommodates the strain accumulation in the step-over between the Askja and Krafla fissure swarms.

In Figure 6.17 we show the decomposition of the MInTS time series into linear (constant velocity) and spline portions. It is evident that the deformation from the MInTS inversion is largely dominated by a linear rate. The decay in velocities observed in the profile-based analysis (Section 6.3) is difficult to discern in the MInTS time series, but plausibly present. The MInTS time series also shows a possible burst of higher velocities for the broad, double-lobed deformation feature around 2003. Decay in the amplitude of velocities is difficult to discern as most of the variance in the data is accounted for by the constant velocity portion of the data (Figure 6.17).

The cumulative displacement solution is shown in Figure 6.18 and the decomposition into linear and spline components of the time series are shown in Figures 6.19 and 6.20, respectively. Note that the color scale in 6.20 is scaled by a factor of 0.1; the majority of the deformation is taken up by the linear term. Figure 6.21 is the displacement time series along with linear and spline components at four locations in the NVZ. The transient deformation at Theistareykir is captured by the spline basis. There is an apparent slow decay in the negative velocities at Krafla volcano while Askja and the broad deformation field have nearly constant velocities.

6.6 Discussion and Conclusions

The vertical velocities in the inversions of the profiles leads us to believe that viscoelastic relaxation could contribute to the anomalously high velocities near the Krafla fissure swarm. In addition, the deformation is largest where the amount of opening was largest indicating that what we see is a direct result of the diking of 1975 – 1984 (Figure 6.22). This correlation between known shallow diking and post-diking deformation appears to favor a mechanism that is a direct response to the diking as opposed to accumulation of magma near the Moho as proposed by de Zeeuw-van Dalfsen et al. (2004). The horizontal velocities are presumably dominated by plate spreading as they do not significantly change over the time period of the observations (see also Árnadóttir et al. (2009)).

Jouanne et al. (2006) have measured horizontal displacements in the NVZ using campaign GPS in 1997, 1999, and 2002. They observed anomalous velocities on the west side of the Krafla fissure swarm that decrease over the observation period. The measured deformation is restricted to a narrow band within the fissure swarm, but their GPS campaign did not have many observations in the 50 km zone surrounding the narrow fissure swarm where InSAR measurements show the greatest variability in velocities.

Using campaign GPS, Árnadóttir et al. (2009) see some evidence for continuing post-rifting deformation between 1993 and 2004 including a slightly elevated spreading rate near Krafla (approximately 3 ± 2 mm yr^{-1} larger horizontal rates then rates measured at other locations along the Iceland plate boundary and rates predicted by plate tectonic models (Demets et al., 1994)). Additionally, after removing their favored glacial rebound model, they find up to 8 mm yr^{-1} of residual uplift in the NVZ, though the density of the campaign GPS network is not dense enough to infer specific sources of such deformation.

MInTS has been shown to be a powerful tool for revealing deformation not previously detected at Theistareykir and the step-over between Askja and Krafla. However, our current results do not constrain the decay rate of the deformation. More interferograms may be needed to detect any decay using the MInTS method.

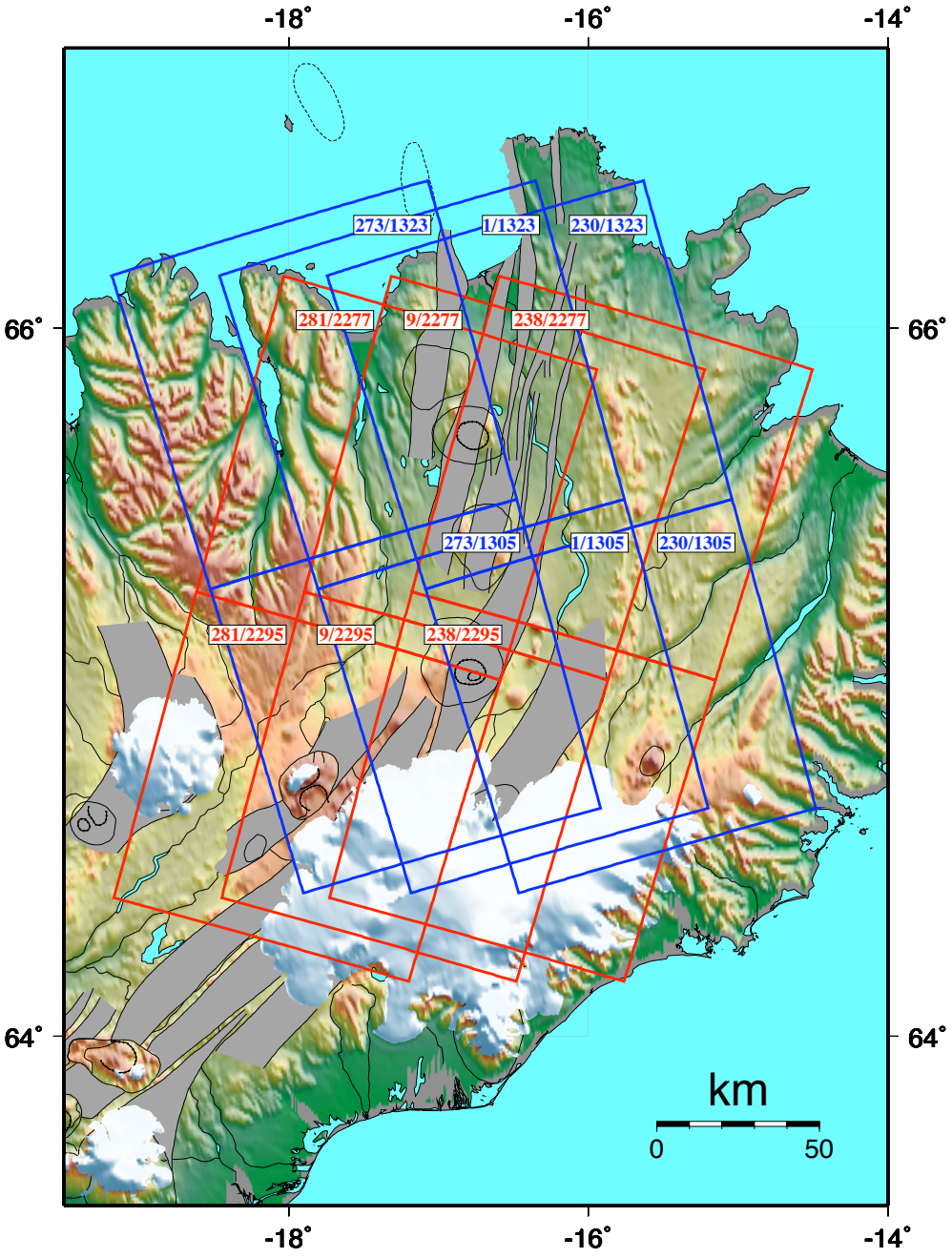

Figure 6.1: Radar footprints for ERS1/2 and Envisat covering the NVZ. Ascending orbits are in blue and descending orbits are in red. Satellite track and frame numbers are in the white boxes.

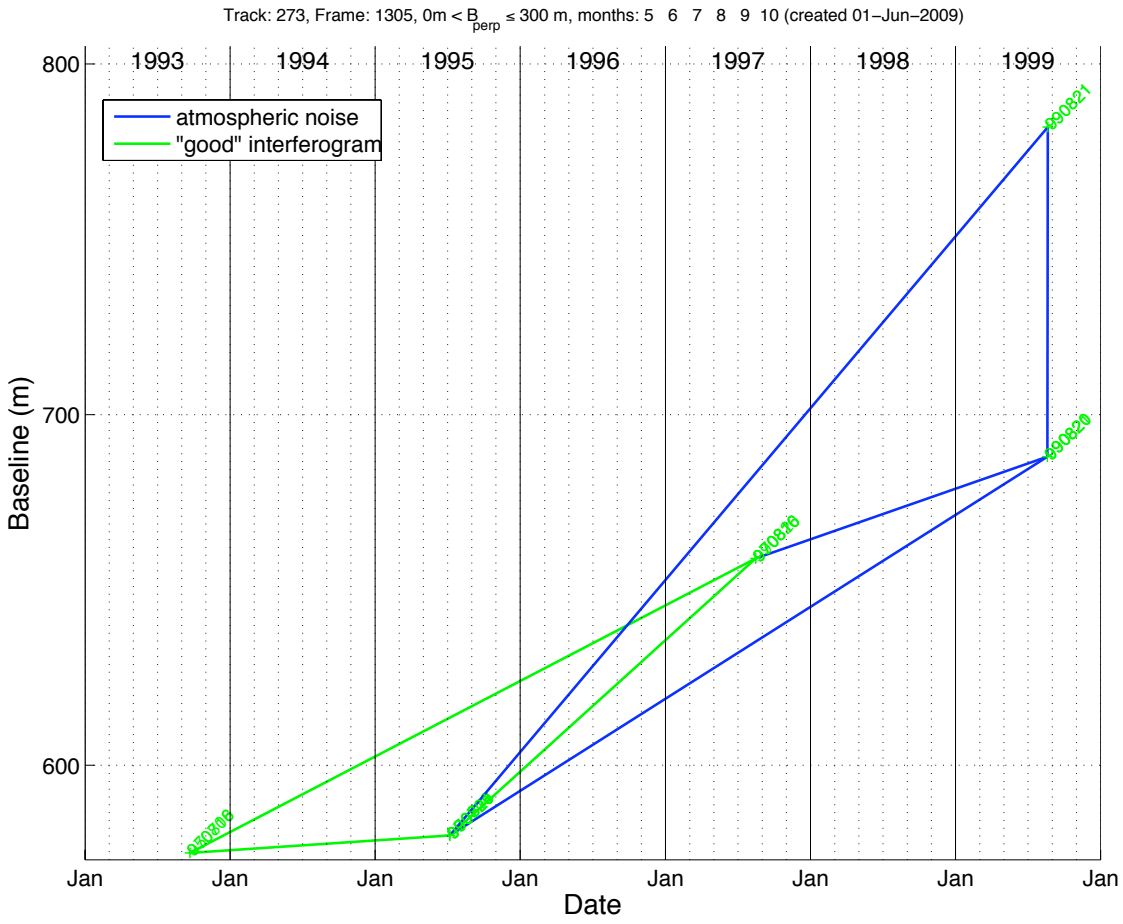

Figure 6.2: Interferometric baselines for SAR data from track 273 for ERS1/2. Green lines are completed interferograms with high quality deformation signal and low amounts of decorrelation. Blue lines are interferograms with significant amounts of atmospheric noise. Pairs that failed to processes and those with large amounts of decorrelation are not plotted.

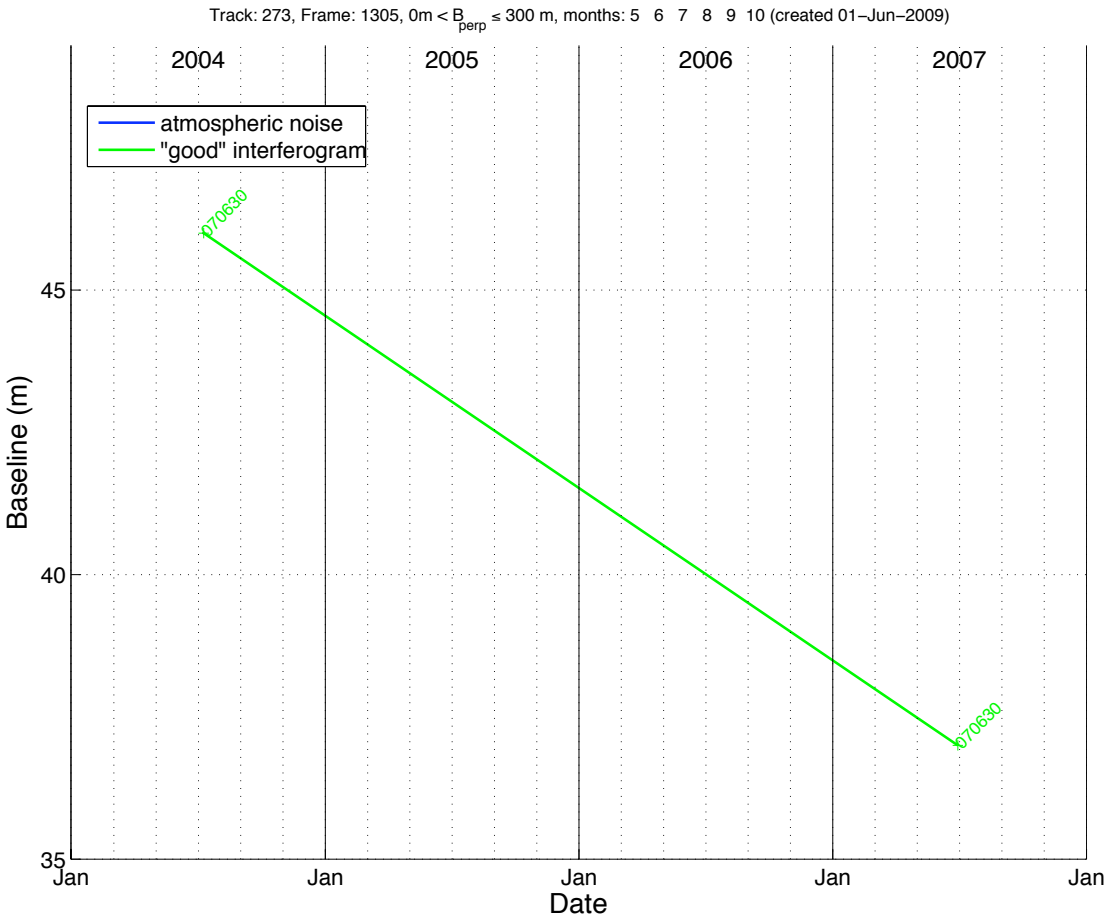

Figure 6.2: Cont. Track 273, Enviast.

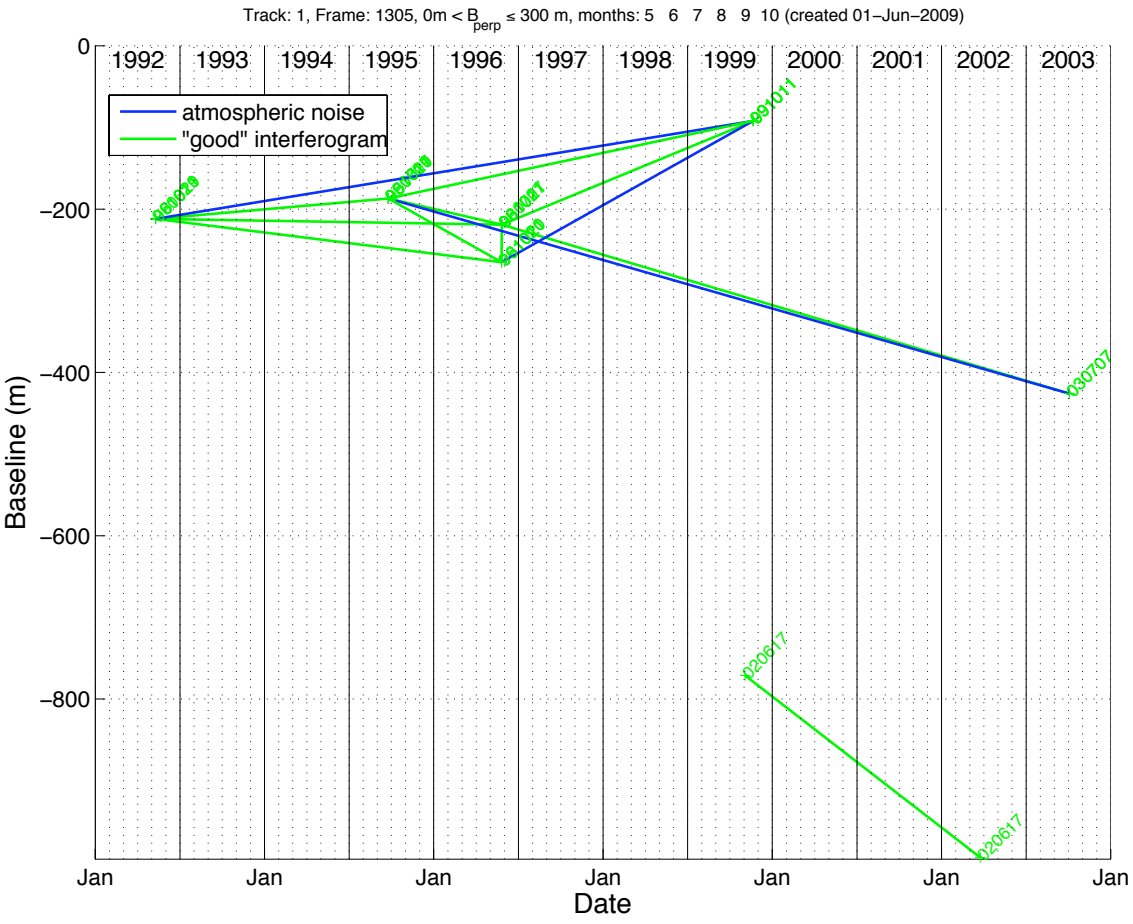

Figure 6.2: Cont. Track 238, ERS1/2.

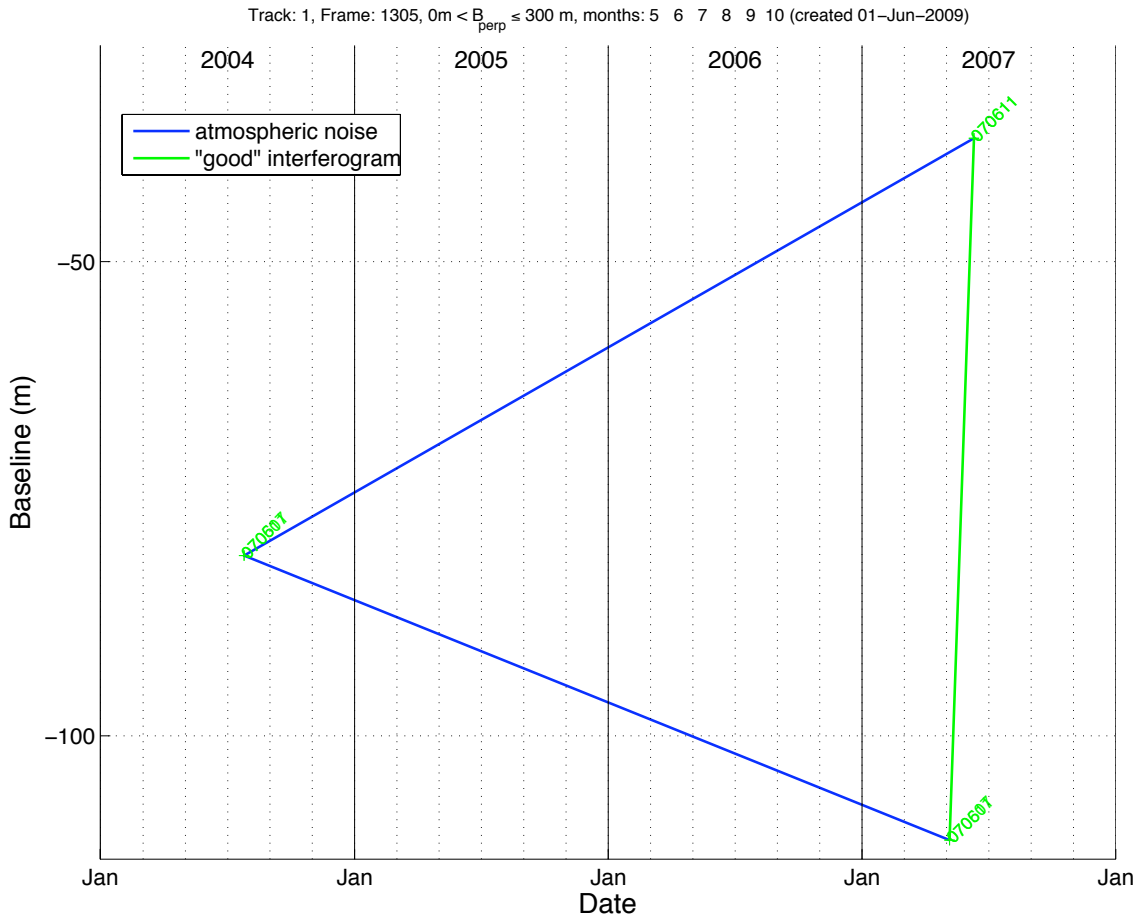

Figure 6.2: Cont. Track 1, Envisat.

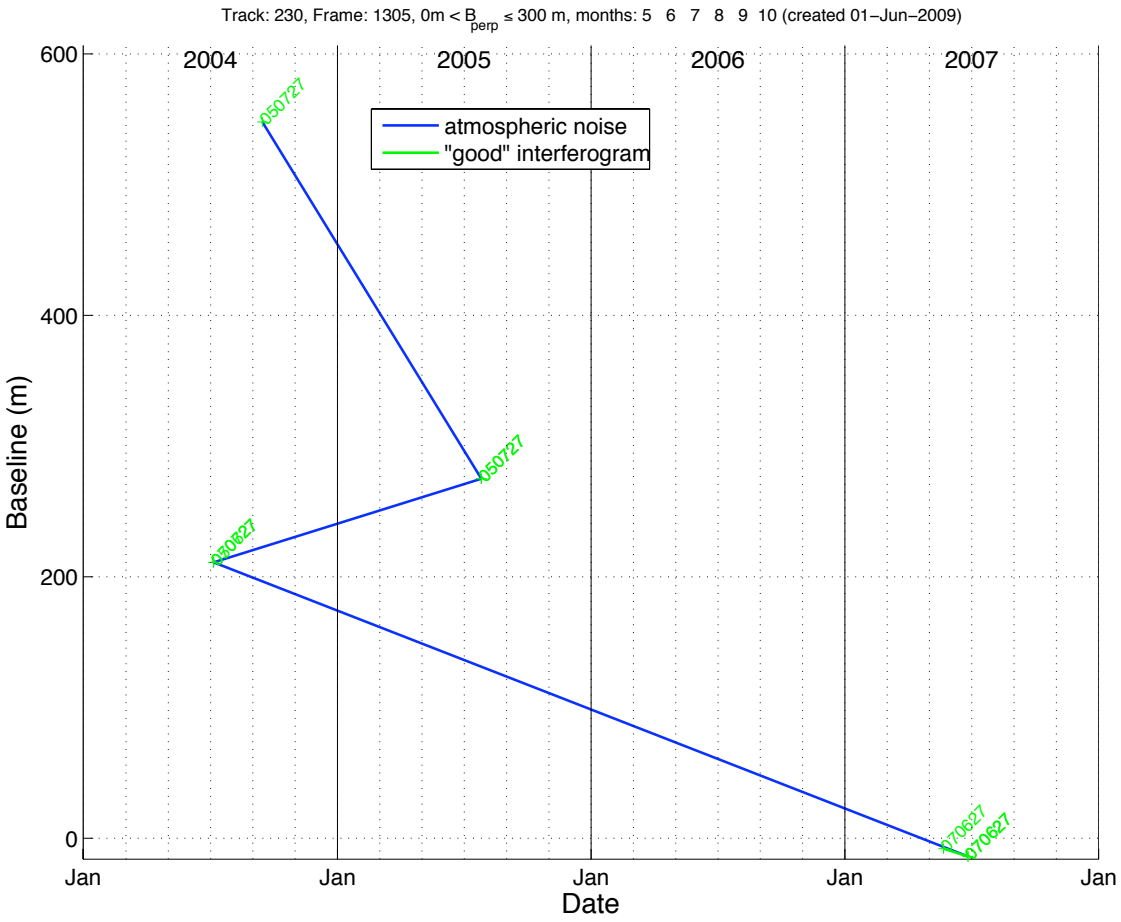

Figure 6.2: Cont. Track 230, Enviast.

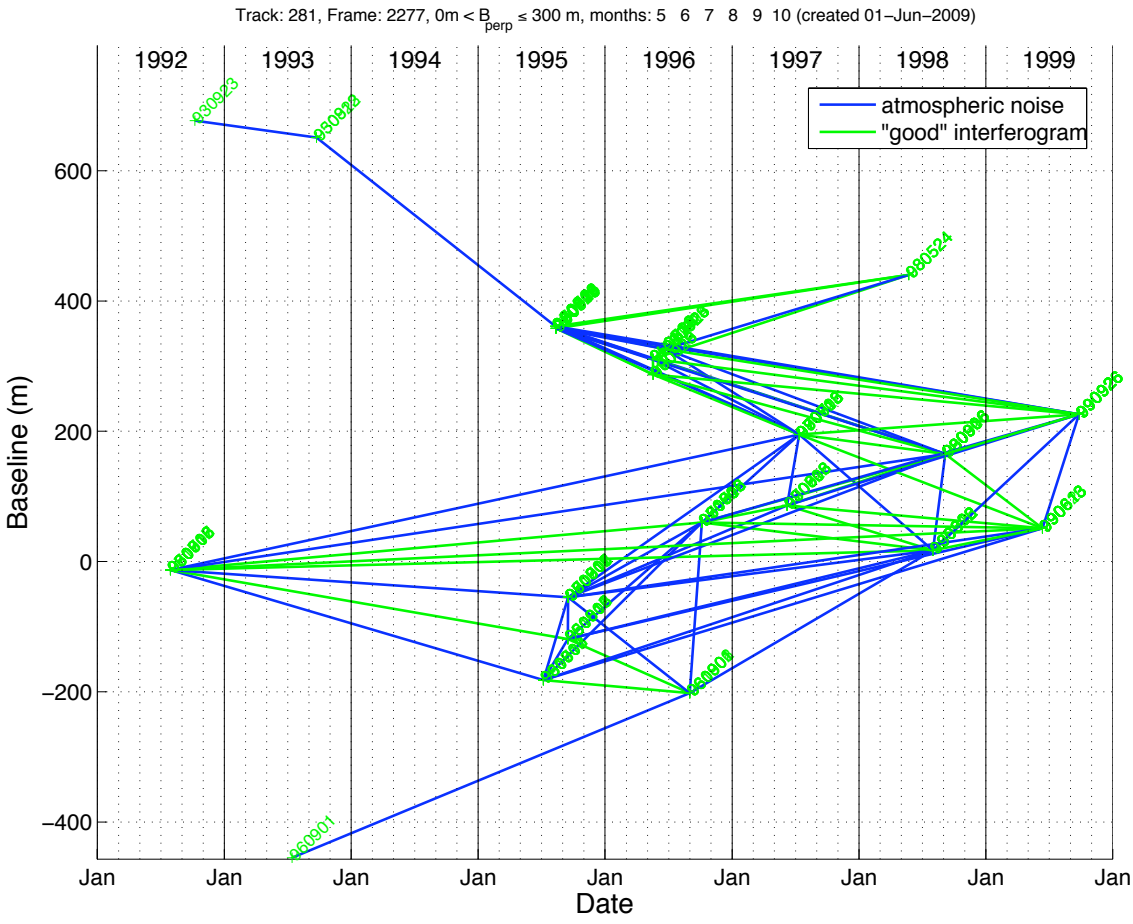

Figure 6.2: Cont. Track 281, ERS1/2.

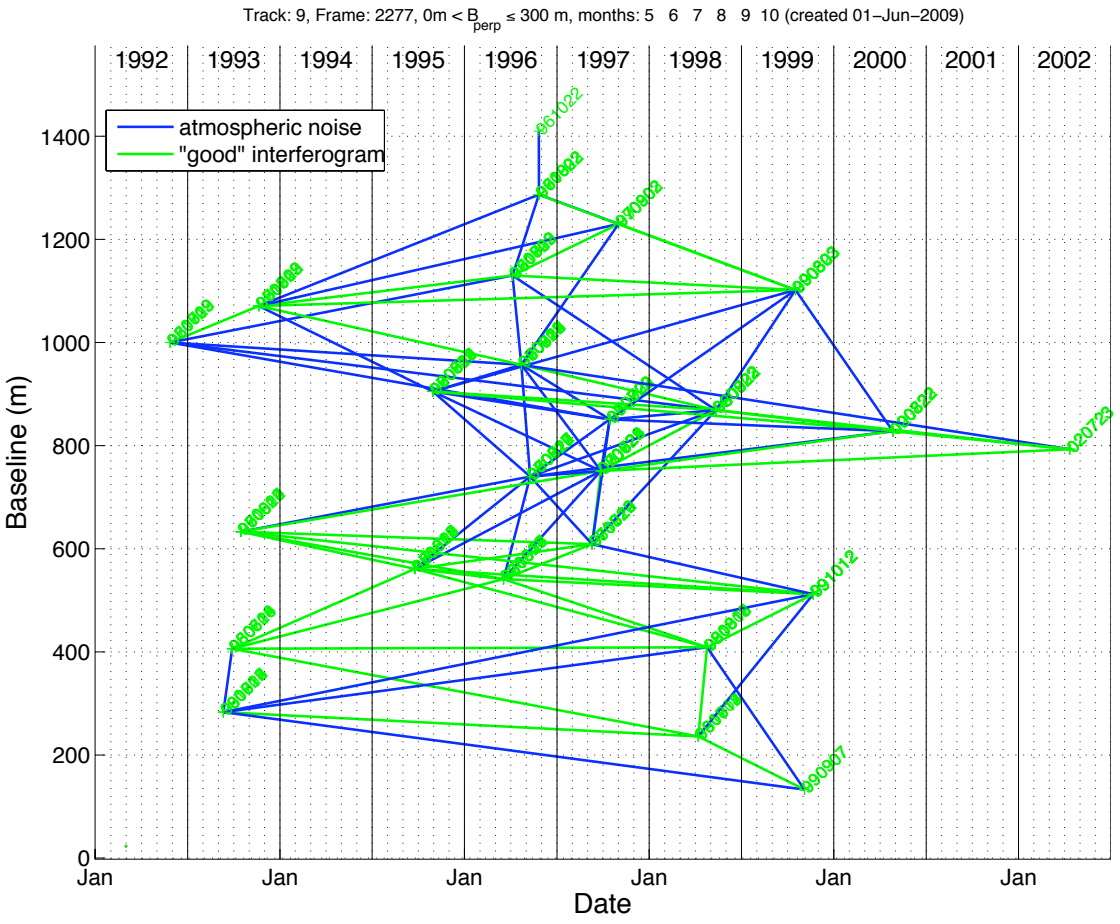

Figure 6.2: Cont. Track 9, ERS1/2.

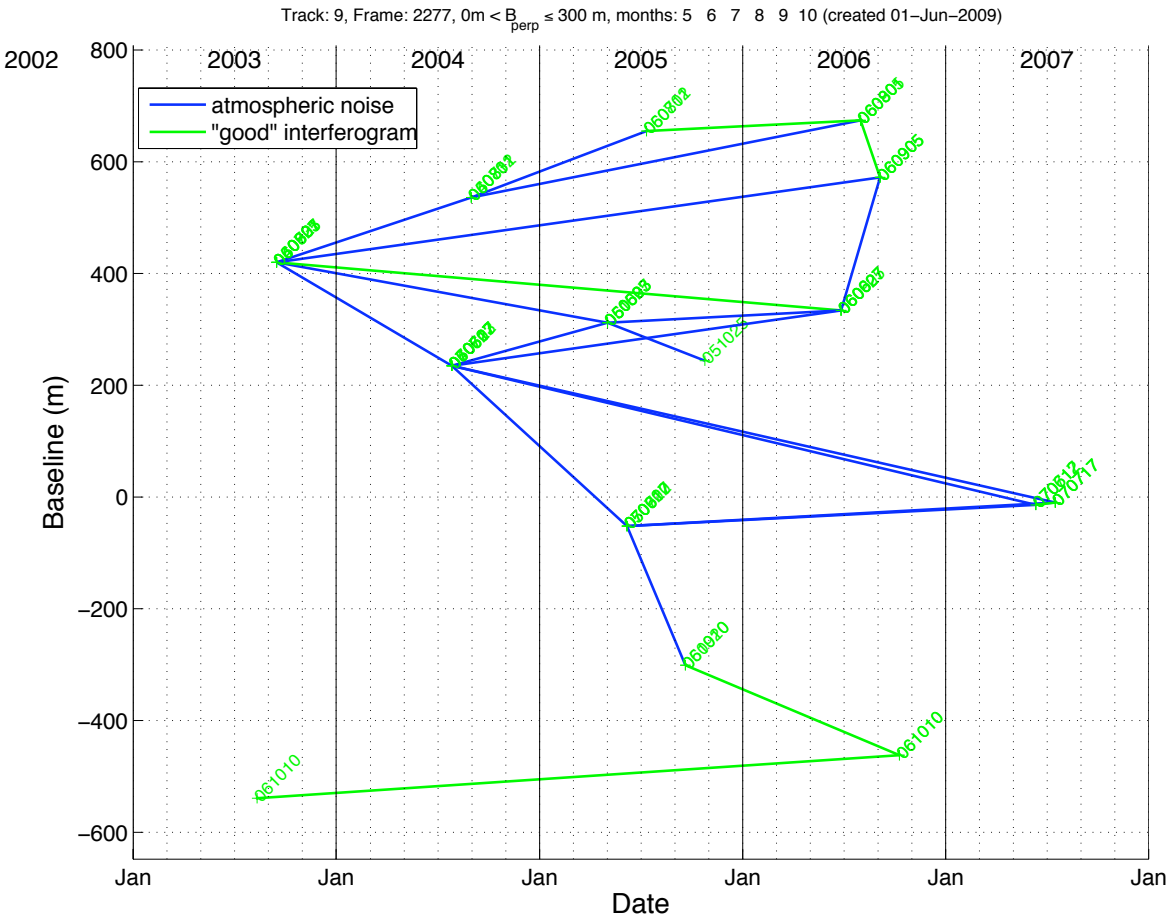

Figure 6.2: Cont. Track 9, Enviast.

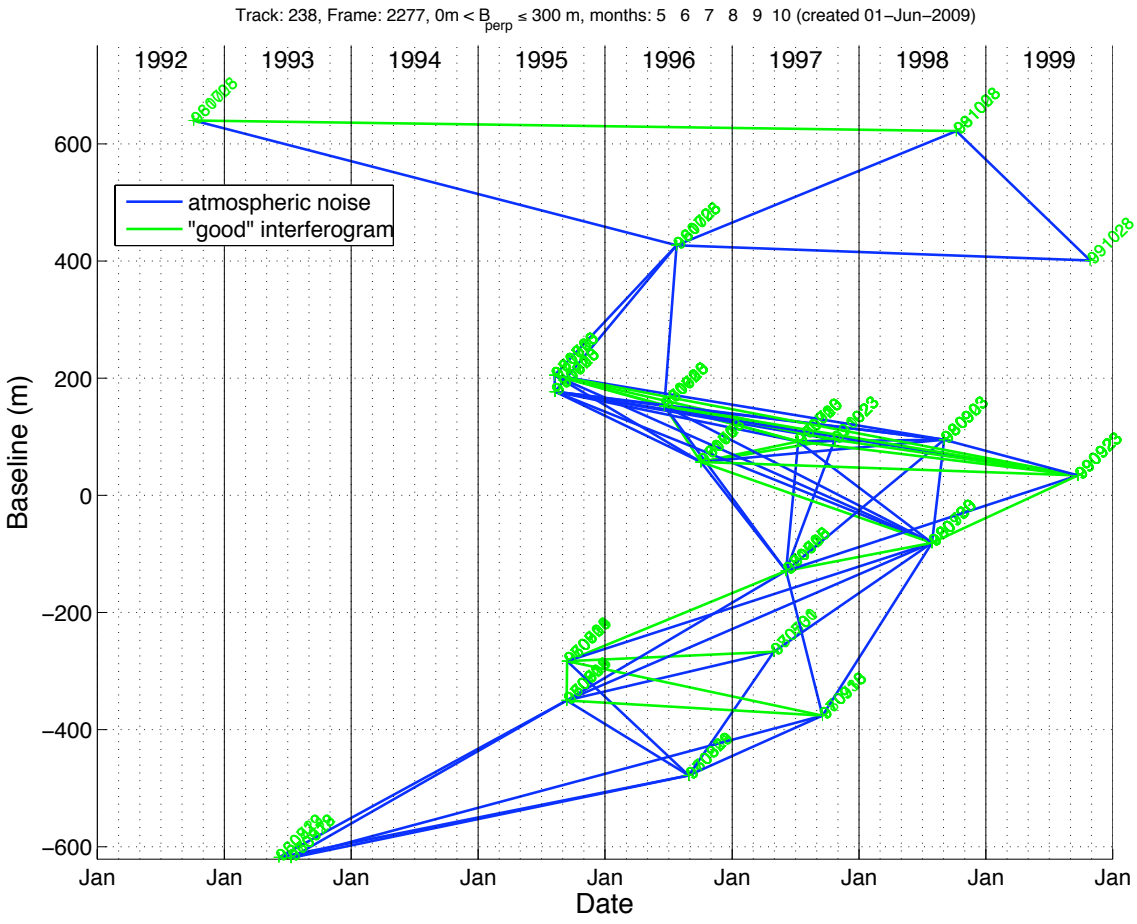

Figure 6.2: Cont. Track 238, ERS1/2.

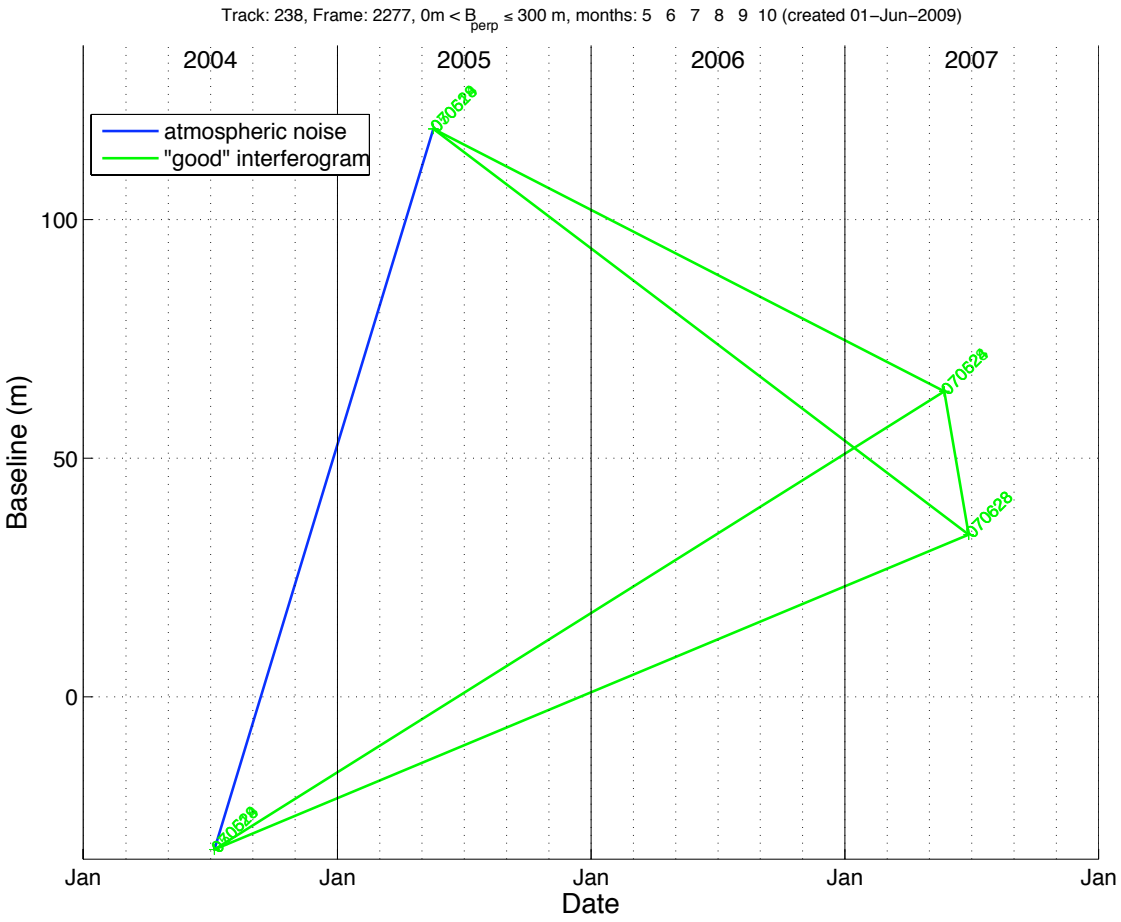

Figure 6.2: Cont. Track 238, Enviast.

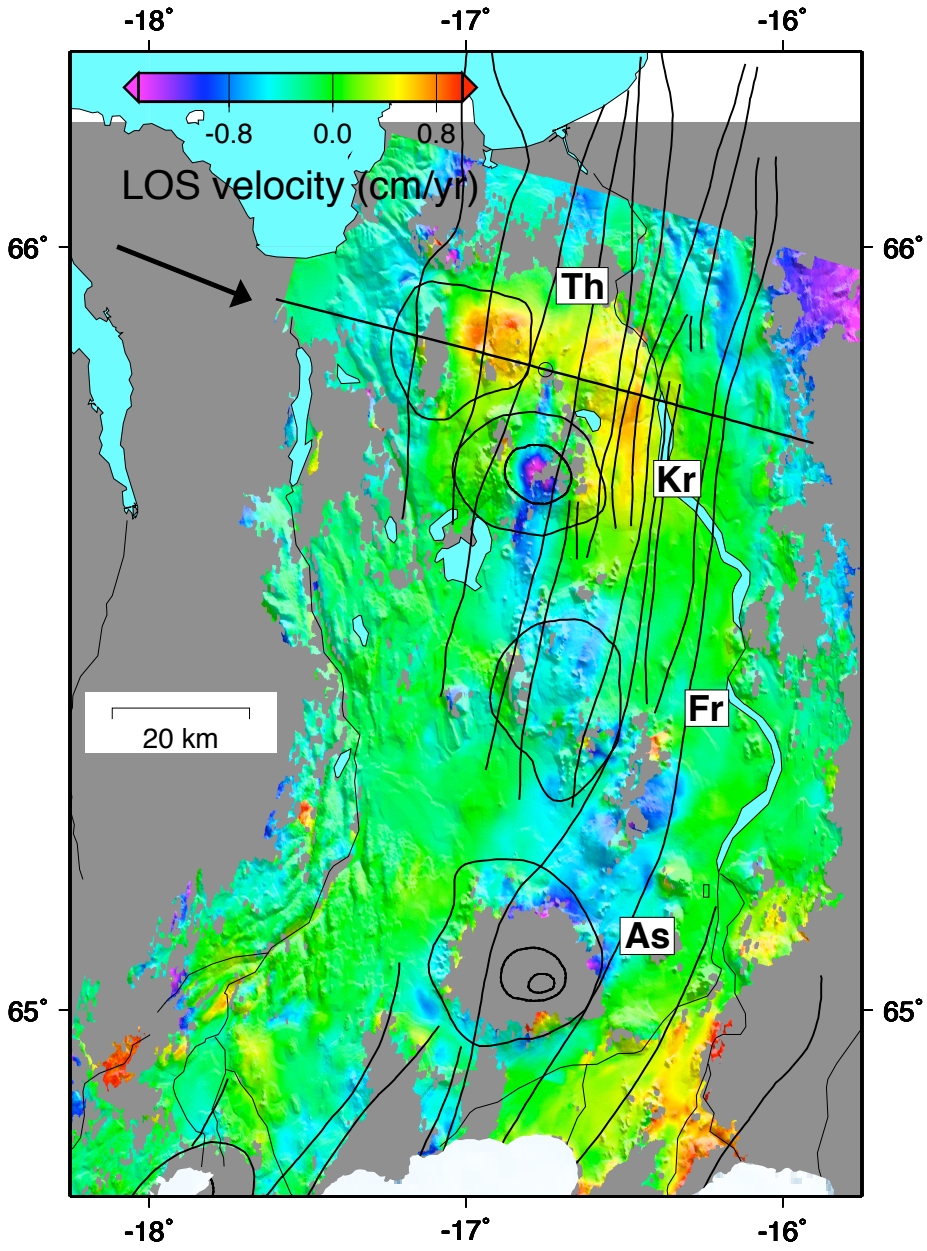

Figure 6.3: Typical descending interferogram from track 9 spanning 1996/06/04 – 1993/07/31. The volcanic systems are drawn as in Figure 6.1. Positive displacements are towards the satellite. The arrow indicates the ground projection of the radar line-of-sight. The black line perpendicular to the Krafla rift system is the location of the profile line used in Section 6.3.

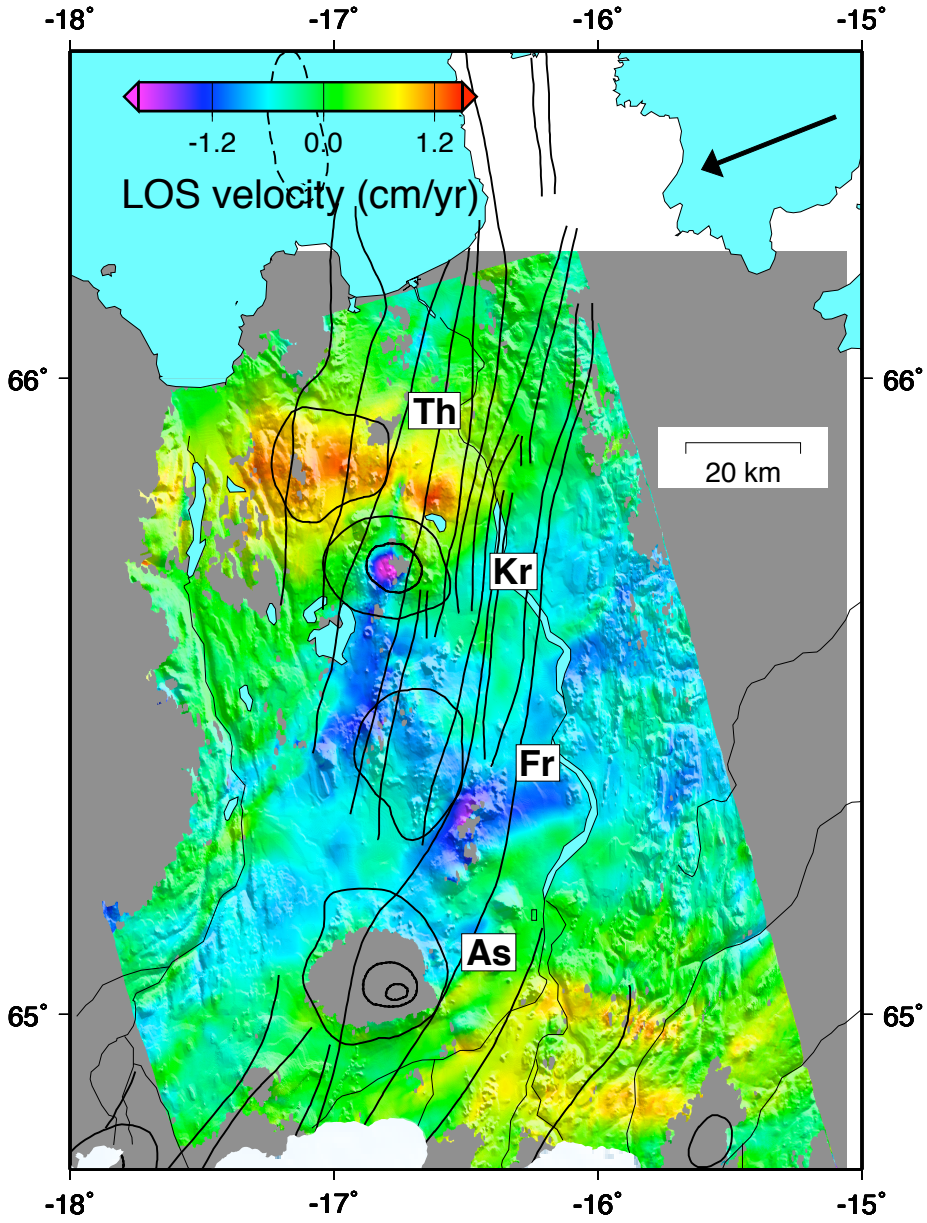

Figure 6.4: Typical ascending interferogram from track 1 spanning 1995/06/19 – 1992/09/18. See Figure 6.3 for details.

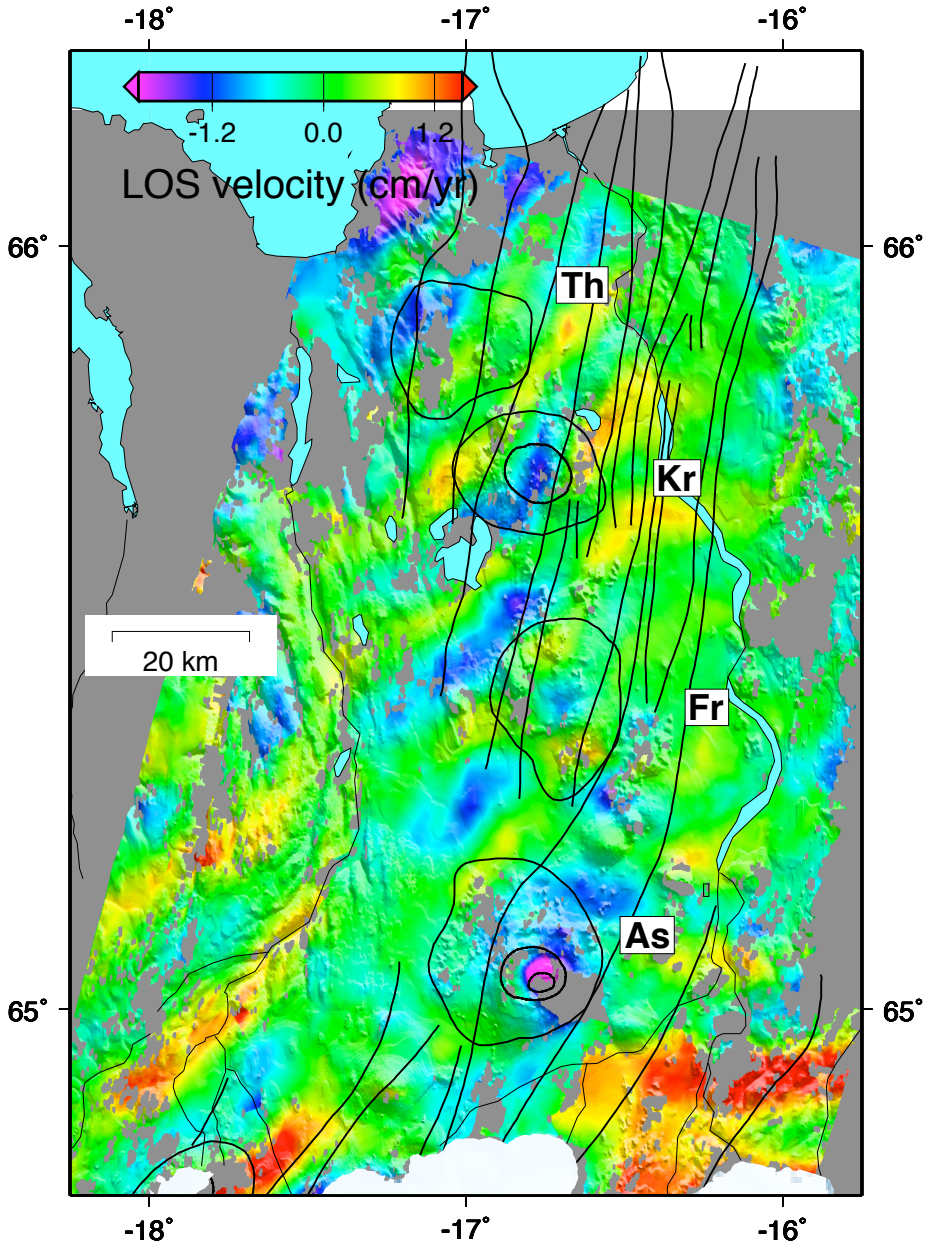

Figure 6.5: Example of an interferogram with a strong atmospheric signal from track 9 2000/08/22 – 1996/09/17.

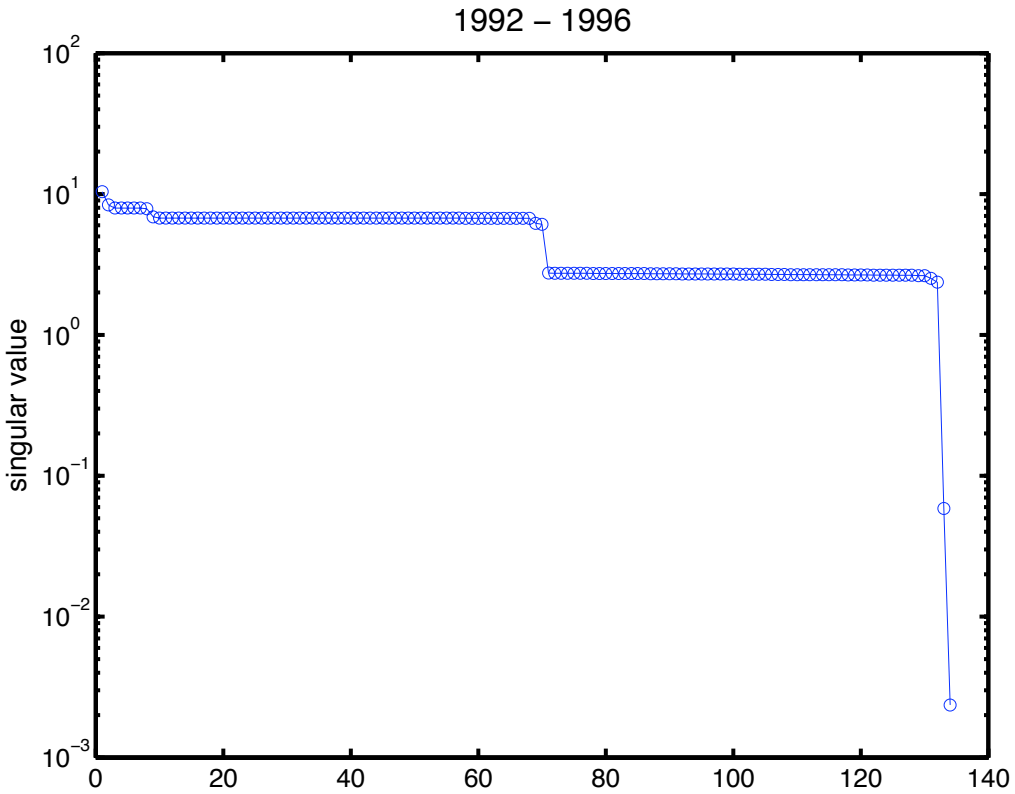

Figure 6.6: The singular values of the rift perpendicular and vertical velocity inversion. There are two model parameters near the model null space.

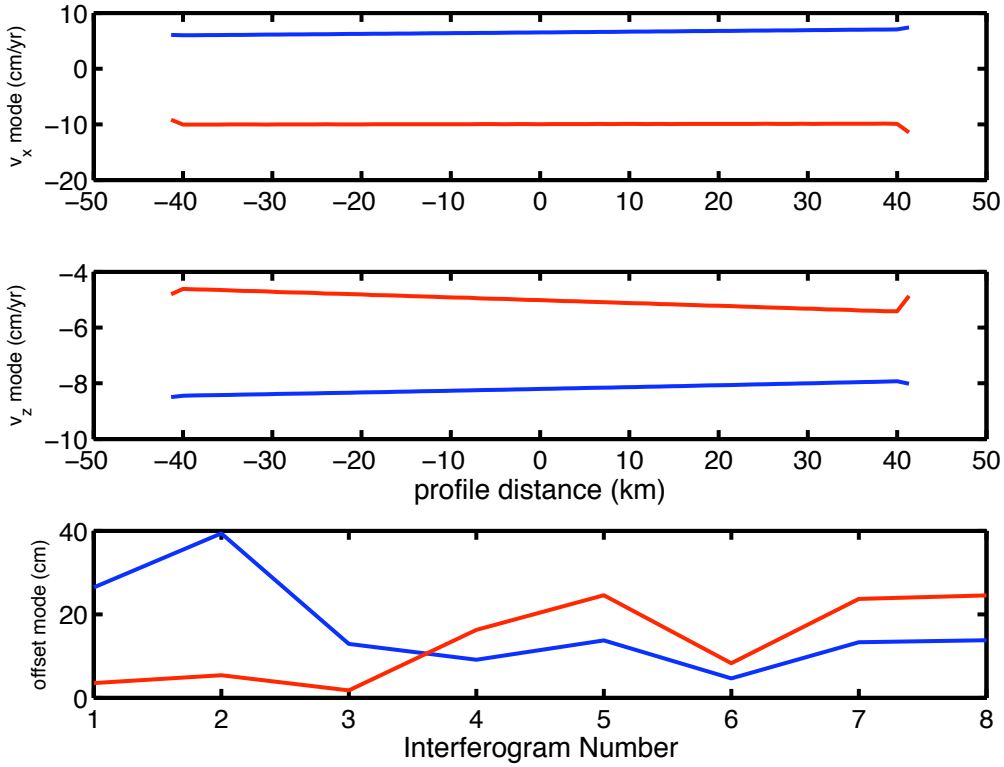

Figure 6.7: The model space vectors associated with the two smallest singular values in Figure 6.6. The blue lines correspond to the smallest singular value and the red lines to the next smallest. These vectors are close to the null space of the solution and are therefore highly sensitive to noise. Portions of any solution that are in this space are removed before interpreting the solution. The velocity modes are approximately linear ramps.

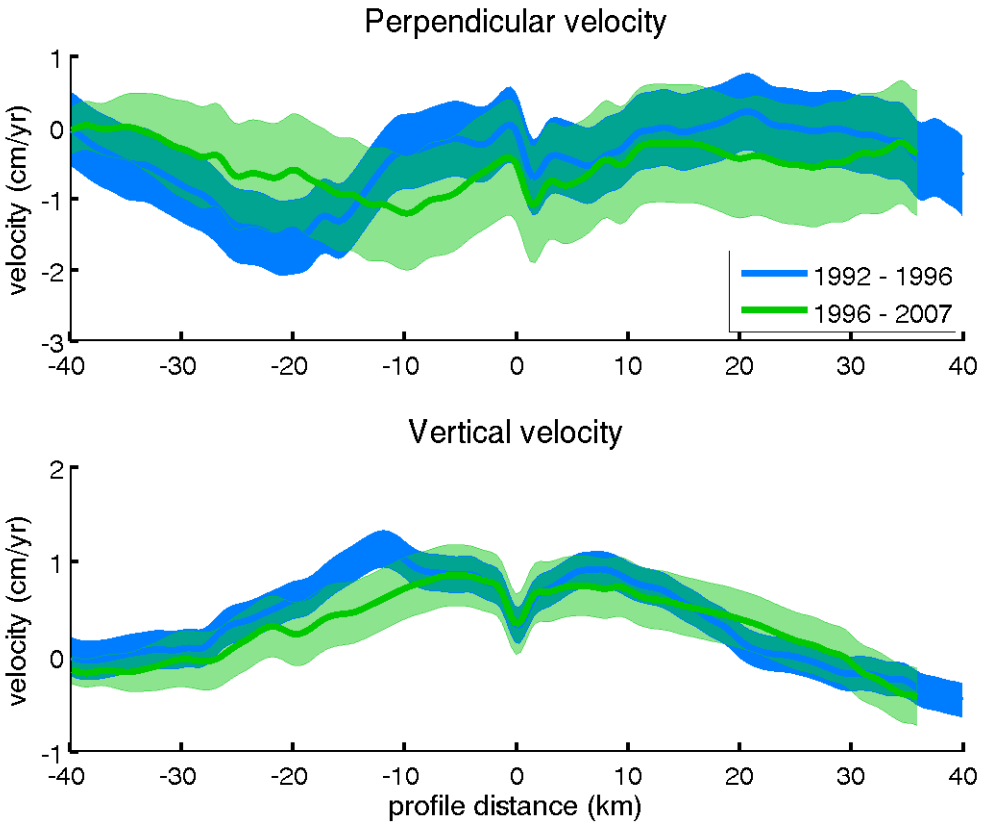

Figure 6.8: Result of inversion for rift perpendicular and vertical velocities for two time periods: 1992-1996 and 1996-2007. The shaded areas are the one standard deviation model errors. A linear trend has been removed and the velocity profile shifted to zero at $x = 32$ km.

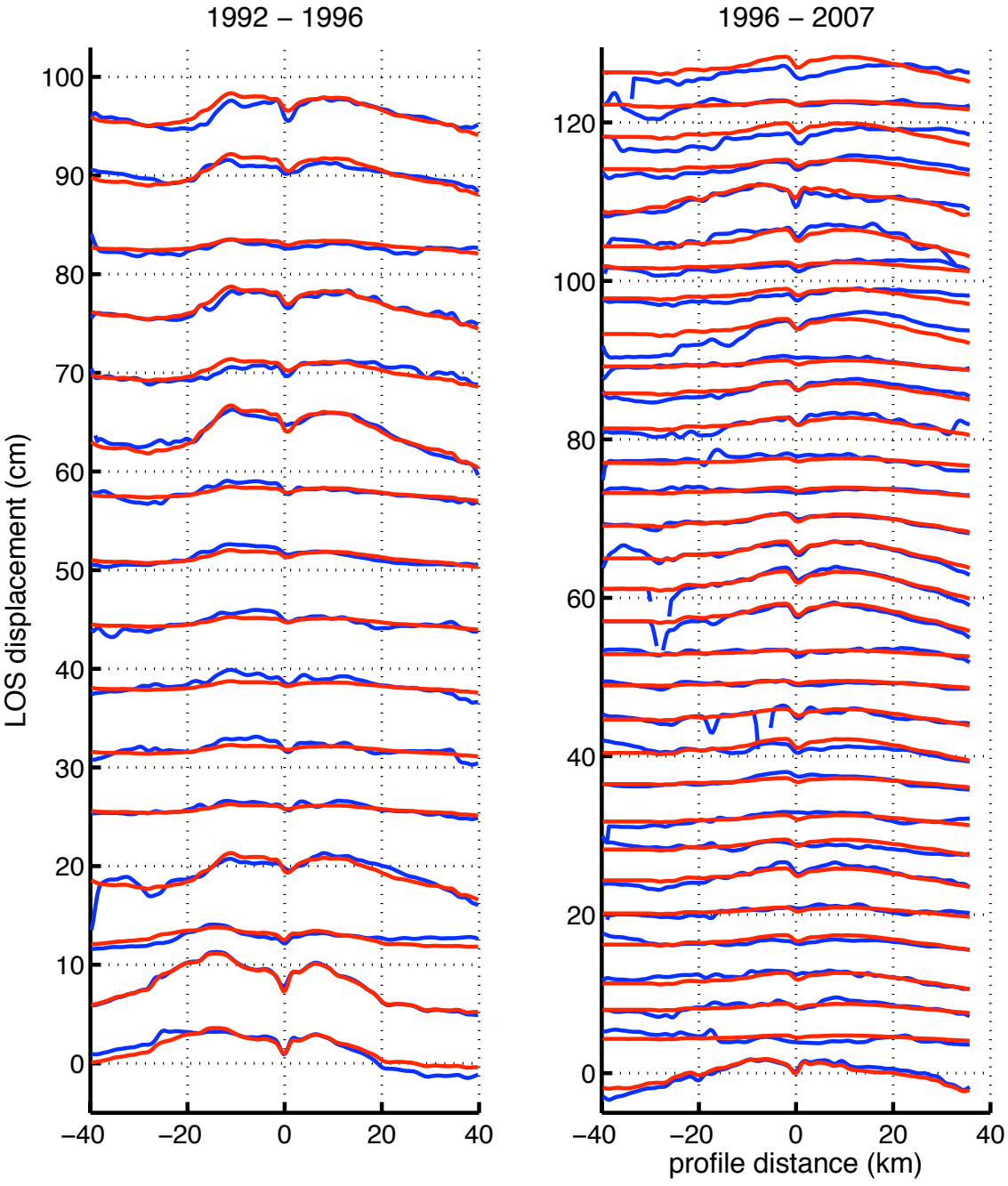

Figure 6.9: line-of-sight displacement data used for inversion (Figure 6.8 in blue and estimated displacements from the inversion in red. Displacements are plotted on the same scale and shifted for viewing.

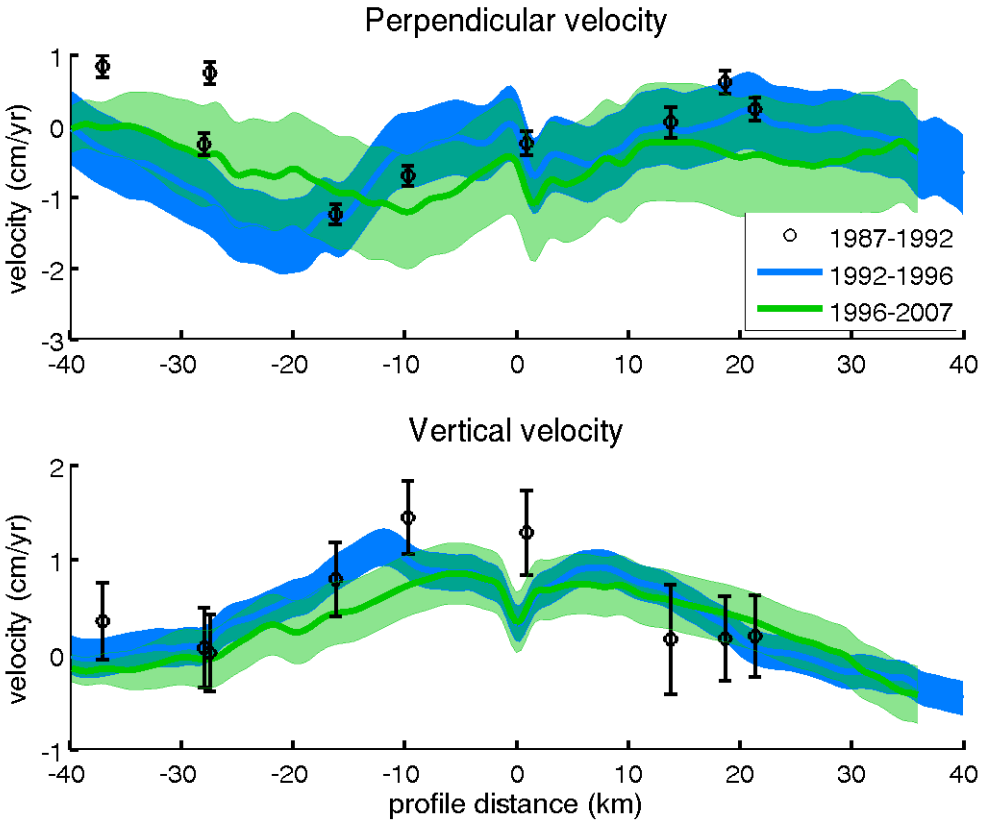

Figure 6.10: 1987 – 1992 GPS velocities from Hofton & Foulger (1996) compared to the two-dimensional InSAR velocities.

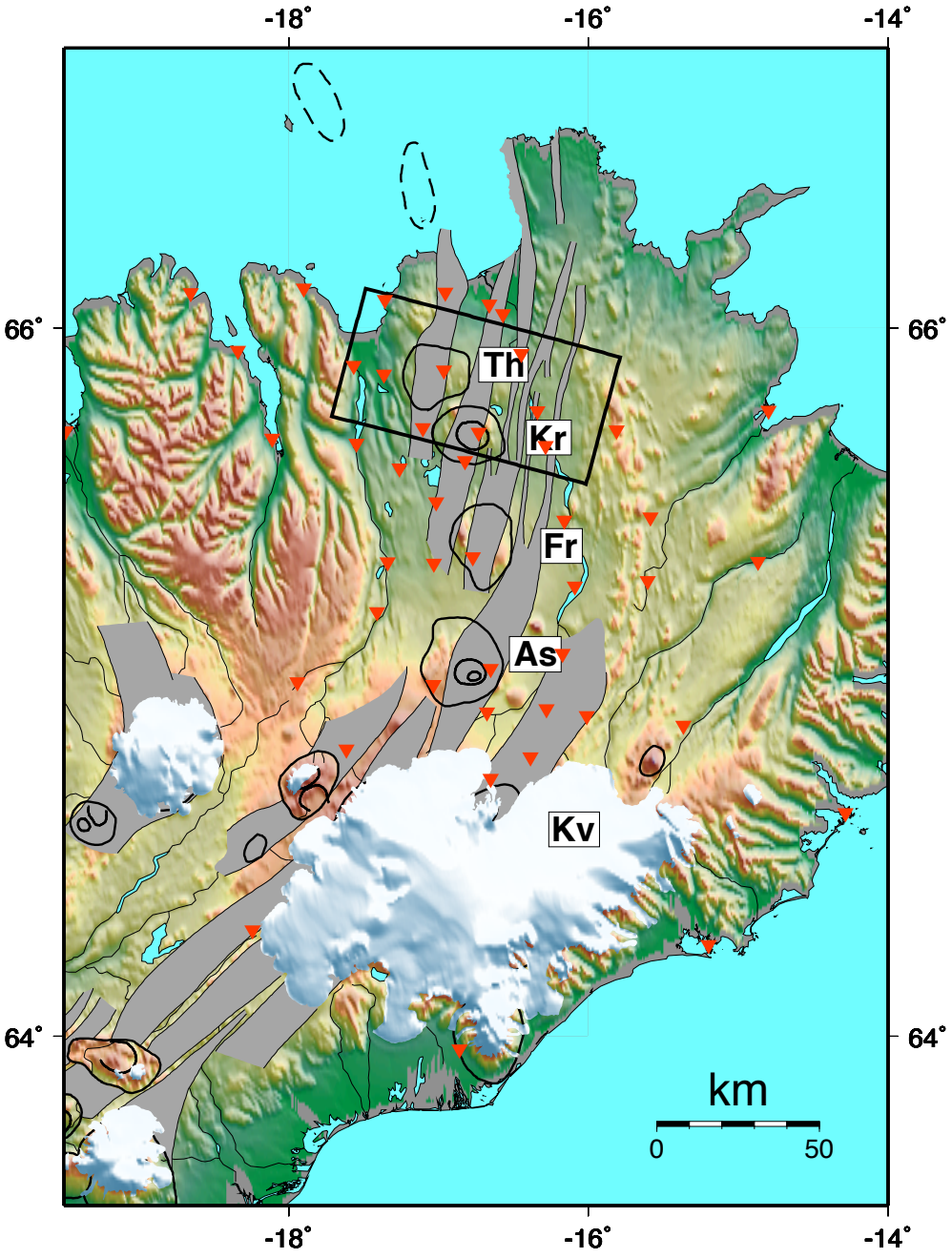

Figure 6.11: [
Locations of GPS sites used in Hofton & Foulger (1996). The black box outline indicates the stations used to compare to InSAR data in Figure 6.10.

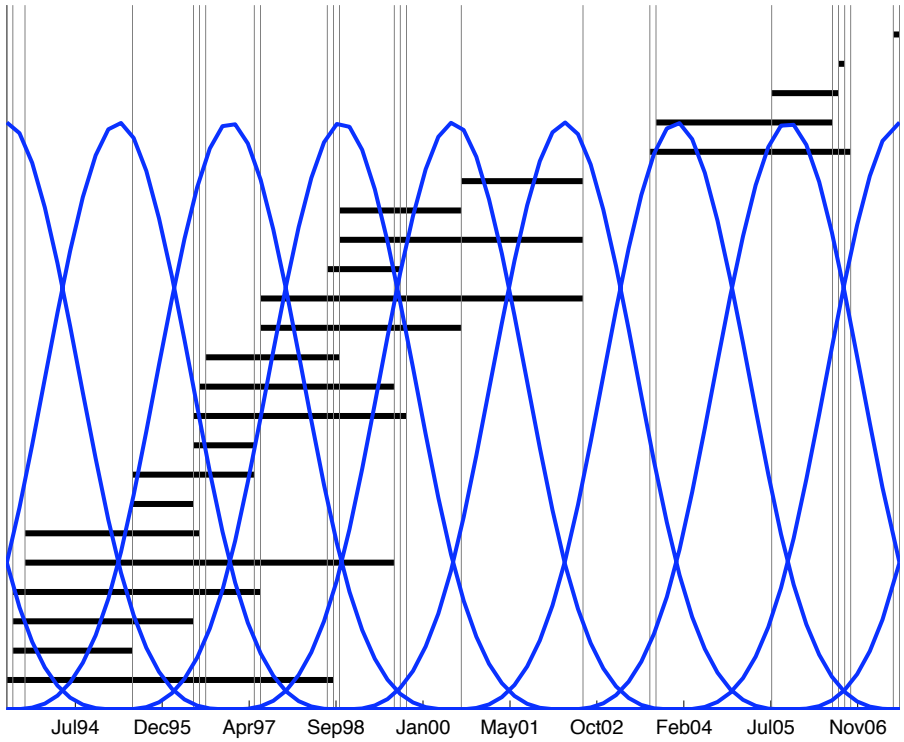

Figure 6.12: Interferometric pairs and B-spline basis functions used in MInTS time series inversion. The interferometric pairs are shown in black and the spline basis in blue. The vertical axis only has meaning for the spline functions which are all normalized to a maximum amplitude of unity.

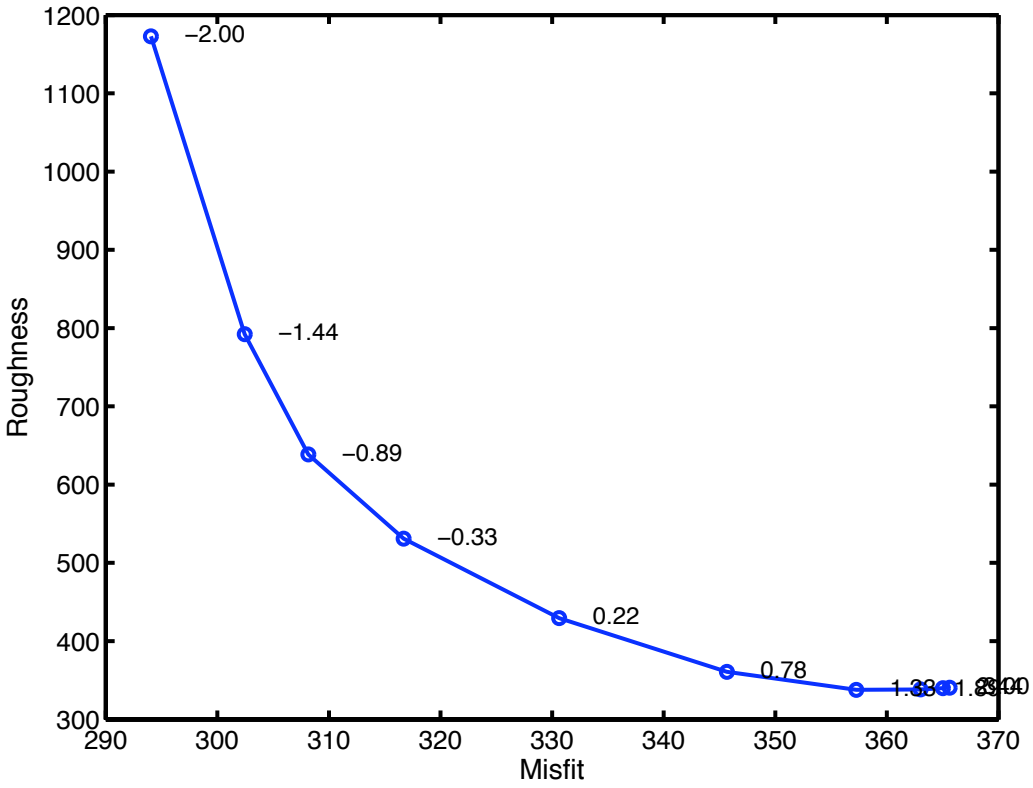

Figure 6.13: L-curve for search for optimum MInTS time series damping parameter. Each point is labeled with the log_{10} of the damping parameter, λ, in Equation 6.7. Misfit is the RMS of the residual interferograms, and roughness is the RMS of $\nabla_t^2 u(x, y, t)$, where $u(x, y, t)$ is the displacement function solution.

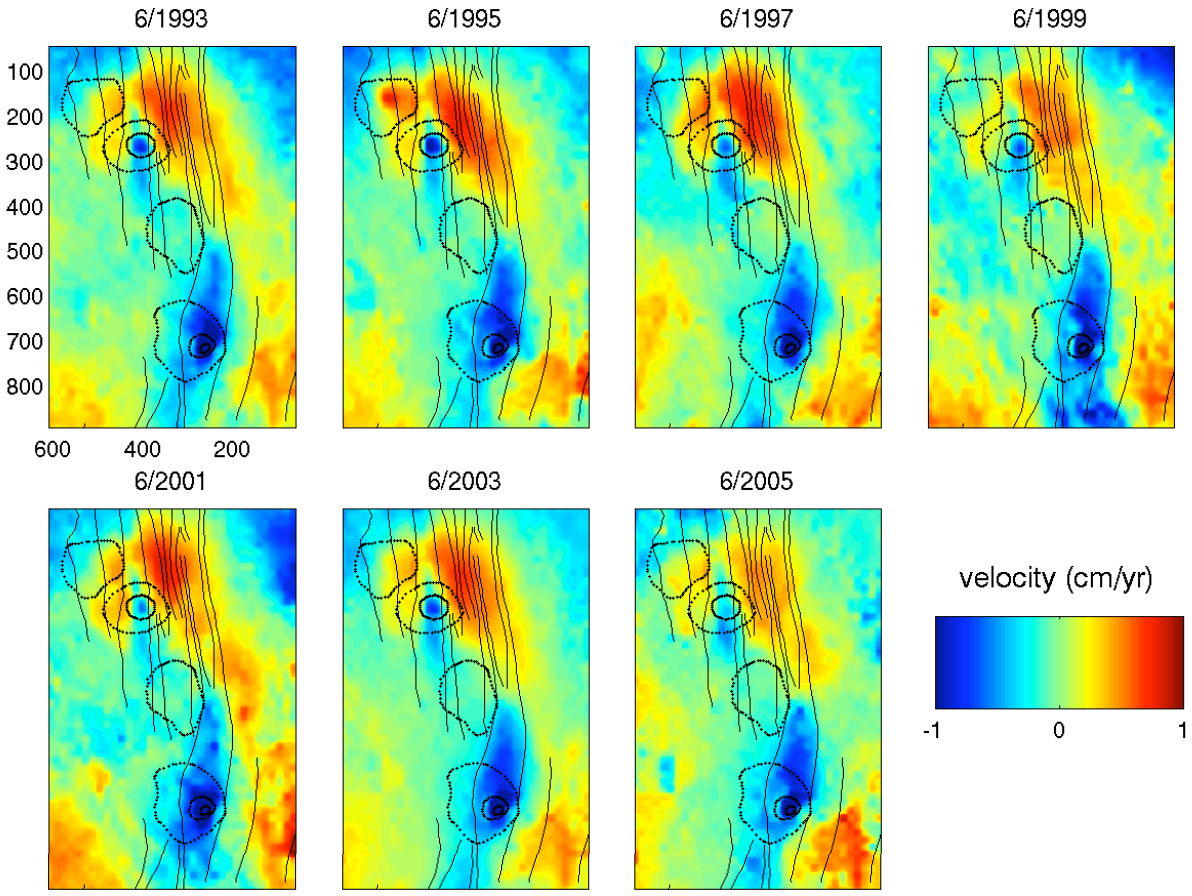

Figure 6.14: Velocity snapshots of MInTS solution. Velocities are in centimeters per year and dates of model evaluation are shown above each. Range and azimuth coordinates in pixels are indicated on the ordinate and abscissa; pixel size is approximately 160 m. Note that the coordinate directions have been reversed to make these descending radar images oriented approximately geographically. Central volcanoes and fissure swarms are drawn in black; they are from north to south: Theistareykir, Krafla, Fremri-Namar, and Askja.

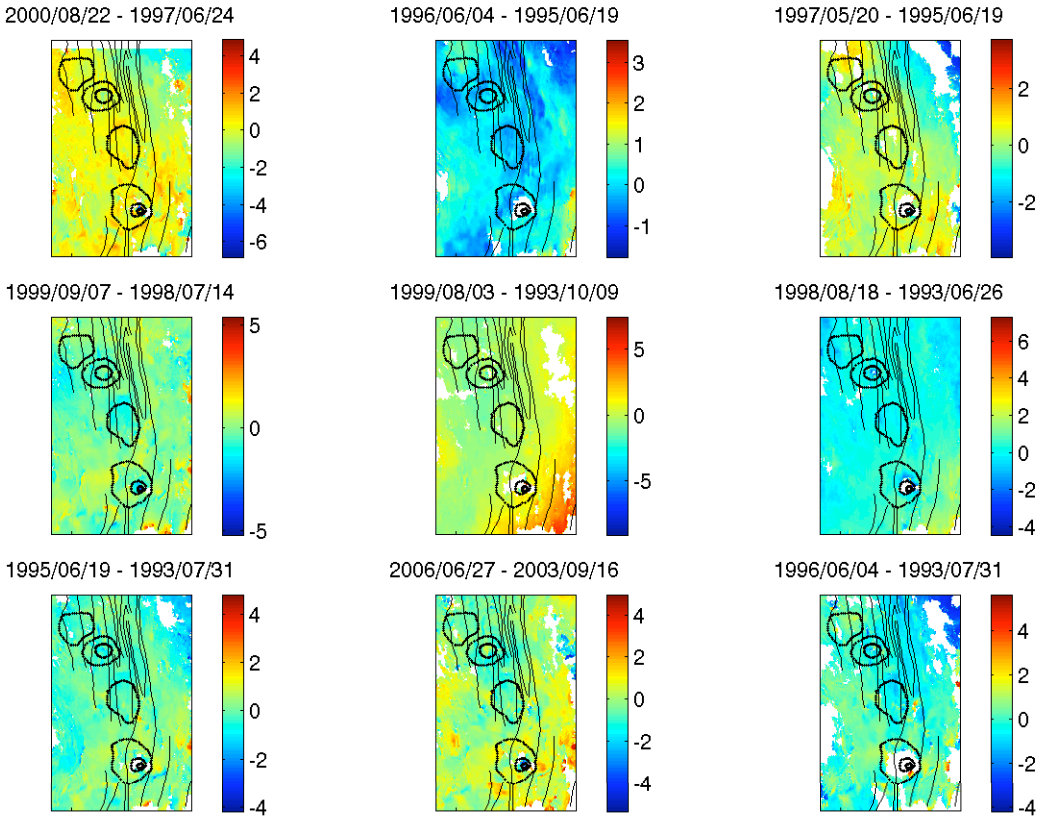

Figure 6.15: Residual interferograms after removing MInTS time series using minimum length damping with $\lambda = 10^{0.22}$. Residuals are in cm and coordinates are radar (range and azimuth) pixels. Axes and geologic features are as in Figure 6.14.

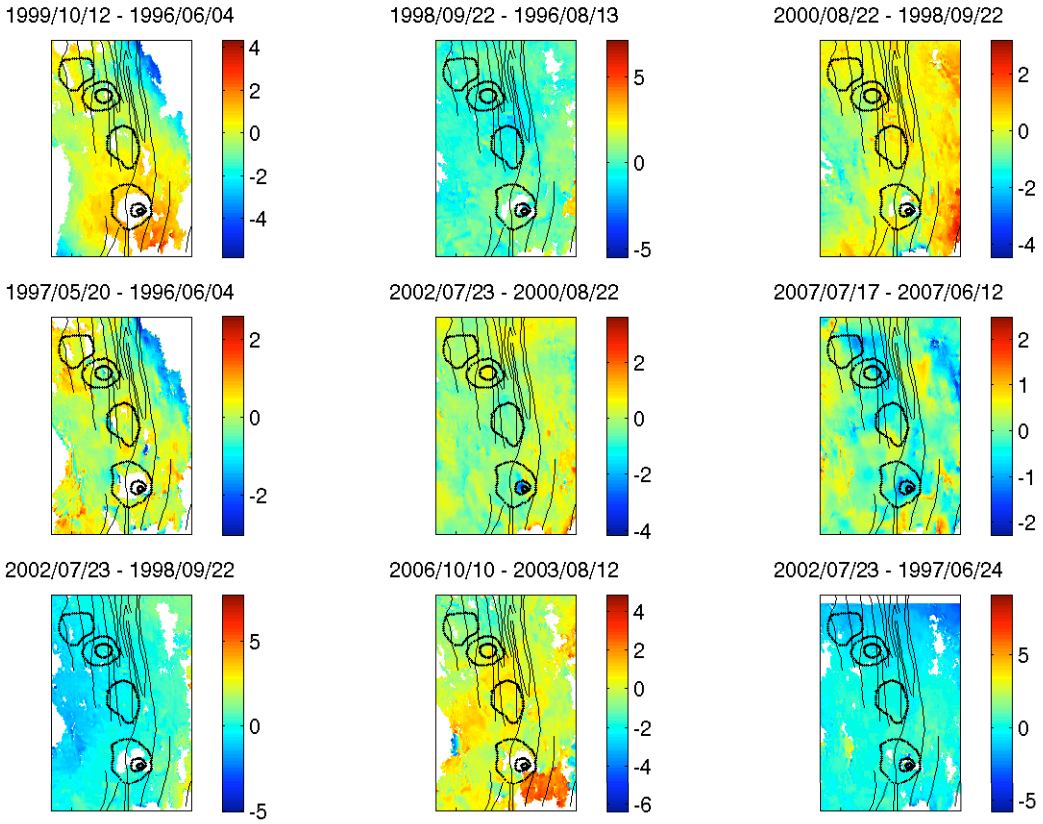

Figure 6.15: Cont.

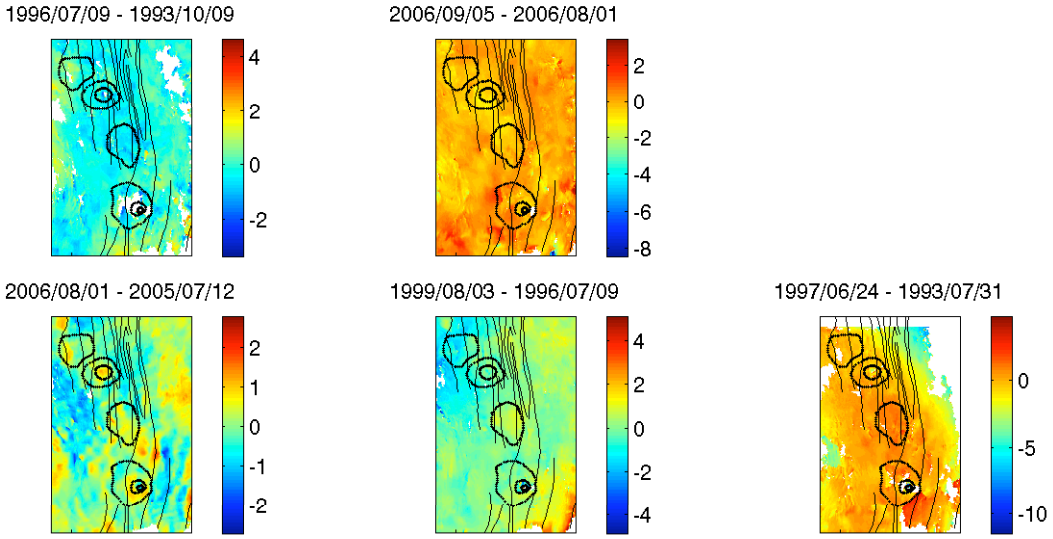

Figure 6.15: Cont.

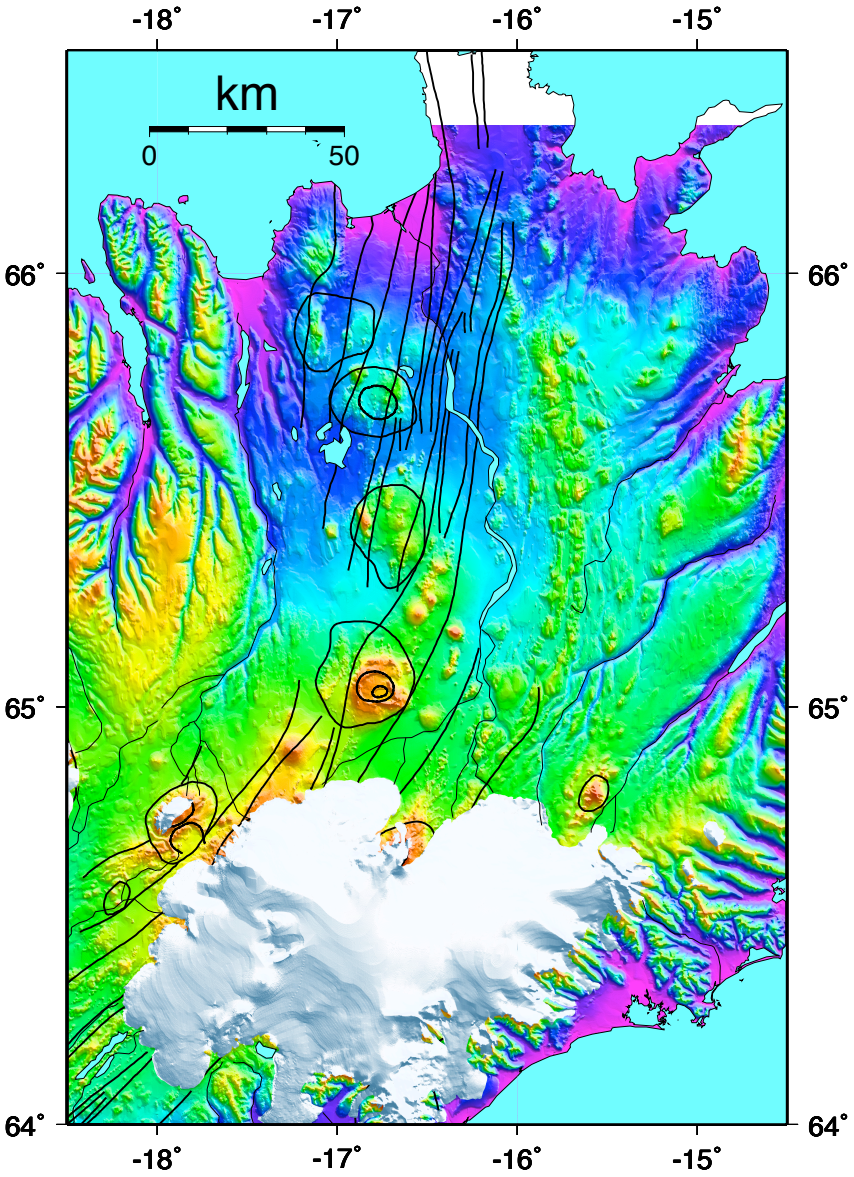

Figure 6.16: DEM of the NVZ with 90 m resolution. Volcanoes and associated fissure swarms are drawn in black.

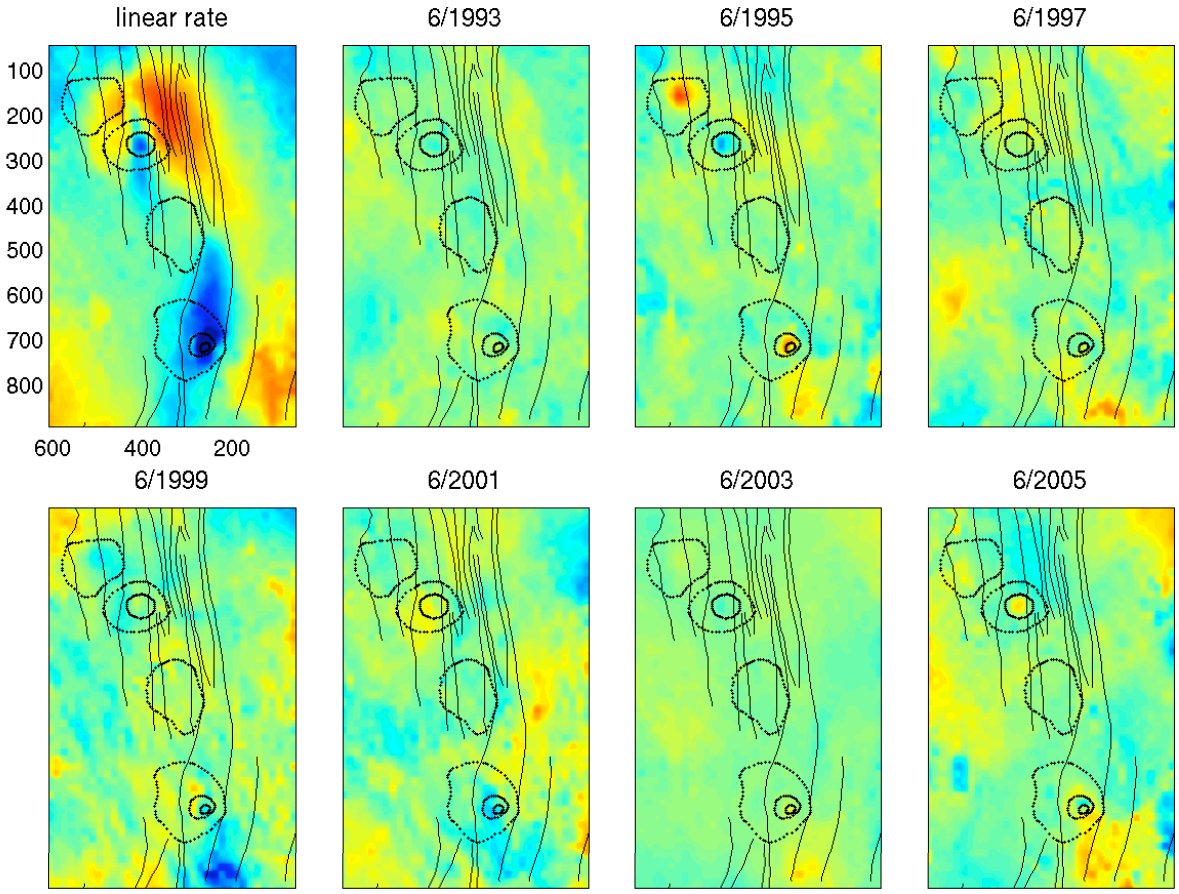

Figure 6.17: Velocity snapshots of a decomposition of the MInTS solution. The first panel is the linear rate; all other panels are only the spline component of the time series. Labels and scale are as in Figure 6.14.

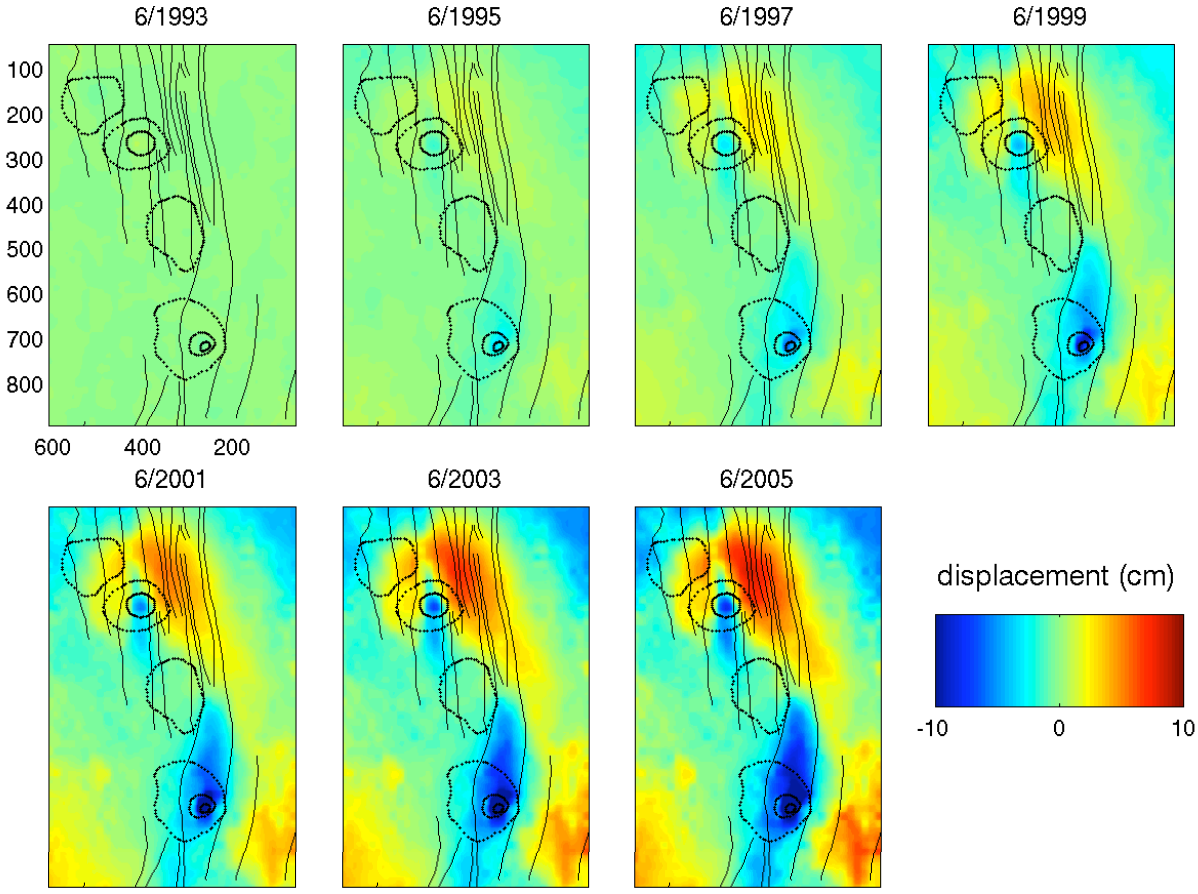

Figure 6.18: MInTS solution plotted as cumulative displacement in centimeters. See Figure 6.14 for explanation of outlines of geologic features and radar coordinates.

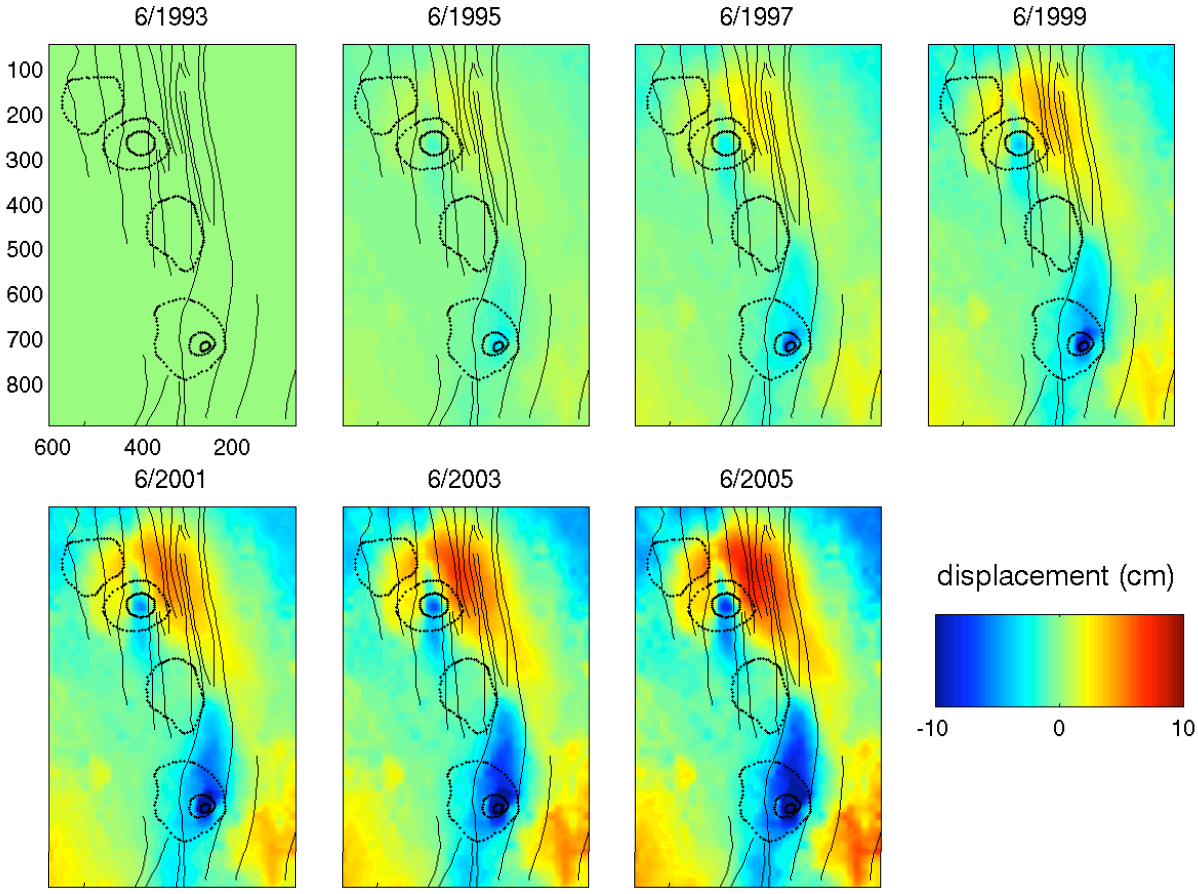

Figure 6.19: Linear portion of the displacement field for MInTS solution shown in Figure 6.18

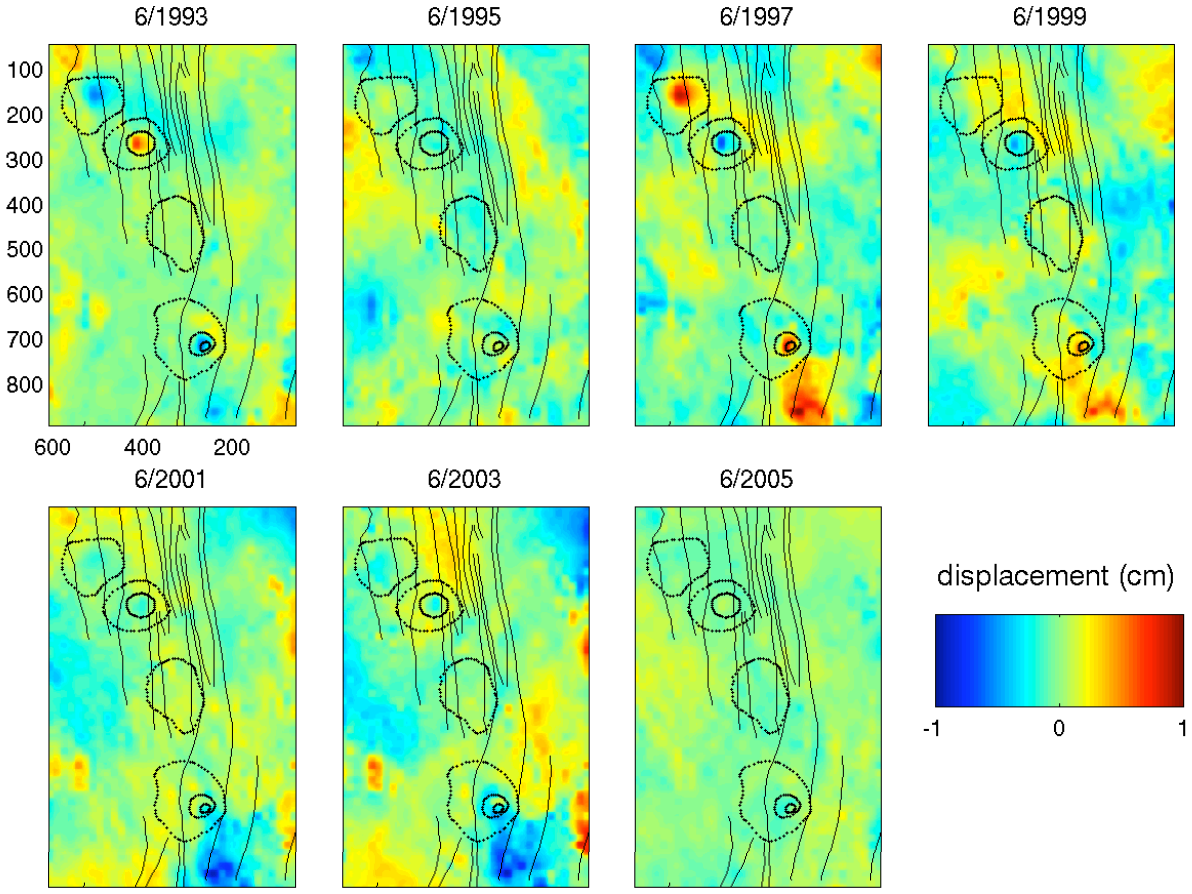

Figure 6.20: Spline portion of displacement solution shown in Figure 6.18. Note the factor of 0.1 change in color scale from Figures 6.18 and 6.19.

Figure 6.21: MInTS displacement time series plotted at four points of interest in the NVZ. (1) Center of Theistareykir volcano; (2) center of Krafla volcano; (3) broad post-rifting deformation field; (4) center of Askja volcano. The full displacement along with the linear and spline components are plotted. The components are scaled to be a percentage of the full dynamic range of the displacement at that particular point. Year tick marks are for January 1 of the corresponding year. Axes and geologic features for the color plot on the left are as in Figure 6.14

.

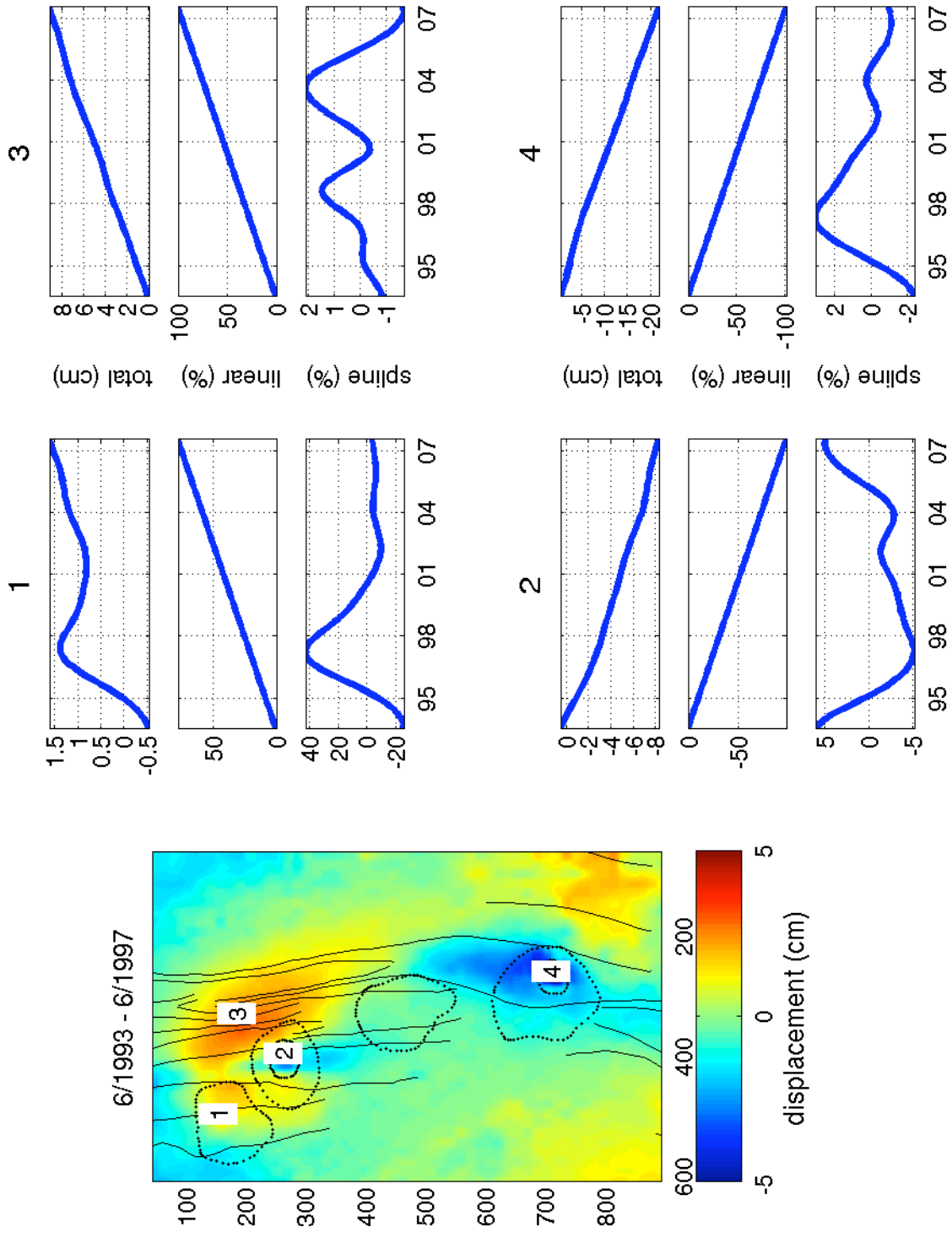
6/1993 - 6/1997
displacement (cm)
1
2
3
4
total (cm)
linear (%)
spline (%)
95
98
01
04
07

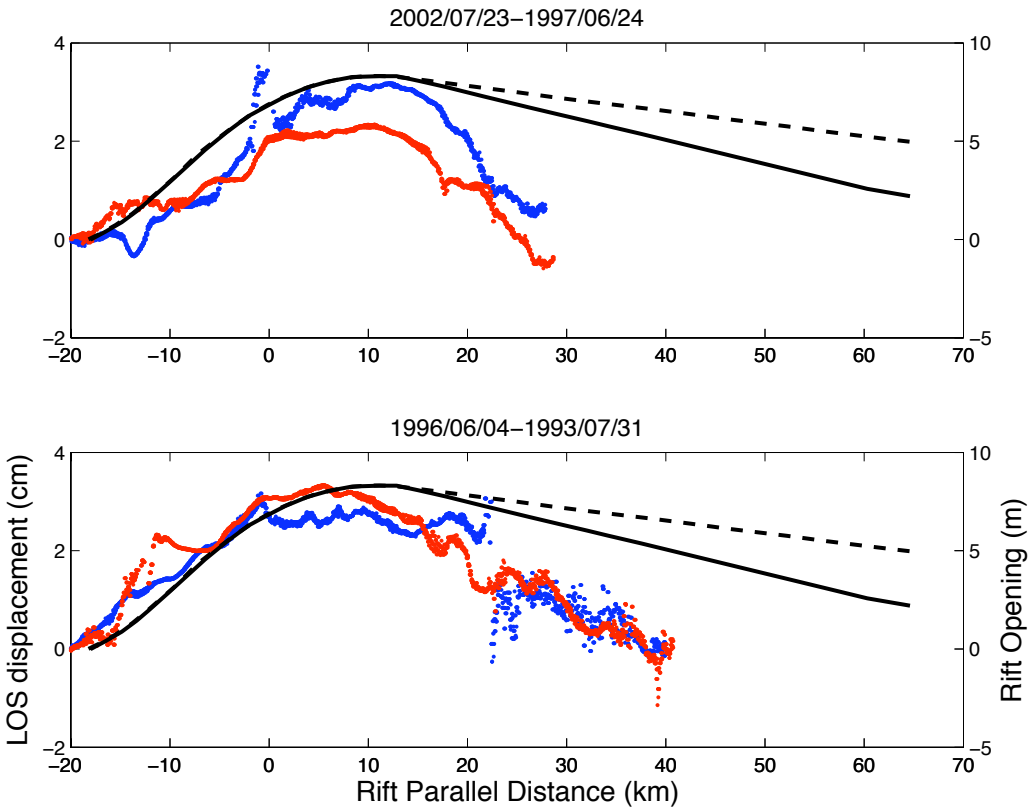

Figure 6.22: Estimate of amount of opening along the rift from Tryggvason (1984) and displacement as measured by track 9 with two independent interferograms (i.e., they do not share a common radar scene). The solid black line is the lower bound estimate of the total amount of rift opening and the dashed line is the upper bound. The blue InSAR displacements are from the profile closer to the central rift axis and the red from the profile farther away. See figure 6.23 for the locations of the profiles.

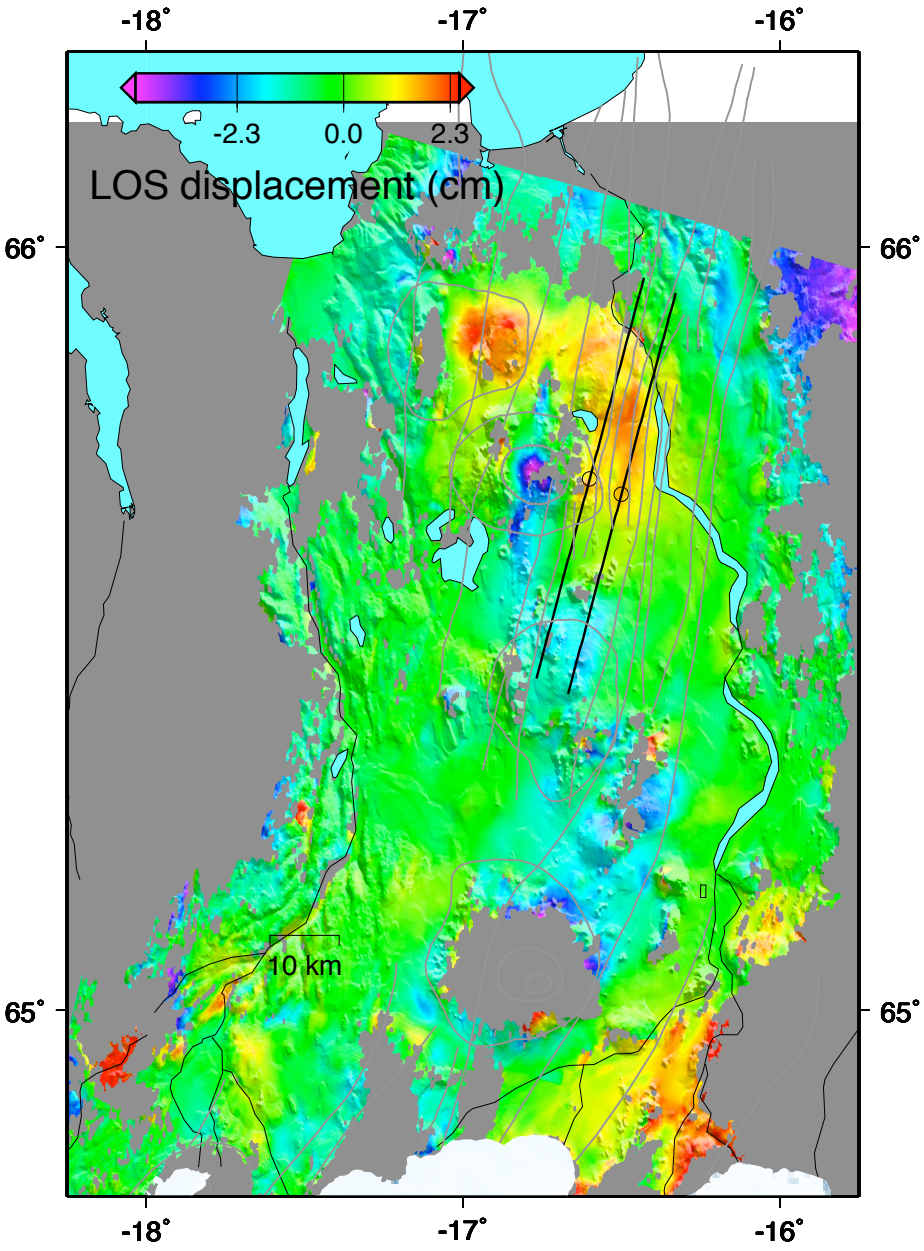

Figure 6.23: Location of profile lines for figure 6.22.

Track (A/D)	Scenes	"Clean" Interferograms	"Good" Interferograms
273 (A)	9	8	4
1 (A)	19	16	11
230 (A)	27	4	1
281 (D)	31	81	36
9 (D)	52	118	54
238 (D)	27	77	29
Total	165	304	135

Table 6.1: Interferometric data set available for the Northern Volcanic Zone of Iceland. Track is the orbital track appended with an "A" or "D" indicating ascending or descending orbit. Scenes is total number of radar scenes. "Clean" interferograms are the total number of interferograms formed with low amounts of decorrelation. "Good" interferograms are the total number of interferograms with observable surface deformation and low amounts of atmospheric noise.

Chapter 7

Modeling Post-Rifting Relaxation in the Northern Volcanic Zone, Iceland

7.1 Introduction

Motivated by the apparent diffusion of the surface deformation pattern seen in chapter 6, we model the post-rifting deformation as the viscoelastic response to the stress perturbation created by the 1975-1984 Krafla rifting episode. As we are interested in testing the effects of laterally heterogeneous rheological structure on the modeled displacements, semi-analytical methods will not work, and thus we rely on a finite element method (FEM) solution. The presence of strong lateral heterogeneities in the Icelandic lithosphere have already been suggested by seismic models (Staples et al., 1997; Brandsdottir et al., 1997; Allen et al., 2002b) and previous modeling of the plate spreading process along the Askja fissure swarm constrained by InSAR (Pedersen et al., 2009).

Viscoelastic sources of deformation are diffusive by nature and therefore will cause the surface deformation to decay in amplitude and broaden in space as time progresses. Stationary sources, such as continued diking at depth, however, are expected to result in a deformation pattern with constant geometry. This simple interpretation of stationary and

changing geometry is not strictly true, as gradients in viscosity can cause stationary displacement geometries during viscoelastic relaxation.

To illustrate the role of gradients in viscosity, we consider the force balance for a quasi-static material (Chandrasekharaiah & Debnath, 1994):

$$\overline{\nabla} \cdot \overline{\overline{\tau}} = -\rho \overline{g}, \tag{7.1}$$

where $\overline{\overline{\tau}}$ is the stress tensor, ρ is the density, and $\overline{g}$ is the gravitational force. Then, for a Newtonian viscous fluid, we have the constitutive law

$$\overline{\overline{\tau}} = -p\overline{\overline{I}} + \eta \overline{\overline{\dot{\epsilon}}}, \tag{7.2}$$

where p is the pressure, $\overline{\overline{\dot{\epsilon}}}$ is the strain rate tensor, and η is the viscosity. If the viscosity is a function of space, $\eta = \eta(x, y, z)$, then when we combine Equations 7.1 and 7.2 we get

$$\eta \overline{\nabla} \cdot \overline{\overline{\dot{\epsilon}}} = -\rho \overline{g} + \overline{\nabla} p - \overline{\nabla} \eta \cdot \overline{\overline{\dot{\epsilon}}}. \tag{7.3}$$

It is evident that gradients in viscosity act as apparent sources of deformation just as gradients in pressure do. This is true only when the strain rate is non-zero, i.e., the deformation must "probe" the gradients in material properties to detect them.

Previous modeling efforts of the Krafla post-rifting deformation have only considered vertically stratified rheological models with flat laying material boundaries. Foulger et al. (1992) and Heki et al. (1993) modeled the 1987 and 1990 post-rifting GPS data with an elastic layer over a Newtonian viscous channel using an infinitely long dike (Foulger et al., 1992) and a finite length dike (Heki et al., 1993), while the studies of Pollitz & Sacks (1996)

and Hofton & Foulger (1996) explored three-dimensional, but still laterally homogeneous, viscoelastic models of the Icelandic lithosphere.

Pollitz & Sacks (1996) used a spherical model of an elastic crust over two viscoelastic layers. The elastic crust is 12 km thick and the rifting extends through the entire layer. Between 12 km and 20 km they assume a viscoelastic standard linear solid, underlain by a Maxwell viscoelastic solid. They invert their model for the amount of displacement across the Grímsey fault in the Tjörnes Fracture Zone (TFZ) and the amount of opening on the Askja and Krafla rifts. They perform a grid search using 25 different rheological parameter combinations; their preferred model having a crustal viscosity of 3.3×10^{19} Pa s and a mantle viscosity of 3.3×10^{18} Pa s.

Hofton & Foulger (1996) used a forward model of a dike rupturing an elastic layer (10 km thick) overlying a Maxwell viscoelastic half-space. They divide the Krafla rift into four segments and define the amount of opening on each segment *a priori*. Several values for the viscosity of the half-space were tested against the campaign GPS data and the best fit, in the least squares sense, was 1.1×10^{18} Pa s.

Pedersen et al. (2009) compared models of stretching Icelandic lithosphere at the Askja rift to InSAR deformation from a single look geometry. Their models consisted of an elastic layer overlaying a Maxwell viscoelastic layer. Their best fitting models had a boundary between the elastic and viscoelastic layers that shallow towards the rift axis over a distance of 5 to 10 km and a weak elastic wedge below the rift axis. They, however, did not include any rifting events in their model, only far-field plate tectonic stretching.

We generate a number of models to explore the effect of various distributions and values of viscosity in the lithosphere on post-rifting surface displacements. We consider both two-dimensional and three-dimensional models. The two-dimensional models approximate the

NVZ assuming longitudinal homogeneity in structure and rifting. We assume that much of the dynamics of the post-rifting deformation is captured in the two-dimensional assumption and that most of the horizontal rheological heterogeneity is in the rift-perpendicular direction. These two-dimensional models are useful for testing a large range of model parameters quickly in order to build an intuition about the controls on post-rifting behavior and what classes of models approximate the deformation observed via InSAR. We use three-dimensional models as a more realistic representation of the rifting process.

7.2 The Structure of the Icelandic Lithosphere

Most recent seismic studies of the Icelandic crust support the model of a cold, thick crust. The Faroe-Iceland Ridge Experiment (FIRE) seismic line across the Northern Volcanic Zone (NVZ) (Staples et al., 1997) suggested a 20 km thick crust beneath the Krafla volcano, thickening to 35 km beneath the older Tertiary crust several tens of km away from the rift zone. S-to-P-wave arrival times give a Poisson's ratio of 0.27 ± 0.01 and steep Moho topography indicate that the lower crust is at sub-solidus temperatures (below 800°C). Menke et al. (1995) found low seismic attenuation ($Q \sim 500$) in the mid to lower crust of south-western Iceland indicating the absence of significant melting in the crust. Focusing on the crustal structure near the Krafla volcano, Brandsdottir et al. (1997) found that S-wave propagation through the lower crust indicates very little melt except in the shallow magma chamber.

The competing Icelandic model is the thin-hot-crustal model. Beblo et al. (1983) located a 5 km thick low-resistivity zone at 10 km depth under the NVZ deepening to 20 – 30 km away from the rift zone. This low resistivity zone is seen as evidence of a partially molten layer (5% – 20% melt) underlying most of Iceland. The resultant low viscosity zone is

thought to decouple the crust from the mantle and cause jumps in the rift zone (Bjornsson, 1985). Björnsson (2008) argues that the surface temperature gradient, depth of seismicity, and magnetotelluric data favor a thin crust model and that the reflectors interpreted to be the Moho are possibly melt pockets in the mantle. While most seismic studies agree on P-wave velocities of 7.4 km/s below 10 km depth (Allen et al., 2002b), some interpret this velocity to be hot mantle material (e.g., Tryggvason, 1962; Angenheister et al., 1980) as opposed to lower crust.

Tomographic modeling of the crust using the HOTSPOT-SIL networks (Allen et al., 2002b) produced a model of crustal velocity and crustal thickness for all of Iceland with a 50 km horizontal resolution. This model has the thinnest crust (15 – 20 km) beneath Krafla, the Reykjanes Peninsula, and just east of the western fjords. The thickest crust is found in central Iceland beneath the Vatnajökull ice cap in the EVZ. S-wave velocities are anomalously low at 10 km beneath most volcanoes in southern Iceland. At deeper depths (30 km), low velocities are constrained to a 150 km wide cylinder below central Iceland, interpreted to be a magma plumbing system connecting the mantle upwelling to magma chambers at 10 km depth (Allen et al., 2002b).

Although estimates of dike heights for the 1975-1984 Krafla Fires, based on the volume change calculated for the the central caldera, are 2.4 – 2.8 km, it is possible that larger dikes could have been feed by a deeper magma source (Bjornsson, 1985). Using EDM data from before and after the final large fissure eruption of the Krafla Fires, Árnadóttir et al. (1998) inverted diking source parameters and concluded that a dike extending from the surface to 7 km depth was emplaced. Gudmundsson (1983) estimated dikes in eroded dike swarms in eastern Iceland to be approximately 10 km tall. Furthermore, if the rifting events in the NVZ do not rupture the entire elastic upper crust, then another mechanism must be

introduced to accommodate the divergent motion across Iceland. Based on the arguments presented above, we assume diking to extend from the surface to 10 km depth in our models.

While magma chambers in the EVZ are thought to be at 10 km depth (Allen et al., 2002b), magma chambers in the NVZ beneath Askja and Krafla are much shallower (approximately 3 km) (e.g., Einarsson, 1978; Tryggvason, 1986, 1989; Brandsdottir & Menke, 1992; Camitz et al., 1995; Brandsdottir et al., 1997). Crustal formation by passive melting may form the crust in the NVZ while the thicker crust in central Iceland could be caused by enhanced melting driven by deeper mantle upwelling (Darbyshire et al., 2000). As mentioned above, if dikes emplaced during the latest Krafla event are taller than 3 km, an additional source of magma in addition to the shallow Krafla magma chamber is required. Additionally, each dike emplacement episode during the Krafla Fires was accompanied by deflation of the Krafla magma chamber and followed by inflation of the magma chamber Tryggvason (1984) – a ready source of magma is required to re-pressurize the magma chamber between diking events.

A low velocity zone is detected in the lower crust 10 – 15 km, possibly due to near-solidus temperatures or partial melt; though, due to the propagation of S-waves through the lower crust, the amount of melt is thought to be small and it is not interconnected. Higher temperatures below the neovolcanic zone north of the Krafla volcano are indicated by an anomalously high V_p/V_s ratio of 1.88 (Darbyshire et al., 2000). The FIRE seismic survey (Brandsdottir et al., 1997) found a high P-wave velocity "chimney" below the Krafla volcano. Menke et al. (1998) found that this chimney extends 50 km along the strike of the Krafla rift. Modeling Bouguer gravity anomalies guided by seismic structure gives a density contrast across the Moho in the NVZ of 120 kg/m^3 directly beneath the rift zone and 190 kg/m^3 $\sim$50 km away from the rift zone (Staples et al., 1997). The low density in

the mantle directly below the rift zone being attributed to increased temperatures.

It may be useful to draw parallels between the structure of the NVZ and other rift systems. Wright et al. (2006) and Keir et al. (2009) found evidence from GPS and InSAR measurements for deep magma accumulation during the recent rifting of the Dabbahu segment, Afar. Seismic studies have suggested the presence of melt lenses in the crust at the Reykjanes Ridge and the Mid-Atlantic Ridge near the Azores, and low P-wave velocities at the Mid-Atlantic Ridge at 35°N may be due to low amounts (3 %) of melt located in the lower crust (Dunn & Forsyth, 2007). Tomographic imaging of a segment of the Mid-Atlantic Ridge revealed a possible magma plumbing system in the lower crust consisting of two 10 km diameter, vertical cylinders with a -0.4 km/s P-wave velocity anomaly (Magde et al., 2000). Magde et al. (2000) estimated the cylindrical anomalies are due to a small percentage of melt and are part of the magma pluming system that feeds the rift.

7.3 Methods

In order to model post-rifting viscoelastic relaxation we use the PyLith finite element program developed by the Computational Infrastructure for Geodynamics (Williams et al., 2005; Williams, 2006; Aagaard et al., 2007, 2008). PyLith has the ability to model elastic and linear Maxwell viscoelastic materials. For both two-dimensional and three-dimensional problems we employ linear hexahedral elements ("bricks"). Two-dimensional models are implemented via a single layer of elements and plane strain boundary conditions.

The majority of widening during the Krafla Fires occurred episodically over five years (Tryggvason, 1984). In the models presented here, we condense all widening episodes to a single event in January 1979, approximately the peak period of deformation (Figure 5.4). By changing the time scale, this simplification may introduce a systematic error in the

estimation of the absolute values of the relaxation times and therefore the inferred value of the viscosities.

Rift opening is implemented using the cohesive element fault formulation; cohesive elements are zero-volume cells that allow for relative fault displacement (both slip and opening) by adding additional degrees of freedom to the finite element model. Fault opening is imposed kinematically at a predetermined time and specified to be purely perpendicular (i.e., no slip is imposed on the cohesive elements). Formation of additional crustal material from magmatisim is not addressed in the models presented here. The amount of opening used is based on Tryggvason's (1984) estimates of surface displacements. We would expect the amount of opening to vary with depth – indeed, the peak widening of the Dabbahu event in the Afar is estimated to be at 5 to 6 km depth (Wright et al., 2006). However, for this study we make the simplifying assumption that the widening is uniform with depth. No gravitational body forces are included in the models.

7.3.1 Model Spin-up

Before modeling the viscoelastic response to the most recent Krafla rifting event, the model must be spun-up to a cycle invariant state. Viscoelastic materials have a memory of past perturbations (e.g., rifting events). The actual Icelandic lithosphere before 1975 did not exist in a state with zero stress. The need to spin-up a model with repeated rupture events has been recognized by several authors (e.g., Reches et al., 1994; Hager et al., 1999; Kenner & Simons, 2005; Hetland & Hager, 2006a). The spun-up state is achieved when each rifting cycle is indistinguishable from the previous one.

Figure 7.1 demonstrates the change in surface velocities at the same relative time in the rifting cycle for several events in a sequence for a simple, vertically stratified model.

The number of events needed to reach a steady state depends on the viscosity; in fact, the number of events needed to reach steady state scales inversely with the Savage parameter, $\tau_o = T/2\tau_m$, where T is the inter-seismic or inter-rifting time interval and τ_m is the Maxwell relaxation time of the system (Hetland & Hager, 2006a).

We take advantage of the fact that we use linear material models in order to spin-up the problem in a computationally efficient way (section 2.4.1). We calculate a spatio-temporal Green's function response to a single rift event by running the model with no tectonic loading and a unit opening displacement imposed on the fault at the first time step. The model is run for thousands of model years to ensure that all transient deformation has ceased. The spatio-temporal Green's functions are then scaled to the desired size of the rifting events, time shifted, and summed to form a periodic event sequence. Tectonic loading is added using the results of a model with steady state velocity boundary conditions and no rifting event.

7.4 Two-Dimensional Models

7.4.1 Two-Layer Models

Figure 7.2 represents the geometry and boundary conditions of the two-dimensional, two-layer models. The lithosphere consists of a 10 km elastic layer (referred to as layer 1) over a 300 km Maxwell viscoelastic layer (referred to as layer 2). The active rift extends from the surface to 12 km depth. The top boundary is free, the bottom and side boundaries are free slip (zero shear traction), and a constant perpendicular spreading velocity (i.e., tectonic loading) is applied to both side boundaries. Models of an elastic layer over a homogeneous viscoelastic layer are tested along with variants containing local heterogeneities. These

heterogeneities take the form of viscoelastic anomalies and/or elastic weak zones in the upper 10 km (Figure 7.2, insets a and b). In section 7.4.2 we investigate models with longer wavelength heterogeneities and a material boundary based on the location of the Moho from seismic data. See table 7.1 for nominal values of the elastic parameters.

7.4.1.1 Laterally Homogeneous Models

We first test simple models with no lateral heterogeneities and flat laying material boundaries (the "base" model in Figure 7.2). The velocities for models with a range of viscosities for layer 2 are compared to the two-dimensional velocity profiles estimated in Chapter 6 (Figure 7.3). None of the tested laterally homogeneous models are able to match the shape of the deformation field. Comparison to rift-perpendicular GPS velocities for 1987 to 1992 from Hofton & Foulger (1996) (Figure) indicate a model with a viscosity of 10^{19} Pa s may fit, but comparison to vertical velocities is difficult due to the large error on those data.

While none of the laterally homogeneous models are able to match the pattern of deformation observed in the NVZ by InSAR, we can use these results to estimate a gross viscosity – i.e., the viscosity that dominates the relaxation rate of the system. Over the width of the interferograms, the vertical velocities given by the two-dimensional velocity inversion vary by approximately 1 cm/yr (Figure 6.8). From the MInTS time series we have determined that velocities are largely constant over the time period of InSAR data acquisition, 1992 – 2007 (Figure 6.14). In Figure 7.5 we show the evolution of velocities from 1992 – 2004 for the laterally homogeneous models. The model with a viscosity of 10^{19} Pa s comes closest to matching the observed velocities and largely linear displacement rate. For the elastic parameters we have assigned to the materials a viscosity of 10^{19} Pa s corresponds to a Maxwell relaxation time of approximately 15 years. This estimation is made with the

caveat that a laterally homogeneous model is not the appropriate representation of the Icelandic lithosphere. A lithosphere with multiple viscosities will have multiple relaxation time scales, rather than a single average relaxation time (Hetland & Hager, 2006b); however, we expect the dominant relaxation time to be similar to the laterally homogeneous model with a viscosity of 10^{19} Pa s.

The time period of our observations is limited and that, in turn, limits our ability to resolve the decay times of the lithosphere in response to rifting at Krafla. Models with short relaxation times have, for the most part, finished the post-rifting phase of their cycle, while models with large relaxation times deform slowly on the time scale of the observations and therefore do not exhibit much displacement (Figure 7.6). Models with relaxation time scales that are quite different (large or small) compared to the scale of observation time appear similar to each other.

7.4.1.2 Heterogeneous Structure Below Fissure Swarm

The persistent, localized deformation north of the Krafla volcano observed in the InSAR measurements suggests a local rheological gradient (Equation 7.3). The long duration of the rifting at Krafla is anomalous when compared to historic rifting at the Askja fissure system in the NVZ (Tryggvason, 1984) and both the 1978 (Doubre & Peltzer, 2007) and 2005 rifting in the Afar (Wright et al., 2006). Tryggvason (1984) suggests that the anomalously long duration of the rifting at Krafla may be due to a high viscosity zone below the brittle crust limiting the rifting rate. Local heterogeneities in elastic strength may be present along the rift axis due to the faulting and diking in the fissure swarm. In addition, the magma plumbing system that supplies the dikes and shallow magma chamber (as yet, not well understood) may modify rheological properties in the crust.

Adding a shallow viscosity anomaly to the nominally elastic layer 1 (Figure 7.2a) produces a double-lobed deformation pattern in the vertical velocity similar to that measured by InSAR (Figure 7.7). The lobes occur at approximately the location of the edges of the anomaly. If the anomaly is narrower than approximately 10 km the bulges positively interfere, removing the zone of negative vertical velocities. This interference places a lower bound on the width of the proposed viscosity gradient.

If the anomaly has a different viscosity from that of layer 2, the velocity bulges occur farther apart and the negative vertical velocity valley becomes larger. There is a trade-off between r, the ratio of the viscosity of the anomaly to the viscosity of layer 2, and W_a, the width of the viscosity anomaly (Figure 7.8).

We test our assertion that the viscosity anomaly must be near the surface to have the desired double-lobe effect. In Figure 7.9 we show the difference between the surface velocity for a model with a shallow viscosity anomaly and one with the viscosity anomaly buried in layer 2. Burying the anomaly deeper than 10 km (i.e., placing it in layer 2) dramatically changes the observed pattern of vertical deformation.

A narrow viscosity anomaly will not create the narrow (approximately 4 km) depression seen in the data. Adding a narrow elastic weak zone (EWZ) (Figure 7.2b), however, creates such a feature due to the excess thinning of a weak elastic structure caused by tectonic stretching (Figure 7.10). We define the EWZ by a reduction of the elastic moduli a factor of four (table 7.1). To construct these models we have added an EWZ to the favored viscosity anomaly model ($\log(r) = 1$, $\eta_2 = 10^{19}$ Pa s); the results are then compared to the two-dimensional InSAR velocity inversion results. Comparison to GPS data does not help distinguish models due to lack of vertical precision in the GPS data (Figure 7.11).

From the results presented in this section it is clear that models are primarily distin-

guished by their vertical velocities. Horizontal velocities do not differ much from one model to the next. This sensitivity to vertical deformation makes the InSAR observations particularly valuable for investigating post-rifting phenomena, as the current satellite based radar systems have viewing geometries that are highly sensitive to vertical deformation.

7.4.2 Models with Dipping Moho

The models presented so far have not been able to match the broad curvature covering the entire width of the InSAR profiles in the vertical velocities. Presumably, a correspondingly large wavelength feature in the rheological structure of the lithosphere is necessary to produce the large wavelength deformation. To this end, we have tested models with two viscoelastic layers (the lower crust and the upper mantle) overlain by a thin elastic layer (the upper crust). Using a rift-perpendicular profile 15 km north of the Krafla caldera of the Moho depth determined by Allen et al. (2002b), we developed a two-dimensional "thick crust" model (Figure 7.12). The thick crust model is compared to a "thin crust" model created by translating the Moho surface 10 km closer to the surface. In addition, "strong" crust models where $\eta_{lc} > \eta_m$ are compared to "weak" crust models in which $\eta_{lc} < \eta_m$, where η_{lc} is the viscosity of the lower crust and η_m is the viscosity of the mantle lithosphere. See Table 7.1 for values of the elastic moduli for the dipping Moho models.

The difference between the thin crust and thick crust models is difficult to discern over the time period of InSAR observations. However, the difference between the strong crust models and weak crust model is readily apparent and the strong crust model is clearly favored by the data (Figure 7.13). The preference for strong crust models is also evident when the models are compared to the 1987 – 1992 GPS data from Hofton & Foulger (1996) (Figure 7.13).

7.5 Three-Dimensional Models

With three-dimensional models of the NVZ we are able to test if post-rifting, viscoelastic relaxation can account for the along-axis variations in deformation that are observed in the InSAR data. Our approach is to simplify the problem by assuming along-axis homogeneity in the rheological structure of the lithosphere. We also ignore the Askja rift system to the south and the TFZ to the north of the Krafla rift. The finite element model has a rift surface that extends across the entire model in the along axis direction and from the surface to 12 km depth (Figure 7.15). As in the two-dimensional dipping Moho models (section 7.4.2), the Moho surface is taken from Allen et al. (2002b), though we ignore along axis variations in Moho depth. The elastic parameters are the same as in the two-dimensional models (table 7.1), and the viscosities of the lower crust and upper mantle are 10^{19} Pa s and 10^{18} Pa s, respectively. For computational efficiency, the model is limited to a 200 km cube; as a result, the tectonic loading is not identical to the two-dimensional models which had a rift perpendicular extent of 1000 km. However, much of the difference is eliminated because for both the two-dimensional and three-dimensional models we remove a liner ramp from the surface displacements over the 80 km width of the InSAR data coverage.

We use the same spatio-temporal Green's function approach to spinning up the model as we do for the two-dimensional models. However, the amount of rifting during the last event is known to have varied along axis (Tryggvason, 1984). In order to avoid stress concentrations at the tips of the rift, we spin-up the model with events uniformly that rift the entire along-axis length of the crust. For the final event, we impose along-axis variation in opening displacement following measurements of the amount of rifting from Tryggvason (1984). In the actual Icelandic rift system, rifting tends to alternate so that a diking episode

will occur along a length of the rift that underwent little or no opening during the previous episode (Tryggvason, 1984).

Cumulative displacements from the three-dimensional FEM, viscoelastic model compared to those from the MInTS time series are shown in Figure 7.16. The broad shape of the post-rifting displacements observed in data are well matched by the model results. However, the model overestimates displacements at the north end of the Krafla fissure swarm where the NVZ meets the TFZ. The displacement in the southeast end of the displacement field, where the Krafla system overlaps with the Askja system, is underestimated.

There is also a narrow zone of negative velocities along the rift axis that the model does not match. The local subsidence along the Krafla axis has been attributed to post-rifting deformation (Sigmundsson et al., 1997), magma cooling (Sigmundsson et al., 1997; Henriot et al., 2001; de Zeeuw-van Dalfsen et al., 2004), and tectonic stretching of a weak elastic zone (Pedersen et al., 2009, this study). In our two-dimensional modeling we found that local heterogeneities in material properties result in the type of post-rifting displacements observed within 15 km of the rift axis. Therefore, we test a model that combines a dipping Moho with local, axially located rheological anomalies (Figure 7.17). We employ a 6 km deep, 10 km wide, 10^{18} Pa s viscosity anomaly embedded in a lower crust with a nominal viscosity of 10^{19} Pa s, and a 4 km wide EWZ, in which elastic moduli are reduced by a factor of four, extending from the surface to the Moho (see table 7.1 for the values of the elastic parameters).

Figure 7.18 compares the cumulative displacement of this dipping Moho/local heterogeneity model to the MInTS displacements. The magnitude and shape of the large eastern deformation lobe is improved over the model with only a dipping Moho; however, the model overestimates the axial subsidence. It may be that the elastic moduli of the putative elastic

weak zone are too low.

The three-dimensional models of the Icelandic lithosphere presented here are a simplified version of what is likely a complex lithosphere structure. Allen et al.'s (2002b) preferred model of crustal thickness shows thinning from the south end of the NVZ to the north where it meets the TFZ; though, we find that much of the variation in post-rifting deformation can be accounted for by the variable amount of opening imposed along axis in an axially homogeneous rheological model.

Ideally, a three-dimensional model would take into account the faulting in the TFZ and activity along the Askja fissure swarm. In the MInTS time series, we see deformation in the valley between the Askja and Krafla systems that is not captured in our models. The amount of post-rifting deformation modeled at the northern terminus of the Krafla rift is larger than what is observed in the InSAR data. The last significant earthquake in the TFZ was a M6.4 strike-slip event on the Grímsey Seismic Lineament in 1976, presumably in response to the rifting along the Krafla fissure swarm (Sigmundsson, 2006). We have also assumed that the amount of opening as a function of depth is constant over the entire length of the co-rifting segment. It may be that reducing the depth extent of diking at the northern end of the rift could improve the fit to data.

One challenge in attempting to model the interaction between fissure swarms and between fissure swarms and transform zones is dealing with stress concentrations that build up at crack tips. As a rift repeatedly opens an elastic crust, the stress built up at the crack tip must be relieved. An upper crust with an elasto-plastic rheology that allows for failure at the crack tip is one possible solution. The crack tips could also be linked to strike-slip fault structures to kinematically compensate for the dike tips, as is done by Pollitz & Sacks (1996).

7.6 Elastic Models

It is possible that continued aseismic dike intrusion is the cause of some or all of the post-rifting deformation we measure. Savage & Prescott (1978) observed that one can duplicate the surface deformation produced by viscoelastic, post-seismic relaxation using a distribution of slip on a localized fault in a purely elastic medium. We explore the possibility of continued diking using the Okada (1985) formulation for the surface displacements caused by an opening dislocation in an elastic half-space.

The elastic diking models have a large along-axis length relative to the size of the region of interest making them essentially two-dimensional models (geometrically similar to those in section 7.4). We used an opening rate of 4 cm/yr and varied both the depth to the top of the diking source, d_1, and the depth to the bottom of the diking source, d_2, to match the two-dimensional velocity field inverted from the InSAR data (Figure 7.19). The best fitting elastic diking models have a shallow depth to the top of the diking source (3 km) and large depth to the bottom of the diking source (40 km).

There is likely deformation throughout the crust and upper mantle causing the measured surface displacements. The question becomes: could part or all of the observed surface deformation be due to continued aseismic diking? It is not likely that very shallow diking has continued for the past several years without being detected by other means. In addition, we expect continued diking to largely occur at the tips of previously emplaced dikes (Buck et al., 2006); however, our modeling shows that much of the needed continued diking is at the same depth as the original dike emplacement. Additionally, in the along-axis direction, the post-rifting surface deformation is largest where the co-rifting displacement was largest (Figure 6.22). Of course, we cannot eliminate the possibility of deep, aseismic dike growth;

it is possible that the measured surface deformation is due to a combination of viscoelastic and elastic processes.

7.7 Discussion and Conclusions

We know from numerous seismic studies that the Icelandic lithosphere is highly laterally heterogeneous on the scale of rifting deformation (e.g., Brandsdottir et al., 1997; Staples et al., 1997; Menke et al., 1998; Darbyshire et al., 2000; Allen et al., 2002a). The modeling in this study demonstrates the impact that lateral heterogeneities in rheology, both on the scale of the Moho topography and the fissure swarm, have on surface deformation. Previous post-rifting deformation modeling (Foulger et al., 1992; Heki et al., 1993; Hofton & Foulger, 1996; Pollitz & Sacks, 1996) has ignored lateral heterogeneity.

We have employed a range of two-dimensional and three-dimensional viscoelastic models to test the effect of various viscosities, local heterogeneities, and Moho topography on the post-rifting surface deformation. The models were compared to surface deformation data obtained by InSAR. Models with relaxation times dominated by 10^{19} Pa s viscosity best matched amplitude of the velocity in the InSAR data. The best fitting two-dimensional models have a shallow ($\sim$ 6 km deep) viscosity anomaly in the lower crust that is approximately 10 km to 20 km wide with a viscosity lower than the surrounding material and a narrow ($\sim$ 4 km wide) weak zone that causes an axial depression due to tectonic stretching. We were able to match the large wavelength ($\gtrsim$ 60 km) deformation using a steeply dipping Moho topography from Allen et al. (2002b) and a lower crustal viscosity higher than the mantle viscosity thus supporting the model of a strong, thick Icelandic crust. Table 7.2 summarizes the results of the viscoelastic modeling performed in this study.

Using the results of the two-dimensional models to guide rheological structure, we use

three-dimensional models to explore along-rift variations in surface displacement. The three-dimensional models with a strong Moho topography and a shallow viscosity anomaly along the rift produce the double-lobed displacement field observed in the InSAR data. The data show an axial subsidence located from the southern end of the Krafla rift to just north of the Krafla volcano; however, the elastic weak zone model favored in the two-dimensional case overestimates this axial subsidence, particularly north of the volcano.

The simplified axial geometry of our three-dimensional models results in improperly modeling the displacements at the northern and southern ends of the Krafla rift. The displacement at the north end may be affected by earthquakes on the TFZ and/or changes in dike height at the terminus of diking. Displacements to the south of the Krafla volcano are affected by the interaction between the Krafla and Askja rift systems that is not modeled.

While we have not been able to fit all of the observed surface deformation with our models, the results presented here show the following: that viscoelastic relaxation is a likely deformation mechanism for the displacements seen in the InSAR data which indicate the existence of a shallow, diffuse weak zone, perhaps associated with the fissure swarm and its magma plumbing system; a steeply dipping Moho such as those modeled seismically by Staples et al. (1997) and Allen et al. (2002b); and a lower crust with a higher viscosity than the upper mantle. The fact that InSAR data is only available starting 11 years after the majority of the rifting was completed limits its ability to detect more rapid post-rifting deformation mechanisms, if they exist. The earlier GPS data (used by Foulger et al. (1992), Hofton & Foulger (1996), and Pollitz & Sacks (1996)) has poor vertical precision, limiting our ability to distinguish among different post-rifting models. The GPS data has an additional disadvantage of having sparse coverage: 10 km near the rift, and 100 km at a distance of 100 km from the rift (Hofton & Foulger, 1996).

The shallow viscosity anomaly below rift suggests a diffuse magma network in addition to the known shallow magma chamber, similar to the findings of Pedersen et al. (2009). The generation of crust at multiple depths is supported by geochemical evidence. Clinopyroxene compositions in rocks from northern Iceland indicates that crystallization has occurred over a large range of depths in the crust and upper mantle (Darbyshire et al., 2000).

The high viscosity of the lower crust agrees with recent seismic data showing a V_p/V_s ratio near 1.76 (Brandsdottir et al., 1997; Menke et al., 1998) and a shear wave quality factors in the 100 – 1500 range (Menke et al., 1995), suggesting sub-solidus temperatures. As for the origin of the low resistivity layer that has previously been attributed to large percentages of partial melt at the top of a shallow mantle (Bjornsson, 1985; Björnsson, 2008), Gaillard et al. (2008) propose that small amounts of carbonate melts (0.035 – 0.35 volume %) could cause the low resistivity measured at 60 km depths in the Pacific Ocean mantle. Molten carbonates are 1000 times more conductive than molten silicates at 1000°C. The resistivities measured in the Pacific are comparable to the resistivity of the layer measured in Iceland by Beblo et al. (1983).

Neither Hofton & Foulger (1996) and Pollitz & Sacks (1996) spin-up their viscoelastic models. Hofton & Foulger (1996) include historic rifting and seismic events, but they do not formally address the issue of spin-up. Both Pollitz & Sacks (1996) and Hofton & Foulger (1996) account for the recent earthquake on the Grímsey fault which the three-dimensional models in this study do not. Neglecting of transform faulting in the NVZ may be the reason our models overestimate displacements at the north end of the NVZ.

Pedersen et al. (2009) use laterally heterogeneous viscoelastic models to study the inter-rifting deformation in the NVZ, primarily at Askja which last underwent a rifting event in 1874. The rheological structures they test are similar to the locally heterogeneous models

presented here. However, the only loading they impose on the model is due to tectonic stretching – there are no rifting events. Large post-rifting velocities at Askja will have dissipated by now, but the effects of such an event will affect velocities throughout the rifting cycle. Meade & Hager (2004) showed that in a viscoelastic system, velocities are anomalously high immediately after an earthquake and anomalously low in the period proceeding the next earthquake. This must be true based on kinematic arguments that the displacements over many earthquake or rifting cycles will result in block displacement. Ignoring the effect of rifting events on velocities late in the rifting cycle will cause an underestimation of the magnitude of the rheological gradients.

de Zeeuw-van Dalfsen et al. (2004) propose that the broad, double-lobed deformation field observed in the InSAR data, which we have attributed to viscoelastic relaxation, can be modeled by an elastic, isotropic point source – a Mogi source (Mogi, 1958). This inflating source is interpreted to be magma accumulation in a deep magma chamber at the crust-mantle boundary. Our own work has shown that an elastic opening source is able to produce modeled ground deformations that agree with the InSAR data. The locus of the identified source could be an indication that either elastic or anelastic deformation sources are active in that region of the lithosphere. By the correspondence principle (Nur & Mavko, 1974), if there is an elastic source that provides a given surface displacement, then a viscoelastic solution can also be found. de Zeeuw-van Dalfsen et al. (2004) assume that the observed deformation cannot be primarily due to post-rifting, viscoelastic relaxation based on the estimated velocities from Pollitz & Sacks's (1996) preferred viscoelastic model of the Icelandic lithosphere. The model of Pollitz & Sacks (1996) provides vertical velocities of only 2 mm/yr; however, we have shown that alternative post-rifting, viscoelastic models can exhibit much larger velocities.

Glacial rebound observations and modeling indicate an average viscosity for the mantle of $10^{18} - 10^{19}$ Pa s (Sigmundsson, 1991; Sigmundsson & Einarsson, 1992). Using GPS measurements, Árnadóttir et al. (2009) find a best fit glacial rebound model using a 10 km elastic layer over a 30 km thick Maxwell viscoelastic layer with a viscosity of 10^{20} Pa s over a Maxwell viscoelastic half-space with a viscosity of 10^{19} Pa s. It must be noted, however, that post-glacial rebound is probing the viscosity structure of the crust and mantle at longer wavelengths than post-rifting relaxation and may not be directly related to the estimates of viscosity from post-rifting studies.

The favored model presented here is done with the knowledge that there is not a unique solution for the best fitting rheological structure of the lithosphere when comparing viscoelastic relaxation models to surface deformation data. The large differences in the favored models of Hofton & Foulger (1996) and Pollitz & Sacks (1996) show that more than one model can satisfactorily fit a particular data set. We present these results as a first best guess as to the lateral heterogeneities in the rheological properties of the Icelandic lithosphere. The particular models tested are guided by independent geophysical data described in Section 7.2. This study is not a formal inverse approach, but instead a test of several forward models to understand how particular rheological features control the surface deformation and to begin to constrain likely model parameters such as approximate structures and gross relaxation rates. When approaching a non-unique problem, such as this one, one requires *a priori* knowledge to constrain the possible parameter space. In the Northern Volcanic Zone of Iceland, this is possible thanks to the large amount of previous geophysical and geological work that has been done.

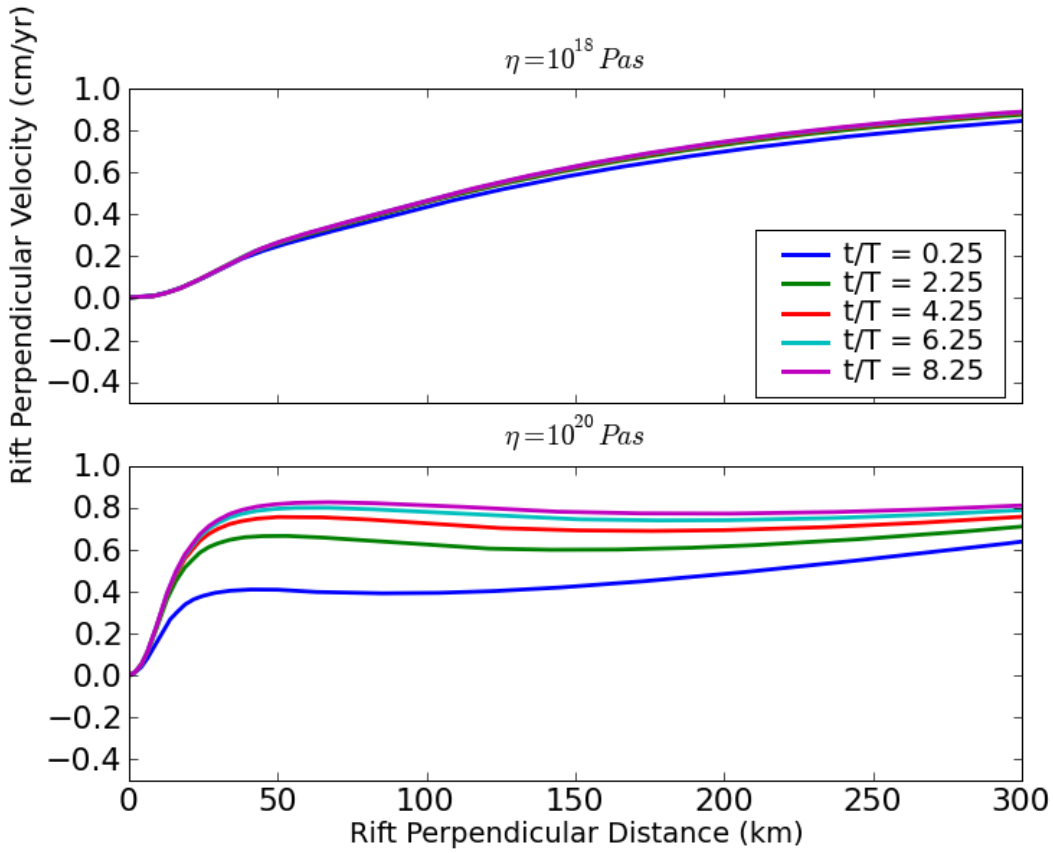

Figure 7.1: Spin-up of two models with homogeneous viscosity structures. The velocity at 1/4 of the way through the rift cycle for 5 cycles is plotted. Top: model with a viscosity of 10^{18} Pa s. Bottom: model with a viscosity of 10^{20} Pa s. Systems with low viscosity (short relaxation time) require fewer rift cycles to reach steady state then systems with high viscosity (large relaxation time).

Figure 7.2: Two-dimensional FEM model of Icelandic lithosphere with flat material interfaces. The model consists of a 10 km thick elastic layer (layer 1) over a 290 km Maxwell viscoelastic layer (layer 2). The rifting surface, represented by the red line, penetrates the entire elastic layer. Constant tectonic loading of 2 cm/yr (full rate) is applied to the ends of the model. All boundaries are free slip, except the top which is completely free. Two modifications to the basic two-layer model are shown in the insets. In both (a) and (b) a viscoelastic anomaly penetrates the upper elastic layer. r is the ratio of the viscosity of the anomaly to the viscosity of layer 2. Model (b) has both a viscoelastic anomaly and an elastic weak zone (EWZ) through the entire elastic layer. Note that the figure is not to scale.

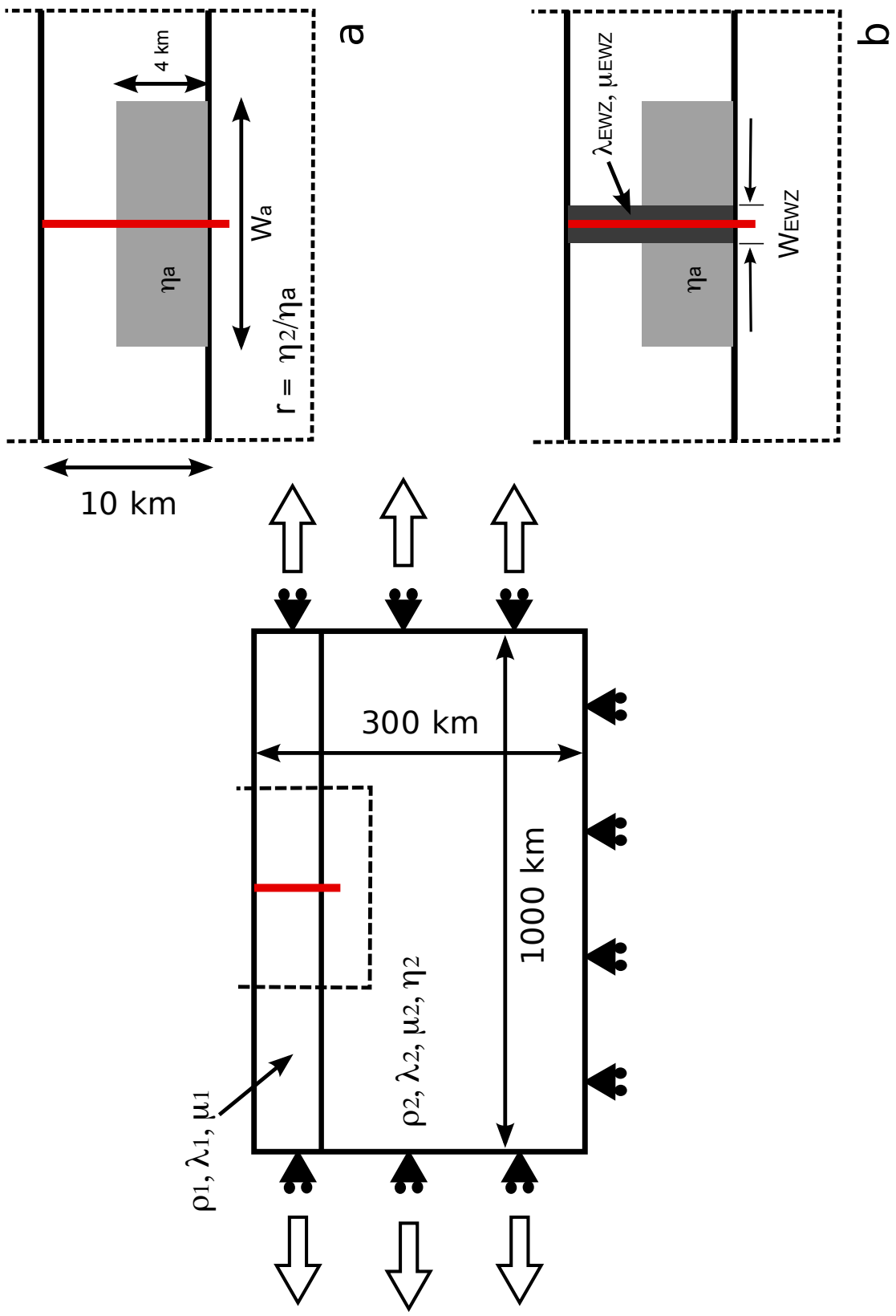
a
4 km
W_a
η_a
$r = \eta_2/\eta_a$
10 km
b
λ_{EWZ}, μ_{EWZ}
w_{EWZ}
η_a
300 km
1000 km
$\rho_2, \lambda_2, \mu_2, \eta_2$
ρ_1, λ_1, μ_1

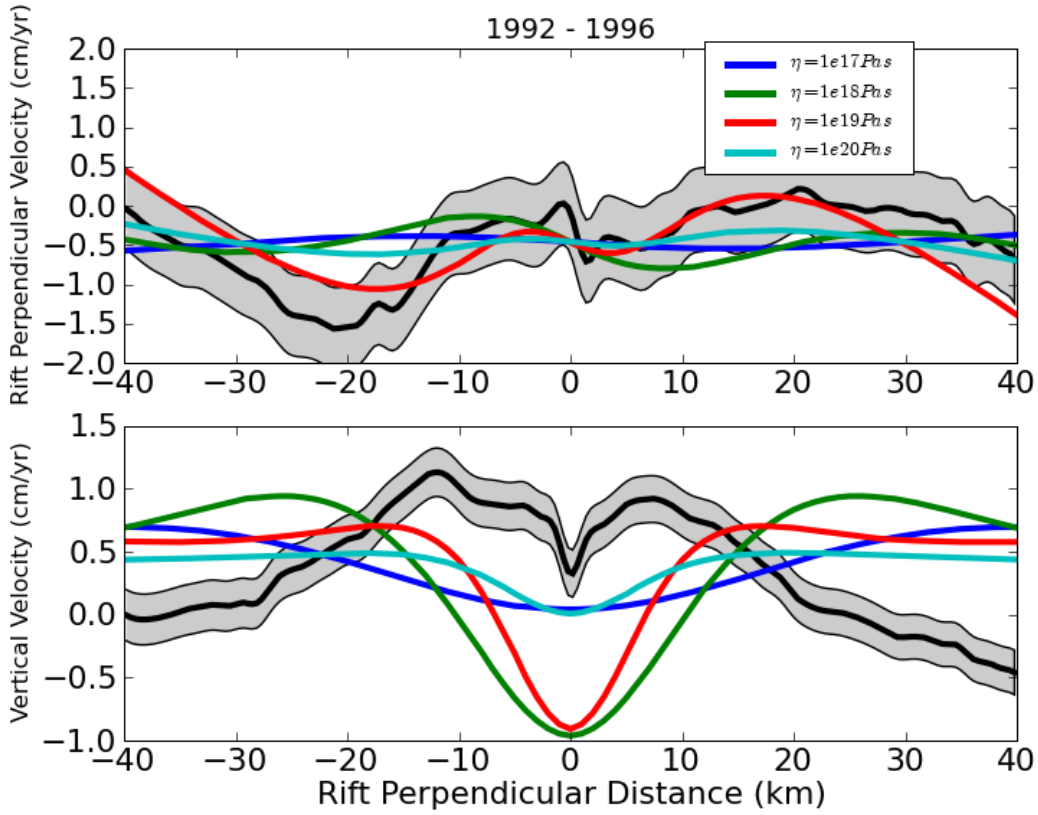

Figure 7.3: Horizontal and vertical velocities for laterally homogeneous models (base model in Figure 7.2). The velocities from the InSAR measurements are plotten in black with one standard devaiation error. Mean velocities for the period 1992 – 1996.

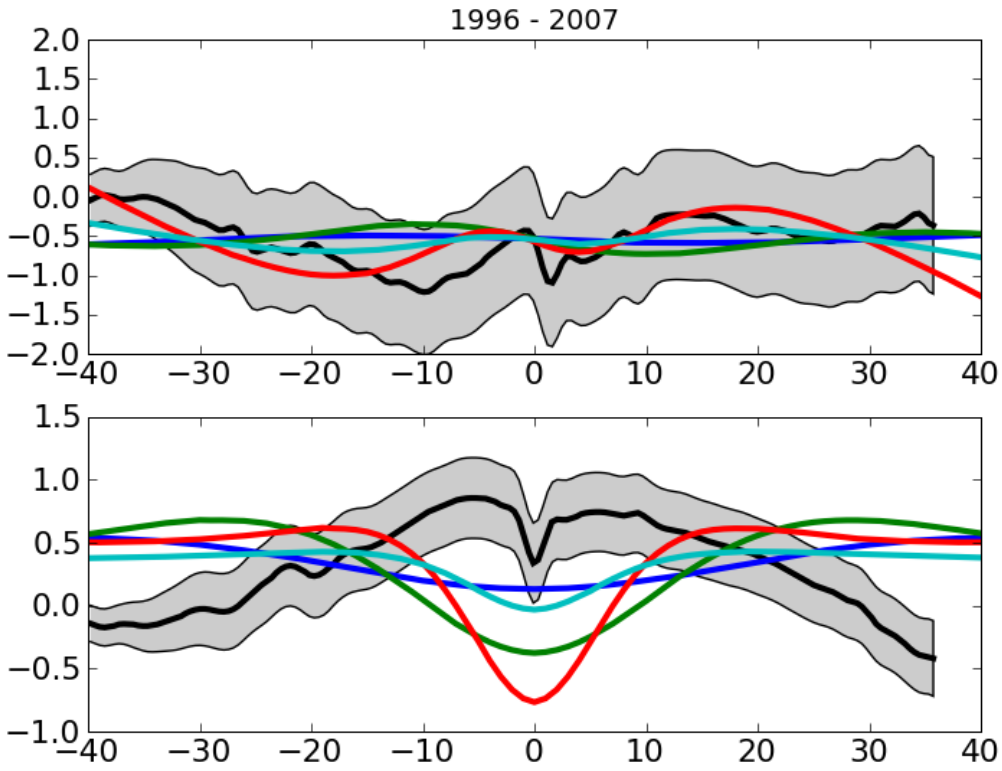

Figure 7.3: Cont. Mean velocities over the period 1996-2007 plotted with InSAR velocities in black.

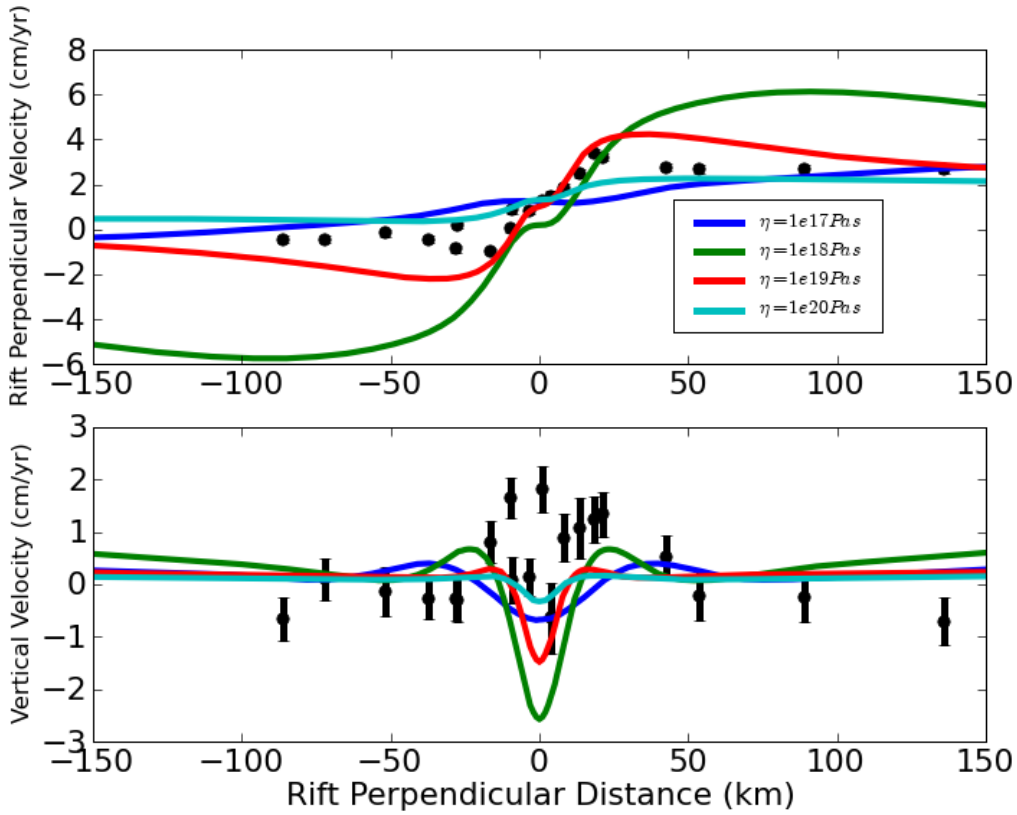

Figure 7.4: Same as Figure 7.3 with compairison to GPS data from Hofton & Foulger (1996) (in black with one standard deviation errors). Mean velocities over 1987 – 1992 are shown.

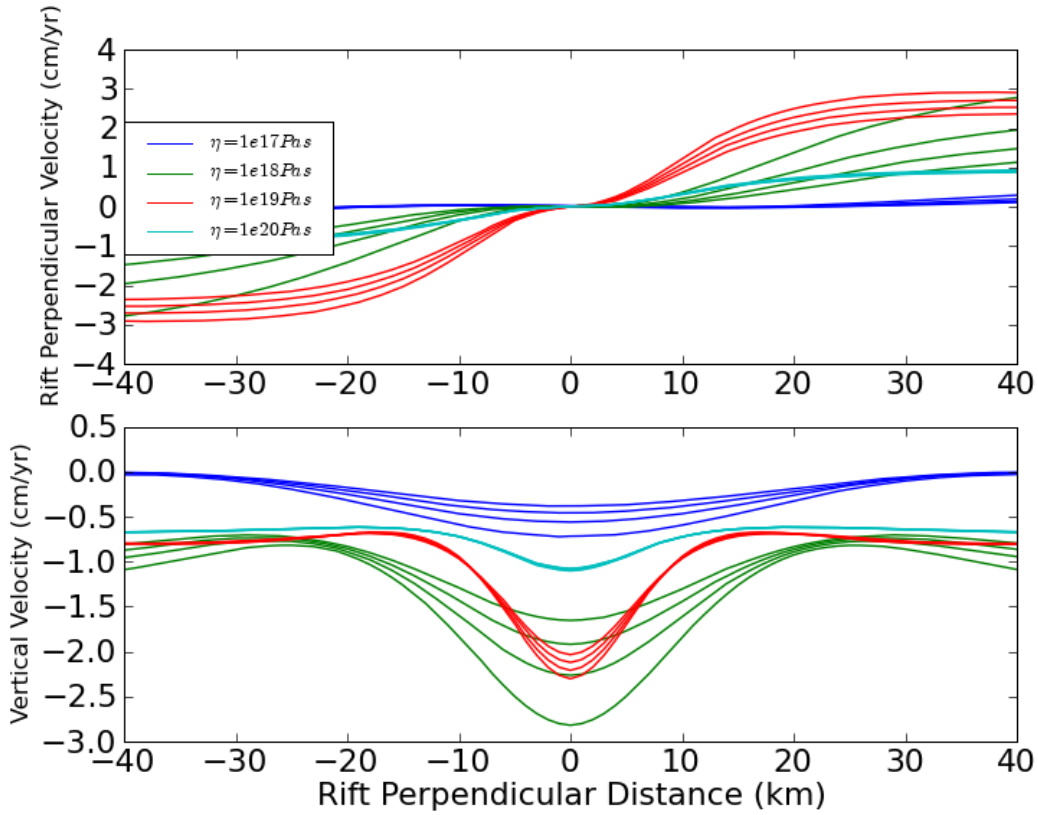

Figure 7.5: Mean velocities (averaged over a three year period) from 1992 to 2004 for laterally homogeneous models.

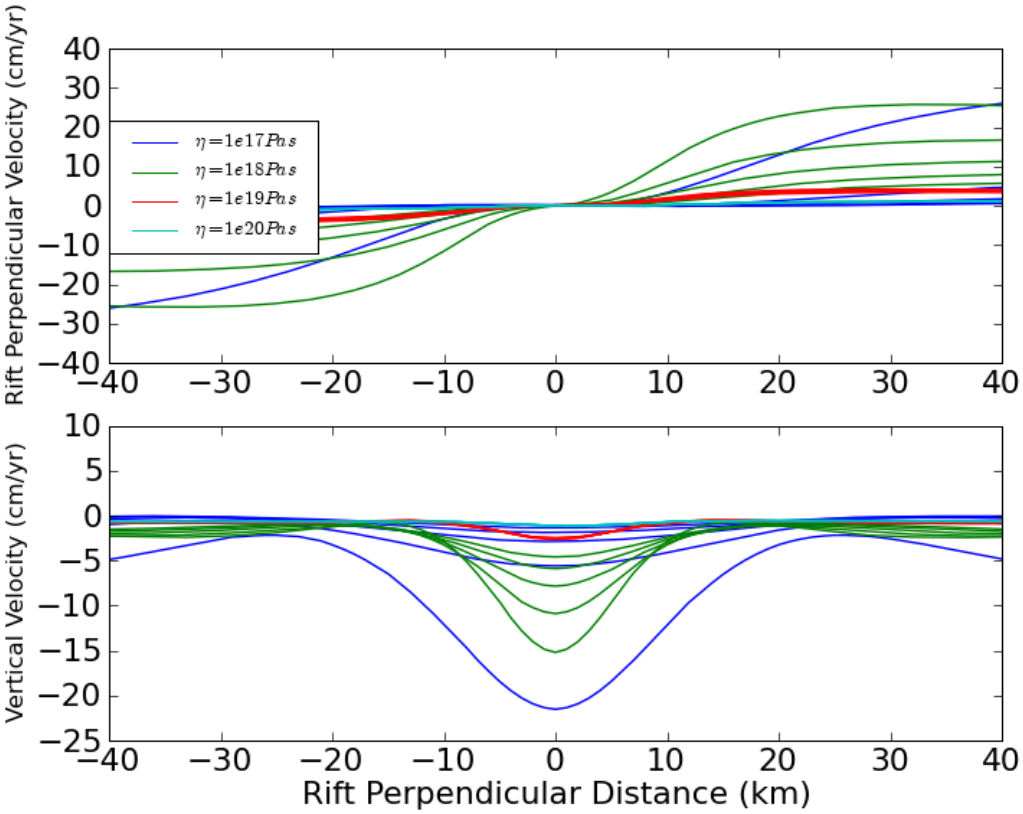

Figure 7.6: Early post-rifting deformation models with a laterally homogeneous viscosity structure. The average velocity for each year, in each of the first eight years of the post-rifting period, is plotted.

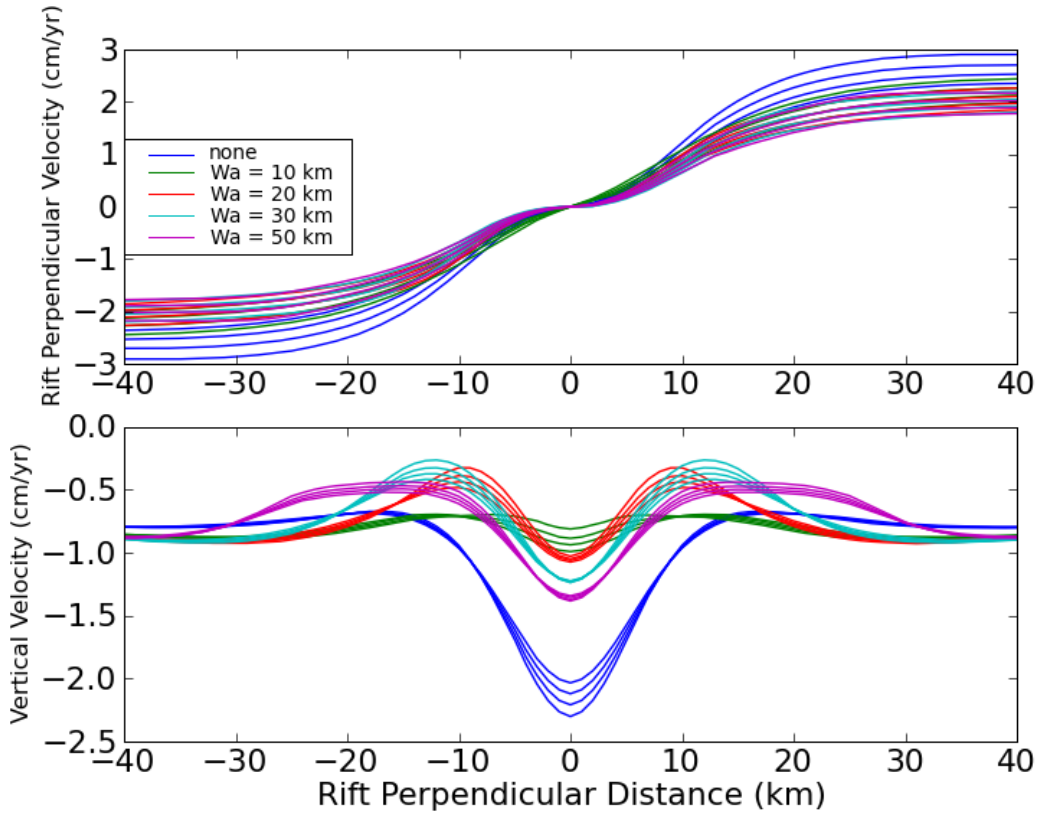

Figure 7.7: Velocities of models with a viscous anomaly in layer 1 (Figure 7.2a). Models with various widths of the anomaly, W_a are shown. A uniform viscosity of 10^{19} Pa s for both η_2 and η_a was used. The mean velocity over a three year period is plotted for every three years in the time span 1992 – 2004.

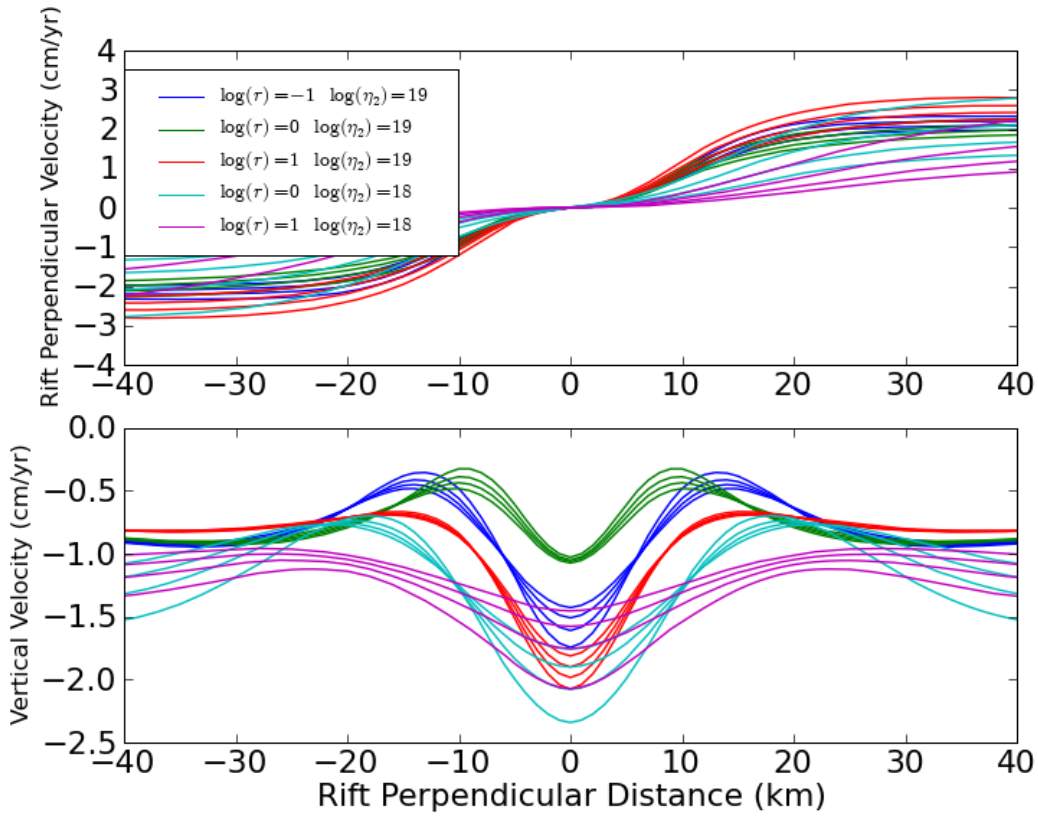

Figure 7.8: Similar to Figure 7.7 with the width of the viscosity anomaly fixed at 20 km and several viscosities tested. r is the ratio, η_a/η_2, of the viscosity of the anomaly to the viscosity of layer 2.

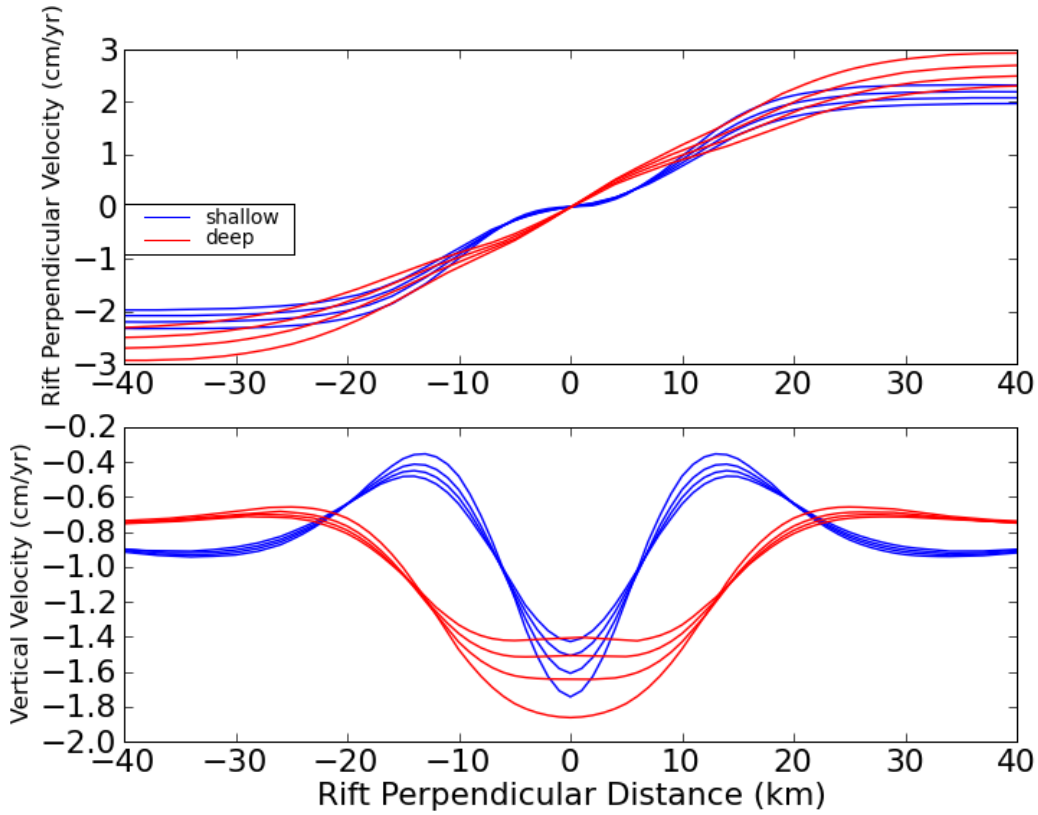

Figure 7.9: Comparison of model with a viscosity anomaly in layer 1 ("shallow", Figure 7.2a) to a model with a viscosity anomaly of the same dimensions in layer 2 ("deep", not drawn). The width of the anomaly is 20 km and $\log \eta_a/\eta_2 = -1$, where η_a is the viscosity of the anomaly and η_2 is the viscosity of layer 2.

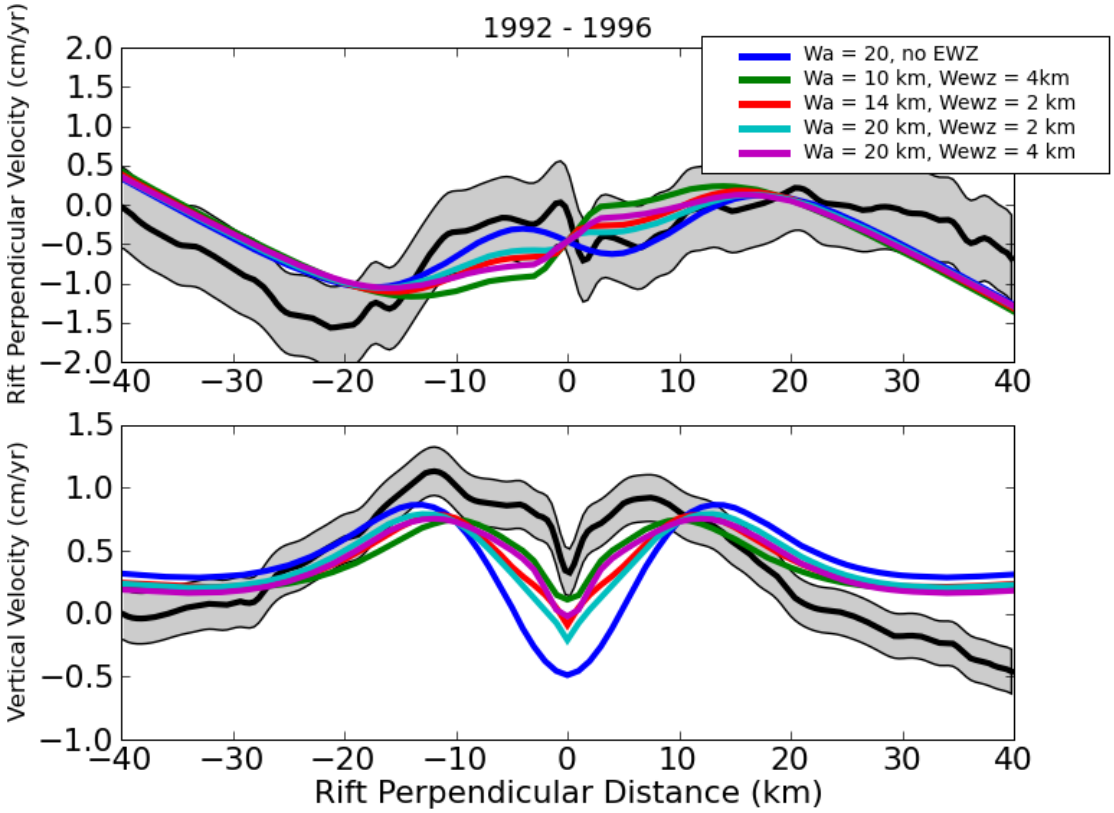

Figure 7.10: Models with a viscosity anomaly and an elastic weak zone (EWZ) in layer 1 (Figure 7.2b). The width of the anomaly is W_a and the width of the EWZ is W_{ewz}. $\log \eta_2 = 19$, $\log \eta_a/\eta_2 = -1$. The InSAR velocity measurements are in black with one standard deviation error.

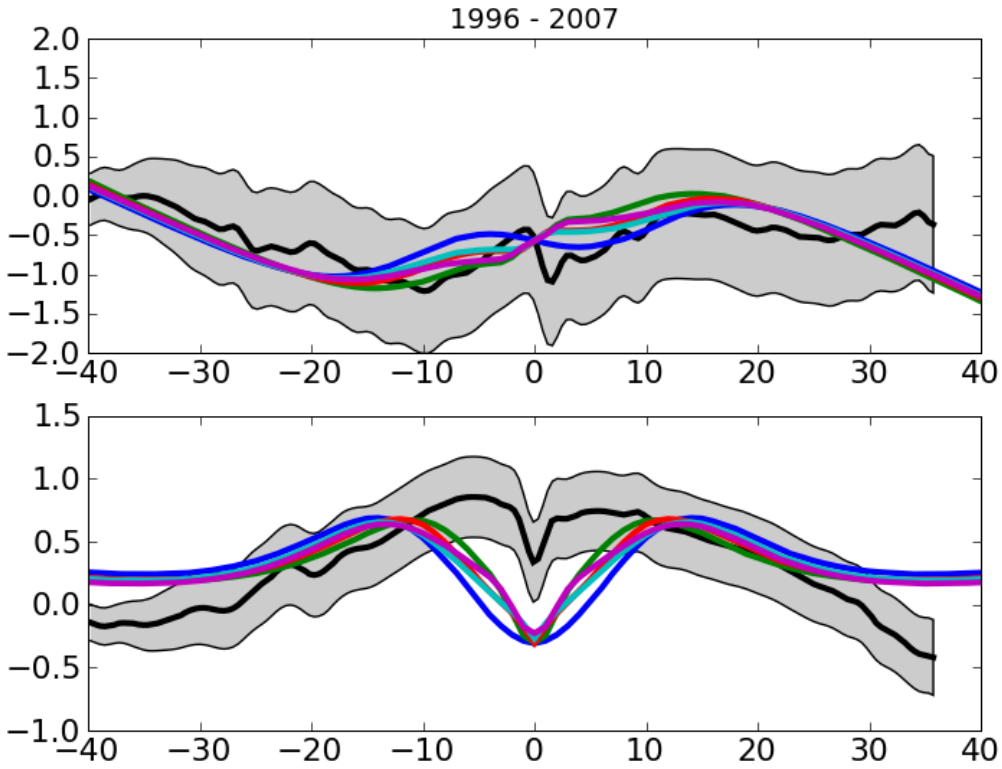

Figure 7.10: Cont. Mean velocities over the period 1996 – 2007

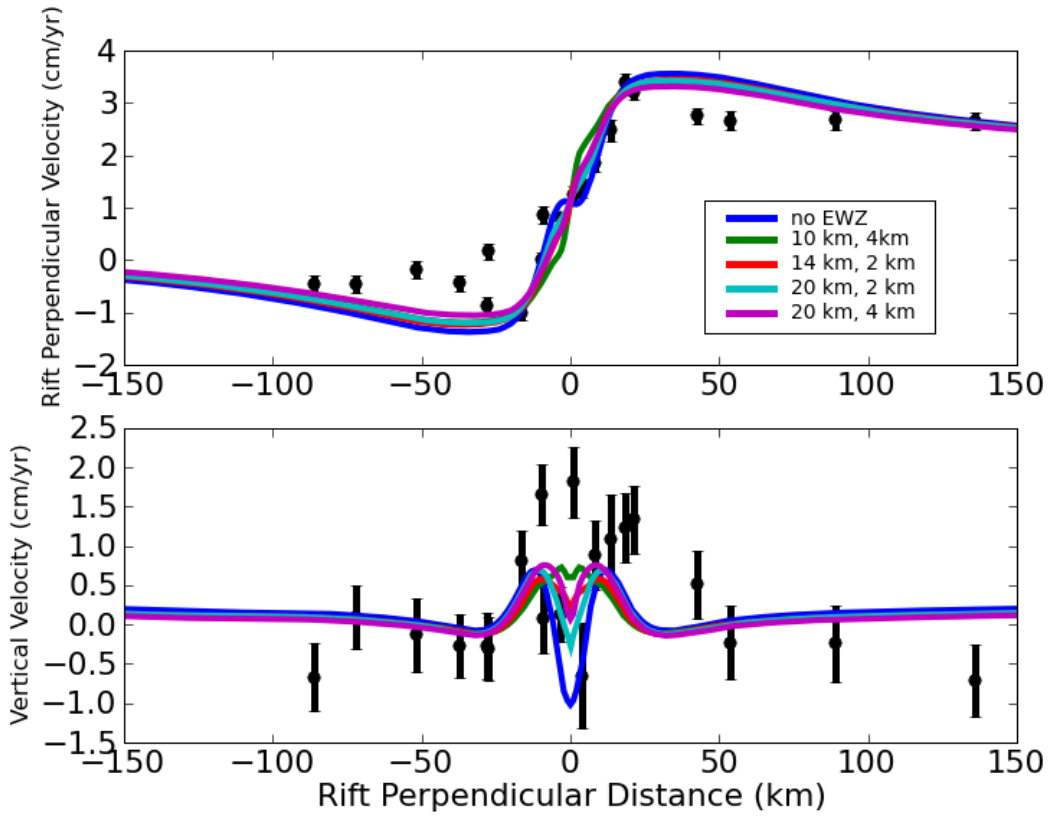

Figure 7.11: Same as Figure 7.10 with compairison to GPS data from Hofton & Foulger (1996) (in black with one standard deviation errors). Mean velocities over 1987 – 1992 are shown.

Figure 7.12: Two-dimensional "thick" crust model with dipping Moho. The layers are labeled as UC: upper crust; LC: lower crust; M: mantle. This is a close up of the region of the model near the rift axis. It has the same dimensions and boundary conditions as the model depicted in Figure 7.2. The Moho surface is taken from the model of Allen et al. (2002b). Image is to scale.

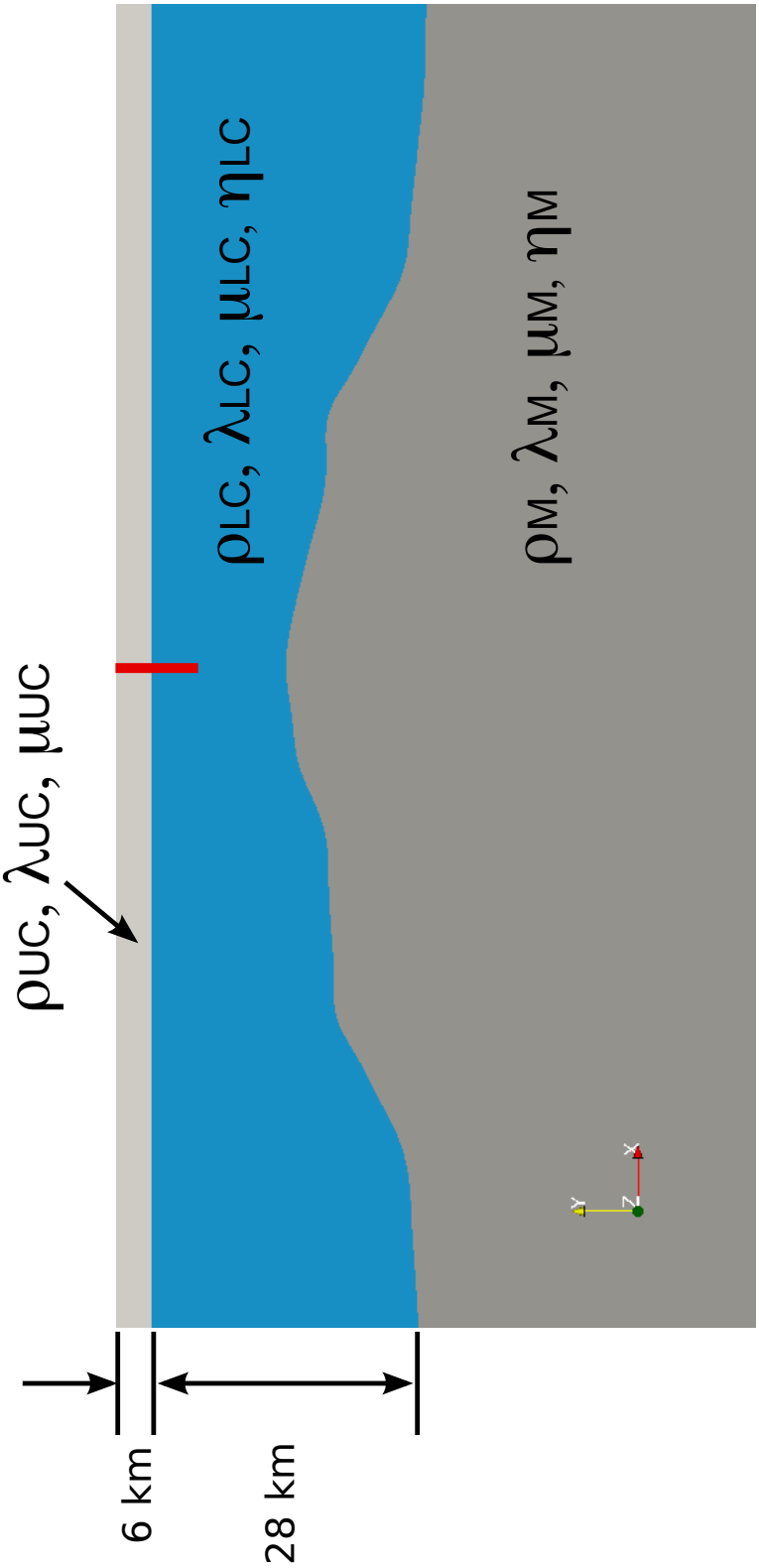
ρUC, λUC, μUC
ρLC, λLC, μLC, ηLC
ρM, λM, μM, ηM
6 km
28 km

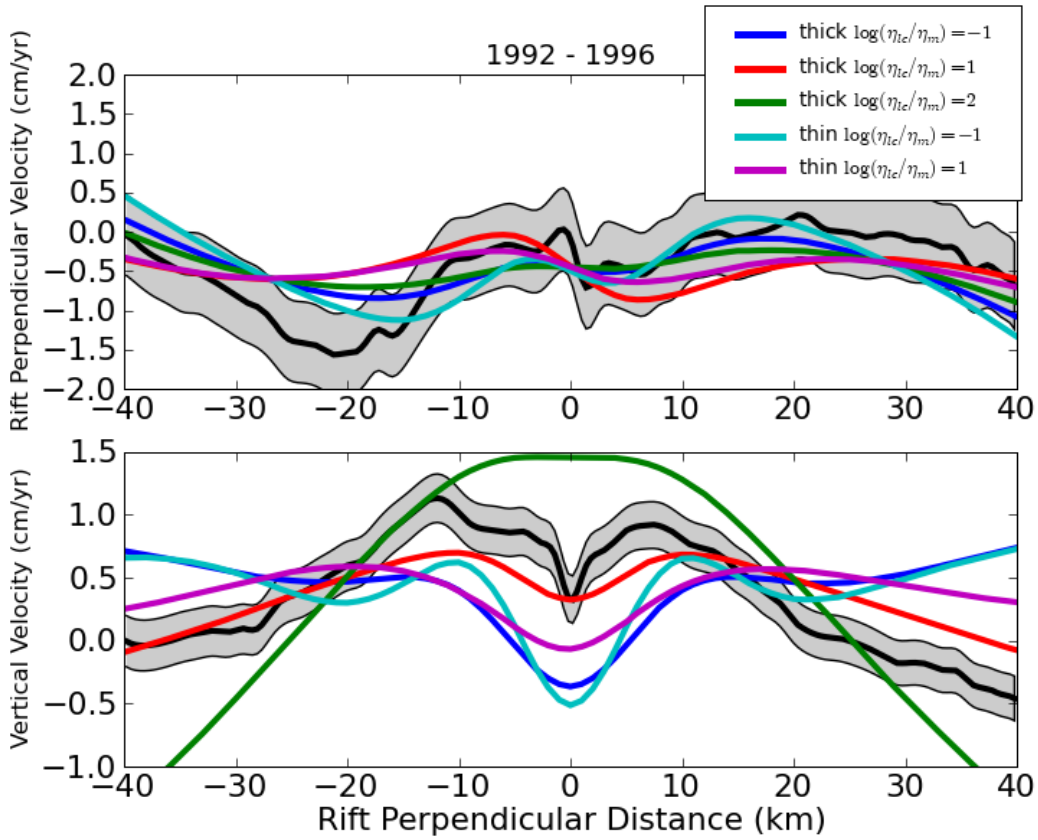

Figure 7.13: Models with large scale heterogeneity in the lithosphere. There are two viscoelastic layers: the lower crust (lc) and the upper mantle (m). "Thick" models have the Moho located according to the model of Allen et al. (2002b). "Thin" models use the same surface translated 10 km closer to the surface. η_{lc} is the viscosity of the lower crust and η_m is the viscosity of the mantle.

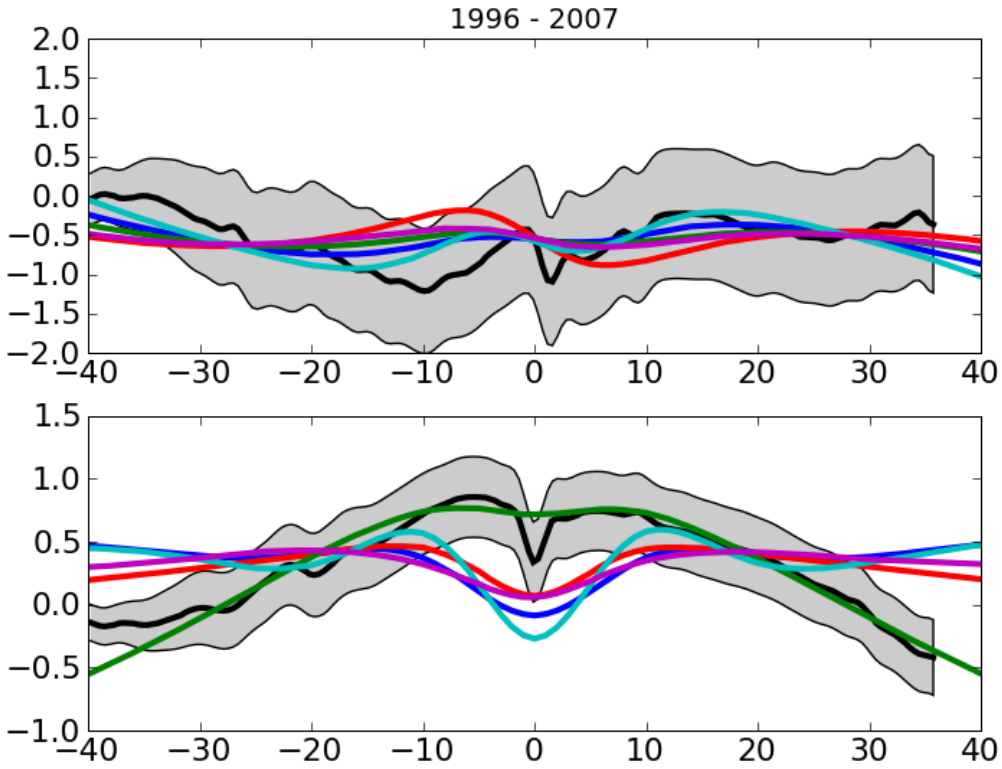

Figure 7.13: Cont. Mean velocities over the period 1996 – 2007

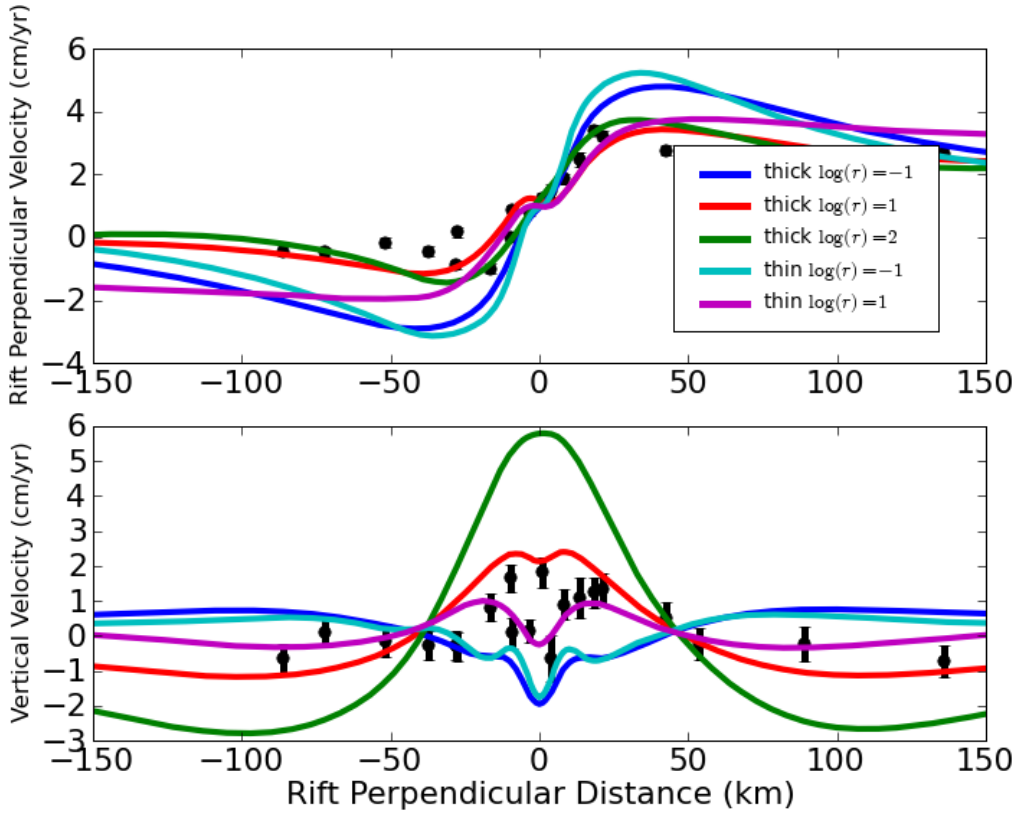

Figure 7.14: Same as Figure 7.13 with compairison to GPS data from Hofton & Foulger (1996) (in black with one standard deviation errors). Mean velocities over 1987 – 1992 are shown. r is the ratio of the viscosity of the lower crust to the viscosity of the mantle.

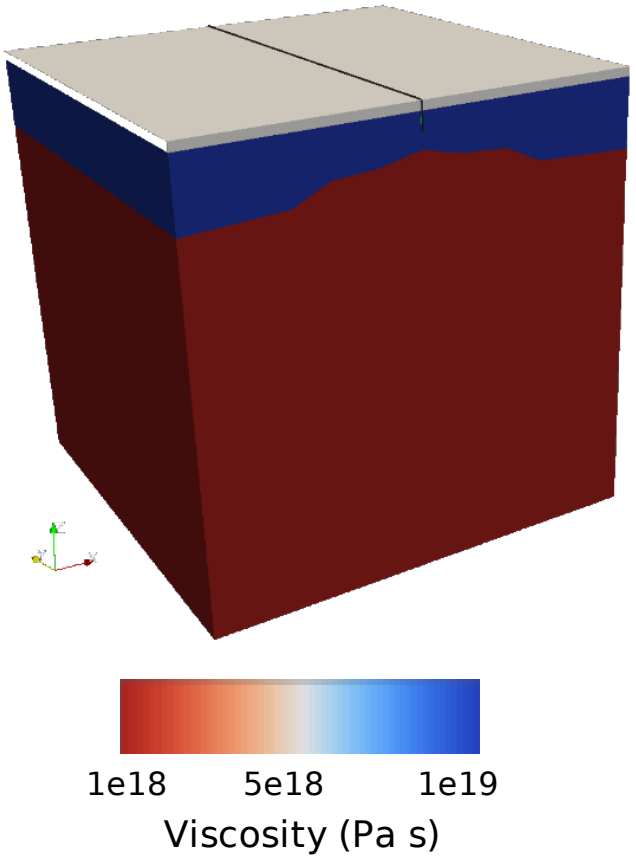

Figure 7.15: Three-dimensional FEM model with a dipping Moho. The tan layer is the elastic upper crust; the blue layer is the viscoelastic lower crust; and the red layer is the viscoelastic upper mantle. The model extends 200 km in every direction. Constant velocity tectonic loading of 1 cm/yr (half rate) is applied to the left and right boundaries. The black line represents the rifting surface. The Moho mimics that of Allen et al. (2002b), except that it is constant the along rift direction.

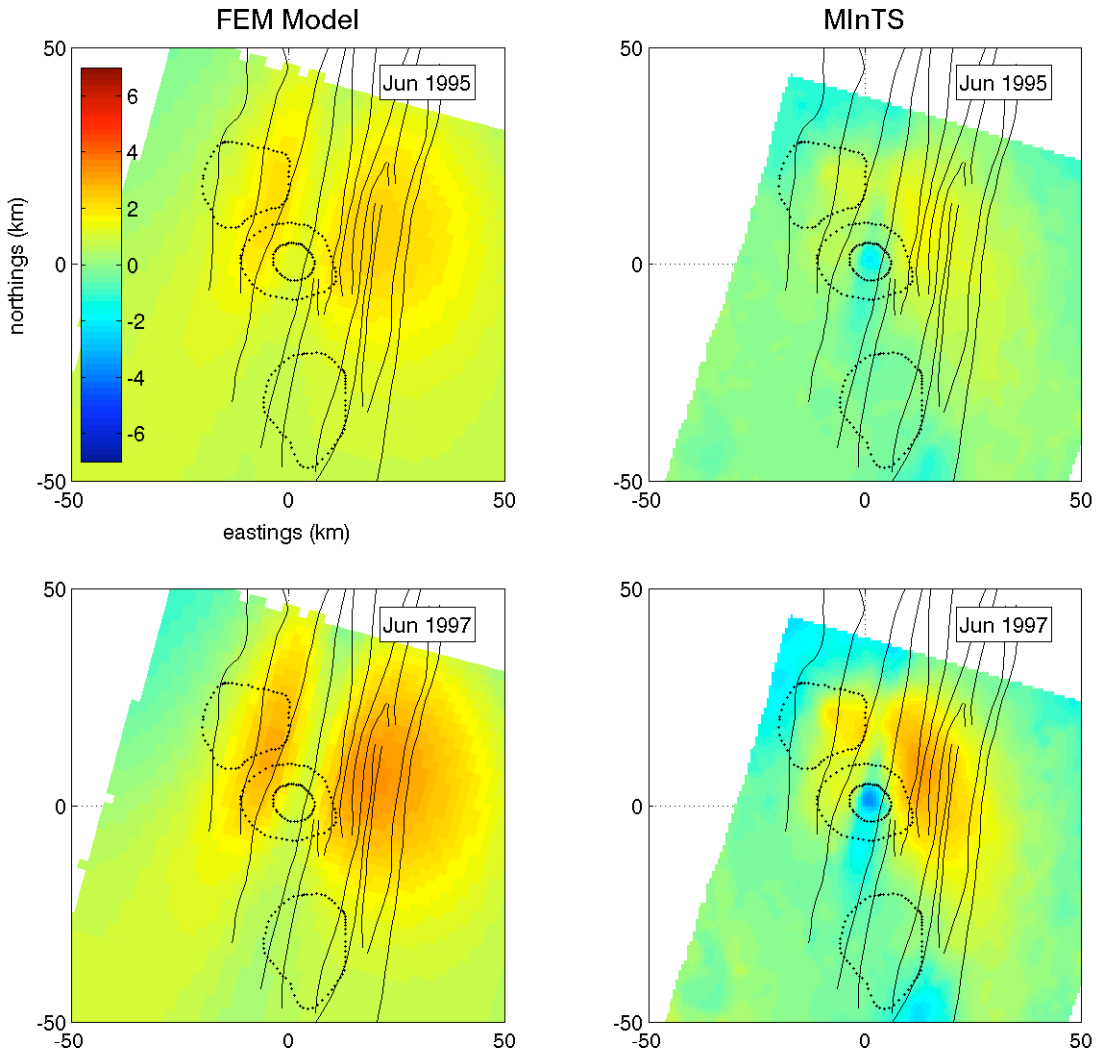

Figure 7.16: Cumulative displacement since June 1993 of dipping Moho three-dimensional model (Figure 7.15) and displacements from MInTS (Section 6.5). Displacements are in cm. Volcanic systems and associated fissure swarms are drawn in black; they are from north to south: Theistareykir, Krafla, and Fremri-Namar. Both data and model have been detrended by removing a bi-linear ramp.

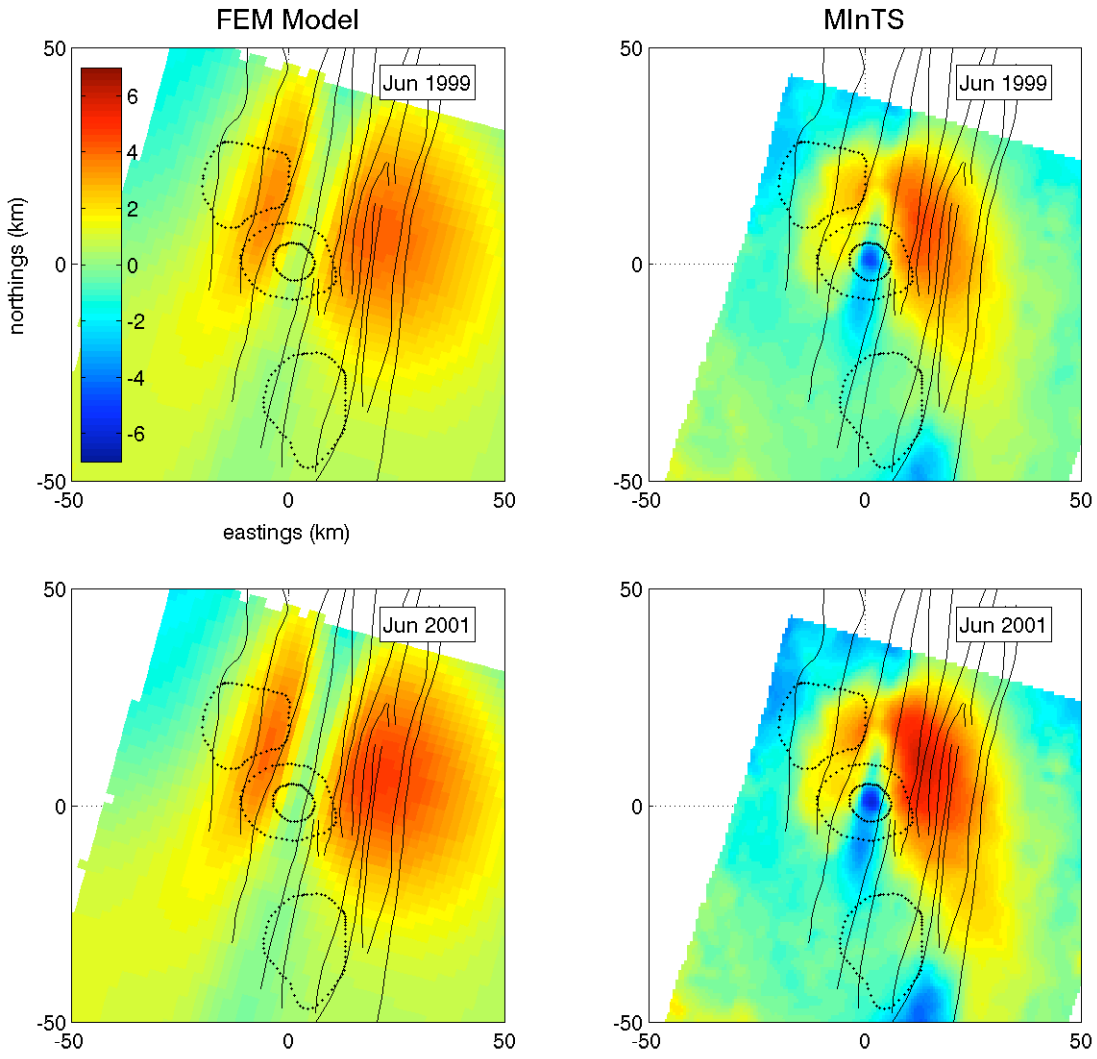

Figure 7.16: Cont.

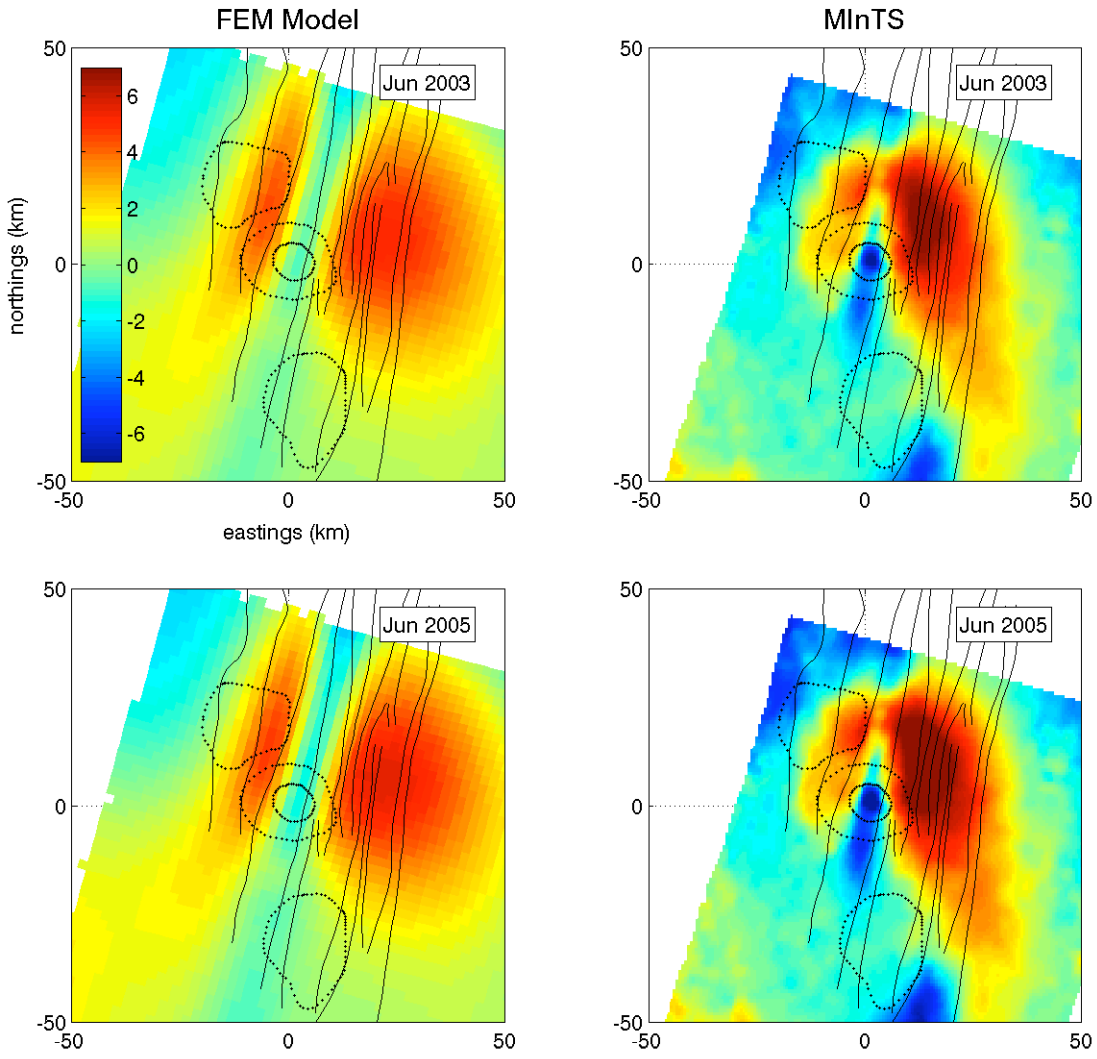

Figure 7.16: Cont.

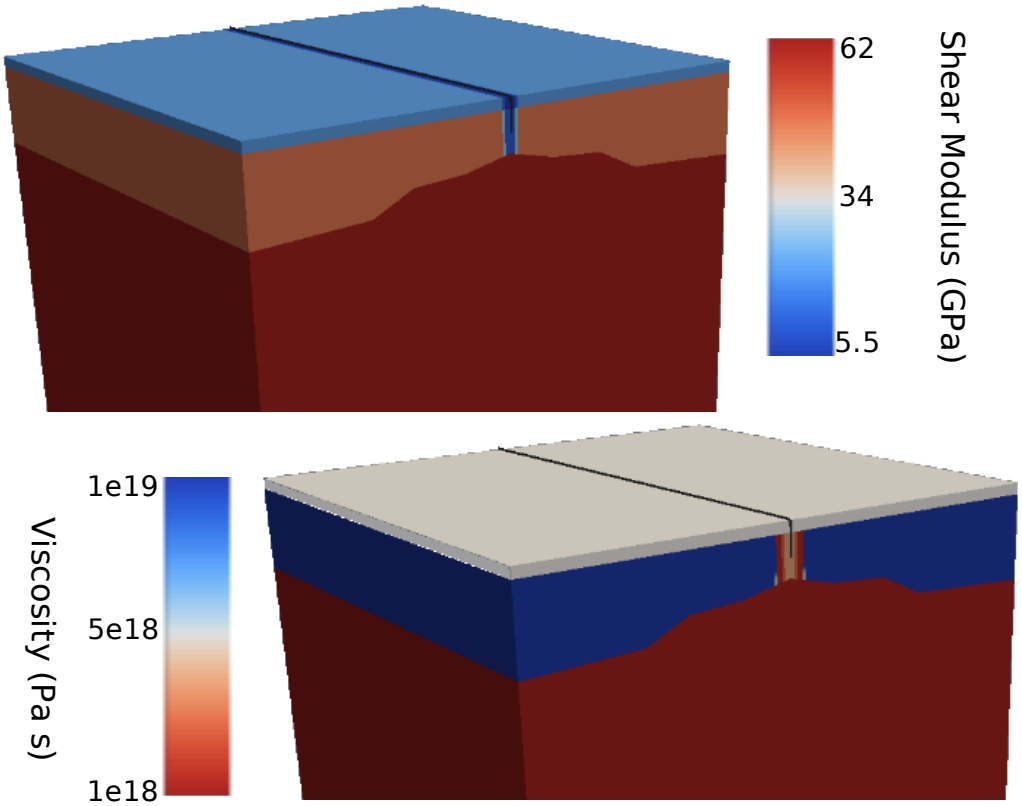

Figure 7.17: Three-dimensional FEM model with dipping Moho and axially located rheological gradients. The local gradients along the rift axis are similar to those in Figure 7.2b. The viscosity anomaly is 10 km wide and 6 km deep. The elastic weak zone is 4 km wide and extends all the way through the upper and lower crust. See Figure 7.15 for a description of other features.

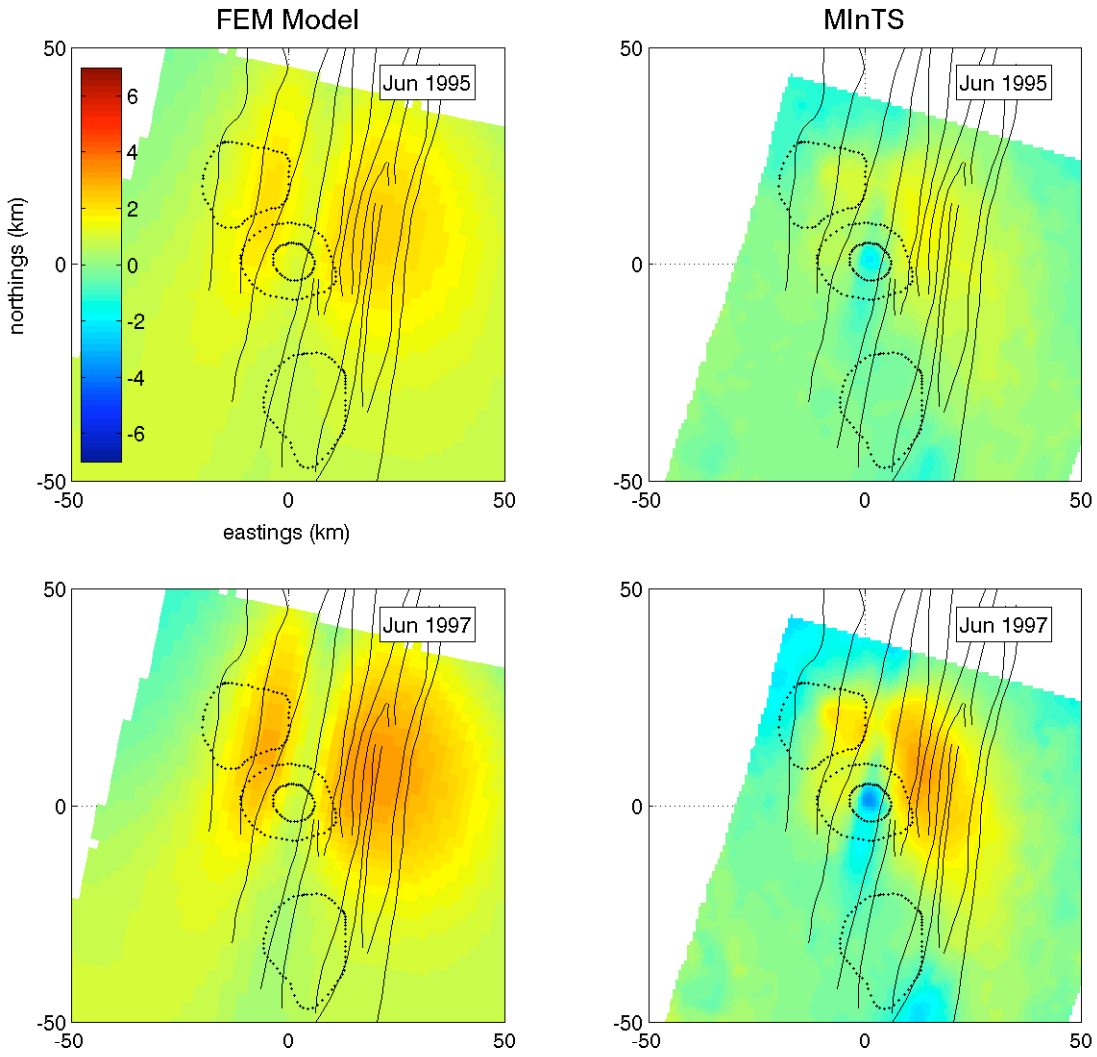

Figure 7.18: Cumulative surface displacement since June 1993 from three-dimensional model with a dipping Moho and axially located rheological gradients (Figure 7.17) and displacements from MInTS (Section 6.5). Displacements are in cm. Volcanic systems and associated fissure swarms are drawn in black; they are from north to south: Theistareykir, Krafla, and Fremri-Namar. Both data and model have been detrended by removing a bi-linear ramp.

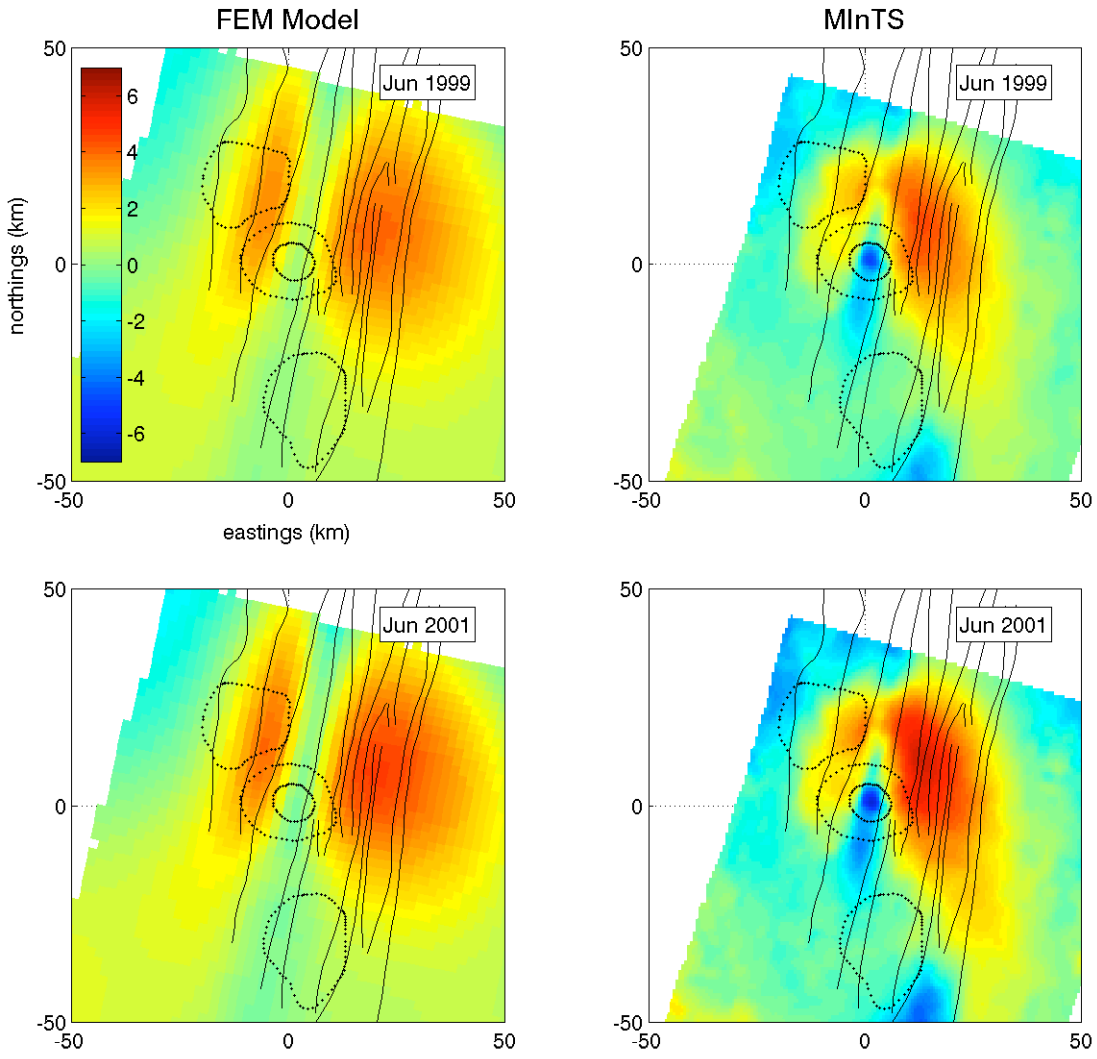

Figure 7.18: Cont.

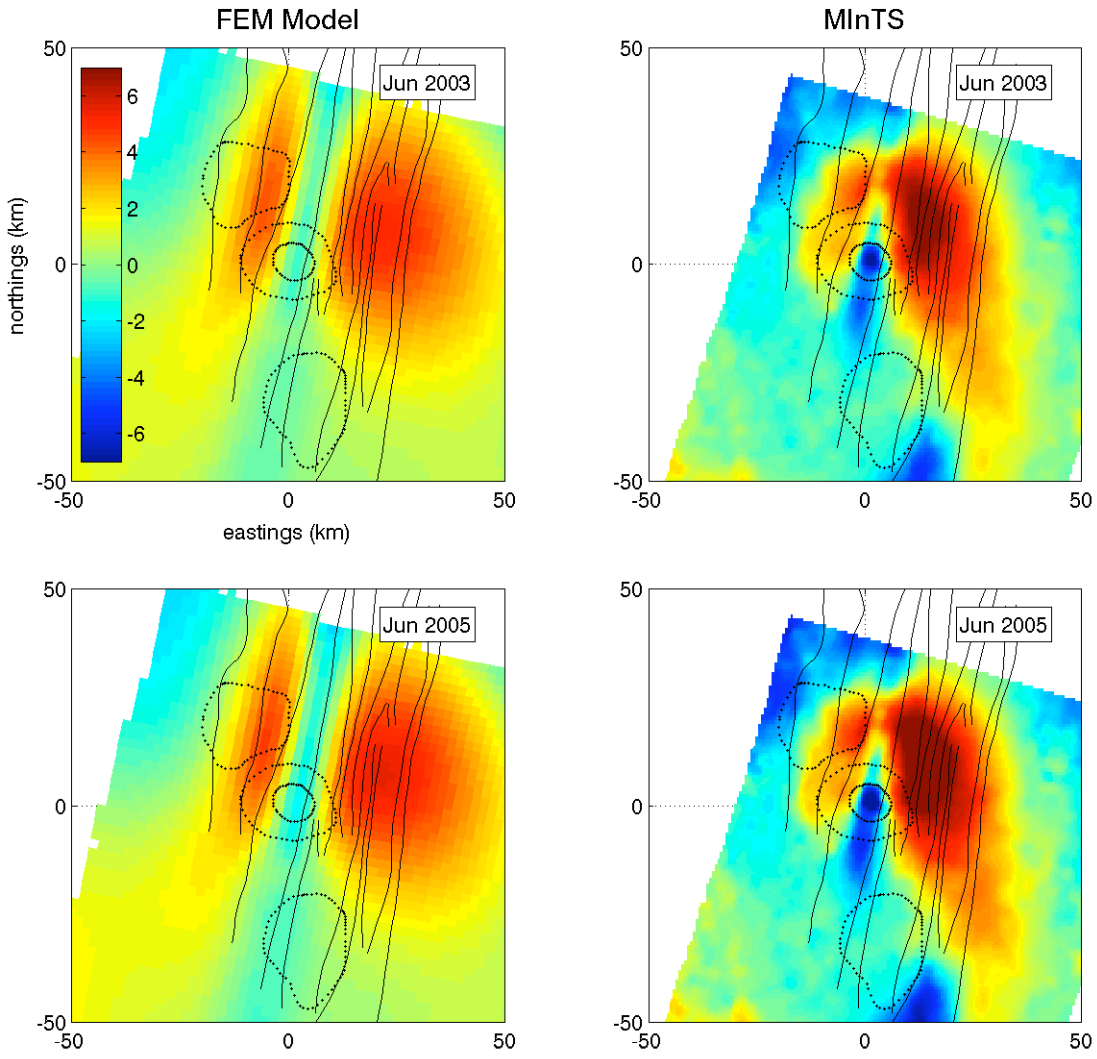

Figure 7.18: Cont.

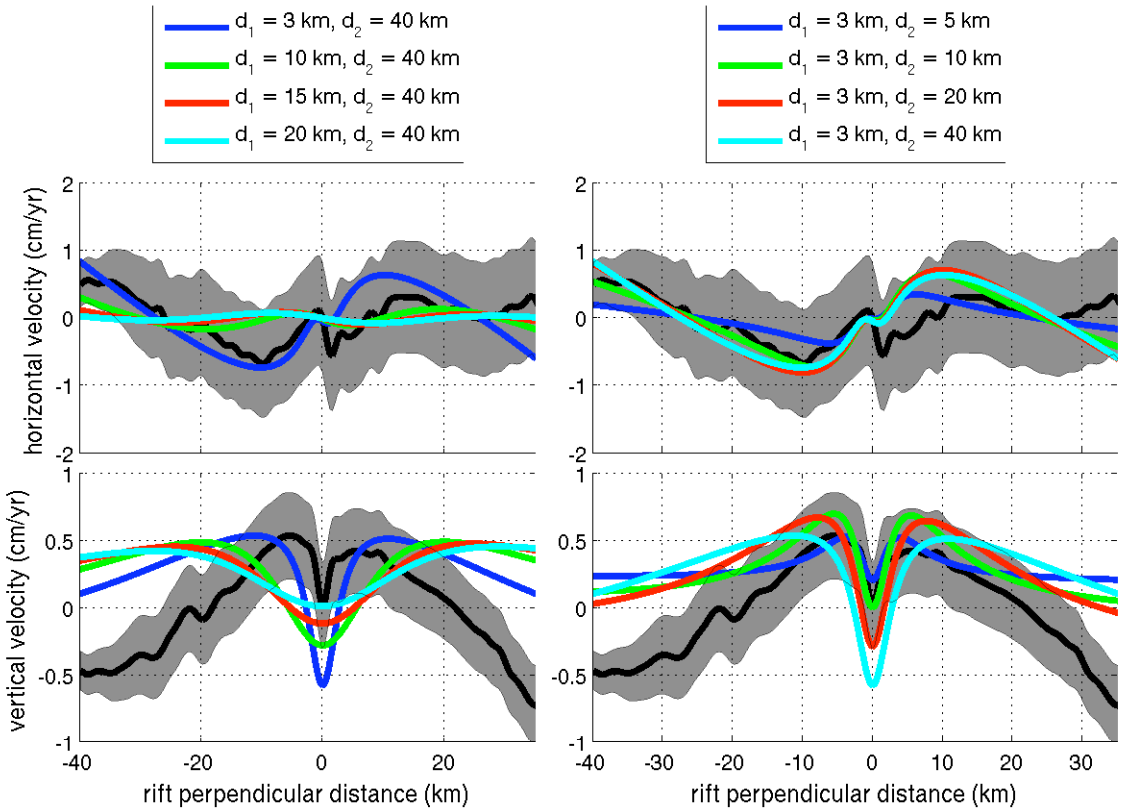

Figure 7.19: Vertical and rift-perpendicular surface deformation along a rift-perpendicular profile from models of uniform dike opening in an elastic half-space (Okada, 1985). We applied an opening rate of 4 cm/yr uniformly for the entire depth of the dike. The mean velocities from 1996 to 2007, as measured by InSAR, are shown in black with one standard deviation error in gray. The depth to the top of the dike is d_1, and the depth to the bottom of the dike is d_2. Left: class of models with different values of d_1 while d_2 is held constant at 40 km. Right; class of models with different values of d_2 while d_1 is held constant at 3 km.

Model Type	Parameter	Value
Two-layer models	λ_1	49 GPa
	μ_1	27 GPa
	ρ_1	2800 kg/m^3
	λ_2	99 GPa
	μ_2	41 GPa
	ρ_2	3100 kg/m^3
	λ_{EWZ}	12.25 GPa
	μ_{EWZ}	6.75 GPa
	ρ_{EWZ}	2800 kg/m^3
Dipping Moho models	λ_{UC}	25 GPa
	μ_{UC}	22 GPa
	ρ_{UC}	2800 kg/m^3
	λ_{LC}	56 GPa
	μ_{LC}	48 GPa
	ρ_{LC}	3100 kg/m^3
	λ_M	73 GPa
	μ_M	62 GPa
	ρ_M	3170 kg/m^3

Table 7.1: Elastic moduli and densities used for FEM models. The subscripts correspond to different layers or zones in the models: (1) layer 1, (2) layer 2, (EWZ) elastic weak zone, (UC) upper crust, (LC) lower crust, (M) mantle. See Figures 7.2 and 7.12 for the geometry of the two-layer and dipping Moho models, respectively.

Model Group	Comments	Figures
2D, 2-layer – Laterally homogeneous Figure 7.2	Cannot match shape of InSAR data. Velocity and decay rates from InSAR data roughly matched by models with $\eta_2 = 10^{19}$ Pa s	7.3, 7.5, 7.6
2D, 2-layer – Viscosity anomaly in elastic layer. Changing width of laterally homogeneous Figure 7.2a	Produces double-lobed vertical velocity field, the width of which depends on the width of the anomaly. Very narrow anomalies (< 10 km) do not produce a double-lobe	7.7
2D, 2-layer – Viscosity anomaly in elastic layer. Changing viscosity of anomaly. Figure 7.2a	Ratios of η_a/η_2 other than unity cause the lobes to be further apart and the lobes are more pronounced. Model with $\log(\eta_a/\eta_2) = 1$ and $\eta_2 = 10^{19}$ Pa s provides the best fit.	7.8
2D, 2-layer – Changing depth anomalies.	Only a shallow anomaly results in a double-lobed vertical velocity.	7.9
2D, 2-layer – Viscosity anomaly and EWZ Figure 7.2b	The EWZ produces the narrow, axially located depression seen in InSAR data.	7.10
2D, Dipping Moho – Figure 7.12	Data favors a strong-crust weak-mantle model ($\log(\eta_{LC}/\eta_M) = 1$). Difficult to distinguish between thick and thin crust models.	7.13
3D – Figures 7.15 and 7.17	Subsidence caused by EWZ too large compared to InSAR data. Displacements at north and south end of rift are likely due to interaction with faults and the Askja rift system.	7.16, 7.18

Table 7.2: Summary of model results. The column labeled "Figures" lists where the results of that particular model are plotted.

Bibliography

Aagaard, B., Williams, C., & Knepley, M., 2007, PyLith: A finite-element code for modeling quasi-static and dynamic crustal deformation, *Eos Trans. AGU*, **88**, 52.

Aagaard, B., Kientz, S., Knepley, M., Strand, L., & Williams, C., 2008, *PyLith User Manual, Version 1.3*, Computational Infrastructure of Geodynamics, Pasadena, CA.

Abaimov, S. G., Turcotte, D. L., & Rundle, J. B., 2007, Recurrence-time and frequency-slip statistics of slip events on the creeping section of the San Andreas fault in central California, *Geophys. J. Int.*, **170**(3), 1289–1299.

Agnew, D. C., 1997, Nloadf: A program for computing ocean-tide loading, *J. Geophys. Res.*, **102**(B3), 5109–5110.

Agnew, D. C., 2007, Earth tides, in *Treatise on Geophysics*, edited by T. Herring, vol. 3, chap. 6, pp. 163–195, Elsevier.

Al-Zoubi, A. & ten Brink, U., 2002, Lower crustal flow and the role of shear in basin subsidence: an example from the Dead Sea basin, *Earth Planet. Sci. Lett.*, **199**(1-2), 67–79.

Allen, R., Nolet, G., Morgan, W., Vogfjord, K., Bergsson, B., Erlendsson, P., Foulger, G., Jakobsdottir, S., Julian, B., Pritchard, M., Ragnarsson, S., & Stefansson, R., 2002,

Imaging the mantle beneath Iceland using integrated seismological techniques, *J. Geophys. Res.*, **107**.

Allen, R., Nolet, G., Morgan, W., Vogfjord, K., Nettles, M., Ekstrom, G., Bergsson, B., Erlendsson, P., Foulger, G., Jakobsdottir, S., Julian, B., Pritchard, M., Ragnarsson, S., & Stefansson, R., 2002, Plume-driven plumbing and crustal formation in Iceland, *J. Geophys. Res.*, **107**.

Angenheister, G., Gebrande, H., Miller, H., Goldflam, P., Weigel, W., Jacoby, W., Palmason, G., Bjornsson, S., Einarsson, P., Pavlenkova, N., Zverev, S., Litvinenko, I., Loncarevic, B., & Solomon, S., 1980, Reykjanes Ridge Iceland seismic experiment (rrisp 77), *Journal of Geophysics-Zeitschrift fur Geophysik*, **47**, 228–238.

Árnadóttir, T., Sigmundsson, F., & Delaney, P. T., 1998, Sources of crustal deformation associated with the Krafla, Iceland, eruption of September 1984, *Geophys. Res. Lett.*, **25**(7), 1043–1046.

Árnadóttir, T., Jónsson, S., Pollitz, F., Jiang, W., & Feigl, K., 2005, Postseismic deformation following the June 2000 earthquake sequence in the south Iceland seismic zone, *J. Geophys. Res*, **110**(B12308).

Árnadóttir, T., Lund, B., Jiang, W., Geirsson, H., Bjornsson, H., Einarsson, P., & Sigurdsson, T., 2009, Glacial rebound and plate spreading: results from the first countrywide GPS observations in Iceland, *Geophys. J. Int.*, **177**(2), 691–716.

Ayele, A., Jacques, E., Kassim, M., Kidane, T., Omar, A., Tait, S., Nercessian, A., de Chabalier, J.-B., & King, G., 2007, The volcano-seismic crisis in Afar, Ethiopia, starting September 2005, *Earth and Planet. Sci. Lett.*, **255**(1-2), 177–187.

Baker, T. F. & Bos, M. S., 2003, Validating earth and ocean tide models using tidal gravity measurements, *Geophys. J. Int.*, **152**(2), 468–485.

Barisin, I., Leprince, S., Parsons, B., & Wright, T., 2009, Surface displacements in the September 2005 Afar rifting event from satellite image matching: Asymmetric uplift and faulting, *Geophys. Res. Lett.*, **36**.

Beblo, M., Bjornsson, A., Arnason, K., Stein, B., & Wolfgram, P., 1983, Electrical-conductivity beneath Iceland - constraints imposed by magnetotelluric results on temperature, partial melt, crust-structure and mantle structure, *Journal of Geophysics-Zeitschrift fur Geophysik*, **53**, 16–23.

Begin, Z., Steinberg, D., Ichinose, G., & Marco, S., 2005, A 40,000 year unchanging seismic regime in the Dead Sea rift, *Geology*, **33**, 257–260.

Ben-Zion, Y., Rice, J., & Dmowska, R., 1993, Interaction of the San Andreas fault creeping segment with adjacent great rupture zones and earthquake recurrence at Parkfield, *J. Geophys. Res.*, **98**, 2135–2144.

Ben-Zion, Y., Dahmen, K., Lyakhovsky, V., Ertas, D., & Agnon, A., 1999, Self-driven mode switching of earthquake activity on a fault system, *Earth Planet. Sci. Lett.*, **172**, 11–21.

Bennati, L., Calais, E., Wright, T., Hamling, I., Lewi, E., Nooner, S., Buck, R., & Ebinger, C., 2008, Post-rifting relaxation processes in the Afar region (Ethiopia) from GPS measurements and numerical modelling, in *Eos Trans. AGU*.

Berardino, P., Fornaro, G., Lanari, R., & sansosti, E., 2002, A new algorithm for surface deformation monitoring based on small baseline differential SAR interferograms, *IEEE Trans. Geosci. Rem. Sens.*, **40**, 2375–2383.

Bjornsson, A., 1985, Dynamics of crustal rifting in NE Iceland, *J. Geophys. Res.*, **90**, 151–162.

Björnsson, A., 2008, Temperature of the Icelandic crust: Inferred from electrical conductivity, temperature surface gradient, and maximum depth of earthquakes, *Tectonophysics*, **447**, 136–141.

Bjornsson, A., Johnsen, G., Sigurdsson, S., Thorbergsson, G., & Tryggvason, E., 1979, Rifting of the plate boundary in north Iceland 1975-1978, *J. Geophys. Res.*, **84**, 3029–3038.

Blewitt, G., 2007, GPS and space-based geodetic methods, in *Treatise on Geophysics*, edited by T. Herring, vol. 3, chap. 11, pp. 351–390, Elsevier.

Bos, M. & Baker, T., 2005, An estimate of the errors in gravity ocean tide loading computations, *J. Geod.*, **71**(1–3), 50–63.

Brandsdottir, B. & Menke, W., 1992, Thin low-velocity zone within the Krafla caldera, NE-Iceland attributed to a small magma chamber, *Geophys. Res. Lett.*, **19**, 2381–2384.

Brandsdottir, B., Menke, W., Einarsson, P., White, R., & Staples, R., 1997, Faroe-Iceland ridge experiment .2. crustal structure of the Krafla central volcano, *J. Geophys. Res.*, **102**, 7867–7886.

Buck, W., Einarsson, P., & Brandsdóttir, B., 2006, Tectonic stress and magma chamber size as controls on dike propagation: Constraints from the 1975-1984 Krafla rifting episode, *J. Geophys. Res*, **111**.

Burgmann, R., Rosen, P., & Fielding, E., 2000, Synthetic aperture radar interferometry to

measure Earth's surface topography and its deformation, *Annu. Rev. Earth Planet. Sci.*, **28**(1), 169–209.

Burgmann, R., Ergintav, S., Segall, P., Hearn, E., McClusky, S., Reilinger, R., Woith, H., & Zschau, J., 2002, Time-dependent distributed afterslip on and deep below the Izmit earthquake rupture, *Bull. Seismol. Soc. Am.*, **92**(1), 126–137.

Camitz, J., Sigmundsson, F., Foulger, G., Jahn, C., Volksen, C., & Einarsson, P., 1995, Plate boundary deformation and continuing deflation of the Askja volcano, north Iceland, determined with GPS, 1987-1993, *Bull. Volcanol.*, **57**, 136–145.

Cattin, R., Doubre, C., de Chabalier, J., King, G., Vigny, C., Avouac, J., & Ruegg, J., 2005, Numerical modelling of quaternary deformation and post-rifting displacement in the Asal-Ghoubbet rift (Djibouti, Africa), *Earth and Planet. Sci. Lett.*, **239**, 352–367.

Chandrasekharaiah, D. & Debnath, L., 1994, *Continuum Mehanics*, Academic Press.

Chery, J. & Vernant, P., 2006, Lithospheric elasticity promotes episodic fault activity, *Earth and Planet. Sci. Lett.*, **243**(1-2), 211–217.

Chery, J., Merkel, S., & Bouissou, S., 2001, A physical basis for time clustering of large earthquakes, *Bull. Seismol. Soc. Am.*, **91**, 1685–1693.

Chlieh, M., Avouac, J., Hjorleifsdottir, V., Song, T., Ji, C., Sieh, K., Sladen, A., Hebert, H., Prawirodirdjo, L., Bock, Y., et al., 2007, Coseismic slip and afterslip of the great M w 9.15 Sumatra-Andaman earthquake of 2004, *Bull. Seismol. Soc. Am.*, **97**(1 A), 152–173.

Darbyshire, F., Priestley, K., White, R., Stefansson, R., Gudmundsson, G., & Jakobsdottir, S., 2000, Crustal structure of central and northern Iceland from analysis of teleseismic receiver functions, *Geophys. J. Int.*, **143**, 163–184.

de Zeeuw-van Dalfsen, E., Pedersen, R., Sigmundsson, F., & Pagli, C., 2004, Satellite radar interferometry 1993-1999 suggests deep accumulation of magma near the crust-mantle boundary at the Krafla volcanic system, Iceland, *Geophys. Res. Lett.*, **31**(13), L13611.

de Zeeuw-van Dalfsen, E., Rymer, H., Sigmundsson, F., & Sturkell, E., 2005, Net gravity decrease at Askja volcano, Iceland: constraints on processes responsible for continuous caldera deflation, 1988-2003, *J. Volcanol. Geotherm. Res.*, **139**(3-4), 227–239.

Demets, C., Gordon, R., Argus, D., & Stein, S., 1994, Effect of recent revisions to the geomagnetic reversal time-scale on estimates of current plate motions, *Geophys. Res. Lett.*, **21**, 2191–2194.

DiCaprio, C. & Simons, M., 2008, Importance of ocean tidal load corrections for differential InSAR, *Geophys. Res. Lett.*, **35**(22), L22309.

DiCaprio, C. J., Simons, M., Kenner, S. J., & Williams, C. A., 2008, Post-seismic reloading and temporal clustering on a single fault, *Geophys. J. Int.*, **172**(2), 581–592.

Dong, D., Fang, P., Bock, Y., Cheng, M. K., & Miyazaki, S., 2002, Anatomy of apparent seasonal variations from GPS-derived site position time series, *J. Geophys. Res.*, **107**(B4), 2075.

Doubre, C. & Peltzer, G., 2007, Fluid-controlled faulting process in the Asal rift, Djibouti, from 8 yr of radar interferometry observations, *Geology*, **35**(1), 69–72.

Dunn, R. & Forsyth, D., 2007, Crust and lithospheric structure – seismic structure of mid-ocean ridges, in *Treatise on Geophysics*, edited by B. Romanowicz & A. Dziewonski, vol. 1, Elsevier.

Eanes, R. & Bettadpur, S., 1995, The CSR 3.0 global ocean tide model, Tech. Rep. Technial Memorandum CSR-TM-96-05, Center for Space Research, University of Texas at Austin.

Egbert, G. D. & Erofeeva, S. Y., 2002, Efficient inverse modeling of barotropic ocean tides, *J. Atmos. Ocean. Tech.*, **19**(2), 183–204.

Einarsson, P., 1978, S-wave shadows in the Krafla caldera in NE-Iceland, evidence for a magma chamber in the crust, *Bull. Volcanol.*, **41**, 187–195.

Einarsson, P., 1991, Earthquakes and present-day tectonism in Iceland, *Tectonophysics*, **189**, 261–279.

Emardson, T. R., Simons, M., & Webb, F. H., 2003, Neutral atmospheric delay in interferometric synthetic aperture radar applications: Statistical description and mitigation, *J. Geophys. Res.*, **108**(B5), 2231.

Farrell, W. E., 1972, Deformation of earth by surface loads, *Rev. Geophys. Space. Phys.*, **10**(3), 761–797.

Fay, N. & Humphreys, E., 2005, Fault slip rates, effects of sediments and the strength of the lower crust in the Salton Trough region, Southern California, *J. Geophys. Res.*, **110**.

Fialko, Y., 2004, Evidence of fluid-filled upper crust from observations of postseismic deformation due to the 1992 m(w)7.3 Landers earthquake, *J. Geophys. Res.*, **109**.

Fialko, Y., 2006, Interseismic strain accumulation and the earthquake potential on the southern San Andreas fault system, *Nature*, **441**(7096), 968–971.

Fialko, Y., Simons, M., Agnew, D., et al., 2001, The complete (3-D) surface displacement field in the epicentral area of the 1999 M w 7.1 Hector Mine earthquake, California, from space geodetic observations, *Geophys. Res. Lett*, **28**(16), 3063–3066.

Foulger, G. & Anderson, D., 2005, A cool model for the Iceland hotspot, *J. Volcanol. Geotherm. Res.*, **141**(1-2), 1–22.

Foulger, G., Jahn, C., Seeber, G., Einarsson, P., Julian, B., & Heki, K., 1992, Post-rifting stress-relaxation at the divergent plate boundary in northeast Iceland, *Nature*, **358**, 488–490.

Freed, A. & Bürgmann, R., 2004, Evidence of power-law flow in the Mojave desert mantle, *Nature*, **430**, 548–551.

Friedrich, A., Wernicke, B., Niemi, N., Bennett, R., & Davis, J., 2003, Comparison of geodetic and geologic data from the Wasatch region, Utah, and implications for the spectral character of Earth deformation at periods of 10 to 10 million years, *J. Geophys. Res.*, **108**, 2199.

Gaillard, F., Malki, M., Iacono-Marziano, G., Pichavant, M., & Scaillet, B., 2008, Carbonatite melts and electrical conductivity in the asthenosphere, *Science*, **322**(5906), 1363.

Grant, L. & Sieh, K., 1994, Paleoseismic evidence of clustered earthquakes on the San Andreas fault in the Carrizo Plain, California, *J. Geophys. Res.*, **99**, 6819–6841.

Gudmundsson, A., 1983, Form and dimensions of dykes in eastern Iceland, *Tectonophysics*, **95**(3-4), 295–307.

Gudmundsson, A., 1995, Infrastructure and mechanics of volcanic systems in Iceland, *J. Volcanol. Geotherm. Res.*, **64**, 1–22.

Gudmundsson, A., 2000, Dynamics of volcanic systems in Iceland: Example of tectonism and volcanism at juxtaposed hot spot and mid-ocean ridge systems, *Annu. Rev. Earth Planet. Sci.*, **28**, 107–140.

Hager, B., Lyzenga, G., Donnellan, A., & Dong, D., 1999, Reconciling rapid strain accumulation with deep seismogenic fault planes in the Ventura basin, California, *J. Geophys. Res.*, **104**, 25.

Hanssen, R., 2002, *Radar interferometry: data interpretation and error analysis*, Plenum Publishing Corporation.

Heki, K., Foulger, G., Julian, B., & Jahn, C., 1993, Plate dynamics near divergent boundaries - geophysical implications of postrifting crustal deformation in NE Iceland, *J. Geophys. Res.*, **98**, 14279–14297.

Henriot, O., Villemin, T., & Jouanne, F., 2001, Long period interferograms reveal 1992-1998 steady rate of deformation at Krafla volcano (north Iceland)., *Geophys. Res. Lett.*, **28**, 1067–1070.

Hetland, E. & Hager, B., 2005, Postseismic and interseismic displacements near a strike-slip fault: A two-dimensional theory for general linear viscoelastic rheologies, *J. Geophys. Res.*, **110**.

Hetland, E. A. & Hager, B. H., 2006, Interseismic strain accumulation: Spin-up, cycle invariance, and irregular rupture sequences, *Geochem. Geophys. Geosyst.*, **7**, Q05004.

Hetland, E. A. & Hager, B. H., 2006, The effects of rheological layering on post-seismic deformation, *Geophys. J. Int.*, **166**(1), 277–292.

Hetland, E. A., Muse, P., & Simons, M., 2009, Multi-scale insar time series analysis, in prep.

Hirn, A., Lepine, J., & Sapin, M., 1993, Triple junction and ridge hotspots - earthquakes, faults, and volcanism in Afar, the Azores, and Iceland, *J. Geophys. Res.*, **98**, 11995–12001.

Hofton, M. & Foulger, G., 1996, Postrifting anelastic deformation around the spreading plate boundary, north Iceland .1. modeling of the 1987-1992 deformation field using a viscoelastic Earth structure, *J. Geophys. Res.*, **101**, 25403–25421.

Hsu, Y., Simons, M., Avouac, J., Galetzka, J., Sieh, K., Chlieh, M., Natawidjaja, D., Prawirodirdjo, L., & Bock, Y., 2006, Frictional afterslip following the 2005 Nias-Simeulue earthquake, Sumatra, *Science*, **312**(5782), 1921–1926.

Hsu, Y., Yu, S., Simons, M., Kuo, L., & Chen, H., 2008, Interseismic crustal deformation in the Taiwan plate boundary zone revealed by GPS observations, seismicity, and earthquake focal mechanisms, *Tectonophysics*, **479**, 4–18.

Ito, G., Lin, J., & Graham, D., 2003, Observational and theoretical studies of the dynamics of mantle plume-mid-ocean ridge interaction, *Rev. Geophys.*, **41**(4), 1017.

Jackson, D. D., Aki, K., Cornell, C. A., Dieterich, J. H., Henyey, T. L., Mahdyiar, M., Schwartz, D., & Ward, S. N., 1995, Seismic hazards in southern California - probable earthquakes, 1994 to 2024, *Bull. Seismol. Soc. Am.*, **85**(2), 379–439.

Jackson, J., 2002, Strength of the continental lithosphere: Time to abandon the jelly sandwich?, *GSA Today*, **12**(9), 4–10.

Jouanne, F., Villemin, T., Berger, A., & Henriot, O., 2006, Rift-transform junction in north Iceland: rigid blocks and narrow accommodation zones revealed by GPS 1997-1999-2002, *Geophys. J. Int.*, **167**(3), 1439–1446.

Kagan, Y. & Jackson, D., 1991, Long-term earthquake clustering, *Geophys. J. Int.*, **104**, 117–133.

Kanamori, H. & Anderson, D. L., 1975, Theoretical basis of some empirical relations in seismology, *Bull. Seismol. Soc. Am.*, **65**(5), 1073–1095.

Keir, D., Hamling, I. J., Ayele, A., Calais, E., Ebinger, C., Wright, T. J., Jacques, E., Mohamed, K., Hammond, J. O. S., Belachew, M., Baker, E., Rowland, J. V., Lewi, E., & Bennati, L., 2009, Evidence for focused magmatic accretion at segment centers from lateral dike injections captured beneath the Red Sea rift in Afar, *Geology*, **37**(1), 59–62.

Kenner, S. & Segall, P., 2000, Postseismic deformation following the 1906 San Francisco earthquake, *J. Geophys. Res.*, **105**, 13195–13209.

Kenner, S. & Simons, M., 2005, Temporal clustering of major earthquakes along individual faults due to post-seismic reloading, *Geophys. J. Int.*, **160**, 179–194.

Klinger, Y., Avouac, J. P., Abou Karaki, N., Dorbath, L., Bourles, D., & Reyss, J. L., 2000, Slip rate on the Dead Sea transform fault in northern Araba valley (Jordan), *Geophys. J. Int.*, **142**(3), 755–768.

LaFemina, P. C., Dixon, T. H., Malservisi, R., Arnadottir, T., Sturkell, E., Sigmundsson, F., & Einarsson, P., 2005, Geodetic GPS measurements in south Iceland: Strain accumulation and partitioning in a propagating ridge system, *J. Geophys. Res.*, **110**(B11), B11405.

Lefevre, F., Yard, F. H., Le Provost, C., & Schrama, E. J. O., 2002, Fes99: A global tide finite element solution assimilating tide gauge and altimetric information, *J. Atmos. Ocean. Tech.*, **19**(9), 1345–1356.

Li, V. & Rice, J., 1987, Crustal deformation in great California earthquake cycles, *J. Geophys. Res.*, **92**, 11533–11551.

Lohman, R. B. & Simons, M., 2005, Some thoughts on the use of InSAR data to constrain models of surface deformation: Noise structure and data downsampling, *Geochem. Geophys. Geosyst.*, **6**, Q01007.

Lyakhovsky, V., Ben-Zion, Y., & Agnon, A., 2001, Earthquake cycle, fault zones, and seismicity patterns in a rheologically layered lithosphere, *J. Geophys. Res.*, **106**, 4103–4120.

Lynch, J., Burgmann, R., Richards, M., & Ferencz, R., 2003, When faults communicate: Viscoelastic coupling and earthquake clustering in a simple two-fault system, *Geophys. Res. Lett.*, **30**.

Magde, L., Barclay, A., Toomey, D., Detrick, R., & Collins, J., 2000, Crustal magma plumbing within a segment of the Mid-Atlantic Ridge, 35 N, *Earth and Planet. Sci. Lett.*, **175**(1-2), 55–67.

Marco, S., Stein, M., Agnon, A., & Ron, H., 1996, Long-term earthquake clustering: A 50,000-year paleoseismic record in the Dead Sea graben, *J. Geophys. Res.*, **101**, 6179–6191.

Massonnet, D., Rossi, M., Carmona, C., Adragna, F., Peltzer, G., Feigl, K., & Rabaute, T., 1993, The displacement field of the Landers earthquake mapped by radar interferometry, *Nature*, **364**, 138–142.

Matsumoto, K., Takanezawa, T., & Ooe, M., 2000, Ocean tide models developed by assimilating TOPEX/Poseidon altimeter data into hydrodynamical model: a global model and a regional model around japan, *J. Oceanogr.*, **56**, 567–581.

Matsumoto, K., Sato, T., Takanezawa, T., & Ooe, M., 2005, GOTIC2: A program for computation of oceanic tidal loading effect, *J. Geod. Soc. Japan.*, **47**, 243–248.

Matthews, M. V., Ellsworth, W. L., & Reasenberg, P. A., 2002, A Brownian model for recurrent earthquakes, *Bull. Seismol. Soc. Am.*, **92**(6), 2233–2250.

Meade, B. & Hager, B., 2004, Viscoelastic deformation for a clustered earthquake cycle, *Geophys. Res. Lett.*, **31**.

Melachroinos, S. A., Biancale, R., Llubes, M., Perosanz, F., Lyard, F., Vergnolle, M., Bouin, M.-N., Masson, F., Nicolas, J., Morel, L., & Durand, S., 2007, Ocean tide loading (OTL) displacements from global and local grids: comparisons to GPS estimates over the shelf of Brittany, France, *J. Geod.*, p. 67.

Melosh, H. & Raefsky, A., 1980, Dynamical origin of subduction zone topography, *Geophys. J. Int.*, **60**, 333–354.

Menke, W., 1989, *Geophysical data analysis: discrete inverse theory*, Academic Press.

Menke, W. & Levin, V., 1994, Cold crust in a hot-spot, *Geophys. Res. Lett.*, **21**, 1967–1970.

Menke, W., Levin, V., & Sethi, R., 1995, Seismic attenuation in the crust at the mid-atlantic plate boundary in south-west iceland, *Geophys. J. Int.*, **122**, 175–182.

Menke, W., West, M., Brandsdottir, B., & Sparks, D., 1998, Compressional and shear velocity structure of the lithosphere in northern Iceland, *Bulletin Of The Seismological Society Of America*, **88**, 1561–1571.

Mogi, K., 1958, Relations between the eruptions of various volcanoes and the deformations of the ground surfaces around them, *Bull. Earthquake Res. Inst. Univ. Tokyo*, pp. 99–134.

Morgan, W., 1971, Convection plumes in the lower mantle, *Nature*, **230**(5288), 42–43.

Nur, A. & Mavko, G., 1974, Postseismic viscoelastic rebound, *Science*, **183**, 204–206.

Okada, Y., 1985, Surface deformation due to shear and tensile faults in a half-space, *Bull. Seismol. Soc. Am.*, **75**(4), 1135–1154.

Parker, J., Lyzenga, G., Norton, C., Tisdale, E., & Donnellan, A., 2004, A community faulted-crust model using pyramid on cluster platforms, in *Cluster Computing, 2004 IEEE International Conference on*, p. 491.

Pedersen, R., Sigmundsson, F., & Masterlark, T., 2009, Rheologic controls on inter-rifting deformation of the Northern Volcanic Zone, Iceland, *Earth and Planet. Sci. Lett.*, **281**(1-2), 14 – 26.

Peltzer, G., Rosen, P., Rogez, F., & Hudnut, K., 1996, Postseismic rebound in fault step-overs caused by pore fluid flow, *Science*, **273**(5279), 1202–1204.

Penna, N., King, M., & Stewart, M., 2007, GPS height time series: Short-period origins of spurious long-period signals, *J. Geophys. Res.*, **112**(B2).

Penna, N. T., Bos, M. S., Baker, T. F., & Scherneck, H.-G., 2008, Assessing the accuracy of predicted ocean tide loading displacement values, *J. Geod.*, **82**(12), 893–907.

Pollitz, F., 1992, Postseismic relaxation theory on the spherical earth, *Bull. Seismol. Soc. Am.*, **82**(1), 422–453.

Pollitz, F., 2003, Post-seismic relaxation theory on a laterally heterogeneous viscoelastic model, *Geophys. J. Int.*, **155**(1), 57–78.

Pollitz, F. & Sacks, I., 1996, Viscosity structure beneath northeast Iceland, *J. Geophys. Res.*, **101**, 17771–17793.

Pollitz, F., Peltzer, G., & Burgmann, R., 2000, Mobility of continental mantle: Evidence from postseismic geodetic observations following the 1992 landers earthquake, *J. Geophys. Res.*, **105**, 8035–8054.

Pollitz, F., Wicks, C., & Thatcher, W., 2001, Mantle flow beneath a continental strike-slip fault: postseismic deformation after the 1999 Hector Mine earthquake., *Science*, **293**(5536), 1814.

Prescott, W. H., Savage, J. C., Svarc, J. L., & Manaker, D., 2001, Deformation across the Pacific-North America plate boundary near San Francisco, California, *J. Geophys. Res.*, **106**(B4), 6673–6682.

Pritchard, M., Ji, C., & Simons, M., 2006, Distribution of slip from 11 Mw $>$ 6 earthquakes in the northern Chile subduction zone, *J. Geophys. Res*, **111**.

Ranalli, G., 1990, The microphysical approach to mantle rheology, in *Glacial Isostasy, Sea-Level and Mantle Rheology*, edited by R. Sabadini, K. Lambeck, & E. Boschi, pp. 493–513, Kluwer Academic Publishers.

Ray, R., 1999, A global ocean tide model from TOPEX/POSEIDON altimetry: GOT99. 2, Tech. rep., NASA.

Reches, Z., Schubert, G., & Anderson, C., 1994, Modeling of periodic great earthquakes on the San Andreas fault: Effects of nonlinear crustal rheology, *J. Geophys. Res.*, **99**(B11).

Rosen, P., Hensley, S., Joughin, I., Li, F., Madsen, S., Rodriguez, E., & Goldstein, R., 2000, Synthetic aperture radar interferometry, *Proceedings of the IEEE*, **88**(3), 333–382.

Rosen, P., Hensley, S., Peltzer, G., & Simons, M., 2004, Updated repeat orbit interferometry package released, *Eos Trans. AGU*, **85**(5), 47.

Saemundsson, K., 1974, Evolution of axial rifting zone in northern Iceland and Tjornes Fracture Zone, *Geol. Soc. Am. Bull.*, **85**, 495–504.

Saemundsson, K., 1979, Outline of the geology of Iceland, *Jokull*, **29**, 7–28.

Savage, J. C. & Prescott, W. H., 1978, Asthenosphere readjustment and earthquake cycle, *J. Geophys. Res.*, **83**(NB7), 3369–3376.

Scherneck, H. G., 1991, A parametrized solid earth tide model and ocean tide loading effects for global geodetic base-line measurements, *Geophys. J. Int.*, **106**(3), 677–694.

Schmalzle, G., Dixon, T., Malservisi, R., & Govers, R., 2006, Strain accumulation across the Carrizo segment of the San Andreas Fault, California: Impact of laterally varying crustal properties, *J. Geophys. Res*, **111**.

Schwartz, D. & Coppersmith, K., 1984, Fault behavior and characteristic earthquakes - Examples from the Wasatch and San Andreas fault zones, *J. Geophys. Res.*, **89**, 5681–5698.

Sella, G., Dixon, T., & Mao, A., 2002, Revel: A model for recent plate velocities from space geodesy, *J. Geophys. Res.*, **107**.

Sigmundsson, F., 1991, Postglacial rebound and asthenosphere viscosity in iceland, *Geophys. Res. Lett.*, **18**, 1131–1134.

Sigmundsson, F., 2006, *Iceland geodynamics: crustal deformation and divergent plate tectonics*, Springer.

Sigmundsson, F. & Einarsson, P., 1992, Glacio-isostatic crustal movements caused by historical volume change of the Vatnajokull ice cap, Iceland, *Geophys. Res. Lett.*, **19**, 21.

Sigmundsson, F., Vadon, H., & Massonnet, D., 1997, Readjustment of the Krafla spreading segment to crustal rifting measured by satellite radar interferometry, *Geophys. Res. Lett.*, **24**, 1843–1846.

Simons, M. & Rosen, P., 2007, Interferometric synthetic aperture radar geodesy, in *Treatise on Geophysics*, edited by T. Herring, vol. 3, chap. 12, pp. 391–446, Elsevier.

Simons, M., Fialko, Y., & Rivera, L., 2002, Coseismic deformation from the 1999 M w 7.1 Hector Mine, California, earthquake as inferred from InSAR and GPS observations, *Bull. Seismol. Soc. Am.*, **92**(4), 1390–1402.

Spence, D. & Turcotte, D., 1979, Viscoelastic relaxation of cyclic displacements on the San Andreas fault, *Proceedings of the Royal Society of London. Series A, Mathematical and Physical Sciences*, pp. 121–144.

Staples, R., White, R., Brandsdottir, B., Menke, W., Maguire, P., & Mcbride, J., 1997, Faroe-Iceland ridge experiment .1. crustal structure of northeastern Iceland, *J. Geophys. Res.*, **102**, 7849–7866.

Sturkell, E., Sigmundsson, F., & Slunga, R., 2006, 1983-2003 decaying rate of deflation at Askja caldera: Pressure decrease in an extensive magma plumbing system at a spreading plate boundary, *Bull. Volcanol.*, **68**(7-8), 727–735.

Tarantola, 2006, *Elements for Physics: Quantities, Qualities, and Intrinsic Theories*, Springer.

Thatcher, W., 1983, Non-linear strain buildup and the earthquake cycle on the San Andreas fault, *J. Geophys. Res.*, **88**(NB7), 5893–5902.

Thatcher, W., Foulger, G., Julian, B., Svarc, J., Quilty, E., & Bawden, G., 1999, Present-day deformation across the Basin and Range province, western United States, *Science*, **283**(5408), 1714.

Thomas, I. D., King, M. A., & Clarke, P. J., 2007, A comparison of GPS, VLBI and model estimates of ocean tide loading displacements, *J. Geod.*, **81**(5), 359–368.

Tryggvason, E., 1962, Curstal structure of the iceland region from dispersion of surface waves, *Bull. Seismol. Soc. Am.*, **52**, 359–388.

Tryggvason, E., 1984, Widening of the Krafla Fissure Swarm during the 1975-1981 valcano-tectonic episode, *Bull. Volcanol.*, **47**, 47–69.

Tryggvason, E., 1986, Multiple magma reservoirs in a rift-zone volcano - ground deformation and magma transport during the September 1984 eruption of Krafla, Iceland, *J. Volcanol. Geotherm. Res.*, **28**, 1–44.

Tryggvason, E., 1989, Ground deformation in Askja, Iceland - its source and possible relation to flow of the mantle plume, *J. Volcanol. Geotherm. Res.*, **39**, 61–71.

Urschl, C., Dach, R., Hugentobler, U., Schaer, S., & Beutler, G., 2005, Validating ocean tide loading models using GPS, *J. Geod.*, **78**(10), 616–625.

Vergnolle, M., Bouin, M.-N., Morel, L., Masson, F., Durand, S., Nicolas, J., & Melachroinos, S. A., 2008, GPS estimates of ocean tide loading in NW-France: determination of ocean tide loading constituents and comparison with a recent ocean tide model, *Geophys. J. Int.*, **173**(2), 444–458.

Vigny, C., de Chabalier, J., Ruegg, J., Huchon, P., Feigl, K., Cattin, R., Asfaw, L., & Kanbari, K., 2007, Twenty-five years of geodetic measurements along the Tadjoura-Asal rift system, Djibouti, East Africa, *J. Geophys. Res*, **112**.

Wallace, R., 1987, Grouping and migration of surface faulting and variations in slip rates on faults in the Great Basin province, *Bull. Seismol. Soc. Am.*, **77**, 868–876.

Weldon, R. J., Scharer, K. M., Fumal, T. E., & Biasi, G. P., 2004, Wrightwood and the earthquake cycle: What a long recurrence record tells us about how faults work, *GSA Today*, **14**, 4–10.

Williams, C., 2006, Development of a package for modeling stress in the lithosphere, *Eos Trans. AGU*, **87**, 36.

Williams, C. & Wadge, G., 2000, An accurate and efficient method for including the effects of topography in three-dimensional elastic models of ground deformation with applications to radar interferometry, *J. Geophys. Res.*, **105**, 8103–8120.

Williams, C., Aagaard, B., & Knepley, M., 2005, Development of software for studying earthquakes across multiple spatial and temporal scales by coupling quasi-static and dynamic simulations, *Eos Trans. AGU*, **86**, 52.

Wright, T., Ebinger, C., Biggs, J., Ayele, A., Yirgu, G., Keir, D., & Stork, A., 2006, Magma-maintained rift segmentation at continental rupture in the 2005 Afar dyking episode, *Nature*, **442**(7100), 291–294.

Wright, T. J., Parsons, B. E., & Lu, Z., 2004, Toward mapping surface deformation in three dimensions using InSAR, *Geophys. Res. Lett.*, **31**(1), L01607.

Zebker, H. & Villasenor, J., 1992, Decorrelation in interferometric radar echoes, *IEEE Trans. Geosci. Remote Sens.*, **30**(5), 950–959.

Zebker, H., Rosen, R., Goldstein, R., Gabriel, A., & Werner, C., 1994, On the derivation of coseismic displacement fields using differential radar interferometry: The Landers earthquake, *J. Geophys. Res.*, **99**(B 10), 19617–19634.